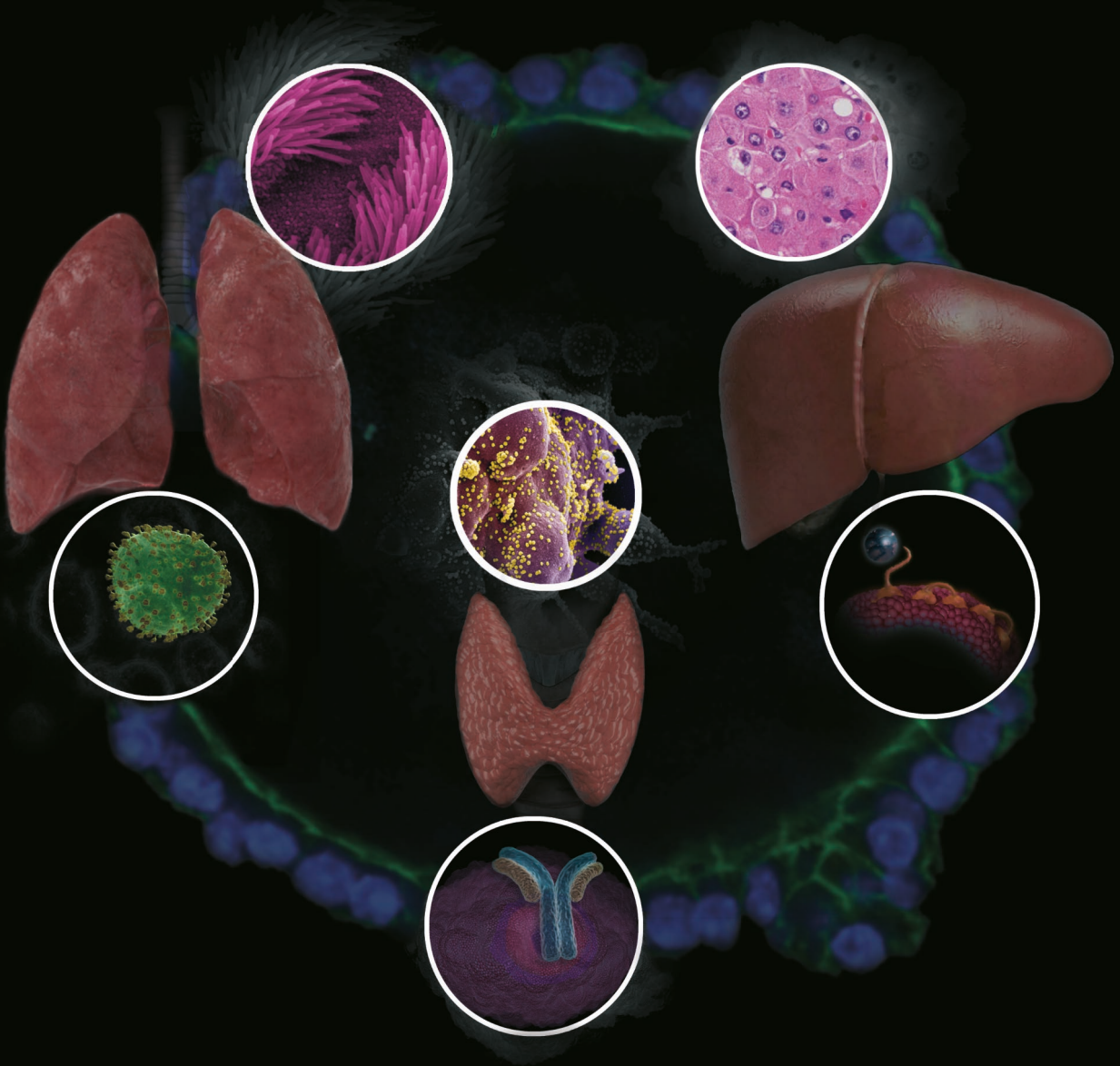


MODELLING OF A WIDE VARIETY OF DISEASE USING ADULT STEM CELL-DERIVED ORGANOIDS



JELTE VAN DER VAART

ADULT STEM CELL-DERIVED ORGANOIDS AS MODEL SYSTEMS FOR A WIDE VARIETY OF HUMAN DISEASES

Jelte Yoran van der Vaart

ISBN: 978-94-93278-04-2

Author: Jelte van der Vaart

Cover illustration: Joachim van Vondel

Layout and printing: Off Page, Amsterdam

Copyright © Jelte van der Vaart, All rights reserved

No part of this thesis may be reproduced, stored or transmitted in any form by any means without prior permission of the author. The copyright of the publications remains with the publishers.

Research described in this thesis was performed at the group of Prof. Dr. Hans Clevers at the Hubrecht Institute, Utrecht, The Netherlands

Printing of this thesis was financially supported by AMSBIO Europe B.V.

ADULT STEM CELL-DERIVED ORGANOIDS AS MODEL SYSTEMS FOR A WIDE VARIETY OF HUMAN DISEASES

ORGANOIDS UIT VOLWASSEN STAMCELLEN ALS MODEL VOOR EEN BREED SPECTRUM AAN ZIEKTEN

(met een samenvatting in het Nederlands)

Proefschrift

ter verkrijging van de graad van doctor aan de
Universiteit Utrecht
op gezag van de
rector magnificus, prof.dr. H.R.B.M. Kummeling,
ingevolge het besluit van het college voor promoties
in het openbaar te verdedigen op

donderdag 28 april 2022

des ochtends te

10.15 uur

door

Jelte Yoran van der Vaart
geboren op 2 januari 1994
te Zwijndrecht

PROMOTOR

Prof. dr. J.C. Clevers

TABLE OF CONTENTS

	Scope of the thesis	7
Chapter 1	Airway Organoids as Models of Human Disease	11
Chapter 2	Modelling of Primary Ciliary Dyskinesia using Patient-derived Airway Organoids	27
Chapter 3	The Organoid Platform: Promises and Challenges as Tools in the Fight against COVID-19	61
Chapter 4	SARS-CoV-2 productively Infects Human Gut Enterocytes	75
Chapter 5	Advancing Lung Organoids for COVID-19 Research	103
Chapter 6	An Organoid-derived Bronchioalveolar Model for SARS-CoV-2 Infection of Human Alveolar-type II-like Cells	117
Chapter 7	Adult Mouse and Human Organoids derived from Thyroid Follicular Cells and modelling of Graves' Hyperthyroidism	155
Chapter 8	Bacterially produced R-spondin3 increases Hepatocyte Proliferation independent of Liver Zonation	185
Chapter 9	Summarising Discussion	207
Addendum	Nederlandse samenvatting	221
	Curriculum Vitae and List of Publications	226
	Acknowledgements/Dankwoord	228

SCOPE OF THE THESIS

The research presented in this thesis focusses on the development of new model systems that allow deeper understanding of biology of diseases. Described model systems make use of adult stem cells. Stem cells can, in general, be subdivided into embryonal and adult stem cells. While embryonal stem cells are only present during development and have the potential to make up many diverse organs, adult stem cells can only be identified throughout the adult lifetime of the organism and are retained within the organ of interest. These adult stem cells replace the tissues in which they reside by undergoing cell division and subsequent differentiation into various other cell types. This replacement is required when cells are lost due to damage or because of natural organ turnover. This process is essential during development and growth but also to maintain homeostasis. We can make use of this epithelial renewal capacity to establish model systems that closely recapitulate the organ of origin. When this process leads to a three-dimensional structure resembling the original tissue and it can be maintained over an extensive period of time, we speak of organoids.

Organoids are three-dimensional *in vitro* culture systems derived from stem cells. In this thesis, we discuss organoids generated from earlier described adult stem cells. These adult stem cell-derived organoids are close representatives of the organ of interest due to the capabilities of self-renewal and differentiation of the stem cell population present in the culture. The culturing of adult stem cells was long believed to be impossible until Sato and colleagues generated the first organoid systems of the mouse intestine. By applying similar techniques, the arsenal was extended to a variety of mouse as well as human organoid systems including airway, stomach and liver organoids. Due to their representability to the *in vivo* situation, the organoids and their derivatives are useful tools to study fundamental biology but also human disease. Both disease biology as therapeutic interventions are characterised in a higher throughput setting when compared to clinical trials or mouse studies. Since organoids can be generated from limited patient material, a patient-specific biobank can be generated to cover all aspects of the disease. Additionally, organoids have been shown to be genetically editable with the use of CRISPR-Cas9. This allows for the modelling of genetic diseases by generating known mutation leading to a disease phenotype in organoids as well as repairing patient mutations in patient-derived organoids. Their expansion capacity as well as genomic stability could eventually allow organoids as replacement for transplantations. Presented adult stem cell-derived organoids, therefore, show great promise for the modelling of disease as well as provide potential new therapeutic opportunities. The studies in this thesis make use of the earlier developed intestinal or airway organoids as well as present the development of a new organoid culture of the thyroid.

Many signals are required to sustain the above-mentioned adult stem cells *in vivo* as well as *in vitro*. One of the most established pathway involved in adult stem cell survival is the Wnt pathway. Surrounding cells secrete Wnt ligands, which specifically bind

receptors present on stem cells. When the right receptors are bound, essential processes required for the maintenance of the stem cell population are upregulated. By tweaking the levels of downstream Wnt signalling, the stem cell population can be expanded, maintained or differentiated. Therefore, tight regulation of Wnt signalling is required to maintain homeostasis. Wnt signalling is regulated by downregulation of Wnt receptors on the cellular membrane to generate a stable level of receptors and thereby activation. External regulators of this homeostatic condition, like the molecule R-spondin, can potentiate Wnt signalling by decreasing Wnt receptor breakdown, stabilising the receptor on the membrane and maintaining or even increasing stem cell numbers. The essence of R-spondin is exemplified by the presence of the ligand in most to all adult stem cell-derived organoid culture systems. In parallel, *in vivo* manipulation of the R-spondin-Wnt axis could therefore allow for faster organ regeneration by potentiating stem cell population expansion.

In **Chapter 1**, we discuss the current literature of airway organoid systems and how they can be applied as models for disease. While the advances in airway organoids have grown exponentially in the last decade, many gaps remain, which require further development of new or more sophisticated (organoid) model systems. An example of the development of an adjusted model system using organoids is described in **Chapter 2**. We present a new differentiation protocol that allows extensive visualisation of ciliated cells in airway organoids. This protocol is applied to organoids derived from patients suffering from primary ciliary dyskinesia to study the biology of the disease. Additionally, we show the value of the patient-derived organoid systems on top of the current diagnostic procedures.

In **Chapter 3**, we discuss the use of organoids as tools for the research on COVID-19. We describe the current and potential future model systems for SARS-CoV-2 infections and potential future pandemics. **Chapter 4** illustrates the advantages of using intestinal organoids as well as airway organoid-derived cultures to study SARS-CoV-2 infection. We show the capability of SARS-CoV-2 to infect proliferating enterocytes. Since COVID-19 is classified with lung-related symptoms, we discuss the use of existing and newly developed lung organoid systems to model COVID-19 in **Chapter 5**. An example of the rapid extension of lung organoid-derived systems is shown in **Chapter 6** by the development of a SARS-CoV-2 permissive bronchioalveolar culture system. These cultures show upregulation of interferon pathways after SARS-CoV-2 infection similar to those observed in COVID-19 patients.

In **Chapter 7**, we describe the generation of a novel organoid system of thyroid follicular cells. We used adult tissue of mouse and human thyroid glands to develop an *in vitro* organoid system. The cells in the organoids express thyroid hormone machinery genes and show active secretion of thyroid hormones after stimulation. Moreover, we show the potential of using these organoids as models for Graves' disease. The results of our study is the first to report an organoid-based model of a human autoimmune disease.

Chapter 8 extends the knowledge of adult stem cells and the requirement of Wnt signalling in organoid culture to in vivo. We optimised earlier developed R-spondin production methods to allow systemic injection of the Wnt potentiator in mice. We show increased proliferation in hepatocytes over seven days after injection. This proliferation is not limited to Wnt-active zones in the liver.

Chapter 9 summarises and discusses the presented data. Additionally, I explore future applications of the results presented in this thesis and potential future efforts for other disease models.

CHAPTER

AIRWAY ORGANOID AS MODELS OF HUMAN DISEASE

Jelte van der Vaart^{1,2}, Hans Clevers^{1,2,3}

¹ Hubrecht Institute, Royal Netherlands Academy of Arts and Sciences
(KNAW) and University Medical Centre Utrecht,
3584 CT Utrecht, the Netherlands

² Oncode Institute, Hubrecht Institute, 3584 CT Utrecht, the Netherlands

³ Princess Máxima Center for Paediatric Oncology,
3584 CS Utrecht, The Netherlands.

*Published in Journal of Internal Medicine (2021);
doi: 10.1111/joim.13075*



ABSTRACT

Studies developing and applying organoid technology have greatly increased in volume and visibility over the past decade. Organoids are three-dimensional structures that are established from pluripotent stem cells (PSCs) or adult tissue stem cells (ASCs). They consist of organ-specific cell types that self-organise through cell-sorting and spatially restricted lineage commitment to generate architectural and functional characteristics of the tissue of interest. The field of respiratory development and disease has been particularly productive in this regard. Starting from human cells (PSCs or ASCs), models of the two segments of the lung, the airways and the alveoli, can be built. Such organoids allow the study of development, physiology and disease and thus bridge the gap between animal models and clinical studies. This review discusses current developments in the pulmonary organoid field, highlighting the potential and limitations of current models.

INTRODUCTION

The primary role of the pulmonary system is the exchange of O_2 and CO_2 . The epithelium of the lung derives from the endodermal foregut through progressive branching. Anatomically, the airways can be divided into two main compartments: the airways and the alveoli. The upper and lower airways conduct the airflow to the distal alveoli where the vital process of gas exchange between outside air and the underlying vasculature takes place. An essential function of the pulmonary tree is the clearance of dust particles and microbes. To fulfil these processes, the upper airway epithelium consists of multiple cell types: club-, goblet-, ciliated-, neuroendocrine- and basal cells (**Figure 1**). The alveoli are comprised of two main subtypes of epithelial cells that serve independent functions. Gas exchange is facilitated by alveolar epithelial cells type one (AEC1s) while alveolar epithelial cells type two (AEC2s) are responsible for the secretion of surfactant that reduces surface tension to allow alveolar expansion without collapse (**Figure 1**). Recent studies have described new subclasses within individual cell types¹ and a new rare cell type: the ionocyte². Technologies such as single cell RNA sequencing might reveal further complexity in the cellular composition of the airway³. It appears obvious that model systems that capture this complexity facilitate better understanding of the respiratory system and its cell types.

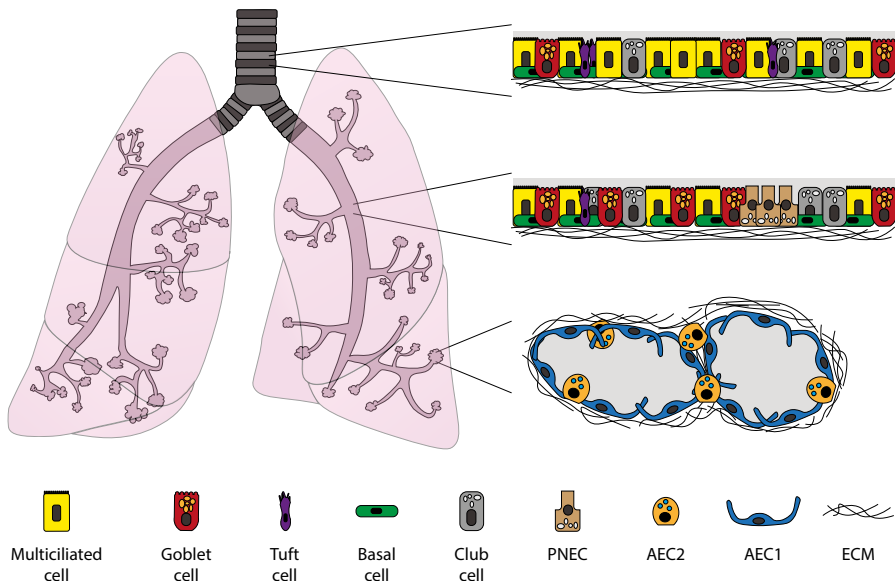


Figure 1. Schematic representation of the different areas in the pulmonary system. The upper panel shows the cell composition of the trachea and upper airways. The middle panel is a schematic representation of the upper bronchioles. The lower shows the most distal area of the lungs, the alveoli. PNEC = pulmonary neuroendocrine cell, AEC2 = alveolar epithelial cell type 2, AEC1 = alveolar epithelial cell type 1, ECM = extracellular matrix. Light grey depicts air flowing through the pulmonary system and thereby apical side of the cells.

Multiple groups have reported on the development of organoids that represent airway and alveolar epithelium. In this review, we discuss these new tools and other recent advances in developing models for human lung development, function and disease.

GENERAL BACKGROUND OF THE ORGANOID FIELD

In adult organs, functionality is dependent on synergistic interaction of the various cell types that are structured in a three-dimensional (3D) architecture. This 3D structure is essential for the function of the organ⁴. However, currently most *in vitro* approaches make use of two-dimensional (2D) monolayers. It has been known since the early 1900s that removing cells from their native environment and architecture into two-dimensional cultures leads to loss of tissue-specific functioning of the cells. The work of Mina Bissell and others has revealed the importance of architectural cues during development⁵ but also in tumorigenesis^{6,7}. Thus, mimicking the 3D architecture appears essential for representative *in vitro* model systems^{7,8}.

During the past decade, the understanding of human stem cell biology has deepened and the availability of tools for 3D cell culturing have increased. This has allowed the establishment of stem cell-derived organoid cultures. While long-term 2D culturing of primary human epidermal cells was already established in 1975 by Rheinwald and Green⁹, 3D human stem cell-derived organoid technology as discussed in this review has been developed over the past decade. In this review, the term organoid will refer to a 3D structure grown from stem cells and consisting of organ-specific cell types that self-organise through cell-sorting and spatially restricted lineage commitment¹⁰. These organoids can be classified into two main types, depending on the stem cell used: 1) Pluripotent stem cells (PSCs) that include both embryonic stem cells (ESCs) and induced pluripotent stem cells (iPSCs). These cells represent the earliest stages of embryonic development. PSCs can in principle generate all cell types of the human body. 2) Organ-specific adult stem cells (ASCs). These stem cells maintain tissues and organs throughout life. Their activity is restricted to the production of cell types of the tissue in which they reside.

EXPLOITING DEVELOPMENTAL PROCESSES TO CREATE PSC-DERIVED ORGANOIDS

PSCs can be derived from cells of a human embryo (referred to as ESCs) and by reprogramming human somatic cells (referred to as iPSCs)¹¹. Both cell types have the ability to differentiate into all cell types. Inspired by insights from embryonic development, serial manipulation of combinations of signalling pathways can be used to generate specific human organoid types. To date, multiple human organoid types, including for the brain¹², kidney¹³, intestine¹⁴, liver¹⁵, retina¹⁶ and stomach¹⁷ have been derived from PSCs. Examples of these PSC-derived organoids have been used for disease modelling in the central nervous system^{12,18–21}, liver¹⁵, intestine^{14,22}, kidney²³ and

stomach^{17,24}. Exploitation of the signals that control pulmonary development has allowed generation of PSC-derived airway organoids.

To generate functional airway organoids PSCs are differentiated via a stepwise protocol (via definitive endoderm- and lung progenitor stages) into mature airway epithelium^{25,26,35,36,27–34}. Over the past years, differentiation protocols have been continuously improved, but most modifications have been minor. Activation of transforming growth factor β (TGF β) signalling is essential for the initial differentiation of PSCs towards definitive endoderm³⁶. Some studies retain Wnt signalling activation as initially proposed by D'Amour *et al.* by adding Wnt3a^{29,30,36} or the Wnt agonist CHIR99021³². Other protocols supplement bone morphogenic protein (BMP) 4 to the medium^{25,27}. After activating TGF β signalling, the inhibition of the same pathway is essential for further differentiation towards anterior foregut. Some studies complement the differentiation medium with BMP4^{26,30,37} while other studies do the opposite: they inhibit BMP signalling by supplying the BMP inhibitor Noggin^{32,33}. The final step of differentiation requires the addition of fibroblast growth factors (FGFs). Differentiation is most efficiently achieved through supplementation of FGF2, FGF7 and FGF10 and the addition of BMP4^{26,27,29,30,33,34,37}. These protocols differentiate the PSCs towards mature airway epithelium. Initial attempts did not fully recapitulate the multiple cell types present in the adult lung^{29,30}. Gotoh *et al.* managed to obtain alveolar as well as bronchiolar epithelium by growing spheroids in three-dimensional cultures. They first generated ventral anterior foregut endoderm cells to subsequently create 3D airway structures from these. Markers of both AEC1s and AEC2s were present in the epithelial structures³⁸. This differentiation was more efficient than previously described differentiation in 2D cultures^{25,26}. A recent study reported the appearance of a branching morphology and proximal-distal compartmentalisation. In addition to the AEC cell types, upper airway goblet cells were observed³⁹. After a culture of more than 160 days, the organoids contained multiple branching points and were macroscopically visible. These pulmonary epithelial organoids were, moreover, susceptible to respiratory syncytial virus (RSV) infection^{39,40}. PSC-derived lung organoids have been used in modelling fibrotic lung disease⁴¹, surfactant deficiencies⁴² and Hermansky-Pudlak Syndrome Type 2⁴³. PSC-derived organoids have also been implemented as models for pneumonitis⁴⁴ and early manifestations of small cell lung cancer⁴⁵.

USING TISSUE-RESIDENT STEM CELLS TO GENERATE ORGANOIDS

To overcome the technical challenges of differentiating the PSCs, the field of lung disease modelling has also tried to use fully committed adult cells to generate organoids. For the development of these model systems, insights into the location and identity of a stem cell pool would appear crucial. Tissue-resident adult stem cells (ASCs) can be identified based on their potential for self-renewal and differentiation into multiple cell lineages. Discovery of the stem cell pool in the small intestine and isolation of these tissue-resident

1

2

3

4

5

6

7

8

9

&

stem cells has allowed the formation of 3D gut organoids. These organoids contain all cell types present in the *in vivo* intestine. They can be maintained and expanded *in vitro* in a 3D-matrix when supplemented with a cocktail of growth factors⁴⁶. Increased efforts using the same principles have allowed the generation of other adult stem cell-derived organoids including stomach^{47,48}, liver⁴⁹⁻⁵³, pancreas^{54,55}, colon⁵⁶⁻⁵⁹, prostate⁶⁰, fallopian tube⁶¹, endometrium^{62,63}, mammary gland⁶⁴, salivary gland^{65,66} and others.

Unlike the gut epithelium, the lung epithelium is only slowly self-renewing under non-damage conditions. Upon injury, basal cells can recreate themselves as well as generate all other cell types of the airway epithelium, identifying these as a lung-resident stem cell pool⁶⁷⁻⁷³. Basal cells rest directly on the basal lamina from where they give rise to the cells needed for mucociliary clearance: secretory and multi-ciliated cells⁷³. Multiple studies have demonstrated that club cells can similarly generate the other airway cell lineages upon damage. Although the airway and alveolar epithelium are generally seen as separately maintained compartments, club cells of the airways are reported to also give rise to the AEC1s and AEC2s of the alveolar epithelium *in vivo*⁷⁴⁻⁷⁶. The transdifferentiation of club cells into basal cells is seen as evidence of plasticity. Additionally, it has been shown that pulmonary neuroendocrine cells (PNECs) are able to self-renew and differentiate into club and ciliated cells⁷⁷. In the alveoli, AEC2s serve as a resident stem cell population. Upon loss of alveolar cells, this cell population is able to self-renew and differentiate into AEC1s⁷⁸. This transition is facilitated by a separate population of AEC2s that receives niche signals such as Wnt⁷⁹⁻⁸². Thus, a picture has emerged that self-renewal and repair of the pulmonary epithelium is driven by extensive plasticity, and not by a single hard-wired and undifferentiated stem cell: while basal cells could be viewed as a classical stem cell, the airway club cells or the fully differentiated AEC2 cells in alveoli definitely do not fit that bill.

As mentioned, recreating the *in vivo* environment *in vitro* is a prerequisite for building tissues in a dish. A favoured technique in the culturing of primary bronchiolar basal cells has been air-liquid interphase (ALI) culturing. These ALI-cultures mimic the interaction of the cells with the outside air at their apical side while being exposed to a nutrient- and growth factor-rich medium on their basal side. These ALI-cultures allow cells to form 2D monolayers, unlike the 3D structures that they form *in vivo*⁸³. Initial attempts at growing the cells in 3D used basal cells sorted for expression of Nerve Growth Factor Receptor (NGFR) and Integrin Subunit Alpha 6 (ITGA6)⁶⁷. When seeded into ALI cultures, these basal cells self-organise into 3D-structures termed bronchospheres. These spheres are comprised of an outer layer of basal cells while the inner layer shows signs of mucociliary differentiation⁶⁷. Bronchospheres can serve to identify essential signals for pulmonary ASC (basal cell) proliferation and maintenance. Bronchosphere can also be used to study which signals drive directional differentiation into any of the epithelial cell types. The latter approach was exemplified by the discovery that NOTCH inhibition limits goblet cell metaplasia *in vitro*. Multiple Notch-inhibitory compounds are available, promising a role for NOTCH inhibition in the treatment of chronic obstructive pulmonary disease (COPD)⁸⁴.

The culturing of bronchospheres was further optimised to generate mature bronchospheres in a high-throughput system by Hild and Jaffe⁸⁵. This optimised protocol demonstrated the potential of the system for large screens for respiratory disease therapeutics.

AEC2s show a comparable behaviour when cultured in 3D-ALI cultures. In combination with lung stromal cells, AEC2s form alveolospheres and differentiate into 3D structures that are comprised of both AEC2s and AEC1s⁷⁸. The ASC-derived alveolospheres appear comparable to the PSC-derived organoids from Gotoh *et al.*³⁸. ASC-derived alveolospheres have shown potential for disease modelling of lower airway deficiencies such as idiopathic pulmonary fibrosis^{78,86}. Kobayashi *et al.* used murine alveolospheres to identify the mechanism of transition of AEC2s to AEC1s. Pre-alveolar type 1 transitional cell state (PATS) cells were identified in alveolosphere organoid cultures. These cells are marked by *keratin19* (*Krt19*), *claudin4* (*Cldn4*) and *stratifin* (*Sfn*). PATS cells arise from AEC2s upon injury and allow differentiation into AEC1s. PATS-like cells were also enriched in human fibrotic lungs⁸². Understanding PATS-like cell biology may contribute to our understanding of idiopathic pulmonary fibrosis.

Similar to AEC2s (and somewhat surprisingly), club cells can reportedly also give rise to alveolospheres. When club cells are cultured in a 3-dimensional matrix, they yield both AEC1s and AEC2s organised in a 3D architecture⁸⁷.

While these 3D spheres show promise in generating human-relevant model systems for disease, the organoids described above can only be maintained for a short time period and can for instance not be subcloned. While long-term culturing of basal cells was achieved in 2016 in the form of 2D monolayers³⁷, the field was still in need of an ASC-derived long-term model system that allows *in vitro* representation of all epithelial cell types while also generating 3D-structures in a more natural configuration.

Emma Rawlins and co-workers were the first to generate a model system that allowed long-term disease modelling in ASC-derived organoids. They used primary foetal lung tip progenitors to generate 3D structures. These murine organoids can be maintained long-term in expansion conditions but can also be differentiated into bronchiolar and alveolar cell types⁸⁸. Recently, we reported long-term culture conditions for adult human lung tissue-derived airway organoids⁸⁹. Primary human lung tissue was digested and seeded in a growth factor cocktail and 3D Matrigel. The cells self-organised into spheres similar to the bronchospheres observed by Hogan and colleagues⁶⁷. The cocktail of growth factors resembles that found in the final differentiation step of the PSCs (i.e. in including FGF7 and FGF10). Organoids grown under this condition proliferate and can be expanded for at least a year as 3D-structures (**Figure 2A**). The ASC-derived organoids also require BMP- and TGF β -inhibition that allow the maintenance of the basal cell population that is required for long-term culture. Similar to the bronchospheres, the outer layer of the organoids is comprised of basal cells while most bronchiolar cell types can be found on the luminal side of the organoid (**Figure 2B**).

It was shown that human lung cancers can be grown under the same culture conditions. The tumour organoids displayed similar mRNA expression and histological profiles as

1

2

3

4

5

6

7

8

9

&

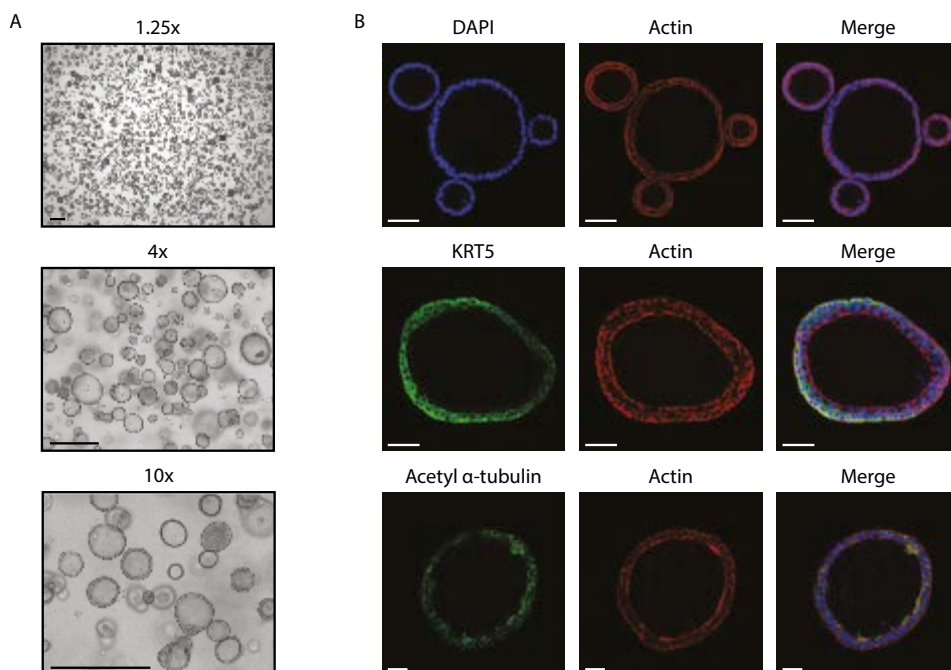


Figure 2. Airway organoids derived from human adult tissue. (a) Brightfield images of 1.25 \times , 4 \times and 10 \times magnification of airway organoids. Scale bar = 500 μ m. (b) Confocal images taken from whole mount stained airway organoids. Middle panel shows basal cell layer with KRT5- cells apical of this cell layer. Lower panel shows multiciliated cells on the inner cell layer of the organoid. Scale bar is 50 μ m. All images are taken by JvdV.

the original tumours. Tumour organoids could be used for drug screening *in vitro* or upon xenotransplantation⁸⁹. Of note, an earlier version of this approach (lacking extracellular matrix and the complex growth factor cocktail had already been shown to allow the outgrowth of ‘tumour spheroids’, that did however not maintain the full heterogeneity of the tumour⁹⁰. The airway organoids were shown to model a genetic disease (cystic fibrosis)⁸⁹ and infectious diseases like RSV⁸⁹, enterovirus⁹¹, cryptosporidium⁹² and influenza virus infection^{93,94}. The diversity in cell types and the availability of these cell types over long periods of culture promises that airway organoids can be applied for the modelling of many additional diseases.

DISCUSSION AND FUTURE PERSPECTIVES

We have discussed the two main strategies for growing 3D lung organoids. These strategies use different starting cells (PSCs versus ASCs) and different growth factor protocols but share the same goal: to generate a model system that phenocopies key structural and functional aspects of the *in vivo* pulmonary epithelium. Both PSC- as ASC-derived organoids are beginning to contribute to answer a variety of basic and clinical































	Multiple cell types	3D	Long-term modelling (Passaging)	Adult/ Developmental		
 Air-liquid interphase				Adult		Mesenchymal cell
 Alveolospheres				Adult		Tuft cell
 Bronchospheres				Adult		Club cell
 iPSC-derived lung organoid				Development		PNEC
 ASC-derived lung organoid				Adult		Lung progenitor cell
						Goblet cell
						Basal cell
						AEC2
						AEC1
						Multiciliated cell

Figure 3. Overview of available primary pulmonary cell culture systems. The characteristics are indicated for the latest development of the system: Air-liquid interphase, alveolospheres, bronchospheres, iPSC-derived lung organoids and ASC-derived lung organoid. PNEC = pulmonary neuroendocrine cell, AEC2 = alveolar epithelial cell type 2, AEC1 = alveolar epithelial cell type 1.

questions. The two approaches are largely complementary. For example, PSC-derived organoids can be generated from iPS cells that derive from patients with genetic diseases in order to model the effects of the genetic defect on the various developmental stages of the lung. PSC-derived organoids can thus be useful to simulate embryonic development and aid research on diseases that have a developmental origin. Generally, iPSC-derived organoids do not yield the mature cell types seen in adult tissues and may therefore not always closely resemble the adult manifestations of a disease^{33,38,39}. This holds true in particular for lung cancer, where the derivation of iPSC cells from the tumor (rather than directly deriving cancer organoids) would appear to be an unnecessary detour. ASC-derived organoids reflect the more mature stages of the adult lung and can be directly derived from bronchoalveolar lavage material from individual patient. One important remark: no protocols have been published that support long-term expansion of alveolar organoids established from adult human lung.

Organoid technology can be combined with recent advances in genome editing based on CRISPR/Cas9^{95,96}. Questions that recently could only be answered with genetic mouse models can now be addressed using *in vitro* created human airway organoids.

Apart from the genetic tools available for gene-specific research questions, PSC- as well as ASC-derived organoids can make direct use of patient-derived cells. This allows for personalised disease modelling, crucial for defining patient variation in therapeutic response and disease progression. This personalised model approach has already shown promise in predicting patient-specific drug response for gastrointestinal cancers^{97,98} and cystic fibrosis⁹⁹⁻¹⁰¹.

Having said all this, organoids remain highly reductionist versions of real tissues. ASC-derived organoids are comprised of multiple lung epithelial cell types^{39,89}, while PSC-derived organoids even contain some mesenchymal cells³⁹. Yet, key non-epithelial components are absent from the current version of organoids. Functional interactions between the epithelium and the surrounding mesenchyme are not modelled beyond the presence of fixed concentrations of mesenchyme-derived signalling molecules and extracellular matrix. Such interactions are essential in controlling developmental processes and defining the characteristics of a respiratory disease¹⁰². Incorporation of non-epithelial cells such as endothelial, smooth muscle and immune cells will eventually yield more faithful phenocopies of the real organ¹⁰³. Indeed, the introduction of mesenchymal cells in the culture has already been shown to improve the culture of alveolospheres⁷⁸.

Finally, one long-term goal of the organoid technology may be in regenerative medicine, e.g. to complement whole-organ transplantation. Cultured organoids may serve as a sustainable source of functional cells. Several hurdles remain to accomplish this. Safety of cultured stem cells will need to be assessed, as one may fear the development of neoplasms from the cultured stem cells. Efficient approaches will have to be developed to deliver the organoid cells to the lungs. To increase engraftment of lung epithelial cells, Rosen *et al.* employed a strategy of 'preconditioning', routinely used for bone marrow transplantation: After ablation of resident stem cells by sublethal irradiation, engraftment of fetal lung epithelial cell preparations injected intravenously was increased significantly¹⁰⁴. Similarly, de-epithelialisation by infusing a detergent in rat lungs allowed engraftment of iPSC-derived human lung organoids. These organoids were implanted through the airways, which minimises the possibility of ectopic engraftment compared to intravenous injection. The grafts were present in the distal alveolar tips and showed cells expressing apical markers specific to AEC1s and AEC2s¹⁰⁵. Better characterisation of long-term engraftment and functionality is however still needed.

Altogether, organoids hold promise for basic research and clinical application in pulmonology.

REFERENCES

1. Reyfman, P. A. et al. Single-Cell Transcriptomic Analysis of Human Lung Provides Insights into the Pathobiology of Pulmonary Fibrosis. *Am. J. Respir. Crit. Care Med.* **199**, 1517–1536 (2019).
2. Plasschaert, L. W. et al. A single-cell atlas of the airway epithelium reveals the CFTR-rich pulmonary ionocyte. *Nature* **560**, 377–381 (2018).
3. Schiller, H. B. et al. The Human Lung Cell Atlas: A High-Resolution Reference Map of the Human Lung in Health and Disease. *Am. J. Respir. Cell Mol. Biol.* **61**, 31–41 (2019).
4. Nadkarni, R. R., Abed, S. & Draper, J. S. Organoids as a model system for studying human lung development and disease. *Biochem. Biophys. Res. Commun.* **473**, 675–682 (2016).
5. Mammoto, T. & Ingber, D. E. Mechanical control of tissue and organ development. *Development* **137**, 1407–1420 (2010).
6. Bissell, M. J. & Radisky, D. Putting tumours in context. *Nat. Rev. Cancer* **1**, 46–54 (2001).
7. Inman, J. L. & Bissell, M. J. Apical polarity in three-dimensional culture systems: where to now? *J. Biol.* **9**, 2 (2010).
8. Bissell, M. J., Kenny, P. A. & Radisky, D. C. Microenvironmental Regulators of Tissue Structure and Function Also Regulate Tumor Induction and Progression: The Role of Extracellular Matrix and Its Degrading Enzymes. *Cold Spring Harb. Symp. Quant. Biol.* **70**, 343–356 (2005).
9. Rheinwald, J. G. & Green, H. Serial cultivation of strains of human epidermal keratinocytes: the formation of keratinizing colonies from single cells. *Cell* **6**, 331–43 (1975).
10. Clevers, H. Modeling Development and Disease with Organoids. *Cell* **165**, 1586–1597 (2016).
11. Takahashi, K. et al. Induction of Pluripotent Stem Cells from Adult Human Fibroblasts by Defined Factors. *Cell* **131**, 861–872 (2007).
12. Lancaster, M. A. et al. Cerebral organoids model human brain development and microcephaly. *Nature* **501**, 373–379 (2013).
13. Takasato, M. et al. Directing human embryonic stem cell differentiation towards a renal lineage generates a self-organizing kidney. *Nat. Cell Biol.* **16**, 118–126 (2014).
14. Spence, J. R. et al. Directed differentiation of human pluripotent stem cells into intestinal tissue in vitro. *Nature* **470**, 105–109 (2011).
15. Coll, M. et al. Generation of Hepatic Stellate Cells from Human Pluripotent Stem Cells Enables In Vitro Modeling of Liver Fibrosis. *Cell Stem Cell* **23**, 101–113.e7 (2018).
16. Nakano, T. et al. Self-Formation of Optic Cups and Storable Stratified Neural Retina from Human ESCs. *Cell Stem Cell* **10**, 771–785 (2012).
17. McCracken, K. W. et al. Modelling human development and disease in pluripotent stem-cell-derived gastric organoids. *Nature* **516**, 400–4 (2014).
18. Cugola, F. R. et al. The Brazilian Zika virus strain causes birth defects in experimental models. *Nature* **534**, 267–71 (2016).
19. Dang, J. et al. Zika Virus Depletes Neural Progenitors in Human Cerebral Organoids through Activation of the Innate Immune Receptor TLR3. *Cell Stem Cell* **19**, 258–265 (2016).
20. Garcez, P. P. et al. Zika virus impairs growth in human neurospheres and brain organoids. *Science* **352**, 816–8 (2016).
21. Qian, X. et al. Brain-Region-Specific Organoids Using Mini-bioreactors for Modeling ZIKV Exposure. *Cell* **165**, 1238–1254 (2016).
22. Leslie, J. L. et al. Persistence and Toxin Production by *Clostridium difficile* within Human Intestinal Organoids Result in Disruption of Epithelial Paracellular Barrier Function. *Infect. Immun.* **83**, 138–145 (2015).
23. Freedman, B. S. et al. Modelling kidney disease with CRISPR-mutant kidney organoids derived from human pluripotent epiblast spheroids. *Nat. Commun.* **6**, 8715 (2015).
24. Bertaux-Skeirik, N. et al. CD44 Plays a Functional Role in *Helicobacter pylori*-

- induced Epithelial Cell Proliferation. *PLOS Pathog.* **11**, e1004663 (2015).
25. Green, M. D. et al. Generation of anterior foregut endoderm from human embryonic and induced pluripotent stem cells. *Nat. Biotechnol.* **29**, 267–272 (2011).
 26. Longmire, T. A. et al. Efficient derivation of purified lung and thyroid progenitors from embryonic stem cells. *Cell Stem Cell* **10**, 398–411 (2012).
 27. Huang, S. X. L. et al. Efficient generation of lung and airway epithelial cells from human pluripotent stem cells. *Nat. Biotechnol.* **32**, 84–91 (2014).
 28. Mou, H. et al. Generation of Multipotent Lung and Airway Progenitors from Mouse ESCs and Patient-Specific Cystic Fibrosis iPSCs. *Cell Stem Cell* **10**, 385–397 (2012).
 29. Wong, A. P. et al. Directed differentiation of human pluripotent stem cells into mature airway epithelia expressing functional CFTR protein. *Nat. Biotechnol.* **30**, 876–82 (2012).
 30. Firth, A. L. et al. Generation of multiciliated cells in functional airway epithelia from human induced pluripotent stem cells. *Proc. Natl. Acad. Sci. U. S. A.* **111**, E1723-30 (2014).
 31. McIntyre, B. A. S. et al. Expansive Generation of Functional Airway Epithelium From Human Embryonic Stem Cells. *Stem Cells Transl. Med.* **3**, 7–17 (2014).
 32. Konishi, S. et al. Directed Induction of Functional Multi-ciliated Cells in Proximal Airway Epithelial Spheroids from Human Pluripotent Stem Cells. *Stem cell reports* **6**, 18–25 (2016).
 33. Dye, B. R. et al. In vitro generation of human pluripotent stem cell derived lung organoids. *Elife* **4**, (2015).
 34. McCauley, K. B. et al. Efficient Derivation of Functional Human Airway Epithelium from Pluripotent Stem Cells via Temporal Regulation of Wnt Signaling. *Cell Stem Cell* **20**, 844-857.e6 (2017).
 35. Wilkinson, D. C. et al. Development of a Three-Dimensional Bioengineering Technology to Generate Lung Tissue for Personalized Disease Modeling. *Stem Cells Transl. Med.* **6**, 622–633 (2017).
 36. D'Amour, K. A. et al. Efficient differentiation of human embryonic stem cells to definitive endoderm. *Nat. Biotechnol.* **23**, 1534–1541 (2005).
 37. Mou, H. et al. Dual SMAD Signaling Inhibition Enables Long-Term Expansion of Diverse Epithelial Basal Cells. *Cell Stem Cell* **19**, 217–231 (2016).
 38. Gotoh, S. et al. Generation of alveolar epithelial spheroids via isolated progenitor cells from human pluripotent stem cells. *Stem cell reports* **3**, 394–403 (2014).
 39. Chen, Y.-W. et al. A three-dimensional model of human lung development and disease from pluripotent stem cells. *Nat. Cell Biol.* **19**, 542–549 (2017).
 40. Porotto, M. et al. Authentic Modeling of Human Respiratory Virus Infection in Human Pluripotent Stem Cell-Derived Lung Organoids. *MBio* **10**, e00723-19 (2019).
 41. Strikoudis, A. et al. Modeling of Fibrotic Lung Disease Using 3D Organoids Derived from Human Pluripotent Stem Cells. *Cell Rep.* **27**, 3709-3723.e5 (2019).
 42. Jacob, A. et al. Differentiation of Human Pluripotent Stem Cells into Functional Lung Alveolar Epithelial Cells. *Cell Stem Cell* **21**, 472-488.e10 (2017).
 43. Korogi, Y. et al. In Vitro Disease Modeling of Hermansky-Pudlak Syndrome Type 2 Using Human Induced Pluripotent Stem Cell-Derived Alveolar Organoids. *Stem Cell Reports* **12**, 431–440 (2019).
 44. Lim, H. K. et al. Severe influenza pneumonitis in children with inherited TLR3 deficiency. *J. Exp. Med.* **216**, 2038–2056 (2019).
 45. Chen, H. J. et al. Generation of pulmonary neuroendocrine cells and SCLC-like tumors from human embryonic stem cells. *J. Exp. Med.* **216**, 674–687 (2019).
 46. Sato, T. et al. Single Lgr5 stem cells build crypt-villus structures in vitro without a mesenchymal niche. *Nature* **459**, 262–265 (2009).
 47. Stange, D. E. et al. Differentiated Troy+ Chief Cells Act as Reserve Stem Cells to Generate All Lineages of the Stomach Epithelium. *Cell* **155**, 357–368 (2013).
 48. Barker, N. et al. Lgr5+ve Stem Cells Drive Self-Renewal in the Stomach and Build

- Long-Lived Gastric Units In Vitro. *Cell Stem Cell* **6**, 25–36 (2010).
49. Huch, M. et al. Long-term culture of genome-stable bipotent stem cells from adult human liver. *Cell* **160**, 299–312 (2015).
 50. Huch, M. et al. In vitro expansion of single Lgr5+ liver stem cells induced by Wnt-driven regeneration. *Nature* **494**, 247–250 (2013).
 51. Peng, W. C. et al. Inflammatory Cytokine TNF α Promotes the Long-Term Expansion of Primary Hepatocytes in 3D Culture. *Cell* **175**, 1607–1619.e15 (2018).
 52. Hu, H. et al. Long-Term Expansion of Functional Mouse and Human Hepatocytes as 3D Organoids. *Cell* **175**, 1591–1606.e19 (2018).
 53. Sampaziotis, F. et al. Reconstruction of the mouse extrahepatic biliary tree using primary human extrahepatic cholangiocyte organoids. *Nat. Med.* **23**, 954–963 (2017).
 54. Huch, M. et al. Unlimited in vitro expansion of adult bi-potent pancreas progenitors through the Lgr5/R-spondin axis. *EMBO J.* **32**, 2708–21 (2013).
 55. Loomans, C. J. M. et al. Expansion of Adult Human Pancreatic Tissue Yields Organoids Harboring Progenitor Cells with Endocrine Differentiation Potential. *Stem cell reports* **10**, 712–724 (2018).
 56. Jung, P. et al. Isolation and in vitro expansion of human colonic stem cells. *Nat. Med.* **17**, 1225–1227 (2011).
 57. Sato, T. et al. Long-term Expansion of Epithelial Organoids From Human Colon, Adenoma, Adenocarcinoma, and Barrett's Epithelium. *Gastroenterology* **141**, 1762–1772 (2011).
 58. Li, X. et al. Oncogenic transformation of diverse gastrointestinal tissues in primary organoid culture. *Nat. Med.* **20**, 769–777 (2014).
 59. van de Wetering, M. et al. Prospective derivation of a living organoid biobank of colorectal cancer patients. *Cell* **161**, (2015).
 60. Karthaus, W. R. et al. Identification of Multipotent Luminal Progenitor Cells in Human Prostate Organoid Cultures. *Cell* **159**, 163–175 (2014).
 61. Kessler, M. et al. The Notch and Wnt pathways regulate stemness and differentiation in human fallopian tube organoids. *Nat. Commun.* **6**, 8989 (2015).
 62. Turco, M. Y. et al. Long-term, hormone-responsive organoid cultures of human endometrium in a chemically defined medium. *Nat. Cell Biol.* **19**, 568–577 (2017).
 63. Boretto, M. et al. Development of organoids from mouse and human endometrium showing endometrial epithelium physiology and long-term expandability. *Development* **144**, 1775–1786 (2017).
 64. Sachs, N. et al. A Living Biobank of Breast Cancer Organoids Captures Disease Heterogeneity. *Cell* **172**, 373–386.e10 (2018).
 65. Maimets, M. et al. Long-Term In Vitro Expansion of Salivary Gland Stem Cells Driven by Wnt Signals. *Stem Cell Reports* **6**, 150–162 (2016).
 66. Pringle, S. et al. Human Salivary Gland Stem Cells Functionally Restore Radiation Damaged Salivary Glands. *Stem Cells* **34**, 640–652 (2016).
 67. Rock, J. R. et al. Basal cells as stem cells of the mouse trachea and human airway epithelium. *Proc. Natl. Acad. Sci.* **106**, 12771–12775 (2009).
 68. Evans, M. J., Van Winkle, L. S., Fanucchi, M. V & Plopper, C. G. Cellular and molecular characteristics of basal cells in airway epithelium. *Exp. Lung Res.* **27**, 401–15 (2001).
 69. Boers, J. E., Ambergen, A. W. & Thunissen, F. B. J. M. Number and Proliferation of Basal and Parabasal Cells in Normal Human Airway Epithelium. *Am. J. Respir. Crit. Care Med.* **157**, 2000–2006 (1998).
 70. Schoch, K. G. et al. A subset of mouse tracheal epithelial basal cells generates large colonies in vitro. *Am. J. Physiol. Cell. Mol. Physiol.* **286**, L631–L642 (2004).
 71. Hong, K. U., Reynolds, S. D., Watkins, S., Fuchs, E. & Stripp, B. R. In vivo differentiation potential of tracheal basal cells: evidence for multipotent and unipotent subpopulations. *Am. J. Physiol. Cell. Mol. Physiol.* **286**, L643–L649 (2004).
 72. Borthwick, D. W., Shahbazian, M., Krantz, Q. T., Dorin, J. R. & Randell, S. H. Evidence

- for stem-cell niches in the tracheal epithelium. *Am. J. Respir. Cell Mol. Biol.* **24**, 662–70 (2001).
73. Rock, J. R., Randell, S. H. & Hogan, B. L. M. Airway basal stem cells: a perspective on their roles in epithelial homeostasis and remodeling. *Dis. Model. Mech.* **3**, 545–56 (2010).
 74. Zheng, D. et al. A Cellular Pathway Involved in Clara Cell to Alveolar Type II Cell Differentiation after Severe Lung Injury. *PLoS One* **8**, e71028 (2013).
 75. Zheng, D. et al. Regeneration of Alveolar Type I and II Cells from Scgb1a1-Expressing Cells following Severe Pulmonary Damage Induced by Bleomycin and Influenza. *PLoS One* **7**, e48451 (2012).
 76. Zheng, D., Yin, L. & Chen, J. Evidence for Scgb1a1⁺ Cells in the Generation of p63⁺ Cells in the Damaged Lung Parenchyma. *Am. J. Respir. Cell Mol. Biol.* **50**, 595–604 (2014).
 77. Song, H. et al. Functional characterization of pulmonary neuroendocrine cells in lung development, injury, and tumorigenesis. *Proc. Natl. Acad. Sci.* **109**, 17531–17536 (2012).
 78. Barkauskas, C. E. et al. Type 2 alveolar cells are stem cells in adult lung. *J. Clin. Invest.* **123**, 3025–3036 (2013).
 79. Zacharias, W. J. et al. Regeneration of the lung alveolus by an evolutionarily conserved epithelial progenitor. *Nature* **555**, 251–255 (2018).
 80. Frank, D. B. et al. Emergence of a Wave of Wnt Signaling that Regulates Lung Alveologenesis by Controlling Epithelial Self-Renewal and Differentiation. *Cell Rep.* **17**, 2312–2325 (2016).
 81. Nabhan, A. N., Brownfield, D. G., Harbury, P. B., Krasnow, M. A. & Desai, T. J. Single-cell Wnt signaling niches maintain stemness of alveolar type 2 cells. *Science (80-.)*. **359**, 1118–1123 (2018).
 82. Kobayashi, Y. et al. Persistence of a novel regeneration-associated transitional cell state in pulmonary fibrosis. *bioRxiv* 855155 (2019). doi:10.1101/855155
 83. Ghio, A. J. et al. Growth of human bronchial epithelial cells at an air-liquid interface alters the response to particle exposure. *Part. Fibre Toxicol.* **10**, 25 (2013).
 84. Danahay, H. et al. Notch2 Is Required for Inflammatory Cytokine-Driven Goblet Cell Metaplasia in the Lung. *Cell Rep.* **10**, 239–252 (2015).
 85. Hild, M. & Jaffe, A. B. Production of 3-D Airway Organoids From Primary Human Airway Basal Cells and Their Use in High-Throughput Screening. in *Current Protocols in Stem Cell Biology* IE.9.1-IE.9.15 (John Wiley & Sons, Inc., 2016). doi:10.1002/cpsc.1
 86. Alder, J. K. et al. Telomere dysfunction causes alveolar stem cell failure. *Proc. Natl. Acad. Sci. U. S. A.* **112**, 5099–104 (2015).
 87. Zheng, D. et al. Differentiation of Club Cells to Alveolar Epithelial Cells In Vitro. *Sci. Rep.* **7**, 41661 (2017).
 88. Nikolić, M. Z. et al. Human embryonic lung epithelial tips are multipotent progenitors that can be expanded in vitro as long-term self-renewing organoids. *Elife* **6**, (2017).
 89. Sachs, N. et al. Long-term expanding human airway organoids for disease modeling. *EMBO J.* e100300 (2019). doi:10.15252/embj.2018100300
 90. Zheng, Y. et al. A rare population of CD24(+) ITGB4(+)Notch(hi) cells drives tumor propagation in NSCLC and requires Notch3 for self-renewal. *Cancer Cell* **24**, 59–74 (2013).
 91. van der Sanden, S. M. G. et al. Enterovirus 71 infection of human airway organoids reveals VP1-145 as a viral infectivity determinant. *Emerg. Microbes Infect.* **7**, 1–9 (2018).
 92. Heo, I. et al. Modelling Cryptosporidium infection in human small intestinal and lung organoids. *Nat. Microbiol.* **3**, 814–823 (2018).
 93. Zhou, J. et al. Differentiated human airway organoids to assess infectivity of emerging influenza virus. *Proc. Natl. Acad. Sci.* **115**, 6822–6827 (2018).
 94. Hui, K. P. Y. et al. Tropism, replication competence, and innate immune responses of influenza virus: an analysis of human airway organoids and ex-vivo bronchus cultures. *Lancet Respir. Med.* **6**, 846–854 (2018).

95. Driehuis, E. & Clevers, H. *CRISPR/Cas 9 genome editing and its applications in organoids*. **312**, G257–G265 (American Physiological Society, 2017).
96. Pickar-Oliver, A. & Gersbach, C. A. The next generation of CRISPR–Cas technologies and applications. *Nat. Rev. Mol. Cell Biol.* **20**, 490–507 (2019).
97. Vlachogiannis, G. *et al.* Patient-derived organoids model treatment response of metastatic gastrointestinal cancers. *Science (80-.)*. **359**, 920–926 (2018).
98. Ooft, S. N. *et al.* Patient-derived organoids can predict response to chemotherapy in metastatic colorectal cancer patients. *Sci. Transl. Med.* **11**, eaay2574 (2019).
99. Dekkers, J. F. *et al.* Characterizing responses to CFTR-modulating drugs using rectal organoids derived from subjects with cystic fibrosis. *Sci. Transl. Med.* **8**, 344ra84–344ra84 (2016).
100. Berkers, G. *et al.* Rectal Organoids Enable Personalized Treatment of Cystic Fibrosis. *Cell Rep.* **26**, 1701–1708.e3 (2019).
101. Van Mourik, P. *et al.* R117H-CFTR function and response to VX-770 correlate with mRNA and protein expression in intestinal organoids. *J. Cyst. Fibros.* (2020). doi:10.1016/j.jcf.2020.02.001
102. Cardoso, W. V. Molecular Regulation of Lung Development. *Annu. Rev. Physiol.* **63**, 471–494 (2001).
103. Takebe, T. *et al.* Vascularized and functional human liver from an iPSC-derived organ bud transplant. *Nature* **499**, 481–484 (2013).
104. Rosen, C. *et al.* Preconditioning allows engraftment of mouse and human embryonic lung cells, enabling lung repair in mice. *Nat. Med.* **21**, 869–879 (2015).
105. Dorrello, N. V. *et al.* Functional vascularized lung grafts for lung bioengineering. *Sci. Adv.* **3**, (2017).

1

2

3

4

5

6

7

8

9

&

CHAPTER

MODELLING OF PRIMARY CILIARY DYSKINESIA USING PATIENT-DERIVED AIRWAY ORGANOIDS

Jelte van der Vaart^{1,2}, Lena Böttinger¹,
Maarten H. Geurts^{1,2}, Willine J. van de Wetering³,
Kèvin Knoops³, Norman Sachs⁴, Harry Begthel^{1,2},
Jeroen Korving^{1,2}, Carmen Lopez-Iglesias³, Peter J. Peters³,
Kerem Eitan⁶, Alex Gileles-Hillel^{5,6}, Hans Clevers^{1,2}

¹ Hubrecht Institute, Royal Netherlands Academy of Arts and Sciences (KNAW) and University Medical Centre Utrecht, 3584 CT Utrecht, the Netherlands;

² Oncode Institute, Hubrecht Institute, 3584 CT Utrecht, the Netherlands.

³ The Maastricht Multimodal Molecular Imaging Institute, Maastricht University, 6229 ER Maastricht, the Netherlands.

⁴ Hubrecht Institute, Royal Netherlands Academy of Arts and Sciences (KNAW) and University Medical Centre Utrecht, 3584 CT Utrecht, the Netherlands; Current address: Vertex Inc, San Diego, CA 92121, United States

⁵ Department of Paediatrics, Paediatric Pulmonology and sleep, Hadassah Hebrew University Medical Centre, Jerusalem, Israel.

⁶ Division of Cell Biology, Immunology and Cancer Research, Hebrew University-Hadassah Medical School, Jerusalem, Israel

*Published in EMBO Reports (2021);
doi: 10.15252/embr.202052058*

2

ABSTRACT

Patient-derived human organoids can be used to model a variety of diseases. Recently, we described conditions for long-term expansion of human airway organoids (AOs) directly from healthy individuals and patients. Here, we first optimize differentiation of AOs towards ciliated cells. After differentiation of the AOs towards ciliated cells, these can be studied for weeks. When returned to expansion conditions, the organoids readily resume their growth. We apply this condition to AOs established from nasal inferior turbinate brush samples of patients suffering from primary ciliary dyskinesia (PCD), a pulmonary disease caused by dysfunction of the motile cilia in the airways. Patient-specific differences in ciliary beating are observed and are in agreement with the patients' genetic mutations. More detailed organoid ciliary phenotypes can thus be documented in addition to the standard diagnostic procedure. Additionally, using genetic editing tools, we show that a patient-specific mutation can be repaired. This study demonstrates the utility of organoid technology for investigating hereditary airway diseases such as PCD.

INTRODUCTION

The human airways are continuously exposed to pathogens and other foreign material. Constitutive clearance is essential for maintaining the healthy state. To this end, a layer of mucus produced by club- and goblet cells is transported towards the oral cavity by ciliated cells. Particles trapped in the layer of secreted mucus are thus removed from the body. Defects in this mucociliary clearance (MCC) mechanism lead to respiratory distress due to impaired oxygen transport, but also to frequent and/or chronic infections¹.

The important role of MCC is best demonstrated in primary ciliary dyskinesia (PCD), a rare genetic disorder, which leads to lifelong recurrent respiratory tract infections. PCD is a rare genetic disorder, which manifests itself in the dysfunction of the cilia, leading to reduced MCC capacity of the airways. While the incidence of PCD is approximately one in 15.000-30.000, this condition is likely underdiagnosed due to suboptimal diagnostic parameters². Symptoms usually begin early in life and include chronic nasal discharge and wet cough, progressing in childhood to recurrent upper and lower airway infections and eventual bronchiectasis. As cilia are also present at the embryonic node, defects in nodal cilia may cause abnormalities of left-right laterality determination (situs abnormalities) in addition to male infertility³⁻⁷. In recent years, major advances have been made in the diagnosis and understanding of PCD, and large-scale sequencing approaches have led to the discovery of new causal genes. So far, mutations in over 40 PCD causing genes have been identified. Ultrastructural ciliary defects are observed in only 70% of the clinically confirmed cases⁵. There remains a group of patients that cannot be diagnosed using standard methods.

Coordination of beating-direction and -frequency of cilia is essential for productive MCC. Motile cilia are evolutionarily conserved. These cilia are complex organelles that are carried by specialized cells of the respiratory tract, brain ventricles and reproductive organs. Disorders of motile cilia are referred commonly as motile ciliopathies and PCD is the most common one. Genes mutated in PCD encode ultrastructural components of the cilia axoneme, or components of cytoplasmic complexes required for preassembly of the structural elements. Contrary to what is traditionally thought, mutations causing PCD do not necessarily affect the ultrastructural composition of the cilia axoneme and may only have a (subtle) effect on ciliary movement. No single test can confirm a diagnosis of motile ciliopathy, which is based on a combination of tests including nasal nitric oxide measurement, transmission electron microscopy, immunofluorescence and genetic testing⁸, and high-speed video microscopy to analyse ciliary beat frequency (CBF) and ciliary motion pattern (CMP)³⁻⁵. Lack of an adaptable, long-term *in vitro* model hampers a more detailed study of ciliary dyskinesia in individual patients: patient-derived primary airway cell cultures are usually only viable for a few weeks.

Other model systems which are currently used for modelling PCD are unicellular organisms and vertebrate animal models including zebrafish and xenopus. While these models allow for the modelling of some aspects of PCD, the models do not fully

1

2

3

4

5

6

7

8

9

&

recapitulate human disease⁹. Similarly, genetic mouse models present with PCD-like phenotypes when known PCD-causing mutations are introduced. However, due to the extensive spectrum of PCD-causing mutations and the underlying patient-specific genome, the variety of PCD phenotypes can not be modelled in mice¹⁰. This underlines the need for a patient-specific model system to identify personalised disease phenotypes. Currently, patient cells are cultured in air-liquid interface (ALI) cultures which requires substantial numbers of cells. More importantly, ALI cultures can not be passaged over long periods of time and thereby provide limited time-span for diagnostics and research^{11,12}. The search for a patient-specific long-term model system therefore remains.

To date, therapeutic interventions can only alleviate PCD patients' symptoms. Most patients suffer from a lifelong chronic respiratory morbidity, with varying severity of the symptoms. Yet, the disease progresses and ultimately may lead to respiratory insufficiency and even the need for lung transplantation. The heterogeneous nature of the disease, explained to some degree by the different ciliary genes involved, suggests the need for personalised therapeutic approaches. The recent development of human airway organoid (AO) culture has opened the possibility of studying airway diseases in patient-specific primary material in models that can be manipulated and studied, while remaining genetically and phenotypically stable over long periods of time. These AOs can be generated from small biopsies and expanded over time while maintaining its potential to differentiate^{13,14}. While 2D cultures can be generated from small biopsies, the expansion of these basal cells is limited for a few passages¹⁴.

Furthermore, MCC and ciliary function are impaired in many chronic respiratory conditions such as COPD, bronchiectasis and chronic smoking. While efforts in generating AOs has resulted in limited ciliated cell numbers when spontaneous differentiation was achieved¹³, differentiation of ciliated cells in 3D model systems was achieved by using undefined commercially available medium¹⁵. Using current knowledge of ciliated cell differentiation could identify robust yet defined conditions that allows for ciliated cell differentiation in AOs. A defined ciliary organoid model will allow to develop drugs that may improve ciliary function, which are currently unavailable¹⁶. This study explores patient-specific AO establishment from PCD patients and the characterization of their ciliary defect, with the aim of establishing long-lived models of this disease.

MATERIALS AND METHODS

Patient samples

Nasal inferior turbinate brushes were obtained from the Hadassah Medical Centre, Jerusalem. All patients were diagnosed with primary ciliary dyskinesia. The study was approved by the ethical committee and was in accordance with the Declaration of Helsinki and according to Israeli law under IRB approval number 075-16 HMO. This study is compliant with all relevant ethical regulations regarding research involving human participants.

Organoid establishment

After NITB sample collection, sample was incubated in Advanced DMEM/F12 (Life Technologies; 12634-034) supplemented with GlutaMax (Life Technologies; 12634-034), HEPES (Life Technologies; 15630-056), penicillin (10,000 IU/mL) and streptomycin (10,000 IU/mL) (Life Technologies; 15140-122) (AdDF+++), with 100µg/mL Primocin (InvivoGen; ant-pm1) for transport. Samples were shipped at 4°C overnight to Utrecht, The Netherlands. Human airway cells were isolated, processed and cultured as described previously¹³. In short, cells were spun down and supernatant was removed. Cells clumps were mechanically sheared using narrowed glass pipette to remove mucus. Cells were resuspended in AdDF+++ supplemented with 100µg/mL Primocin, 1.25mM NAc (Sigma-Aldrich; A9165), 0.15% Pronase E (Sigma-Aldrich; 7433-2) and 0.5mg/ml collagenase (Sigma-Aldrich, C9407) and incubated for 20 min at 37°C. Samples were washed twice with AdDF+++ with Primocin and spun down at 300xg for 5 min. The resulting pellet was resuspended in ice-cold 70% 10 mg/mL cold Cultrex growth factor reduced BME type 2 (Trevigen; 3533-010-02) in airway organoid medium.

Organoid culture

Organoids were grown in airway organoid medium, previously described¹³, which consists of AdDF+++ supplemented with 1× B27 supplement (Life Technologies; 17504-044), 1,25 mM N-acetyl-L-cysteine (Sigma-Aldrich; A9165), 10 mM nicotinamide (Sigma-Aldrich; N0636), 500 nM A83-01 (Tocris; 2939), 5µM Y-27632 (Abmole; Y-27632), 1µM SB202190 (Sigma-Aldrich; S7067), 100 ng/mL human FGF10 (PeproTech; 100-26), 25ng/mL FGF7 (PeproTech; 100-19), 1% (vol/vol) RSPO3, and Noggin (produced via the r-PEX protein expression platform at U-Protein Express BV). This medium was termed airway medium (AO). For passaging, organoids were collected, washed with DMEM (Life Technologies; 10566016) supplemented with penicillin (10,000 IU/mL) and streptomycin (10,000 IU/mL) (DMEM+P/S), and disrupted either by mechanical shearing or digestion with TrypLE Express (Life Technologies; 12605-010). After passaging, organoid fragments were replated in fresh BME. During expansion, medium was replaced twice a week.

Organoids were frozen for long-term storage using CellBanker I (11888; AMSBIO Europe B.V.) following manufacturers protocol. In short, organoids were grown for 2-5 days after splitting. Organoids were removed from BME using DMEM+P/S and spun down. Pellet was resuspended in CellBanker I and immediately transferred to -80°C. For storage over 2 months, vials were moved to liquid nitrogen storage boxes.

Differentiation of airway organoids towards ciliated cell fate

Ciliated cell differentiation was initiated when organoids had visually formed a lumen (1-3 weeks in AO medium). AO medium was replaced with cilia medium; AO medium from which Noggin and A83-01 were removed and 10 µM DAPT (Sigma-Aldrich; D5942)

1

2

3

4

5

6

7

8

9

&

and 10ng/mL human BMP4 (Peprotech; 120-05) was supplemented. Organoids were differentiated for 10-21 days by replacing medium 2 times a week.

Growth of organoids quantification

After dissociation of AOs to single cells using TrypLE Express (Life Technologies; 12605-010), 20,000 cells were plated in 20 μ l droplets of BME and cultured with AO medium for 14 days before starting differentiation. On day 0, 3, 7, 10, 14 and 21 after start of differentiation cells were collected and counted using cell counter grids (KOVA; 87144E). Average cell number of 3 wells per day was calculated. Results were repeated in three different experiments and quantifications were performed in a blinded manner.

Air-liquid interface cultures

Air-liquid interface cultures were established from healthy and patient-derived airway organoid cultures. AOs were dissociated into single cells using trypsin-EDTA (0.25%; Gibco-25200).

250,000 cells were seeded on semi-permeable transwell membranes (Corning-3378) coated with bovine collagen type I (30 μ g ml⁻¹; Purecol; Advanced BioMatrix-#5005). Single cells were seeded in AO growth medium supplemented with 25 ng/mL recombinant human epidermal growth factor (Peprotech; AF-100-15) and cultured in submerged conditions. After 4 days, confluent monolayers were cultured in air-exposed conditions using differentiation medium adapted from Neuberger et al (2011)⁵⁰. Medium was changed every 4 days.

RNA Isolation, cDNA Synthesis, and qPCR.

Organoids were collected from tissue culture plates and washed twice in 10 mL of DMEM+P/S. RNA was extracted using The Qiagen RNeasy Mini Kit according to protocol. For cDNA synthesis, GoScript Reverse Transcriptase (Promega; A5003) was used according to protocol. qPCR reactions were performed in 384-well format using IQ SYBR Green (Bio-Rad; 1708880). Gene expression was quantified using the $\Delta\Delta$ Ct method and normalized by β -ACTIN using primers listed in table 1.

RNA isolation and RNA sequencing

Total RNA was isolated from organoids that were cultured in AO medium or cilia medium for 21 days after initial growth period in AO medium using the Qiagen RNeasy Mini Kit. The quality and quantity of isolated RNA were checked and measured using the Bioanalyzer 2100 RNA Nano 6000 Kit (Agilent; 5067-1511). Library preparation was performed with 500 ng of total input RNA using the Truseq Stranded Total RNA Kit with Ribo-Zero Human/Mouse/Rat Sets A and B (Illumina; RS-122-2201 and RS-122-2202). Library quality was checked using the Agilent High-Sensitivity DNA Kit (5067-4626) and the Qubit dsDNA HS Assay Kit (Thermo Fisher Scientific; Q32854). Libraries were pooled

Table 1. Primers used for RT-qPCR analysis

Target	Forward	Reverse	Used before in
DNAH5	AGAGGCCATTTCGCAAACGTA	CCCGGAAAATGGGCAAACCTG	-
DNAH7	ACTTGCAGAATCGCATCCCA	CTCCTCTCCGCTCACTTGTC	27
DNAI1	AACGACGGCTGTCCCTAAAG	AGCCTACAAAACGCTCCCTC	27
SNTN	GCTGCAAACCCAATTTAGGA	TGCTCATCAAGTTCAGAAAGGA	54
B-ACTIN	CATTCCAATATGAGATGCGTTGT	TGTGGACTTGGGAGAGGACT	-
FOXJ1	CCTGTCGGCCATCTACAAGT	AGACAGGTTGTGGCGGATT	-
SCGB1A1	ACATGAGGGAGGCAGGGGCTC	ACTCAAAGCATGGCAGCGGCA	-
MUC5B	GGGCTTTGACAAGAGAGT	AGGATGGTCGTGTTGATGCG	-

to a final concentration of 2 nM. Library pools (1.0 to 1.4 pM) were loaded and sequenced on an Illumina NextSeq system with 2 × 75-bp high output. After quality control, mapping and counting analyses were performed using our in-house RNA analysis pipeline v2.1.0 (<https://github.com/UMCUGenetics/RNASeq>), based on best practices guidelines (<https://software.broadinstitute.org/gatk/documentation/article.php?id=3891>).

Differential gene expression analysis was performed using the DESeq2 package⁵¹. Batch-variation correction was applied using batch effect correction of the limma package in DESeq2.

Data is deposited at GEO under GSE158775. Significantly upregulated genes were subjected to functional enrichment analysis for a biological process using the Enrichment analysis tool of Geneontology (<http://geneontology.org/>). In short, genes names were copied into the analysis tool from the PANTHER Classification System. The 10 biological processes with highest enrichment (after FDR correction and a pvalue cut-off of 0.05) for differentiation are displayed with the corresponding GO term and corrected FDR p-value.

IHC, fixed whole-mount IF and live staining.

Organoids were collected from tissue culture plates and washed twice in 10 mL of Cell recovery solution (Corning; 734-0107). Organoids were fixed in 4% paraformaldehyde. For immunohistochemistry this was followed by dehydration, paraffin- embedding, sectioning, and standard H&E staining. For whole-mount immunofluorescence staining the organoids were permeabilized for 20 min in 0.5% Triton X-100 (Sigma), and blocked for 45 min in 1% BSA or 2% normal donkey serum. Organoids were incubated with primary antibodies overnight at RT, washed three times with PBS, incubated with secondary antibodies (Invitrogen) and indicated additional stains (DAPI; Life Technologies; D1306 and Phalloidin-Alexa488; Life Technologies; A12379) 2h at RT, washed two times with PBS, and mounted in VECTASHIELD non-hard-set antifade mounting medium (Vectorlabs). For microtubule live stain, organoids were transferred to glass-bottom plates and incubated with medium containing 100nM SiR-tubulin dye (Spirochrome). 12-24 hours later the organoids were imaged.

1

2

3

4

5

6

7

8

9

&

Samples were imaged on SP8 confocal microscope using LAS X software (all Leica) and processed using ImageJ. Staining was performed on acetylated- α -tubulin (Santa Cruz; sc-23950), actin (Sigma-Aldrich; A5228), SCGB1A1 (Santa Cruz; sc-9773) keratin 5 (Covance; PRB 160P-100).

Quantification of apical surface coverage

IHC images of acetylated- α -tubulin-stained AOs were loaded into Fiji image software. Using tracing tool, the surface area was calculated. Secondly the area stained positive was measured. Percentages per organoid were calculated. For PCD AOs differentiation efficiency, each separate experiment shows counts of 10 organoids and quantifications were performed in a blinded manner.

Flow cytometry

AOs were differentiated using described protocols. On the day of the analysis, organoids were harvested and washed in 10 mL DMEM+P/S. Organoids were dissociated into single cells using TrypLE (Gibco) supplemented with Y-27632 at 37°C for 30 minutes. During the single-cell dissociation, the organoid suspension was vigorously pipetted every 5 minutes to keep the solution homogenous. Cells were fixed in 4% paraformaldehyde for 2h at RT. The organoids were permeabilized for 30 min in 0.5% Triton X-100 (Sigma), and blocked for 30 min in 2% normal goat serum in PBS. Organoids were incubated with primary antibody (mouse-anti-acetylated- α -tubulin; Santa Cruz; sc-23950) for 1h at RT, washed three times with PBS, incubated with secondary antibodies (goat-anti-mouse IgG-Alexa488; Invitrogen) for 1h at RT, washed two times with PBS. Cells were strained over 35 μ m mesh into Falcon® 5 mL Round Bottom Polystyrene Test Tube (Corning; 352235). FACS analysis was performed within 30 min on BD LSR Fortessa X20 4 laser FACS machine. Data analysis was performed using FlowJo (v10.7.2).

Scanning EM

Organoids were removed from BME, washed with excess AdDF+++ , fixed for 15 min with 1% (v/v) glutaraldehyde (Sigma) in phosphate-buffered saline (PBS) at room temperature, and transferred onto 12-mm poly-L-lysine coated coverslips (Corning).

Samples were subsequently serially dehydrated by consecutive 10-min incubations in 2 ml of 10% (v/v), 25% (v/v) and 50% (v/v) ethanol-PBS, 75% (v/v) and 90% (v/v) ethanol-H₂O, and 100% ethanol (2 \times), followed by 50% (v/v) ethanol-hexamethyldisilazane (HMDS) and 100% HMDS (Sigma).

Coverslips were removed from the 100% HMDS and air-dried overnight at room temperature.

Organoids were manipulated with 0.5-mm tungsten needles using an Olympus SZX9 light microscope and mounted onto 12-mm specimen stubs (Agar Scientific).

Following gold-coating to 1 nm using a Q150R sputter coater (Quorum Technologies) at 20 mA, samples were examined with a Phenom PRO tabletop scanning electron microscope (Phenom-World).

Transmission EM

Organoids were removed from BME, washed with excess AdDF+++ + 5% FBS. Organoids were fixed with 1.5% glutaraldehyde in 0.1M cacodylate buffer. They were kept in the fixative for 24 h at 4°C. Then, they were washed with 0.1M cacodylate buffer and postfixed with 1% osmium tetroxide in the same buffer containing 1.5% potassium ferricyanide for 1 h (dark) at 4°C. Then the samples were dehydrated in ethanol, infiltrated with Epon resin for 2 days, embedded in the same resin and polymerized at 60°C for 48 h. Ultrathin sections of 50 nm were obtained using a Leica Ultracut UCT ultramicrotome (Leica Microsystems, Vienna) and mounted on Formvar-coated copper grids. They were stained with 2% uranyl acetate in water and lead citrate. Then, sections were observed in a Tecnai T12 electron microscope equipped with an Eagle 4kx4k CCD camera (Thermo Fisher Scientific, the Netherlands).

Electron tomography

Epon sections were cut with a thickness of 200 nm and 10 nm BSA-gold fiducial were placed on top to facilitate tomogram alignment. Dual axis tomograms were recorded inside a FEI T12 electron microscope running at 120 kV using the FEI automated tomography acquisition software and using 1 ° tilt increments and a pixel size of 0.94 nm. Tomogram reconstruction was performed with the IMOD software. Projection images of the cilia were extracted using the ChimeraX and 3D volume renders were made with Amira.

Time-lapse and high-speed microscopy

Bright-field AO time-lapse videos were recorded at 37°C and 5% CO₂ on an AF7000 microscope equipped with a DFC420C camera using LAS AF software (all Leica). Bright-field cilia movement in organoids and air-liquid-interface cultures was recorded using the same setup equipped with a Hamamatsu C9300-221 high-speed CCD camera (Hamamatsu Photonics) at 150 frames per second using Hokawo 2.1 imaging software (Hamamatsu Photonics).

Plasmid construction for prime editing

Human codon optimized prime editing constructs were a kind gift from David Liu; pCMV_PE2 (Addgene plasmid #132775), pU6-pegRNA-GG-acceptor (Addgene plasmid #132777). The empty sgRNA plasmid backbone was a kind gift from Keith Joung (BPK1520, Addgene plasmid #65777). pegRNA were created as previously described⁵². In brief, the pU6-pegRNA-GG-acceptor plasmid was digested overnight using Bsal-HFv2

1

2

3

4

5

6

7

8

9

&

(NEB), loaded on a gel and the 2.2kb band was extracted using the QIAquick Gel extraction kit. Oligonucleotide duplexes for the spacer, scaffold and 3'-extension with their appropriate overhangs were annealed and cloned into the digested pUF-pegRNA-GG-acceptor by golden gate assembly according to the previously described protocol⁵². PE3-guides were cloned using inverse PCR together using BPK1520 as template and Q5 High fidelity polymerase. Upon PCR clean-up (Qiaquick PCR purification kit), amplicons were ligated using T4 ligase and Dpn1 (both NEB) to get rid of template DNA. PEgRNA and PE3-guide combinations were designed using the online web-tool pegFinder (<https://www.nature.com/articles/s41551-020-00622-8>). All transformations in this study were performed using OneShot Mach1t1 (ThermoFisher scientific) cells and plasmid identity was checked by Sanger sequencing (Macrogen). Spacer and 3' extensions for PEgRNA and PE3-Guide can be found in Table 2. Primers for plasmid construction can be found in Table 3.

Organoid electroporation

Organoid electroporation was performed with slight modifications to this previously described protocol^{49,53}. Wild type airway organoids derived from PCD patient 3 (PCD3_DNAH11) were maintained in their respective expansion medium up until 24h before electroporation. 24h in advance, the expansion medium was switched to electroporation medium which adds rho-kinase inhibitor Y-27632 (abmole bioscience) to inhibit anoikis and 1.25%(v/v) DMSO. On the day of electroporation the organoids were dissociated

Table 2. Spacer and 3' extensions for PEgRNA and PE3-Guide used for Prime editing in AOs

Plasmid name	Spacer sequence	3'- extension
DNAH11-PEgRNA	GCTTGATAATCAGAAATCaA	TTGTTCTCCTTtGATTTCTGATTATCAAGC
DNAH11-PE3-guide	GATGGGTATATGGCAATTTT	-

Table 3. Primers used for Prime editing in AOs

5' à 3' sequence	Primer name
CACCGCTTGATAATCAGAAATCaAGTTTT	DNAH11 peg_spacer_F_2
CTCTAAAACCTTGATTTCTGATTATCAAGC	DNAH11 peg_spacer_R_2
GTGCTTGTTCTCCTTAGATTTCTGATTATCAAGC	DNAH11 peg_EXTF_2
AAAAGCTTGATAATCAGAAATCTAAGGAGAACAA	DNAH11 peg_EXTR_2
AAAATTGCCATATACCCATCCGGTGTTTCGTCCTTTCCACAAG	DNAH11 pe3_2
/5phos/AGAGCTAGAAATAGCAAGTTAAAATAAGGCT	gRNA_scaffold Top
AGTCCGTTATCAACTTGAAAAAGTGGCACCGAGTCG	
/5phos/GCACCGACTCGGTGCCACTTTTTCAAGTTGAT	gRNA scaffold bottom
AACGGACTAGCCTTATTTAACTTGCTATTTCTAG	

into single cells using TrypLE (Gibco) supplemented with Y-27632 at 37°C for 30 minutes. During the single-cell dissociation, the organoid suspension was vigorously pipetted every 5 minutes to keep the solution homogenous. Cells were resuspended in 100µl of Opti-MEM™ (Gibco; 11058021) and combined with 10µl plasmid solution containing 7.5 µg pCMV_PE2_P2A_GFP depending on gene editing strategy and 2.5 µg per guide-RNA plasmid. Electroporation was performed using NEPA21 with settings described before⁵³. After electroporation the cells were resuspended in 600ul BME and plated out in 20 µl droplet/well of a pre-warmed 48-wells tissue culture plate (Greiner). After polymerization, the droplets were immersed in 250 µL of expansion medium and the organoids were maintained at 37°C and 5% CO₂.

Genotyping of mutations in PCD AOs

PCD3_DNAH11 AOs were grown in expansion condition. DNA was extracted from AOs using Quick-DNA™ MicroPrep (Zymo research; D3021). PCR on ±500bp genomic context was performed using standard Q5® Hot Start High-Fidelity DNA Polymerase protocol (New England Biolabs; M0493). PCR products were purified using NucleoSpin Gel and PCR Clean-up kit (Bioke; 740609) and Sanger sequenced by MacroGen Europe.

Statistical analysis

Statistical analysis was performed with the GraphPad Prism 8 software.

RESULTS

To establish patient-specific PCD organoids, we obtained airway organoid (AO) cultures from nasal inferior turbinate brush (NITB) samples collected from healthy and affected individuals with known mutations in PCD related genes. Several studies have shown the use of nasal epithelium as model for airway diseases like PCD^{11,17–23}. The non-invasively received NITB samples were obtained from 4 patients and 2 healthy controls. NITB-derived AOs have shown effectiveness as airway epithelium model^{24–26}. Patients were diagnosed with PCD and their genomes sequenced. Clinical data from two of the patients was published previously^{27,28}. The patients carried mutations in *Dynein Axonemal Intermediate Chain 2 (DNAI2)*, *Leucine Rich Repeat Containing 6 (LRRC6)*, *Dynein Axonemal Heavy Chain 11 (DNAH11)* and *Coiled-Coil Domain Containing 65 (CCDC65)* respectively (**Figure 1A**). *DNAI2* mutations are predicted to lead to dysfunctional outer dynein arms in PCD1_DNAI2. Homozygous amino acid alteration D146H in LRRC6 causes aberrations in both outer as inner dynein arms in PCD2_LRRC6. Deletions in CCDC65 lead to loss of microtubule-coupling nexin links in PCD4_CCDC65 (**Figure 1B**). NITB samples of both nostrils were placed in tubes containing transport medium and transported on ice from Jerusalem to Utrecht. Within 24 hours after collection, the samples were received and processed by mechanical and enzymatic digestion. Only limited numbers

1

2

3

4

5

6

7

8

9

&

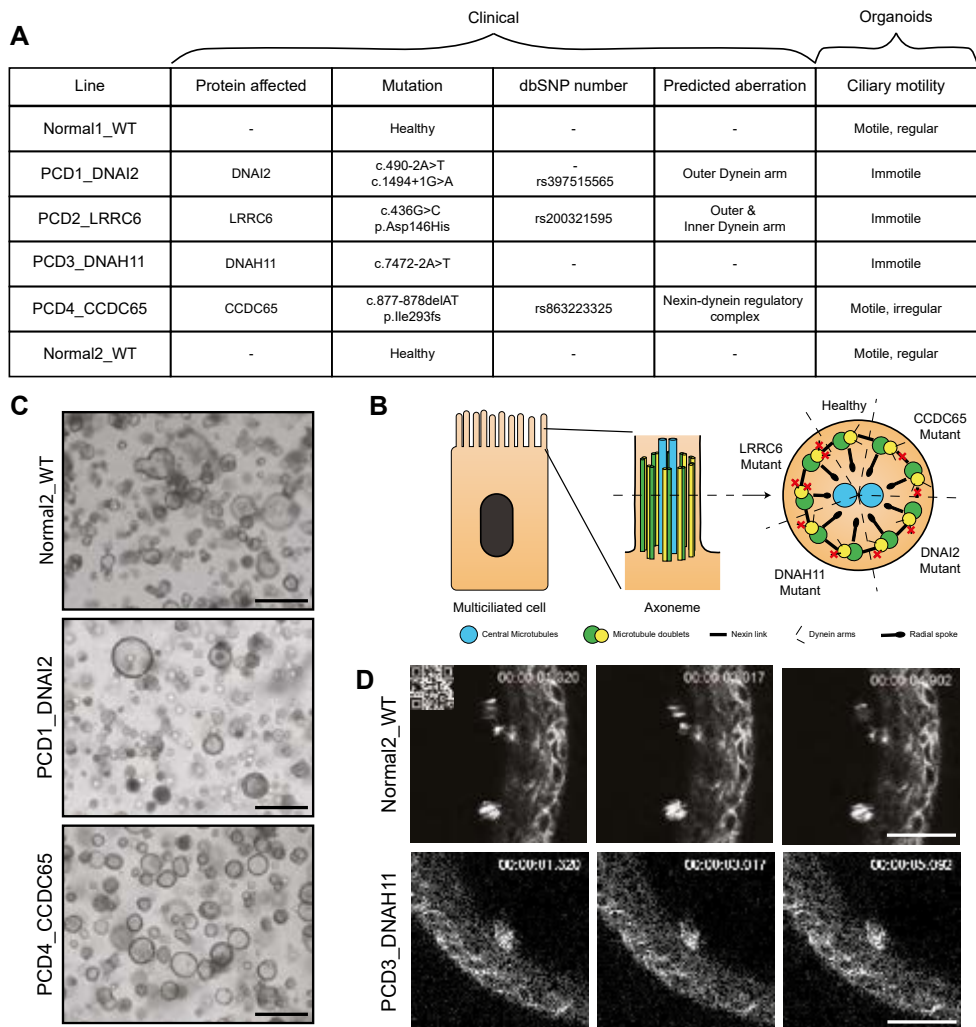


Figure 1. Generation of human airway organoids from primary cilia dyskinesia patients. A) Summary/overview of the airway organoid lines used in this study. Details regarding the mutational status, affected protein, dbSNP number, cilia structural component predicted to be affected and ciliary motility are included. Genetic mutations of generated AOs were confirmed by Sanger sequencing (Supplementary figure S1). B) Schematic figure highlighting the cilia inner structure (axoneme). The cross-section of the axoneme shows the genes affected in generated AOs and their predicted effect on the different structural components of the axoneme. C) Representative brightfield images of PCD (PCD1_DNAI2 and PCD4_CCDC65) and healthy control AOs (Normal2_WT) displaying their morphological similarity. Scale bar = 500µm. D) Representative montage of SiR-Tubulin live imaging (Video EV1) showing the difference in cilia motility between healthy and PCD AOs. Healthy AOs (Normal2_WT) (upper panel) display normal cilia motility whereas cilia in PCD AOs (PCD3_DNAH11) are immotile (lower panel). All organoids were cultured in AO medium. Time is indicated in seconds. Scale bar = 25 µm.

of cells were plated yet AOs formed which could be expanded exponentially, frozen down and thawed repeatedly. The majority of the established organoids were cystic and showed a comparable phenotype to the previously published AOs (**Figure 1C**)¹³. Percentage of cystic organoids varied between donors and passages within a single line; only cystic organoids contained visible ciliary cells. AOs could be maintained for >35 passages (>1 year). Patient mutations were verified in the established organoid lines (**Supplementary figure S1A-E**). While limited numbers of cells with beating cilia were observed in healthy AOs (**Figure 1D**, upper panel and Video EV1a), immotile cilia were observed in 3 out of 4 patient-derived AOs (**Figure 1D**, lower panel and Video EV1b). This observation was confirmed using the standard method of mucociliary differentiation using ALI cultures¹¹ (Video EV2). Using high speed imaging techniques, cultures of healthy AOs showed regular CBF of cilia (Video EV2a,b), while cultures of PCD1_DNAI2 displayed no visible beating in ALI cultures (Video EV2c,d). Taken together, NITB-derived AOs from known PCD patients appeared to maintain disease phenotype in culture but limited numbers of ciliated cells in expansion conditions hampered robust PCD modelling.

To optimise the application of primary AOs in modelling PCD, we aimed to establish a protocol to enhance differentiation towards a ciliated cell fate. Bone morphogenic protein (BMP) and Notch signalling have previously been implied in driving this process²⁹. We inhibited Notch signalling by adding the gamma-secretase inhibitor DAPT, removing the BMP signalling inhibitor Noggin, and replacing it with recombinant BMP4 in the standard AO culture medium. This media, which we termed 'cilia medium' (CiM), induced a strong increase in ciliated cell numbers in the established AOs (Fig. 2). The rate of differentiation appeared somewhat variable; full differentiation required 14 to 21 days. After 21 days in CiM, the apical surface area of AOs that stained for the cilium-marker acetylated- α -tubulin was increased from $\pm 1\%$ to $\pm 35\%$ of total surface area (**Figure 2A,B**). Incubation in CiM arrested the expansion of organoids (**Figure 2C**). To obtain significant numbers of differentiated cells, we applied the following strategy: First, organoids were allowed to grow into large cysts in AO medium for 1-3 weeks. Next, CiM was added to the cultures for at least two weeks. Increasing levels of ciliated cell marker genes were observed over a 16-day period (**Figure EV1A**). The cilia could be visualised by live staining of SiR-tubulin (Video EV3) and, in fixed organoids, by immunofluorescent staining for acetylated- α -tubulin (**Figure 2D**). SiR-tubulin-positive and acetylated- α -tubulin positive cilia were identified on the luminal side of cystic organoids (**Figure 2D**) while dense organoids showed little to no cilia. This underlines the importance of cystic organoids in culture. Similar differentiation potential was observed in patient-derived AOs although some donor-donor variation was observed. While PCD2_LRRC6 AOs showed increased apical presence of acetylated- α -tubulin, the percentage was lower than observed in other PCD AOs (**Figure 2E**). Similarly, this difference in number of ciliated cells was observed using flow cytometry (**Figure EV2A**). Yet, increased ciliated cell numbers in all PCD AOs was observed after 14 days of CiM compared to AO medium (**Figure EV2B-I**). Limited numbers are due to the build-up of the organoids in which only the most apical layer

1

2

3

4

5

6

7

8

9

&

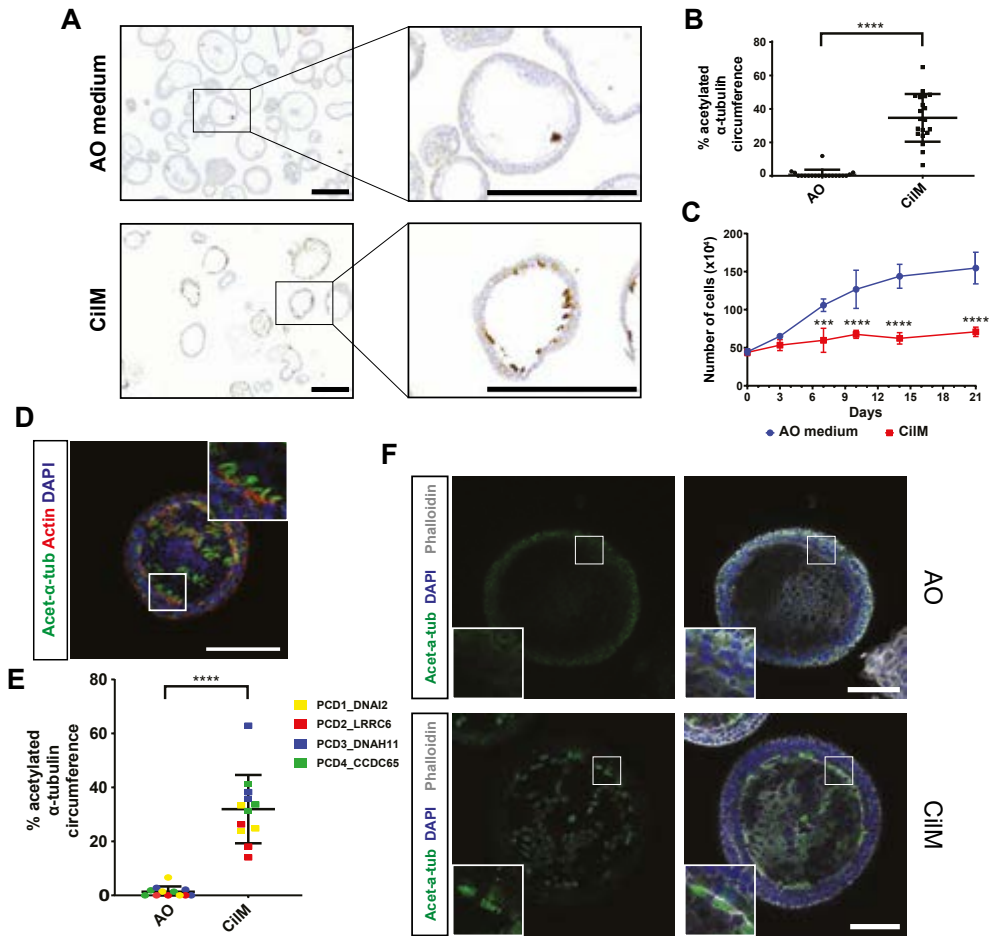


Figure 2. Cilia medium (CiM) promotes differentiation of ciliated cells in human airway organoids. A) Representative immunohistochemistry images of healthy human AOs (Normal1_WT) stained for acetylated- α -tubulin. An increased number of ciliated cells were observed in organoids cultured in CiM (21 days) compared to AO medium. Scale bar = 200 μ m. B) Quantification of acetylated- α -tubulin⁺ circumference as a measure of ciliated cell numbers, shows an increase upon culturing healthy AOs in CiM (21 days) compared to AO. Each dot represents an analysed organoid. **** = $P < 0.0001$ using Student t-test. Bars = mean \pm SD. N=10. C) Quantification of cell numbers following culturing of organoids in CiM (red) or AO (blue) medium. Upon differentiation in CiM, organoids do no longer expand and stabilise in cell number while organoids in AO medium keep expanding seen by an increase in cell number. Organoids were first cultured in AO media for 14 days and were then either continued to be cultured in AO or subjected to CiM. The number of cells were quantified at each indicated timepoint following the first 14 days in AO media. Two donors were tested in triplicate. *** = $P < 0.001$ and **** = $P < 0.0001$ using student t-test. N=3. Error bars = SD. D) Representative image of healthy AOs (Normal1_WT) in CiM (21 days) stained for cilia (acetylated- α -tubulin (Ac- α -tub)), cellular membrane (Actin) and nucleus (DAPI). Scale bar = 100 μ m. Ciliated cells occur throughout the organoid as acetylated- α -tubulin (Ac- α -tub)⁺ cells. E) Quantification of acetylated- α -tubulin⁺ circumference as a measure of ciliated cell numbers, shows an increase upon culturing PCD AOs in CiM (21 days) compared to AO. Each dot represents ten analysed organoids in a single differentiation experiment. Colour of the dot indicates donor line. **** = $P < 0.0001$ using

- student t-test. N = 12. Bars = mean \pm SD. F) Representative IF image of PCD AOs (PCD3_DNAH11) in CilM (14 days) stained for cilia (acetylated- α -tubulin (Ac- α -tub)), cellular membrane (Phalloidin) and nucleus (DAPI). Scale bar = 100 μ m. Ciliated cells can be observed following culture of the organoids in CilM but not in AO medium. Images are similar to Figure EV3.

of cells within the organoids can form cilia. Only cells which possess cilia were counted using flow cytometry while cells in lower cell layers could show ciliated cell characteristics except for cilia formation due to the limited space for cilia build-up.

Moreover, presence of acetylated- α -tubulin positive cells with visible cilia were observed in all donors using immunofluorescence (**Figure 2F** and **Figure EV3**). Coordinated beating of the cilia was visualized using the live stain mentioned above (Video EV3). Taken together, healthy and patient-derived AOs grown in CilM presented increased ciliated cell numbers while healthy AOs also displayed regular CBF.

To better characterize the processes of differentiation towards ciliary fate, bulk mRNA sequencing was performed on three donors (Normal2_WT, PCD1_DNAI2 and PCD4_CCDC65) in CilM and AO medium. Large differences in gene expression were observed in organoids grown in CilM compared to control organoids grown in AO medium (**Figure 3A**, **Supplementary figure S2** and **Table EV1-2**). 193 genes were found differentially expressed (130 upregulated and 63 downregulated) (adjusted p-value < 0.01 and abs(log2fold) > 1.5) (**Table EV3**). Satisfyingly, genes significantly upregulated in CilM organoids were characterised as being involved in 'cilium movement' by GO-term analysis and as well as in the GO terms 'ciliated cell functioning including axoneme assembly' and 'cilium assembly' (**Figure 3b**), as well as 'component of the cilium and axoneme' (**Figure 3C**). We then specifically assessed expression levels of a self-assembled list of genes that have been described to be involved in cilium structure or intra-cilium transport (**Table EV4**)³⁰. A general increase in the expression of cilia-related genes was observed in CilM grown organoids from all donors (**Figure 3D**). Of note, similar to the immunostainings, some donor-donor variation was observed (**Supplementary figure S2** and **Figure EV4A**). PCD4_CCDC65 showed higher levels of ciliated cell marker genes in the generic AO medium compared to the other donors, while these levels still increased in CilM. The data was therefore normalised using batch-to-batch variation correction. In general, highly similar transcriptomic changes can be observed when AOs are differentiated in CilM, independent of the AO's origin (**Figure 4A,B** and **Supplementary figure S2** and **Figure EV4A**). These findings were verified using RT-qPCR in Normal1_WT AOs (**Figure EV1A**) and in all four PCD AOs (**Figure EV1B**) showing the increase of cilia-related genes *DNAH5*, *DNAH7*, *SNTN*, *DNAI1* and *FOXJ1*. Besides inducing ciliated cell differentiation, CilM lowered expression levels of typical secretory cell markers: *SCGB1A1* (Club cells) and *MUC5B*, *MUC5AC* and *TFF3* (Goblet cells) (**Figure 4A** and **C**). Similar downregulation of secretory cell markers *SCGB1A1* and *MUC5B* was observed in the four PCD AO lines after 14 days of differentiation in CilM compared to AO medium (**Figure EV1B**). Using immunofluorescence, secretory cells could be identified in AO medium cultures

1

2

3

4

5

6

7

8

9

&

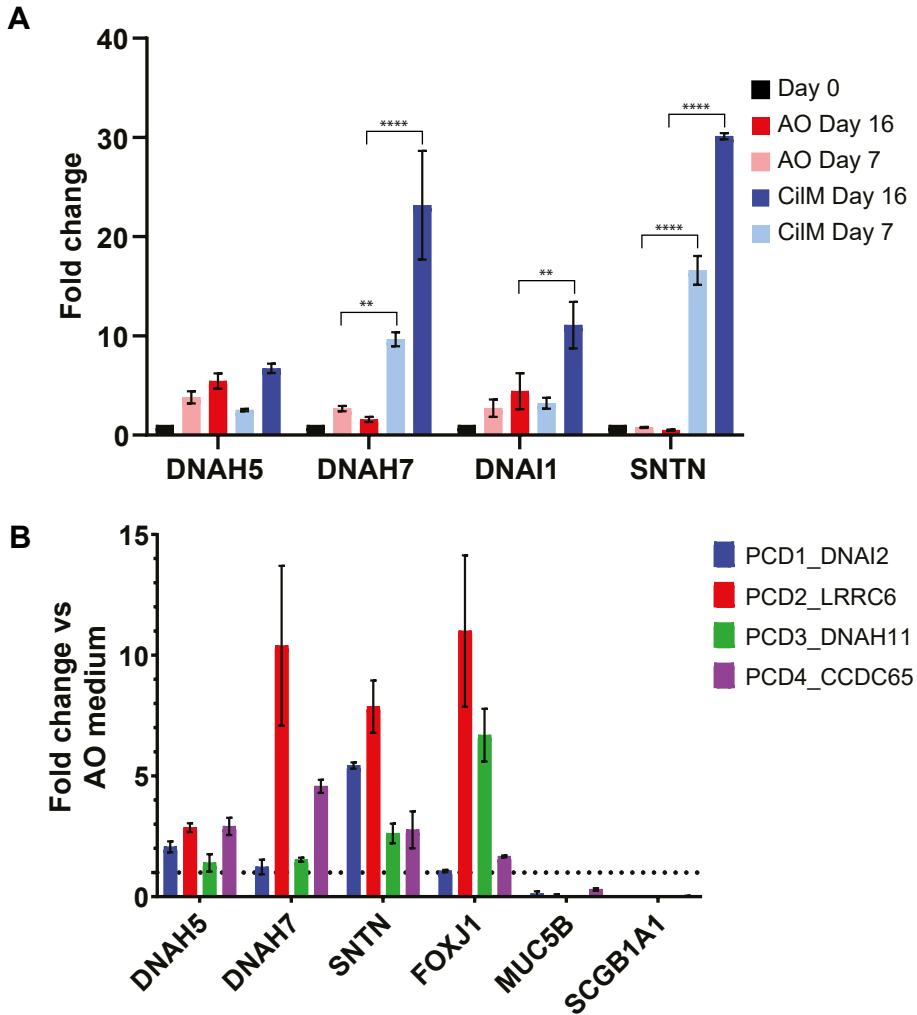


Figure EV1. Healthy and PCD AOs in CiIM upregulate cilia-related genes. A) Cilia-related genes *DNAH5* and *DNAI2* increase over time in AO medium but more strikingly in CiIM. Cilia-related genes *DNAH7* and *SNTN* do not increase over time in AO medium while increasing in CiIM. Error bars = stdev. ** = $P < 0.01$, **** = $P < 0.0001$ using two-way ANOVA. N=3. B) Cilia-related gene *DNAH5*, *DNAH7*, *SNTN* and *FOXJ1* expression is increased after 14 days in CiIM compared to the same donor line in AO medium. The increase shows donor-donor variation. Similarly, the expression of secretory cell markers *MUC5B* and *SCGB1A1* is downregulated in CiIM compared to AO medium after 14 days. Error bars = stdev. N=3.

(Figure 4E and Figure EV5D). These secretory cells were lost in CiIM AOs (Figure 4E). We also noted a general increase of expression of basal cell marker genes (TP63 and KRT5) (Figure 4A and D). No clear differences in KRT5⁺ basal cell number or localisation was identified between organoids grown in AO medium or in CiIM (Figure 4F). Cell type markers for pulmonary neuroendocrine cells, tuft cells and ionocytes were generally low

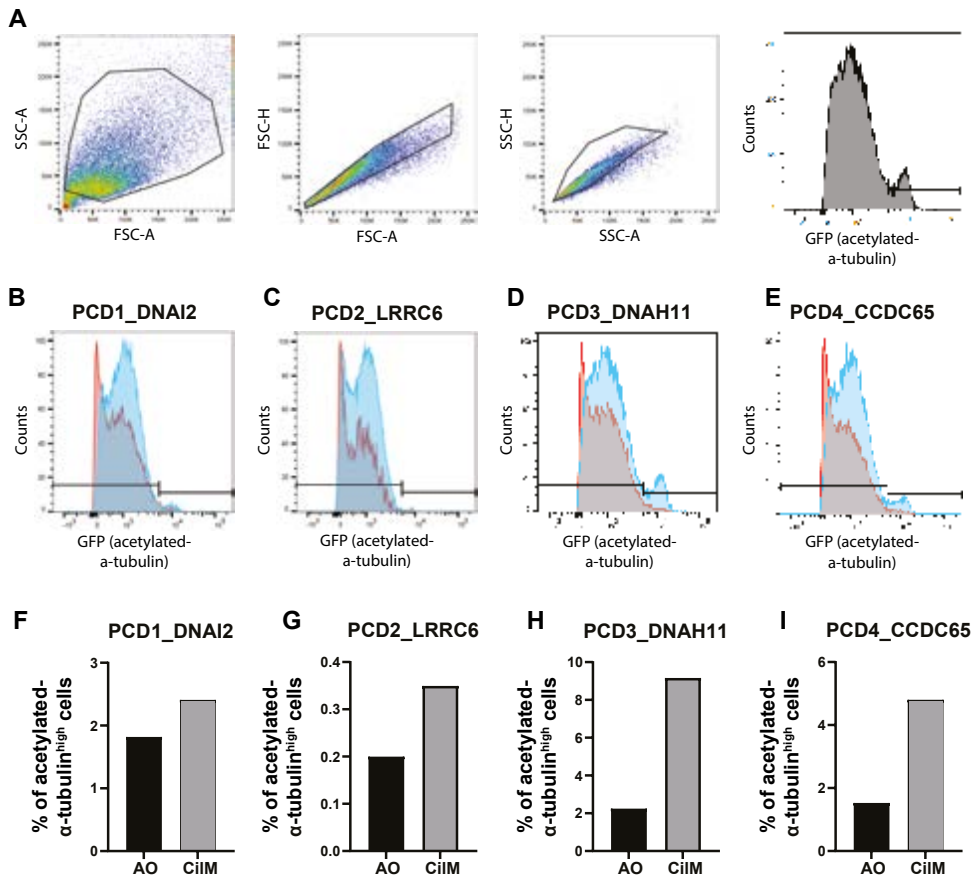


Figure EV2. Ciliated cell numbers increase in all PCD AOs with varying efficiency after differentiation in CiIM. A) Representative FACS plots show that single acetylated- α -tubulin^{high} cells were identified among the population in AOs in CiIM and AO medium. B-E) The histograms show differentiation efficiency based on intensity of acetylated- α -tubulin expression of the four PCD AO lines. Increased counts of GFP^{high} cells could be identified in the single cell population in AOs differentiated for 14 days in CiIM compared to AOs cultured in AO medium. Bar indicates gating strategy for quantification. F-I) Bar plots depicting percentages of acetylated- α -tubulin^{high} cells in AOs differentiated in CiIM for 14 days or cultured for 14 days in AO medium. Increased percentages of ciliated cells can be observed in all donor lines with varying fold changes.

or undetectable and did not appear to change (**Figure EV4B-D**). Taken together, CiIM induces differentiation of AO cells towards a ciliated cell fate at the cost of secretory cell differentiation.

The presence of ciliated cells in CiIM was confirmed for all four PCD AOs using live fluorescent imaging and transmission and scanning electron microscopy (**Figure 5**). After 21 days in CiIM, PCD AOs showed varying, yet abundant levels of ciliated cells in all cystic organoids. The ciliated cells were mostly located on the luminal side of the organoids while some more dense AOs showed an inverse polarity with cilia on the outside of

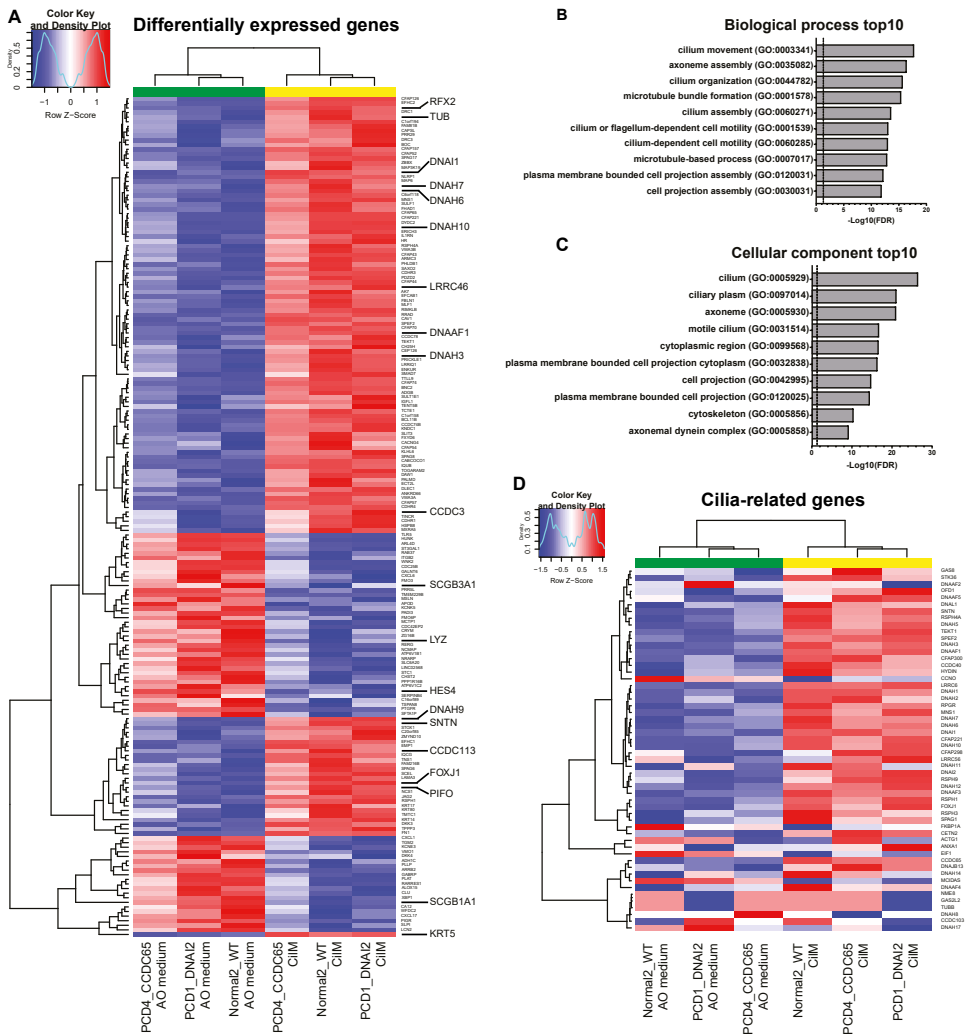


Figure 3. Upregulation of cilia-related genes in human airway organoids after 21 days in CiIM. A) Heatmaps depicting significantly differentially expressed genes of healthy (Normal2_WT) and PCD (PCD1_DNAI2 and PCD4_CCDC65) organoids after 21 days in CiIM compared to AO medium. Both healthy and PCD organoids showed an upregulation of ciliated genes such as RFX2, DNAI1 and CCDC3 and a down regulation of marker genes related to secretory cells. p value < 0.05 and $abs(\text{Log}_2\text{Fold change}) > 1.5$. Colored bar represents row z-scores of donor effect corrected normalised counts. CiIM AOs (yellow) cluster apart from AO medium AOs (green) in unsupervised hierarchical clustering. B) GO term enrichment analysis for biological processes of the significantly up-regulated genes in CiIM compared to AO medium. The top 10 genes are all related to the function of ciliated cells/ cilia function. C) GO term enrichment analysis for cellular component of the significantly up-regulated genes in CiIM compared to AO medium. The top 10 genes are all related to the function of ciliated cells/ cilia function. D) Heatmaps depicting cilia-related genes in healthy (Normal2_WT) and PCD (PCD1_DNAI2 and PCD4_CCDC65) organoids after 21 days in CiIM compared to AO medium. Both healthy and PCD organoids showed an upregulation of most ciliated genes. Colored bar represents row z-scores of donor effect corrected normalised counts. CiIM AOs (yellow) cluster apart from AO medium AOs (green) in unsupervised hierarchical clustering.

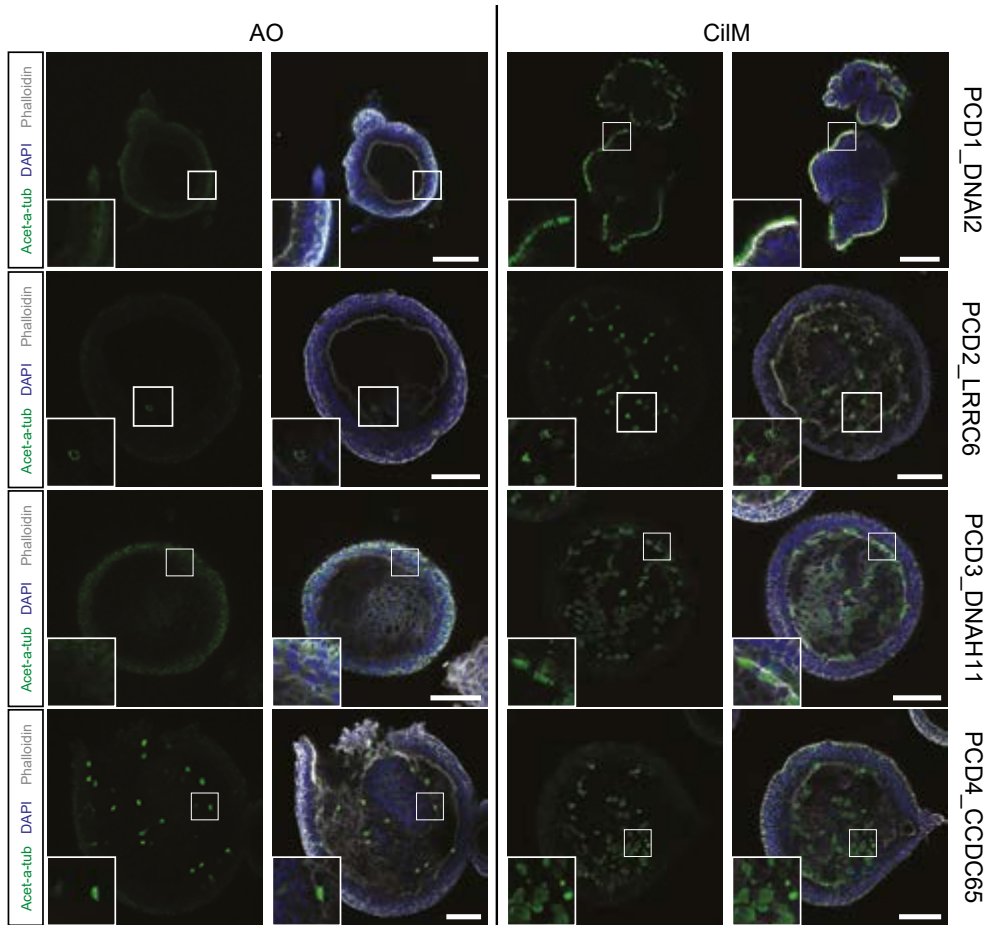


Figure EV3. Varying numbers of cilia are visible on the apical surface of PCD AOs. An increased number of cilia (acetylated- α -tubulin⁺ (acet-a-tub)) is observed in patient-derived PCD AOs after differentiation for 14 days in CiM (right panels) compared to AO Medium (left panels) in all donor lines. Representative images show varying numbers of cilia between donors in both AO medium and CiM. Scale bar = 100 μ m. Images of PCD3_DNAH11 are similar to Figure 2F.

the organoid (**Figure 5A**). Ciliary immobility was observed in all cystic AOs of PCD1_DNAI2, PCD2_LRRC6 and PCD3_DNAH11 (Video EV4). Luminal coverage of cilia was confirmed using scanning electron microscopy in patient derived AOs (**Figure 5B**). Transmission electron microscopy identifies patches of ciliated cells in PCD3_DNAH11 and PCD2_LRRC6 organoids differentiated in CiM (**Figure EV5A-C**). Similar to earlier quantification, PCD2_LRRC6 showed much less cilia when compared to PCD3_DNAH11. Contrarily, rare AOs were identified with patches of cells with secretory vesicles in AO medium PCD2_LRRC6 but never in organoids grown in CiM (**Figure EV7D**). Closer inspection of the cilia in organoids grown in CiM revealed ultrastructural abnormalities in both PCD3_DNAH11 as in PCD2_LRRC6, as described previously²⁷. PCD3_DNAH11

1
2
3
4
5
6
7
8
9
&

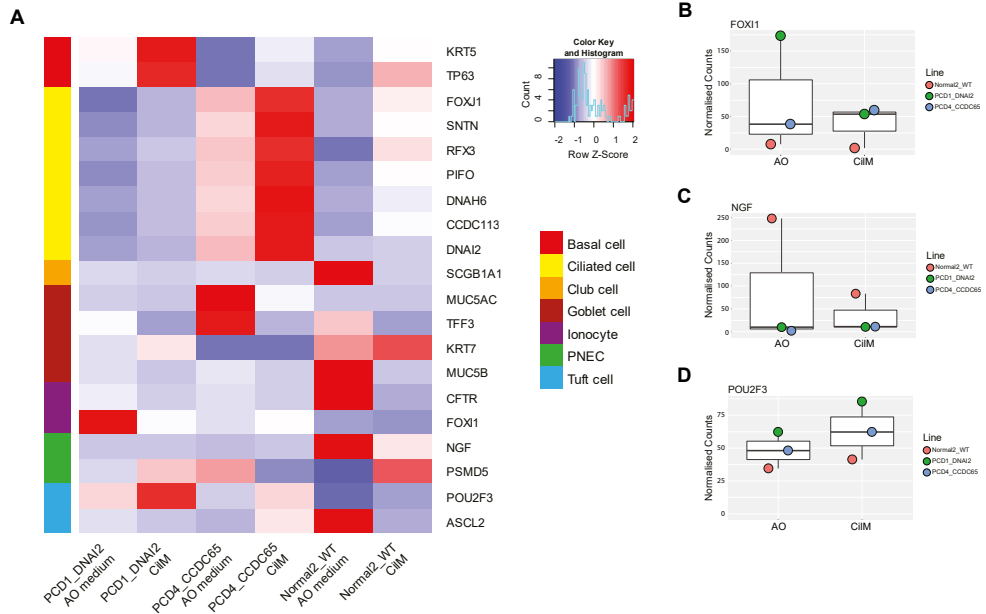


Figure EV4. Contribution of PNEC, ionocyte and tuft cells does not change in CiLM. A) Heatmaps depicting expression of known cell markers for pulmonary cell types in Normal2_WT, PCD1_DNAI2 and PCD4_CCDC65 cultured in CiLM and AO medium. Row color on the left indicates cell type. PNEC = pulmonary neuroendocrine cell. Colored bar represents Z-score of log2 transformed values of bulk mRNA sequencing data. B) No significant differences in normalised counts of ionocyte marker *FOXI1* in Normal2_WT, PCD1_DNAI2 and PCD4_CCDC65 cultured AO or in CiLM was observed as indicated in this dotplot graph. Colors of dots indicate the individual organoid line. Boxplot shows median, two hinges (25th and 75th percentile) and two whiskers (largest and smallest value no further than 1.5x inter-quartile range). C) No significant differences in normalised counts of pulmonary neuroendocrine cell marker *NGF* in Normal2_WT, PCD1_DNAI2 and PCD4_CCDC65 cultured AO medium or in CiLM was observed as indicated in this dotplot graph. Colors of dots indicate the individual organoid line. Boxplot shows median, two hinges (25th and 75th percentile) and two whiskers (largest and smallest value no further than 1.5x inter-quartile range). D) A slight increase normalised counts of tuft cell marker *POU2F3* in Normal2_WT, PCD1_DNAI2 and PCD4_CCDC65 cultured in CiLM was observed compared to AO medium. Colors of dots indicate the individual organoid line. Boxplot shows median, two hinges (25th and 75th percentile) and two whiskers (largest and smallest value no further than 1.5x inter-quartile range).

showed presence of outer dynein arms but misalignment of the inner arm in the cilia analysed (**Figure 5C-E**). This contrasted with the outer arm-location of DNAH11 protein. Ciliary ultrastructures of the PCD3_DNAH11 patient were indicated as normal during diagnostics. This might indicate the need of additional material in the form of AOs to aid diagnostics. PCD2_LRRC6 missed both inner and outer dynein arms (**Figure 5F-H**).

Given that for some patients, diagnostic parameters like ciliary ultrastructures remain inconclusive for a definitive PCD diagnosis (**Table EV5**) and the abundance of ciliated cells in CiLM, we then studied cilia-function in the PCD patient-derived AOs. These observations were compared to available diagnostic data of the same patients. All patients had low nasal

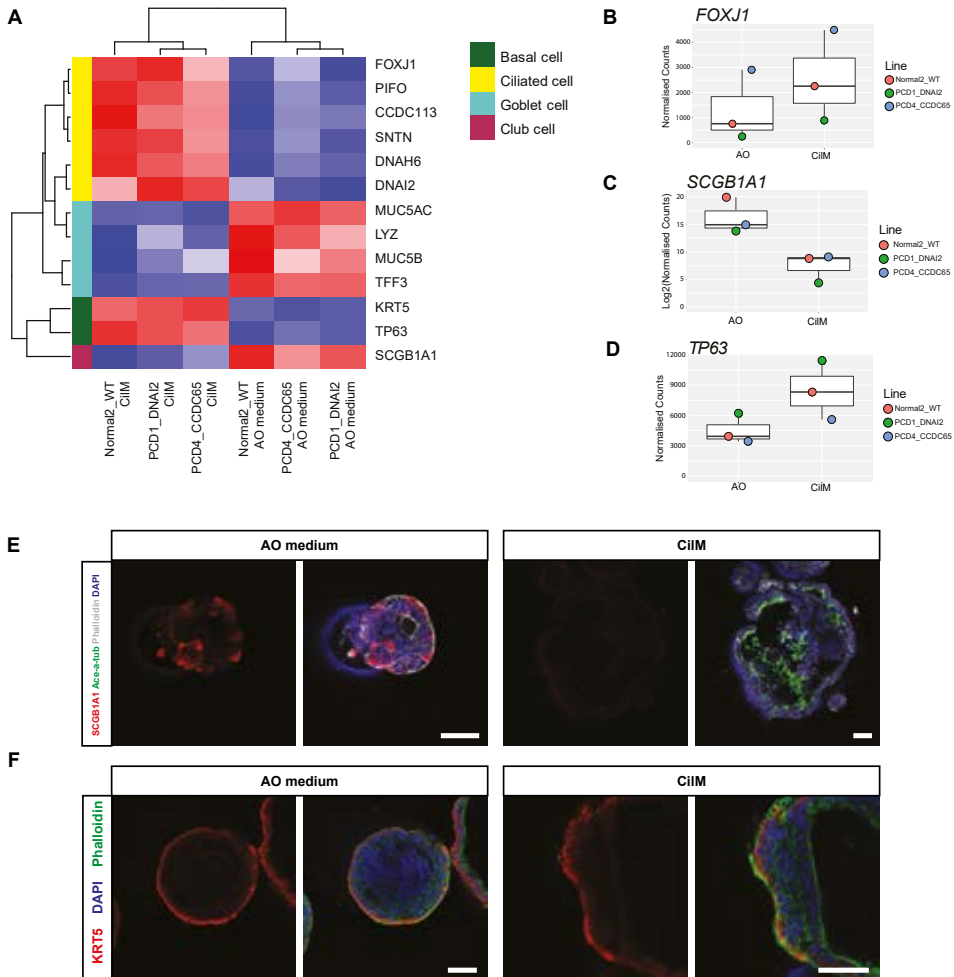


Figure 4. Cellular compositional changes in AOs upon culturing in CiIM by bulk mRNA sequencing. A) Heatmaps depicting the expression of well-established marker genes for the different pulmonary cell types in normal (Normal2_WT) and PCD (PCD1_DNAI2 and PCD4_CCDC65) organoids, cultured for 21 days in CiIM compared to 21 days in AO medium. Colored bar represents row z-scores of donor-corrected normalised counts. B-D) Dotplot graph depicting the normalised counts of ciliated cell marker *FOXJ1* (B), club cell marker *SCGB1A1* (C) and basal cell marker *TP63* (D) in Normal2_WT, PCD1_DNAI2 and PCD4_CCDC65 cultured for 21 days in CiIM or AO medium. Colors of dots indicate the individual organoid line. Boxplot shows median, two hinges (25th and 75th percentile) and two whiskers (largest and smallest value no further than 1.5x inter-quartile range). E) Representative immunofluorescence images of PCD AOs (PCD2_LRRC6) in CiIM (14 days) stained for cilia (acetylated- α -tubulin (Ac- α -tub)), secretory cells (SCGB1A1), cellular membrane (Phalloidin) and nucleus (DAPI). Secretory cells can be identified in AOs cultured for 21 days in AO medium as SCGB1A1⁺ cells but not in AOs cultured in CiIM for 21 days. In contrast, cilia (acetylated- α -tubulin (Ace-a-tub)⁺) can only be identified in AOs cultured in CiIM. Representative image. Scale bar = 50 μ m. F) Representative image of PCD AOs (PCD3_DNAH11) in CiIM (14 days) stained for basal cells (keratin 5 (KRT5)), cellular membrane (Phalloidin) and nucleus (DAPI). No significant difference in the number of basal cells can be observed between organoids cultured in AO medium or CiIM (14 days). Scale bar = 50 μ m.

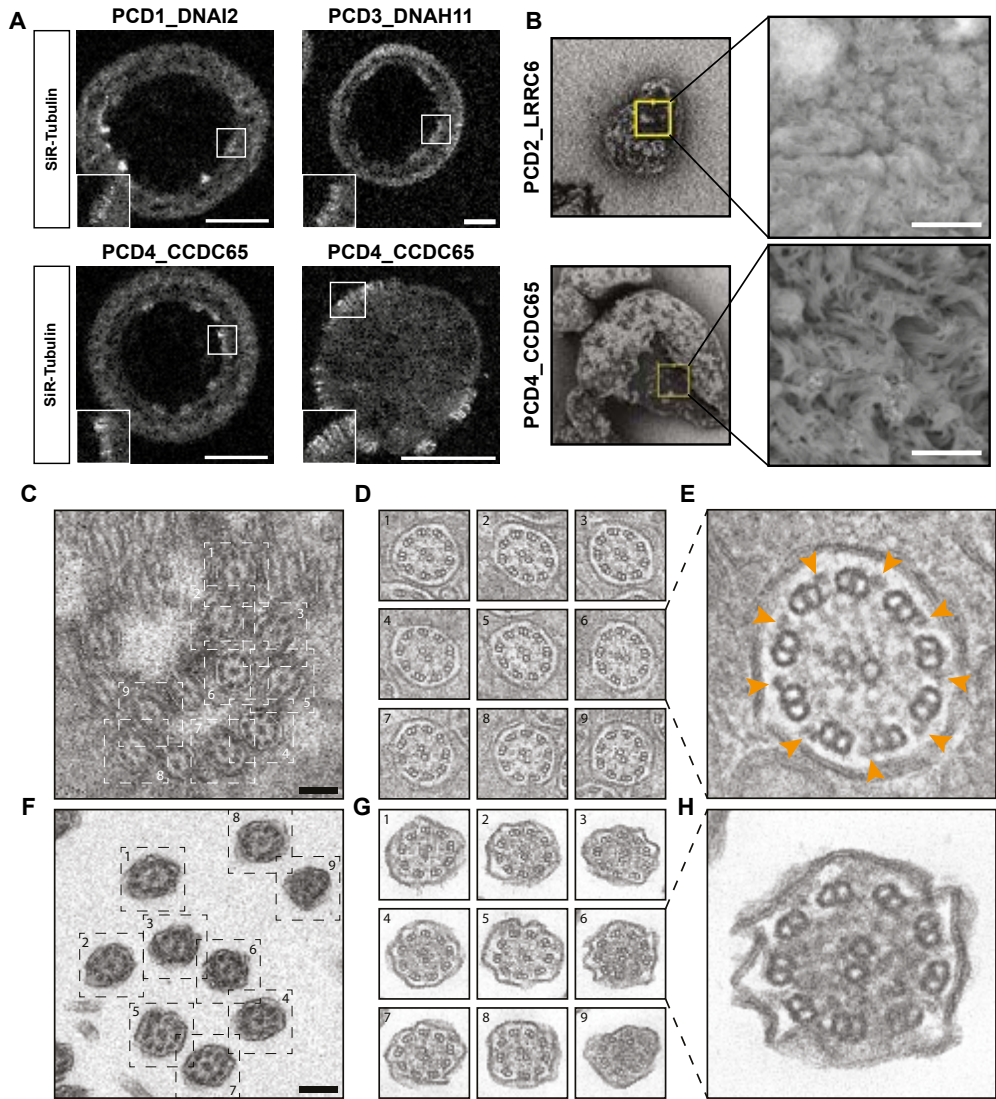


Figure 5. PCD AOs differentiated towards ciliated cells allow live and nanoscopic analysis. A) Representative immunofluorescence images of patient-derived PCD AOs stained with a SiR-tubulin live stain. Differentiation in CiLM results in an increase in the number of ciliated cells. Scale bar = 50 μ m. B) Scanning electron microscopy images of PCD organoids. Luminal cilia occur in patient-derived AOs that differentiated in CiLM for 21 days. Zoom ins shows cilia. Scale bar = 5 μ m. C-H) Electron tomography showing the mutant cilia phenotypes from PDC3_DNAH11 (C-E) and PCD2_LRRC6 (F-H) patient-derived organoids. Dual-axis tilt series were acquired of which the 0 $^{\circ}$ -tilt are represented after erasing the fiducial gold-beads in IMOD (C, F). After the 3D reconstruction, cilia phenotypes were easily recognized by volume visualization in ChimeraX (D, G). PCD2_LRRC6 AOs showed dynein arm disorders (H), although cilia of PCD3_DNAH11 still had clearly recognizable outer and inner dynein arms (E; arrowheads). Scale bars represent 250nm.

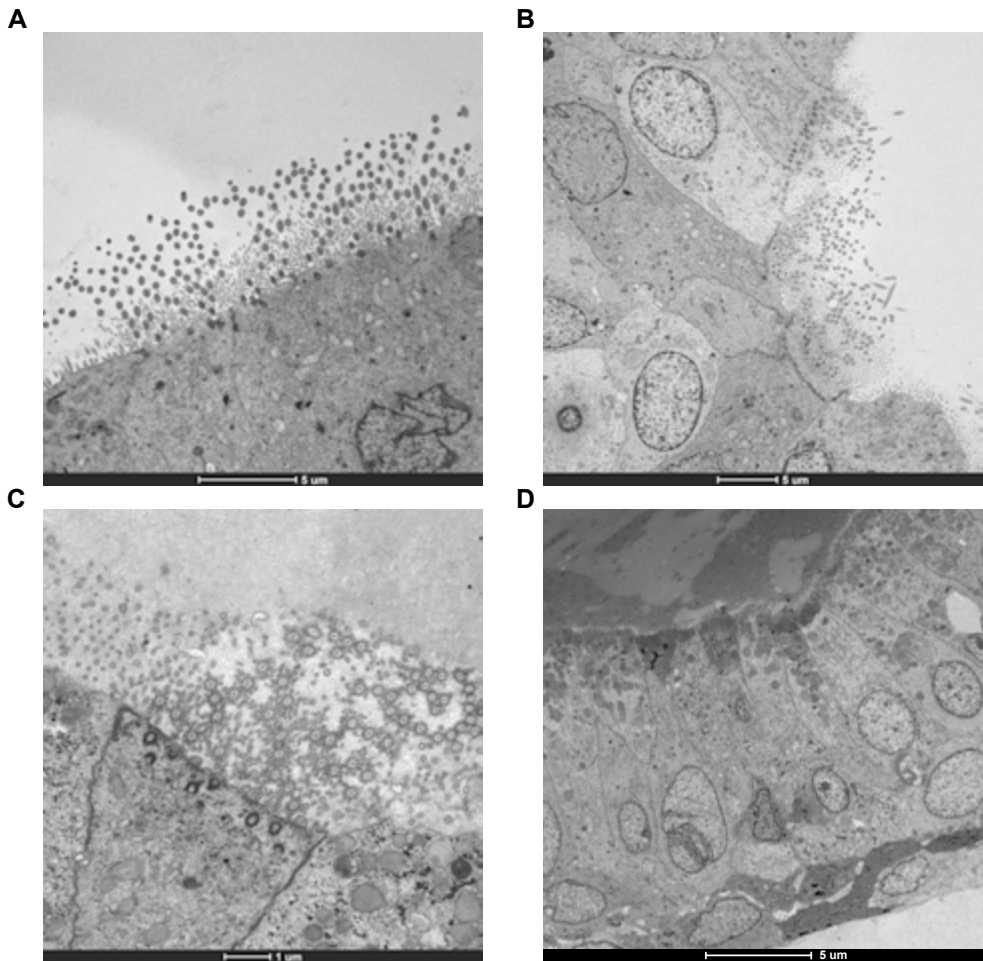


Figure EV5. Transmission electron microscopy reveals patches of ciliated cells.A) Ciliated cells were identified facing the lumen of PCD2_LRRC6 AOs in CiLM. Scale bar = 5μm. B-C) Ciliated cells were more frequently identified in PCD3_DNAH11 AOs in CiLM. Scale bar = 5μm (B) and 1μm (C). D) Rare AOs with secretory cells were identified in PCD2_LRRC6 AOs in AO medium. Scale bar = 5μm.

nitric oxide (nNO) production (12-59 ppb, while the threshold for diagnosis is <200ppb). Apart from nNO levels, each patient lacked important additional diagnostic values. Patient 1 (PCD1_DNAI2) and 4 (PCD4_CCDC65) did not present with otitis media while patient 3 (PCD3_DNAH11) had no signs of bronchiectasis (**Table EV5**). To include a new diagnostic measure, patient-specific functional phenotypes were studied in organoids in CiLM by 4 hour-video recording. While healthy AOs showed directional mucosal spin over this period due to their coordinated ciliary beating, AOs with mutations in the outer dynein arm (PCD1_DNAI2 and PCD3_DNAH11) displayed no ciliary beating, resulting in absent mucosal spin. Surprisingly, both patients presented with inconclusive and normal electron

1
2
3
4
5
6
7
8
9
&

micrograph respectively which could have led to misdiagnosing the patient. Contrarily, PCD3_DNAH11 AOs showed some structural abnormalities in organoid-derived TEM images which confirmed diagnosis of PCD (**Figure 5C-E**). Ciliary beating was observed in AOs of PCD4_CCDC65, but mucosal spin remained absent (Video EV5). The patient presented during diagnosis with a normal electron micrograph. Slow-motion imaging of the ciliary beat of PCD4_CCDC65 revealed uncoordinated and stiff beating characterised by loss of the arching of the cilium (Video EV6). This aberrant cilium movement explained the absence of directional mucosal spin in long-term imaging. Satisfyingly, a PCD phenotype could be identified for all three patients that presented with an inconclusive or a normal electron micrograph. Most importantly, in comparison to ALI cultures, AOs can be expanded over extensive period of time. AO cultures therefore can provide additional and potentially crucial information to the standard PCD diagnosis which involves ALI and electron micrographs and provide additional material for later studies.

To summarise the potential of AOs as diagnostic measures, PCD1_DNAI2, PCD2_LRRC6 and PCD3_DNAH11 showed immotile cilia in the live imaging of AOs while PCD4_CCDC65 showed hyperkinetic and/or stiff ciliary movement. Both in PCD2_LRRC6 as PCD3_DNAH11 AOs ultrastructural abnormalities were observed which was missed in PCD3_DNAH11 during diagnostics. In all four patients no mucosal swirl was observed. Together with nNO levels, these parameters were able to identify PCD patient samples apart from healthy (**Table EV5**). Additional patient-derived lines will be needed to further strengthen this claim.

Apart from increased diagnostic opportunities, organoids allow for genetic manipulation. Repair of the mutated gene and the future perspective of potential autologous transplantation of the organoids could be regarded as definitive treatment of PCD patients. Therefore, we applied prime editing in PCD AOs^{31,32}. PCD3_DNAH11 AOs were transfected with plasmids coding a modified Cas9 with nickase activity and reverse translation of a provided wild-type DNA template (**Figure 6A**). To repair the mutation in *DNAH11* in PCD3_DNAH11 organoids were made into single cells, incubated with the above mentioned DNA and electroporated using earlier described method³³. Outgrowth of clones after recovery and culturing was minimal potentially due to suboptimal conditions. Small AOs that stopped proliferating after several days but survived hygromycin selection, of which resistance was introduced in the same electroporation using the piggyBac system, were genotyped to identify efficiency of the genetic editing. We could identify both homozygous and heterozygous repair of the mutated allele (**Figure 6B**). 62,5% of the organoids showed homozygous repair, 25% of the organoids showed heterozygous repair and 12,5% of the AOs picked were resistant to selection but showed no repair (**Figure 6C**). Unfortunately, none of the repaired organoid lines could be expanded long-term, something we have observed consistently when AO manipulation involves transfection and a sub-cloning step. Although optimisation on generating stable lines is needed, the AOs allow for genetic editing to repair PCD-causing mutations.

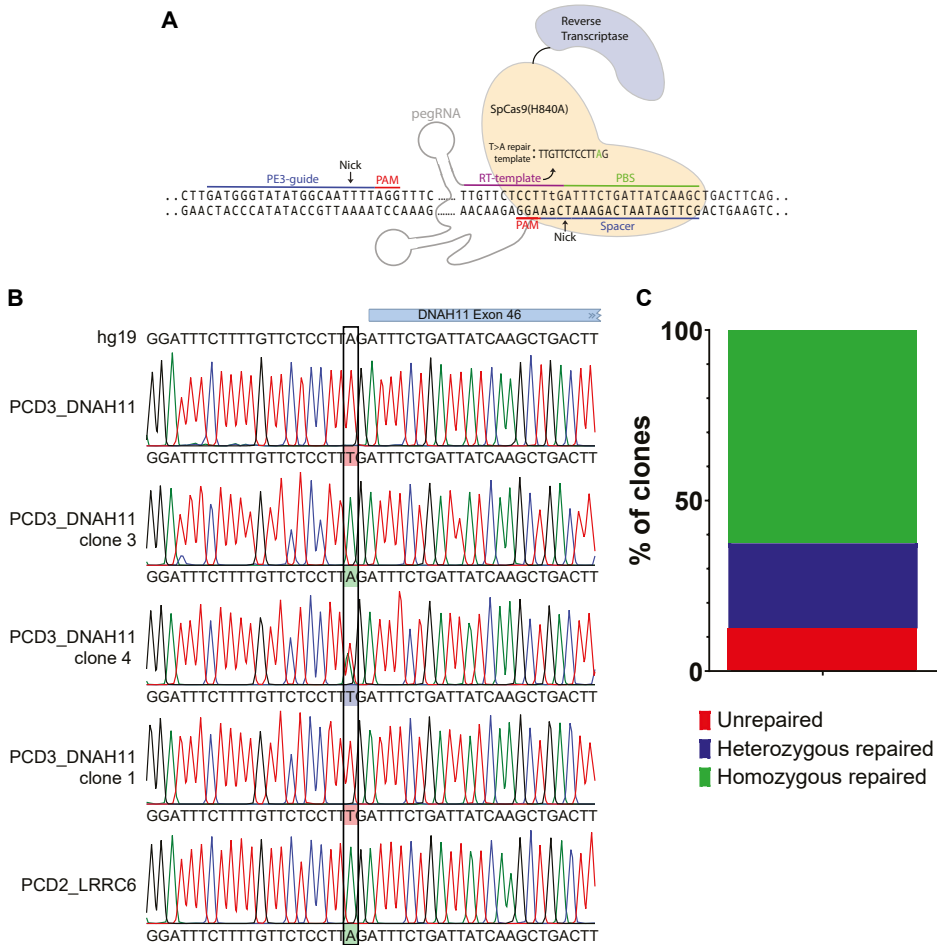


Figure 6. Repair of DNAH11 mutation in PCD3_DNAH11 using prime editing. A) Schematic drawing of the prime editing complex including sequences used for prime editing (PE3)-guide, reverse transcriptase (RT)-template, primer binding site (PBS) and spacer. RT-template indicates the base exchange of T>A to repair c.7472-2A>T in *DNAH11*. B) Sanger sequencing traces from isolated single organoid clones aligned to the reference sequence of *DNAH11* (hg19). PCD3_DNAH11 organoids were electroporated with the primer editor. Clones from PCD3_DNAH11 wild type (green), heterozygous (blue) and mutated (red) were identified. C) Bar plot of quantification of the efficiency of repair with prime editing in picked clones of PCD3_DNAH11. Unrepaired (red), homozygous repaired (green) and heterozygous repaired (blue) sequences could be identified.

DISCUSSION

Here, we describe a long-term disease modelling strategy using AOs derived from NITB samples. Combined treatment with a Notch inhibitor and a BMP activator (CiIM) improves differentiation towards ciliated cells when compared to our original AO protocol¹³. CiIM thereby facilitates easy visualisation of ciliated cell-related biology and disease. Induction of ciliated cells coincides with inhibition of secretory differentiation. This bifurcation is known

1
2
3
4
5
6
7
8
9
&

to be controlled by Notch signalling, a phenomenon exploited in our strategy³⁴. Of note, it is somewhat surprising that Notch inhibition of the intestinal epithelium (both *in vivo* and in organoids) results in the opposite effect: a dramatic increase in secretory lineage cells^{35–38}. The differentiated AO lines retain their multipotency as evidenced upon re-transfer to the original AO medium. One advantage of this model system over conventional diagnostic cultures is the possibility for long-term culture and thereby for more extensive modelling, e.g. by using CRISPR/Cas9 tools³⁹. Currently, AOs show restricted growth after stress by electroporation, lentiviral transduction or subcloning. Expanding these organoids using current conditions do not allow sustained growth. Of note, unmanipulated airway organoids can be expanded >1-2 years¹³ and are thus comparable to classical cell lines, while primary cells can only be cultured for weeks, without significant expansion of the input cells.

Research questions that can be answered by this differentiation protocol specifically address ciliated cell function. The AO cultures, however, remain multipotent as evidenced upon re-transfer to the original AO medium. One advantage of this model system over conventional diagnostic cultures is the possibility for long-term culture and thereby for more extensive modelling, e.g. by using CRISPR/Cas9 tools³⁹. Increased outgrowth potential is however required to generate stable organoid lines. Currently, AOs show limited growth after stress, like electroporation or lentiviral transduction, and of stop in growth is observed after several days. Expanding these organoids using conventional expansion conditions do not allow sustained growth. The organoids can be expanded >1 year in expansion conditions¹³ and are thus comparable to classical cell lines, while primary cells can only be cultured for weeks, without significant expansion of the input cells.

We present an example of ciliated cell disease modelling by using patient-derived AOs from four PCD patients. Our approach requires a very small amount of donor material as compared to current diagnostic practice and allows for standardised tests for a range of PCD phenotypes. Moreover, we show that the AO cultures can identify ciliary movement defects in cases where electron microscopical analysis would not reveal any ultrastructural ciliary changes. The AO approach can therefore be seen as an additional and potentially definitive diagnostic assay of PCD patients.

To date, treatment options for PCD and other disorders involving motile cilia remain limited. Patient-derived organoids have proven to predict individual patient responses in cancer^{40–43}, as well as in cystic fibrosis^{13,44,45}. Treatments for cystic fibrosis can however not be directly translated to PCD^{46–48}. PCD-derived ciliated organoids could be used to identify or develop drugs that target the ciliary defect directly and may facilitate development of gene therapy approaches. Indeed, AOs derived from cystic fibrosis patients have been corrected by CRISPR approaches⁴⁹. While transplantation of human stem cell-derived organoids is not yet feasible, the potential of gene-correcting PCD patient-derived AOs followed by autologous transplantation may become a reality. Taken together, PCD AO models may become instrumental to obtain cell-biological, diagnostic and therapeutic insights into primary ciliary dyskinesia and other ciliated cell-related diseases.

DATA AVAILABILITY

Bulk mRNA sequencing data is deposited at GEO under GSE158775 and publicly available.

ACKNOWLEDGMENTS

We thank A. de Graaff and the Hubrecht Imaging Centre (HIC) for microscopy assistance and the Utrecht Sequencing Facility (subsidized by the University Medical Centre Utrecht, Hubrecht Institute, Utrecht University and NWO project 184.034.019). We thank Medical Microbiology of the University Medical Centre Utrecht for the help with scanning electron microscopy. We thank Talya Dayton and Amanda Andersson-Rolf for their help with writing the manuscript, Carola Ammerlaan for her help with flow cytometry experiments and analysis. This work was supported by the gravitation program CancerGenomiCs.nl from the Netherlands Organisation for Scientific Research.

AUTHOR CONTRIBUTIONS

J.V., L.B. and H.C. designed and conceived the study. J.V. and H.C. wrote the manuscript. J.V., L.B. and N.S. cultured the organoid lines and performed organoid related experiments. J.V. and L.B. analysed the data. J.V., L.B., J.K. and H.B. embedded organoids and performed immunohistochemistry staining. M.G. designed prime editing strategy. W.W. and C.L. performed TEM imaging and K.K. provided tomographic images. P.P. supervised electron microscopy core and helped analyses. K.E. and A.G. provided patient tissue samples. H.C. supervised the project.

CONFLICT OF INTEREST

H.C. is inventor on several patents related to organoid technology together with N.S.; his full disclosure is given at <https://www.uu.nl/staff/JCClevers/>.

1

2

3

4

5

6

7

8

9

&

REFERENCES

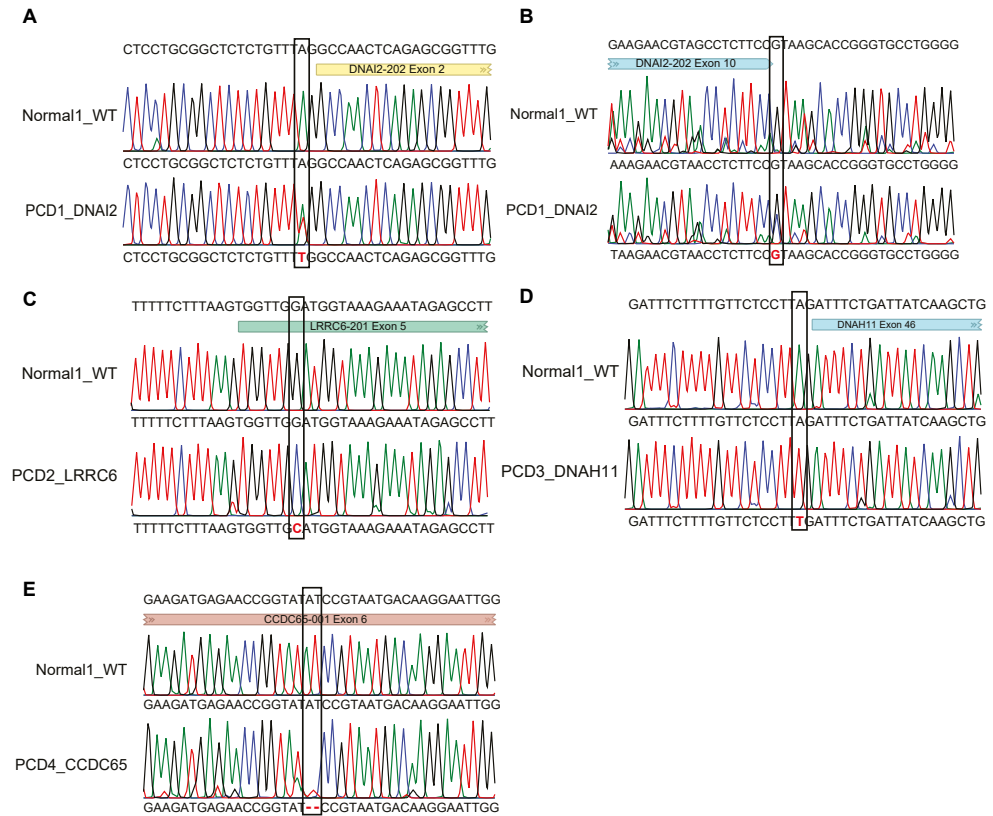
1. Bustamante-Marin, X. M. & Ostrowski, L. E. Cilia and mucociliary clearance. *Cold Spring Harb. Perspect. Biol.* **9**, (2017).
2. Leigh, M. W., O'Callaghan, C. & Knowles, M. R. The challenges of diagnosing primary ciliary dyskinesia. in *Proceedings of the American Thoracic Society* **8**, 434–437 (Proc Am Thorac Soc, 2011).
3. Knowles, M., Zariwala, M. & Leigh, M. Primary Ciliary Dyskinesia. *Clin Chest Med* **37**, 449–461 (2016).
4. Leigh, M. W. et al. Primary Ciliary Dyskinesia (PCD): A genetic disorder of motile cilia. *Transl. Sci. rare Dis.* **4**, 51–75 (2019).
5. Lucas, J. S., Davis, S. D., Omran, H. & Shoemark, A. Primary ciliary dyskinesia in the genomics age. *Rev. Lancet Respir Med* **8**, 202–218 (2020).
6. Goutaki, M. et al. Clinical manifestations in primary ciliary dyskinesia: Systematic review and meta-analysis. *European Respiratory Journal* **48**, 1081–1095 (2016).
7. Mullowney, T. et al. Primary ciliary dyskinesia and neonatal respiratory distress. *Pediatrics* **134**, 1160–1166 (2014).
8. Gileles-Hillel, A. et al. Whole Exome Sequencing Accuracy in the Diagnosis of Primary Ciliary Dyskinesia. in *D95. Advances In Cystic Fibrosis and Primary Ciliary Dyskinesia A7664–A7664* (American Thoracic Society, 2020). doi:10.1164/ajrccm-conference.2020.201.1_MeetingAbstracts.A7664
9. Poprzeczko, M. et al. Rare Human Diseases: Model Organisms in Deciphering the Molecular Basis of Primary Ciliary Dyskinesia. *Cells* **8**, (2019).
10. Norris, D. P. & Grimes, D. T. Mouse models of ciliopathies: The state of the art. *DMM Disease Models and Mechanisms* **5**, 299–312 (2012).
11. Hirst, R. A., Rutman, A., Williams, G. & O'Callaghan, C. Ciliated Air-Liquid Cultures as an Aid to Diagnostic Testing of Primary Ciliary Dyskinesia. *Chest* **138**, 1441–1447 (2010).
12. Hirst, R. A. et al. Culture of Primary Ciliary Dyskinesia Epithelial Cells at Air-Liquid Interface Can Alter Ciliary Phenotype but Remains a Robust and Informative Diagnostic Aid. *PLoS One* **9**, e89675 (2014).
13. Sachs, N. et al. Long-term expanding human airway organoids for disease modeling. *EMBO J.* **38**, e100300 (2019).
14. van der Vaart, J. & Clevers, H. Airway organoids as models of human disease. *Journal of Internal Medicine* (2020). doi:10.1111/joim.13075
15. Zhou, J. et al. Differentiated human airway organoids to assess infectivity of emerging influenza virus. *Proc. Natl. Acad. Sci.* **115**, 6822–6827 (2018).
16. Wallmeier, J. et al. Motile ciliopathies. *Nat. Rev. Dis. Prim.* **6**, (2020).
17. Barlocco, E. G. et al. Ultrastructural ciliary defects in children with recurrent infections of the lower respiratory tract. *Pediatr. Pulmonol.* **10**, 11–17 (1991).
18. Marthin, J. K., Stevens, E. M., Larsen, L. A., Christensen, S. T. & Nielsen, K. G. Patient-specific three-dimensional explant spheroids derived from human nasal airway epithelium: a simple methodological approach for ex vivo studies of primary ciliary dyskinesia. *Cilia* **2017** *6*, 1–9 (2017).
19. Coles, J. L. et al. A Revised Protocol for Culture of Airway Epithelial Cells as a Diagnostic Tool for Primary Ciliary Dyskinesia. *J. Clin. Med.* **2020**, Vol. 9, Page 3753 **9**, 3753 (2020).
20. Adil, E. A., Kawai, K., Dombrowski, N., Irace, A. L. & Cunningham, M. J. Nasal versus tracheobronchial biopsies to diagnose primary ciliary dyskinesia: A meta-analysis. *Laryngoscope* **127**, 6–13 (2017).
21. Bricmont, N. et al. Nasal Brushing Sampling and Processing using Digital High Speed Ciliary Videomicroscopy - Adaptation for the COVID-19 Pandemic. *J. Vis. Exp.* **2020**, 1–30 (2020).
22. Shoemark, A. et al. Accuracy of Immunofluorescence in the Diagnosis of Primary Ciliary Dyskinesia. *Am. J. Respir. Crit. Care Med.* **196**, 94–101 (2017).
23. Lucas, J. S. et al. Diagnosis and management of primary ciliary dyskinesia. *Arch. Dis. Child.* **99**, 850–856 (2014).

24. Liu, Z. *et al.* Human Nasal Epithelial Organoids for Therapeutic Development in Cystic Fibrosis. *Genes (Basel)*. **11**, 1–17 (2020).
25. Anderson, J. D., Liu, Z., Odom, L. V., Kersh, L. & Guimbellot, J. S. CFTR function and clinical response to modulators parallel nasal epithelial organoid swelling. <https://doi.org/10.1152/ajplung.00639.2020> (2021). doi:10.1152/AJPLUNG.00639.2020
26. Rijsbergen, L. C. *et al.* Human Respiratory Syncytial Virus Subgroup A and B Infections in Nasal, Bronchial, Small-Airway, and Organoid-Derived Respiratory Cultures. *mSphere* **6**, (2021).
27. Horani, A. *et al.* LRRC6 Mutation Causes Primary Ciliary Dyskinesia with Dynein Arm Defects. *PLoS One* **8**, 59436 (2013).
28. Horani, A. *et al.* CCDC65 Mutation Causes Primary Ciliary Dyskinesia with Normal Ultrastructure and Hyperkinetic Cilia. *PLoS One* **8**, (2013).
29. Spassky, N. & Meunier, A. The development and functions of multiciliated epithelia. *Nature Reviews Molecular Cell Biology* **18**, 423–436 (2017).
30. Horani, A. & Ferkol, T. W. Advances in the Genetics of Primary Ciliary Dyskinesia: Clinical Implications. *Chest* **154**, 645–652 (2018).
31. Geurts, M. H. *et al.* Evaluating CRISPR-based Prime Editing for cancer modeling and CFTR repair in intestinal organoids. *bioRxiv* (2020). doi:10.1101/2020.10.05.325837
32. Schene, I. F. *et al.* Prime editing for functional repair in patient-derived disease models. *Nat. Commun.* 2020 **111** **11**, 1–8 (2020).
33. Fujii, M., Clevers, H. & Sato, T. Modeling Human Digestive Diseases With CRISPR-Cas9–Modified Organoids. *Gastroenterology* **156**, 562–576 (2019).
34. Guseh, J. S. *et al.* Notch signaling promotes airway mucous metaplasia and inhibits alveolar development. *Development* **136**, 1751–1759 (2009).
35. Van Es, J. H. *et al.* Notch/ γ -secretase inhibition turns proliferative cells in intestinal crypts and adenomas into goblet cells. *Nature* **435**, 959–963 (2005).
36. Milano, J. *et al.* Modulation of Notch processing by γ -secretase inhibitors causes intestinal goblet cell metaplasia and induction of genes known to specify gut secretory lineage differentiation. *Toxicol. Sci.* **82**, 341–358 (2004).
37. Fre, S. *et al.* Notch signals control the fate of immature progenitor cells in the intestine. *Nature* **435**, 964–968 (2005).
38. Yin, X. *et al.* Niche-independent high-purity cultures of Lgr5 + intestinal stem cells and their progeny. *Nat. Methods* **11**, 106–112 (2014).
39. Driehuis, E. & Clevers, H. *CRISPR/Cas 9 genome editing and its applications in organoids*. **312**, G257–G265 (American Physiological Society, 2017).
40. Driehuis, E. *et al.* Pancreatic cancer organoids recapitulate disease and allow personalized drug screening. *Proc. Natl. Acad. Sci. U. S. A.* **116**, 26580–26590 (2019).
41. Driehuis, E. *et al.* Oral Mucosal Organoids as a Potential Platform for Personalized Cancer Therapy. *Cancer Discov.* **9**, 852–871 (2019).
42. Tiriach, H. *et al.* Organoid profiling identifies common responders to chemotherapy in pancreatic cancer. *Cancer Discov.* **8**, 1112–1129 (2018).
43. Lee, S. H. *et al.* Tumor Evolution and Drug Response in Patient-Derived Organoid Models of Bladder Cancer. *Cell* **173**, 515–528.e17 (2018).
44. de Winter-De Groot, K. M. *et al.* Stratifying infants with cystic fibrosis for disease severity using intestinal organoid swelling as a biomarker of CFTR function. *Eur. Respir. J.* **52**, (2018).
45. Dekkers, J. F. *et al.* Characterizing responses to CFTR-modulating drugs using rectal organoids derived from subjects with cystic fibrosis. *Sci. Transl. Med.* **8**, 344ra84–344ra84 (2016).
46. Barbato, A. *et al.* Primary ciliary dyskinesia: A consensus statement on diagnostic and treatment approaches in children. in *European Respiratory Journal* **34**, 1264–1276 (Eur Respir J, 2009).
47. Lucas, J. S. & Carroll, M. Primary ciliary dyskinesia and cystic fibrosis: Different



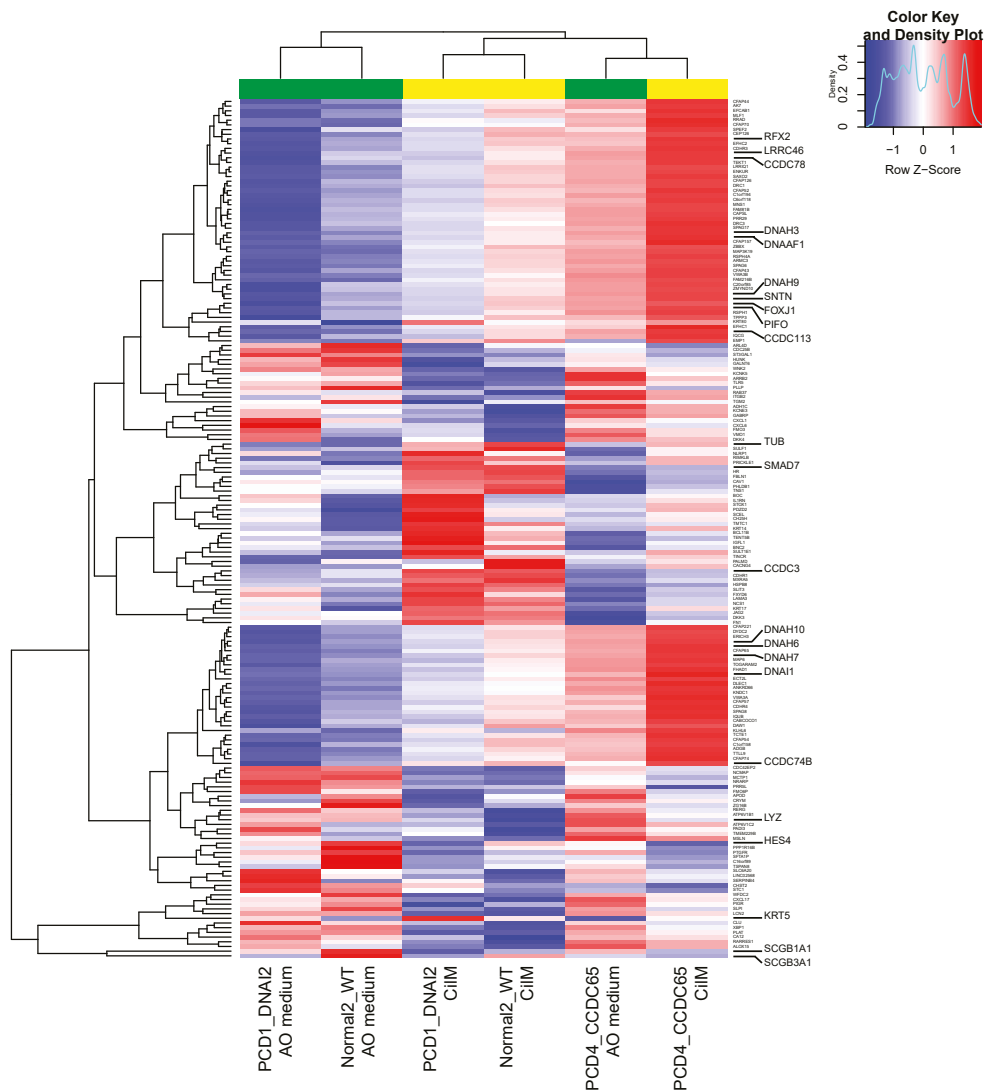
- diseases require different treatment. *Chest* **145**, 674–676 (2014).
48. Shapiro, A. J. et al. Diagnosis, monitoring, and treatment of primary ciliary dyskinesia: PCD foundation consensus recommendations based on state of the art review. *Pediatr. Pulmonol.* **51**, 115–132 (2016).
 49. Geurts, M. H. et al. CRISPR-Based Adenine Editors Correct Nonsense Mutations in a Cystic Fibrosis Organoid Biobank. *Cell Stem Cell* **26**, 503–510.e7 (2020).
 50. Neuberger, T., Burton, B., Clark, H. & Van Goor, F. Use of primary cultures of human bronchial epithelial cells isolated from cystic fibrosis patients for the pre-clinical testing of CFTR modulators. *Methods Mol. Biol.* **741**, 39–54 (2011).
 51. Love, M. I., Huber, W. & Anders, S. Moderated estimation of fold change and dispersion for RNA-seq data with DESeq2. *Genome Biol.* **15**, (2014).
 52. Anzalone, A. V. et al. Search-and-replace genome editing without double-strand breaks or donor DNA. *Nature* **576**, 149–157 (2019).
 53. Fujii, M., Matano, M., Nanki, K. & Sato, T. Efficient genetic engineering of human intestinal organoids using electroporation. *Nat. Protoc.* **10**, 1474–1485 (2015).
 54. Konishi, S. et al. Directed Induction of Functional Multi-ciliated Cells in Proximal Airway Epithelial Spheroids from Human Pluripotent Stem Cells. *Stem cell reports* **6**, 18–25 (2016).

SUPPLEMENTARY FIGURES



Supplementary figure S1. Mutations in various genes identified in PCD AOs. Sanger sequencing traces of PCD AOs reveals mutations in patient-derived organoids in DNAI2 (A-B), LRRC6 (C), DNAH11 (D) or CCDC65 (E). Normal1_WT sequences show wild-type alleles in all genes indicated. Black bar indicated area of mutation in PCD AO line.

1
 2
 3
 4
 5
 6
 7
 8
 9
 &



Supplementary figure S2. Differentially expressed genes show donor-donor variation in expression levels but show similar trends in all donors in CiIM compared to AO medium. Heatmaps depicting expression of significantly differentially expressed genes in PCD1_DNAI2, PCD4_CCDC65 and Normal2_WT differentiated in CiIM for 14 days compared to AOs grown in AO medium. Highlighted genes are known marker genes secretory cells (SCGB3A1, SCGB1A1 and LYZ), known downstream targets of BMP (SMAD7) or Notch (HES4) signalling, known marker genes of basal cells (KRT5) or involved in ciliary build-up. A general trend in expression levels can be observed but also donor-donor variations are visible after hierarchical clustering. PCD4_CCDC65 samples cluster separately independent of their culture method. Green bars indicate AO medium AOs. Yellow bars indicate CiIM AOs. Coloured bar represents Z-score of normalised counts without donor-corrected normalisation of bulk mRNA sequencing data.

Appendix TableS4. Patientdata.xlsx

ID	Sex	Age at		Age sample	Situs Status	Otitis Media	Bronchiectasis	Sinusitis	nNO	EM
		diagnosis/assessment	quirement							
hsLung-PCD3	F	7		33	Situs Solitus	No	Yes	Yes	47	Inconclusive
hsLung-PCD4	M	1		17	Situs Solitus	Yes	Yes	Yes	12	Absent dynein arm
hsLung-PCD5	M	27		31	?	Yes	No	Yes	59	Normal
hsLung-PCD6	M	15		21	Situs Solitus	No	Yes	Yes	35	Normal

1

2

3

4

5

6

7

8

9

&

CHAPTER

THE ORGANOID PLATFORM: PROMISES AND CHALLENGES AS TOOLS IN THE FIGHT AGAINST COVID-19

Maarten H. Geurts^{1,2,*}, Jelte van der Vaart^{1,2,*},
Joep Beumer^{1,2,*} and Hans Clevers^{1,2}

¹ Hubrecht Institute, Royal Netherlands Academy of Arts and Sciences
(KNAW) and University Medical Center Utrecht, 3584 CT Utrecht,
the Netherlands

² Oncode Institute, Hubrecht Institute, 3584 CT Utrecht, the Netherlands

* These authors contributed equally

*Published in Stem Cell Reports (2021);
doi: 10.1016/j.stemcr.2020.11.009*

3

ABSTRACT

Many pathogenic viruses that affect man display species-specificity, limiting the use of animal models. Studying viral biology and identifying potential treatments therefore benefits from the development of *in vitro* cell systems that closely mimic human physiology. In the current COVID-19 pandemic, rapid scientific insights are of the utmost importance to limit the public health and societal impact. Organoids are emerging as versatile tools to progress the understanding of SARS-CoV-2 biology and to aid the quest for novel treatments.

MAIN TEXT

The global outbreak of the novel coronavirus SARS-CoV-2 strains healthcare systems around the world and has already caused over a million deaths. COVID-19 is the third appearance of a lethal coronavirus, after the emergence of Severe Acute Respiratory syndrome coronavirus (SARS-CoV) in 2002 and Middle East respiratory syndrome virus (MERS-CoV) in 2012. It appears likely that more viral pandemics will follow. To develop effective treatment for current and future infectious diseases, it is key to establish *in vitro* models that closely resemble the physiology of the viral host and that are likely to allow -and model- infection by any type of virus. Much of the insight on coronavirus biology has been gathered using 'classical' 2D cell lines such as the Vero E6 cell line, derived from the kidney of the African green monkey¹. These cell lines are often easily infectable by viruses and -if so- can be used to propagate the virus for downstream experiments. However, cell lines are typically malignantly transformed and consist of a homogeneous population of poorly differentiated cells, which hampers culturing of 'picky' viruses. As a case in point, Norovirus has remained unculturable on such cell lines as it requires a differentiated intestinal cell type as its target^{2,3}. Also, the biology of infection and specific pathological effects seen in a patient's tissue may not be reproduced on these transformed cell lines. As an example, the pathogenic effects of Zika-virus on the fetal human brain can not be modeled using cell lines^{4,5}. Moreover, treatment efficacy may not be directly extrapolated to the clinic, as illustrated by the recent controversy around the use of the anti-malaria drug hydroxychloroquine. This drug was quickly adapted world-wide as a promising treatment against SARS-CoV-2 as it was shown effective in Vero cells⁶. However, besides countless side effects, hydroxychloroquine has now been proven to be ineffective in humans⁷. In the search for the most optimal *in vitro* model, organoids are now emerging.

BASICS OF ORGANOID TECHNOLOGY: THE ADULT AND IPSC FLAVOURS

Organoids are three-dimensional (3D) structures grown from stem cells and consist of organ-specific cell types that self-organize through cell sorting and spatially restricted lineage commitment^{8,9}. They can be established from either induced pluripotent stem cells (iPSCs) or multipotent adult tissue stem cells (ASCs). Under optimal culture conditions, stem cell differentiation generates a complete arsenal of cell types as present in the tissue of interest. Organoid models are genetically stable and can be expanded over long periods of time. Organoid derivation from iPSCs or ASCs differs greatly. iPSC derived organoids are formed by first creating a 3D aggregate of iPSCs, a so called embryoid body, after which organ and cell type specialization is initiated by closely mimicking the developmental signals. This process can take multiple weeks, a time during which gastrulation and organogenesis are mimicked in a dish. Apart from the epithelial cell types produced, suboptimal specification of iPSCs can also lead to the production of non-epithelial lineages such as fibroblasts and

1
2
3
4
5
6
7
8
9
&

muscle. Contrary, ASC-derived organoids are established by directly isolating specified ASCs from the tissue of interest and can be propagated over extended periods of time under tissue-specific growth factor conditions¹⁰. ASC-derived organoids are now readily established from most murine and human epithelial tissues¹¹. Tissue specific cell types can subsequently be enriched by modulating individual signaling pathways, such as Notch or BMP¹². The ability to generate a variety of human tissues in the form of organoids has become important in the study of COVID-19 when it was realized that it is a systemic disease much more than just a respiratory infection.

ORGANOIDS GO VIRAL TO STUDY INFECTION DISEASES

The vast majority of viruses, including all respiratory- and enteroviruses, enter the human body through infection of epithelial cells. Multiple studies have used ASC-derived organoids from the intestinal lining, oral mucosa or airway as infection models for their respective viruses. Human oral mucosal organoids recapitulate the stratified architecture of the oral mucosa and have been shown to be receptive to infection by herpes simplex virus (HSV1) and human papilloma virus (HPV)¹³. Human intestinal organoids have become the first in vitro model system to study viral entry and replication of noroviruses^{2,14}. Norovirus infectivity and replication efficiency differs greatly between individuals. Intestinal organoids from individuals indeed recapitulated the diverging norovirus replication efficiency in vitro¹⁵. The pulmonary organoid epithelium is susceptible to a wide range of viruses. Sachs et al used the 3D structure of organoids to identify increased cellular motility after infection with respiratory syncytial virus (RSV)¹⁶. This phenomenon was identified in vivo but could not be recapitulated and studied in traditional 2D cell lines or primary cells in air-liquid interface (ALI) cultures. Subsequent analysis of this increased cellular motility showed that overexpression of the RSV non-structural protein NS2 lead to increased motility and fusion with uninfected organoids. This study thereby suggested an unappreciated role of cellular motility for viral propagation in the airway epithelium¹⁶. Airway organoids have also emerged as tools for influenza viruses that display species-restricted tropism. Zhou et al showed that human airway organoids are readily infected with human infectious influenza virus H7N9 while avian H7N2 showed significantly lower replication levels¹⁷. H1N1 caused a pandemic in 2009. H1N1 isolated from humans readily replicated in airway organoids while the same serotype virus isolated from swine showed much lower replication rates. Organoids could thus be used to study potential zoonotic events¹⁷. During the 2015 Zika virus epidemic, cerebral organoids derived from iPSCs were used to gain evidence that this virus selectively replicates in dividing neural progenitors^{4,5}. This work provided the explanation why the fetal human brain was severely affected, while the virus was less destructive to the postnatal brain.

Many human viruses originate from animals and have undergone small adaptations before transitioning to man. For example, multiple bat species are notorious carriers of

zoonotic viruses that occasionally jump to humans, including the filoviruses Marburg and Ebola, and coronaviruses. ASC-derived intestinal organoids have been derived from non-human species including bat and feline. This has allowed the propagation of strains of coronaviruses directly from bats^{18,19}. These efforts highlight how organoids can be exploited to study (species-specific) viruses that have not yet jumped to humans. The ASC-derived organoid system is also translatable to non-mammalian species, such as reptilians, and could thus facilitate research into viruses affecting other parts of the animal kingdom²⁰. In some areas this may be urgent: Python nidoviruses for example have become the primary cause of fatalities among pythons in captivity²¹. Moreover, organoids could also minimize the impact of studying multiple of the affected and endangered animals, such as pangolins and civets.

FIGHTING THE SARS-COV-2 PANDEMIC WITH ORGANOIDS

SARS-CoV-2 first emerged in December 2019 in the city of Wuhan in China and has led to more than 1 million to date (WHO website). Like SARS, this new family member of the coronaviridae is mainly known for causing symptoms in the airways. Therefore, the virus has been studied using airway-derived culturing platforms: upper airway organoid-derived ALI cultures, as well as distal airway ASC organoids (**Figure 1**)^{22,23}. ALI cultures of adult upper airway-derived organoids were efficiently infected by addition of the virus to the apical side. SARS-CoV-2 infection was observed in ciliated cells which further supported the claim that these cells represent the primary target of the virus. While these ALI cultures could be accessed from the apical side, the distal lung organoids by Salahudeen et al needed to be “flipped” to generate an apical-out morphology before they could be infected by SARS-CoV-2. Within these cultures, contrary to previous studies, SARS-CoV-2 infected only goblet cells but not ciliated cells²³. The development of a feeder-free culture system for alveolar-like cells allowed the generation of an alveolar model for SARS-CoV-2 replication²³. Apart from the dominating respiratory symptoms, gastrointestinal symptoms have been identified in a subset of patients²⁴. To potentially elucidate another mode of transmission, human small intestinal organoids were infected by SARS-CoV-2 in three simultaneous studies. While one study used 2D monolayers generated from organoids to access the apical side, the two others made use of the 3D architecture and inoculated the organoids in suspension, after their mechanical disruption. All three studies concluded that enterocytes of the intestinal lining were successfully infected by SARS-CoV-2^{19,22,25}. These studies imply that the intestine is a potential site of SARS-CoV-2 replication, explaining gastrointestinal symptoms observed in patients. Due to the cellular complexity of these small intestinal organoids, insights in host tropism could be readily identified. Bulk mRNA sequencing of infected organoids uncover the response of the epithelium over time, with multiple cytokines and interferon-stimulated genes displaying different kinetics²². Furthermore, multiple iPSC-derived organoids have been employed to showcase SARS-CoV-2 replication and study its associated pathologies

1
2
3
4
5
6
7
8
9
&

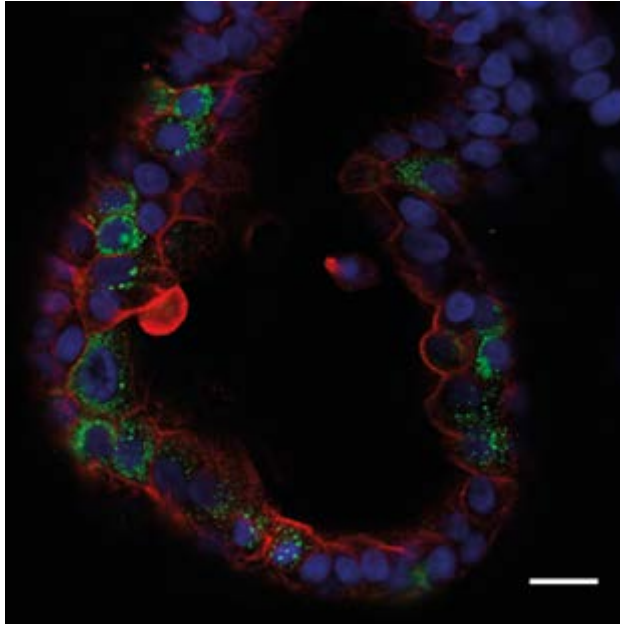


Figure 1. Confocal Image of a SARS-CoV-2 Infected Small Intestinal Organoid The organoid was stained for virus (anti-dsRNA, green), actin (phalloidin, red), and nuclei (DAPI, blue). Scale bar, 20 μm .

in tissues where ASC organoids are less developed. Ramani et al. showed that SARS-CoV-2 enters iPSC-derived cerebral organoids within 2 days, although no replication could be observed in neurons. Extensive cell death was seen in neurons, associated with altered distribution of the structural protein Tau²⁶. Monteil et al used vascular and kidney organoids derived from iPSCs and found these cells to facilitate SARS-CoV2 replication. They used these cultures to verify human recombinant soluble ACE2 as inhibitor of infection of SARS-CoV-2²⁷. Together, the repertoire of ASC and iPSC derived organoids provides a valuable platform to study tissue specific dynamics upon SARS-CoV-2 infection in relevant and physiologic models.

THE CRISPR SEARCH FOR HOST FACTORS OF SARS-COV-2 ENTRY

Much has been elucidated about the way SARS-CoV-2 infects host cells using converging efforts ranging from in vitro cell culture systems to crystallography. Currently it is thought that, as the virus gets in the proximity of the cell, the protease TMPRSS2 cleaves the spike protein of SARS-CoV-2 upon which the virus enters the cells in an ACE2 dependent manner²⁸. However, besides these two proteins many other host factors, such as TMPRSS4, DPP4, and ANPEP (the latter two are well-known from other coronaviruses) have been implicated to play a role in the infection process. Therefore,

to date the exact cell entry pathway of SARS-CoV-2 remains a crucial field of research²⁹. One way of deciphering this conundrum could be by performing loss of function screens. A loss of function screen is efficiently performed by generating knock-out cell-lines with the use of CRISPR/Cas9. Upon target recognition with use of a short guide-RNA, the endonuclease Cas9 creates a double stranded break that results in error-prone DNA repair that often results in indel formation, frameshift and loss of function of the protein of interest³⁰. CRISPR was effectively utilized in organoids by Zang and colleagues to create population-wide knockouts of TMPRSS2 and TMPRSS4 in duodenum enteroids using a lentiviral based system. Abrogation of TMPRSS4 led to a 4-fold reduction of SARS-CoV-2 replication whereas TMPRSS2 knockout did not result in a significant reduction²⁵. CRISPR-loss of function screens can furthermore be performed in a genome-wide manner to identify unknown host-factors in an unbiased manner. By cloning a library of guide-RNAs in a lentiviral vector, a cell library containing individual knock-outs of all genes in the genome can be created. Genome wide CRISPR screens have become an emerging technique for identifying genes involved in a plethora of pathways and have recently been adopted in organoids. Two recent studies have utilized this method in both Vero cells and hepatoma cells and identified host factors ACE2, the protease Cathepsin L and TMEM106B to play a crucial role in viral infection^{31,32}. Another study utilized genome wide CRISPR screens to elucidate the cytotoxicity pathways of remdesivir, a drug that is now commonly administered to SARS-CoV-2 patients³³. These insights gathered from classical cell lines, await confirmation in more physiologically relevant systems such as organoids. Recently, two independent studies described the first genome wide CRISPR screens in organoids, paving the way towards genome-wide CRISPR screens in organoids to elucidate SARS-CoV-2 biology^{34,35}.

TESTING AND DISCOVERING COVID-19 THERAPEUTICS ON ORGANOID PLATFORMS: CURRENT POSSIBILITIES AND THE ROAD AHEAD

Organoids are an emerging tool for predicting drug efficacy and drug discovery that are amenable to high-throughput drug screens. Tumor-derived organoids can for example predict the success of therapeutic regimes in corresponding cancer patients³⁶. Similarly, intestinal organoids from patients suffering from the genetic disease Cystic Fibrosis can be employed to select effective drugs³⁷. Organoids are proving their value in testing the efficacy of antiviral treatments. Intestinal organoids infected with noroviruses were exposed to different blocking antibodies to identify those that slow viral spreading³. Cerebral organoids have similarly provided a platform to identify new drugs capable of mitigating Zika virus-induced cell death in neural progenitors^{4,5}. In the past months, multiple studies have applied organoids to predict clinical success of SARS-CoV-2 treatments. Upon viral infection, cells may upregulate many different interferon-stimulated genes (ISGs) as defence mechanisms. One of these ISGs, cholesterol 25-hydroxylase,

1

2

3

4

5

6

7

8

9

&

was identified upon SARS-CoV-2 infection in organoids and COVID-19 patients and is known to be effective in combating spreading of multiple other viruses. This enzyme produces 25-hydroxycholesterol from cholesterol. Treatment of lung organoids with 25-hydroxycholesterol greatly diminished SARS-CoV-2 replication, potentially through alternating the composition of cellular membranes and preventing fusion of the viral envelope with cells⁶. A mouse adapted strain of SARS-CoV-2, known as MASCP6, is effectively inhibited by the cholesterol derivative, in line with the organoid experiments³⁸. 25-hydroxycholesterol does not have known toxicities at these concentrations and thus appears a therapeutic candidate for COVID-19. Other studies subjected iPSC-derived intestinal organoids and adult human bronchial organoids to multiple drugs currently tested in clinical settings, including the adenosine analogue remdesivir, the histamine-2-blocker famotidine and the TMPRSS2 inhibitor Camostat^{39,40}.

The above studies did exploit a priori knowledge on coronavirus biology or tested well-known viral inhibitors. Drug discovery efforts would greatly benefit from unbiased drug screens to enhance the likelihood of discovering new drugs. Most drug screens currently performed on organoids are based on morphology, fluorescent readouts or ATP-based assays that measure cellular viability. However, coronaviruses do not necessarily induce apoptosis of epithelial cells and thus may require alternative measures of drug efficacy. A specific additional challenge for high-throughput drug screens using pathogenic viruses such as SARS-CoV-2 include the required biosafety level, that could complicate the use of robotics. A recent study employed pseudoviruses (lowering handling risk) containing SARS-CoV-2 spike protein to perform a drug screen in iPSC-derived lung organoids in a 384-well format. An integrated luciferase reporter was used as a measure of viral entry and replication⁴¹. This work revealed multiple FDA-approved drugs, including the Bcr-abl tyrosine kinase inhibitor Imatinib and the immunosuppressant mycophenolic acid to be effective in lowering viral replication. A separate study using human iPSC-derived colorectal organoids utilized a similar set-up and tested more than 1.000 drugs⁴². Many of these hits overlapped with those in lung, indicating effective viral blockade in different epithelial tissues.

These studies provide the first examples of how organoids can aid the quest for novel COVID-19 therapies by allowing medium-throughput drug screening in a physiologically relevant system. Nonetheless, these pioneering efforts in organoids do all depend on pseudoviruses that at best mimic aspects of viral entry but less of downstream responses. High-throughput screens using wild-type strains require effective monitoring of viral spreading, which has to await the development of genetically engineered viruses harboring reporter genes. Alternatively, the epithelial cells could be genetically engineered to report the expression of viral response genes, such as ISGs. Such organoids could be effective, generic tools to study viral entry and responses of any (future) pandemic virus that are amenable to high-throughput readouts. Not only would such fluorescent reporters allow efficient measurement of viral spreading, they would also discriminate infected from non-infected cells. The latter could be used for in-depth

characterization of epithelial responses to the virus. We have recently shown that large biobanks of intestinal organoids can rapidly be genetically engineered to harbor fluorescent reporters of different genes⁴³. COVID-19 drug testing in organoids could also focus on modulating the expression or activity of host products important for the viral replication cycle. Multiple proteins are indispensable for viral replication, including ACE2 and TMPRSS2. Serine protease inhibitors targeting *Tmprss2* have been developed but display many off-target effects that could hamper clinical success. The fact that organoids closely resemble their corresponding native tissue makes these attractive models in an attempt to modulate the expression of key host genes. Again, fluorescent reporters could be utilized as a measure of protein abundance or localization.

FUTURE PERSPECTIVES FOR ORGANOID PLATFORMS IN VIROLOGY

Organoids are proving useful in unraveling SARS-CoV-2 biology, including its cellular tropism. In contrast to many cell lines, human organoids can readily be infected with SARS-CoV-2 without inducing artificial expression of key host factors, such as ACE2. To increase the faithful representation of epithelial tissues, virally-infected organoids could be co-cultured with other cell types. ASC-derived organoids exclusively consist of epithelial cells, while iPSC-based systems can include mesenchymal lineages such as fibroblasts or muscle. Most importantly however, both systems lack immune cells such as B- and T-cells, innate lymphoid cells and macrophages that normally reside in mucosal tissues. All of these lineages play important executive roles in fighting viral infections, including SARS-CoV-2, as reviewed in Vabret et al⁴⁴. Organoids from colorectal and non-small-lung cancer biopsies have previously been co-cultured with circulating T-cells from corresponding patients.

This study revealed successful antigen presentation of tumor organoid cells to T-cells, which subsequently become activated⁴⁵. Similar co-cultures could be applied to virus-infected organoids. We predict that further development and maturation of the organoid viral toolbox, including complex co-cultures and genetically engineered organoids, enable larger drug screens using wildtype viral strains. These efforts would increase the odds for deriving clinically successful COVID-19 therapeutics. Finally, organoids can be used to compare viral responses between individuals. In this review, we have discussed the current and future potential of organoids in virology research (**Figure 2**). Broad application of this culturing technique could contribute significantly toward eradicating COVID-19 and future viral pandemics.

ACKNOWLEDGEMENTS

We would like to thank Mart Lamers for discussions on modeling coronavirus infections with organoids.

1

2

3

4

5

6

7

8

9

&

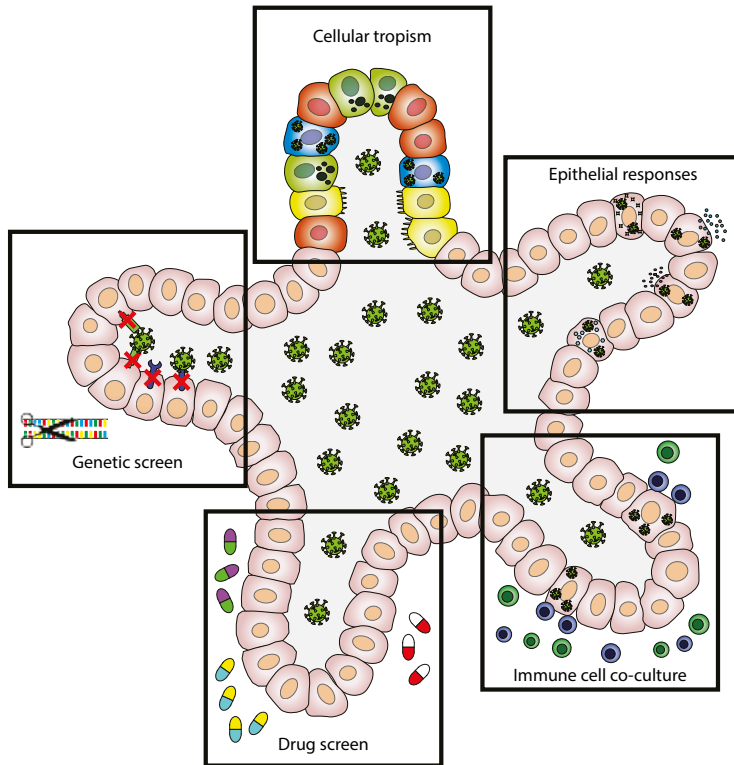


Figure 2. Overview of the Potential of iPSC and ASC-Derived Organoids in Virology Research

AUTHOR CONTRIBUTIONS

M.H.G., J.V., and J.B. wrote the first draft of the manuscript; H.C. was involved in discussing and revising the contents.

DECLARATION OF INTERESTS

H.C. is inventor on several patents related to organoid technology; his full disclosure is given at <https://www.uu.nl/staff/JCClevers/>. M.H.G., J.V. and J.B. declare no competing interests.

BIBLIOGRAPHY

1. Matsuyama, S. *et al.* Enhanced isolation of SARS-CoV-2 by TMPRSS2-expressing cells. *Proc. Natl. Acad. Sci. U. S. A.* **117**, 7001–7003 (2020).
2. Ettayebi, K. *et al.* Replication of human noroviruses in stem cell–derived human enteroids. *Science (80-.)*. **353**, 1387–1394 (2016).
3. Alvarado, G. *et al.* Human Monoclonal Antibodies That Neutralize Pandemic GII.4 Noroviruses. *Gastroenterology* **155**, 1898–1907 (2018).
4. Watanabe, M. *et al.* Self-Organized Cerebral Organoids with Human-Specific Features Predict Effective Drugs to Combat Zika Virus Infection. *Cell Rep.* **21**, 517–532 (2017).
5. Qian, X., Nguyen, H. N., Jacob, F., Song, H. & Ming, G. L. Using brain organoids to understand Zika virus-induced microcephaly. *Dev.* **144**, 952–957 (2017).
6. Wang, M. *et al.* Remdesivir and chloroquine effectively inhibit the recently emerged novel coronavirus (2019-nCoV) in vitro. *Cell Res.* **30**, 269–271 (2020).
7. Hernandez, A. V., Roman, Y. M., Pasupuleti, V., Barboza, J. J. & White, C. M. Hydroxychloroquine or Chloroquine for Treatment or Prophylaxis of COVID-19: A Living Systematic Review. *Ann. Intern. Med.* **173**, 287–296 (2020).
8. Lancaster, M. A. & Knoblich, J. A. Organogenesis in a dish: Modeling development and disease using organoid technologies. *Science (80-.)*. **345**, (2014).
9. Clevers, H. Modeling Development and Disease with Organoids. *Cell* **165**, 1586–1597 (2016).
10. van der Vaart, J. & Clevers, H. Airway organoids as models of human disease. *Journal of Internal Medicine* (2020). doi:10.1111/joim.13075
11. Driehuis, E., Kretzschmar, K. & Clevers, H. Establishment of patient-derived cancer organoids for drug-screening applications. *Nat. Protoc.* **15**, 3380–3409 (2020).
12. Beumer, J. & Clevers, H. Cell fate specification and differentiation in the adult mammalian intestine. *Nat. Rev. Mol. Cell Biol.* (2020). doi:10.1038/s41580-020-0278-0
13. Driehuis, E. *et al.* Oral Mucosal Organoids as a Potential Platform for Personalized Cancer Therapy. *Cancer Discov.* **9**, 852–871 (2019).
14. Haga, K. *et al.* Genetic manipulation of human intestinal enteroids demonstrates the necessity of a functional fucosyltransferase 2 gene for secretor-dependent human norovirus infection. *MBio* **11**, 1–10 (2020).
15. Estes, M. K. *et al.* Human Norovirus Cultivation in Nontransformed Stem Cell-Derived Human Intestinal Enteroid Cultures: Success and Challenges. *Viruses* **11**, 9–11 (2019).
16. Sachs, N. *et al.* Long-term expanding human airway organoids for disease modeling. *EMBO J.* e100300 (2019). doi:10.15252/embj.2018100300
17. Zhou, J. *et al.* Differentiated human airway organoids to assess infectivity of emerging influenza virus. *Proc. Natl. Acad. Sci.* **115**, 6822–6827 (2018).
18. Tekes, G., Ehmann, R., Boulant, S. & Stanifer, M. L. Development of Feline Ileum- and Colon-Derived Organoids and Their Potential Use to Support Feline Coronavirus Infection. *Cells* **9**, (2020).
19. Zhou, J. *et al.* Infection of bat and human intestinal organoids by SARS-CoV-2. *Nat. Med.* **26**, 1077–1083 (2020).
20. Post, Y. *et al.* Snake Venom Gland Organoids. *Cell* **180**, 233–247.e21 (2020).
21. Blahak, S. *et al.* Investigations into the presence of nidoviruses in pythons. *Virology* **17**, 1–14 (2020).
22. Lamers, M. M. *et al.* SARS-CoV-2 productively infects human gut enterocytes. *Science (80-.)*. **369**, 50–54 (2020).
23. Salahudeen, A. A. *et al.* Progenitor identification and SARS-CoV-2 infection in long-term human distal lung organoid

1

2

3

4

5

6

7

8

9

&

- cultures. *bioRxiv* 2020.07.27.212076 (2020). doi:10.1101/2020.07.27.212076
24. Gupta, A. et al. Extrapulmonary manifestations of COVID-19. *Nat. Med.* **26**, 1017–1032 (2020).
 25. Zang, R. et al. TMPRSS2 and TMPRSS4 promote SARS-CoV-2 infection of human small intestinal enterocytes. *Sci. Immunol.* **5**, 1–15 (2020).
 26. Ramani, A. et al. SARS-CoV-2 targets neurons of 3D human brain organoids. *EMBO J.* 1–15 (2020). doi:10.15252/embj.2020106230
 27. Monteil, V. et al. Inhibition of SARS-CoV-2 Infections in Engineered Human Tissues Using Clinical-Grade Soluble Human ACE2. *Cell* **181**, 905-913.e7 (2020).
 28. Hoffmann, M. et al. SARS-CoV-2 Cell Entry Depends on ACE2 and TMPRSS2 and Is Blocked by a Clinically Proven Protease Inhibitor. *Cell* **181**, 271-280.e8 (2020).
 29. LoPresti, M., Beck, D. B., Duggal, P., Cummings, D. A. T. & Solomon, B. D. The Role of Host Genetic Factors in Coronavirus Susceptibility: Review of Animal and Systematic Review of Human Literature. *Am. J. Hum. Genet.* **107**, 381–402 (2020).
 30. Mali, P. et al. RNA-Guided Human Genome Engineering via Cas9. *Science (80-.)*. **339**, (2013).
 31. Wei, J. et al. Genome-wide CRISPR screen reveals host genes that regulate SARS-CoV-2 infection. *bioRxiv* 2020.06.16.155101 (2020). doi:10.1101/2020.06.16.155101
 32. Wang, R. et al. Functional genomic screens identify human host factors for SARS-CoV-2 and common cold coronaviruses. *bioRxiv* 1–52 (2020).
 33. Akinci, E. et al. Elucidation of remdesivir cytotoxicity pathways through genome-wide CRISPR-Cas9 screening and transcriptomics. *bioRxiv* (2020). doi:10.1101/2020.08.27.270819
 34. Ringel, T. et al. Genome-Scale CRISPR Screening in Human Intestinal Organoids Identifies Drivers of TGF- β Resistance. *Cell Stem Cell* **26**, 431-440.e8 (2020).
 35. Michels, B. E. et al. Pooled In Vitro and In Vivo CRISPR-Cas9 Screening Identifies Tumor Suppressors in Human Colon Organoids. *Cell Stem Cell* **26**, 782-792.e7 (2020).
 36. Ooft, S. N. et al. Patient-derived organoids can predict response to chemotherapy in metastatic colorectal cancer patients. *Sci. Transl. Med.* **11**, eaay2574 (2019).
 37. Dekkers, J. F. et al. A functional CFTR assay using primary cystic fibrosis intestinal organoids. *Nat. Med.* **19**, 939–945 (2013).
 38. Zu, S. et al. 25-Hydroxycholesterol is a potent SARS-CoV-2 inhibitor. *Cell Res.* 1–3 (2020). doi:10.1038/s41422-020-00398-1
 39. Suzuki, T. et al. Generation of human bronchial organoids for SARS-CoV-2 research. *bioRxiv* **4**, 2020.05.25.115600 (2020).
 40. Krüger, J. et al. Remdesivir but not famotidine inhibits SARS-CoV-2 replication in human pluripotent stem cell-derived intestinal organoids. *bioRxiv* 2020.06.10.144816 (2020). doi:10.1101/2020.06.10.144816
 41. Han, Y. et al. Identification of Candidate COVID-19 Therapeutics using hPSC-derived Lung Organoids. 16–19 (2020).
 42. Duan, X. et al. Identification of Drugs Blocking SARS-CoV-2 Infection using Human Pluripotent Stem Cell-derived Colonic Organoids. (2020). doi:10.1101/2020.05.02.073320
 43. Beumer, J. et al. High Resolution mRNA and Secretome Atlas of Human Enteroendocrine Cells. *Cell* **181**, 1291-1306.e19 (2020).
 44. Vabret, N. et al. Immunology of COVID-19: Current State of the Science. *Immunity* **52**, 910–941 (2020).
 45. Dijkstra, K. K. et al. Generation of Tumor-Reactive T Cells by Co-culture of Peripheral Blood Lymphocytes and Tumor Organoids. *Cell* **174**, 1586-1598.e12 (2018).

CHAPTER

SARS-COV-2 PRODUCTIVELY INFECTS HUMAN GUT ENTEROCYTES

Mart M. Lamers^{1*}, Joep Beumer^{2*}, Jelte van der Vaart^{2*},
Kèvin Knoops³, Jens Puschhof², Tim I. Breugem¹,
Raimond B.G. Ravelli³, J. Paul van Schayck³, Anna Z. Mykytyn¹,
Hans Q. Duimel³, Elly van Donselaar³, Samra Riesebosch¹,
Helma J.H. Kuijpers³, Debby Schipper¹,
Willine J. van de Wetering³, Miranda de Graaf¹,
Marion Koopmans¹, Edwin Cuppen⁴, Peter J. Peters³,
Bart L. Haagmans¹ and Hans Clevers²

¹Viroscience Department, Erasmus Medical Center,
Rotterdam, Netherlands.

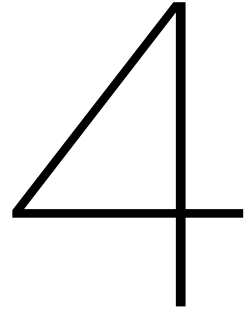
²Oncode Institute, Hubrecht Institute, Royal Netherlands Academy of
Arts and Sciences and University Medical Center, Uppsalalaan 8,
Utrecht, 3584 CT, Netherlands.

³The Maastricht Multimodal Molecular Imaging Institute, Maastricht
University, 6229 ER Maastricht, Netherlands.

⁴Center for Molecular Medicine and Oncode Institute, University Medical
Centre Utrecht, Utrecht, Netherlands; Hartwig Medical Foundation,
Amsterdam, Netherlands

*Equal contribution.

*Published in Science (2020);
doi: 10.1126/science.abc1669*



ABSTRACT

The virus SARS-CoV-2 can cause COVID-19, an influenza-like disease that is primarily thought to infect the lungs with transmission via the respiratory route. However, clinical evidence suggests that the intestine may present another viral target organ. Indeed, the SARS-CoV-2 receptor angiotensin converting enzyme 2 (ACE2) is highly expressed on differentiated enterocytes. In human small intestinal organoids (hSIOs), enterocytes were readily infected by SARS-CoV and SARS-CoV-2 as demonstrated by confocal- and electron-microscopy. Consequently, significant titers of infectious viral particles were detected. mRNA expression analysis revealed strong induction of a generic viral response program. Hence, intestinal epithelium supports SARS-CoV-2 replication, and hSIOs serve as an experimental model for coronavirus infection and biology

INTRODUCTION

Severe Acute Respiratory Syndrome (SARS), caused by coronavirus SARS-CoV, emerged in 2003¹. In late 2019, a novel transmissible coronavirus (SARS-CoV-2) was noted to cause an influenza-like disease ranging from mild respiratory symptoms to severe lung injury, multi-organ failure, and death²⁻⁴. SARS-CoV and SARS-CoV-2 belong to the *Sarbecovirus* subgenus (genus *Betacoronavirus*, family *Coronaviridae*)⁵⁻⁷. The SARS-CoV receptor is the angiotensin-converting enzyme 2 (ACE2)^{8,9}. The spike proteins of both viruses bind to ACE2, whereas soluble ACE2 blocks infection by SARS-CoV as well as by SARS-CoV-2¹⁰⁻¹³. Transmission of SARS-CoV-2 is thought to occur through respiratory droplets and fomites. The virus can be detected in upper respiratory tract samples, implicating the nasopharynx as site of replication. In human lung, ACE2 is expressed mainly in alveolar epithelial type II cells and ciliated cells¹⁴⁻¹⁶. However, highest expression of ACE2 in the human body occurs in the brush border of intestinal enterocytes^{14,17}. Even though respiratory symptoms dominate the clinical presentation of COVID-19, gastrointestinal symptoms are observed in a subset of patients^{18,19}. Moreover, viral RNA can be found in rectal swabs, even after nasopharyngeal testing has turned negative, implying gastro-intestinal infection and a fecal-oral transmission route²⁰⁻²².

SARS-COV-2 INFECTS AIRWAY AND GUT ORGANOID.

Organoids are 3D structures, that can be grown from adult stem cells (ASCs) and recapitulate key aspects of the organ from which the ASCs derive. Since SARS-CoV and SARS-CoV-2 target the lung, we added virus to organoid-derived human airway epithelium cultured in 2D and observed that SARS-CoV and SARS-CoV2 readily infected differentiated airway cultures. (**Figure 1A**). Immunostaining reveal that the viruses targeted ciliated cells, but not goblet cells (**Figure 1B-C**).

Human small intestinal organoids (hSIOs) are established from primary gut epithelial stem cells, can be expanded indefinitely in 3D culture and contain all proliferative and differentiated cell types of the *in vivo* epithelium²³. Of note, hSIOs have allowed the first *in vitro* culturing of Norovirus²⁴. We exposed ileal hSIOs grown under four different culture conditions ('EXP', 'DIF', 'DIF-BMP' and 'EEC') to SARS-CoV and SARS-CoV-2 at a multiplicity of infection (MOI) of 1. hSIOs grown in Wnt-high expansion medium (EXP) overwhelmingly consist of stem cells and enterocyte progenitors. Organoids grown in differentiation medium (DIF) contain enterocytes, goblet cells, and low numbers of enteroendocrine cells (EECs). Addition of BMP2/4 to DIF (DIF-BMP) leads to further maturation²⁵. In the final condition, we induced expression of NeuroG3 from a stably transfected vector with doxycycline to raise EECs numbers (**Supplementary figure S3D**). Samples were harvested at multiple timepoints post infection and processed for the analyses given in **Figures 2-5**. Both SARS-CoV and SARS-CoV-2 productively infected hSIOs as assessed by qRT-PCR for viral sequences and by live virus titrations on VeroE6 cells (**Figure 2 for lysed organoids; Supplementary figure S1 for organoid supernatant**). Infectious virus particles and

1

2

3

4

5

6

7

8

9

&

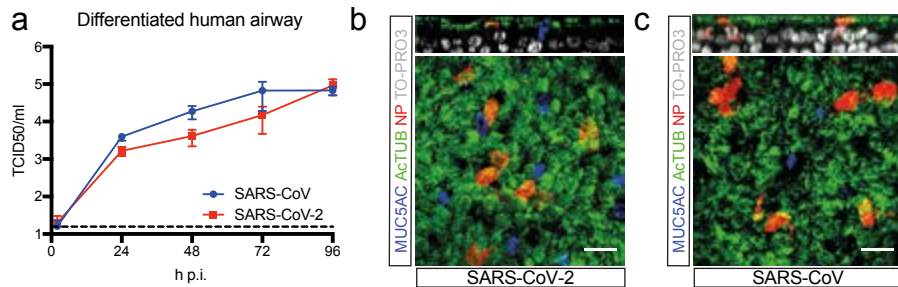


Figure 1. SARS-CoV and SARS-CoV-2 infect 2D human airway cultures. a) Live virus titers can be observed by virus titrations on VeroE6 cells of apical washes at 2, 24, 48, 72 and 96h after infection with SARS-CoV (blue) and SARS-CoV-2 (red). The dotted line indicates the lower limit of detection. Error bars represent SEM. N=4. *P<0.05, **P<0.01, ***P<0.001. b and c) Immunofluorescent staining of SARS-CoV-2 (b) and SARS-CoV (c) infected differentiated airway cultures. Nucleoprotein (NP) stains viral nucleocapsid (red), which colocalized with the ciliated cell marker ActTUB (green). Goblet cells are identified by MUC5AC (blue). Nuclei are stained with TO-PRO3 (white). Scale bars indicate 20µM. Top panels are side-view while bottom panels are top-view.

viral RNA increased to significant titers for both viruses in all conditions. Since EXP medium supported virus replication (**Figure 2A, E**), enterocyte progenitors appeared to be a primary viral target. Differentiated organoids (DIF; DIF-BMP) produced slightly (non-statistically significant) lower levels of infectious virus (**Figure 2; Supplementary figure S1**). In organoids induced to generate EECs, virus yields were similar to those in EXP medium (**Figure 2D, H**). In differentiated hSIOs, SARS-CoV-2 titers remained stable at 60 hours post infection, whereas SARS-CoV titers dropped 1-2 log (**Figure 2B, C, F, G**). The latter decline was not observed in infected hSIOs grown in EXP. Culture supernatants across culture conditions contained lower levels of infectious virus compared to lysed hSIOs, implying that virus was primarily secreted apically (**Supplementary figure S1A-D**). Despite this, viral RNA was detected readily in culture supernatants correlating with the infectious virus levels within hSIOs (**Figure 2E-H; Supplementary figure S1 E-H**).

ACE2 mRNA expression differed greatly between the four conditions. EXP-hSIOs express 300-fold less ACE2 mRNA compared to DIF-hSIOs, when analyzed in bulk (**Supplementary figure S2**). BMP treatment induced 6.5-fold upregulation of ACE2 mRNA compared to DIF treatment alone. Since this did not yield infection rate differences, the DIF-BMP condition was not analyzed further.

SARS-COV-2 INFECTS ENTEROCYTE LINEAGE CELLS

To determine the target cell type, we then performed confocal analysis on hSIOs cultured in EXP, DIF, or EEC conditions. We stained for viral dsRNA, viral nucleocapsid protein, KI67 to visualize proliferative cells, actin (using phalloidin) to visualize enterocyte brush borders, DNA (DAPI) and cleaved caspase 3 to visualize apoptotic cells. Generally, comparable rates of viral infections were observed in the organoids growing in all

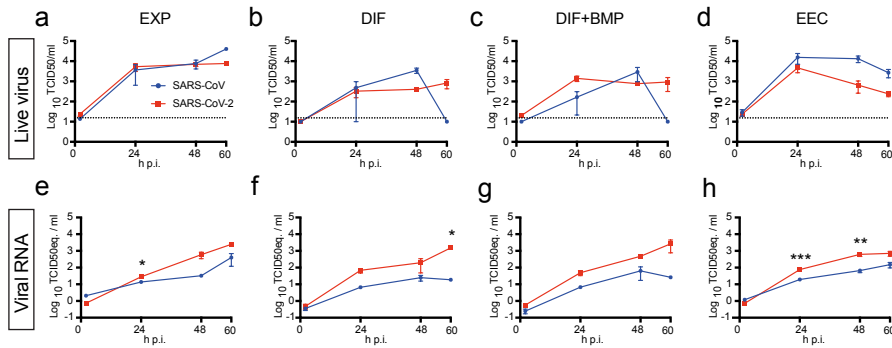


Figure 2. SARS-CoV and SARS-CoV-2 replicate in hSIOs. a-d) Live virus titers can be observed by virus titrations on VeroE6 cells of lysed organoids at 2, 24, 48 and 60h after infection with SARS-CoV (blue) and SARS-CoV-2 (red). Different medium compositions show similar results. e-h) qPCR analysis targeting the E gene of similar timepoints and medium compositions as a-d. The dotted line indicates the lower limit of detection. Error bars represent SEM. N=3. *P<0.05, **P<0.01, ***P<0.001.

three conditions. We typically noted staining for viral components (white) in rare, single cells at 24 hours. At 60 hours, the number of infected cells had dramatically increased (**Figure 3A**). Infected cells invariably displayed proliferative enterocyte progenitor-phenotypes (**EXP, Figure 3B, top**) or ApoA1+ enterocyte-phenotypes (**DIF, Figure 3B, bottom**). Of note, SARS-CoV also readily infected enterocyte lineage cells (**Supplementary figure S3A-B**) as shown previously^{26,27}. Some infected enterocyte progenitors were in mitosis (**Supplementary figure S3C**). Whereas EEC-organoids produced appreciable titers, we never observed infection of Chromogranin-A⁺ EECs (**Supplementary figure S3D-E**). We also did not notice infection of Goblet cells across culture conditions. At 60 hours, apoptosis became prominent in both SARS-CoV and SARS-CoV-2 infected enterocytes (**Supplementary figure S5**). ACE2 protein was readily revealed as a bright and ubiquitous brush border marker in hSIOs in DIF medium (**Figure 3C**). In hSIOs in EXP medium, ACE2 staining was much lower -yet still apical-in occasional cells in a subset of organoids that displayed a more mature morphology (**Figure 3C**). In immature (cystic) organoids within the same cultures, the ACE2 signal was below the detection threshold. The percentage of infected organoids under EXP and DIF conditions are given in **Supplementary figure S4**. **Supplementary figure S5** shows images and quantification of apoptotic cells upon infection.

ULTRASTRUCTURAL ANALYSIS OF THE VIRAL LIFE CYCLE IN ENTEROCYTES

Unsupervised transmission electron microscopy (TEM)²⁸ was performed on selected highly infected samples. Figure 4 shows two hSIOs, selected from 42 imaged hSIOs at 60 h post SARS-CoV-2 infection. These differ in the state of infection: whereas the cellular

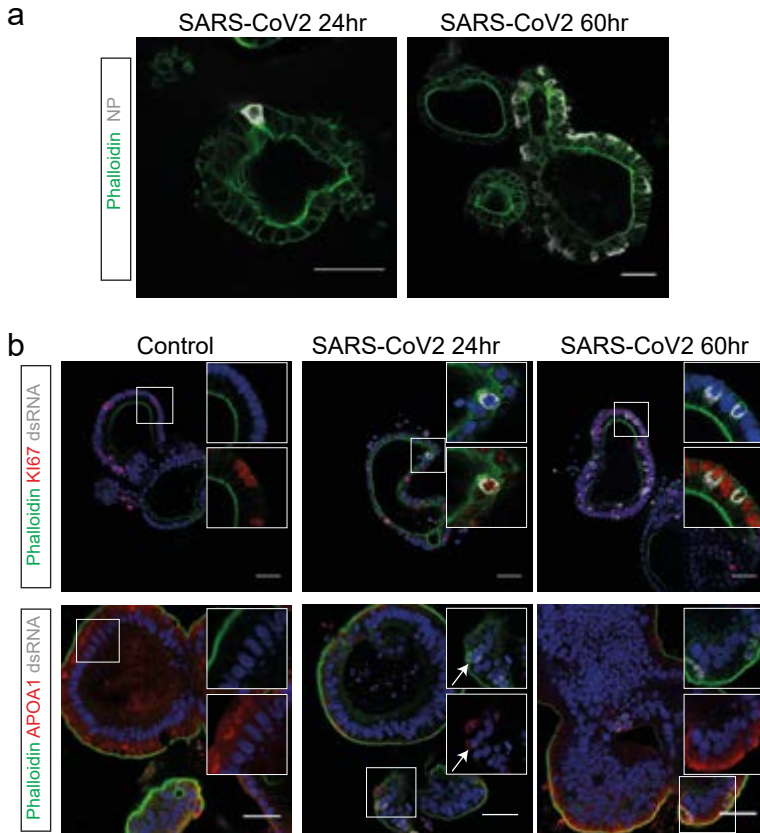


Figure 3. SARS-CoV-2 infects proliferating cells and enterocytes. a) Immunofluorescent staining of SARS-CoV-2-infected intestinal organoids. Nucleoprotein (NP) stains viral capsid. After 24 hours, single virus-infected cells are generally observed in organoids. These small infection clusters spread through the whole organoid after 60 hours. b) SARS-CoV-2 infects both post-mitotic enterocytes identified by Apolipoprotein A1 (APOA1) and dividing cells that are Ki67-positive. Infected cells are visualized by dsRNA staining. Enterocytes are shown in differentiated organoids, and proliferating cells in expanding organoids. Arrows point to APOA1-positive cells. c) Immunofluorescent staining of ACE2 in intestinal organoids in expansion and differentiation condition. All scale bars are 50 μ m.

organization within organoid 1 was still intact (**Figure 4A entire organoid; intermediate magnification B-D; high magnification E-K**), many disintegrated cells can be seen in organoid 2 (**Figure 4 Bottom (Figure 4L entire organoid; intermediate magnification 4M-O; high magnification 4P-R)**). Viral particles of 80-120 nm occurred in the lumen of the organoid (**Figure 4I**), at the basolateral (**Figure 4J**) and apical side (**Figure 4K**) of enterocytes. The double-membrane vesicles which are the subcellular site of viral replication²⁹ are visualized in Figure 4E and 4P. The nuclei in both organoids differed from nuclei in mock-infected organoids by a slightly rounder shape. The nuclear contour index³⁰ was 4.0+/-0.5 vs 4.3+/-0.5 for control set. There was more heterochromatin (**Figure 4N**), and one or two dense nucleoli in the center (**Figure 4O**).

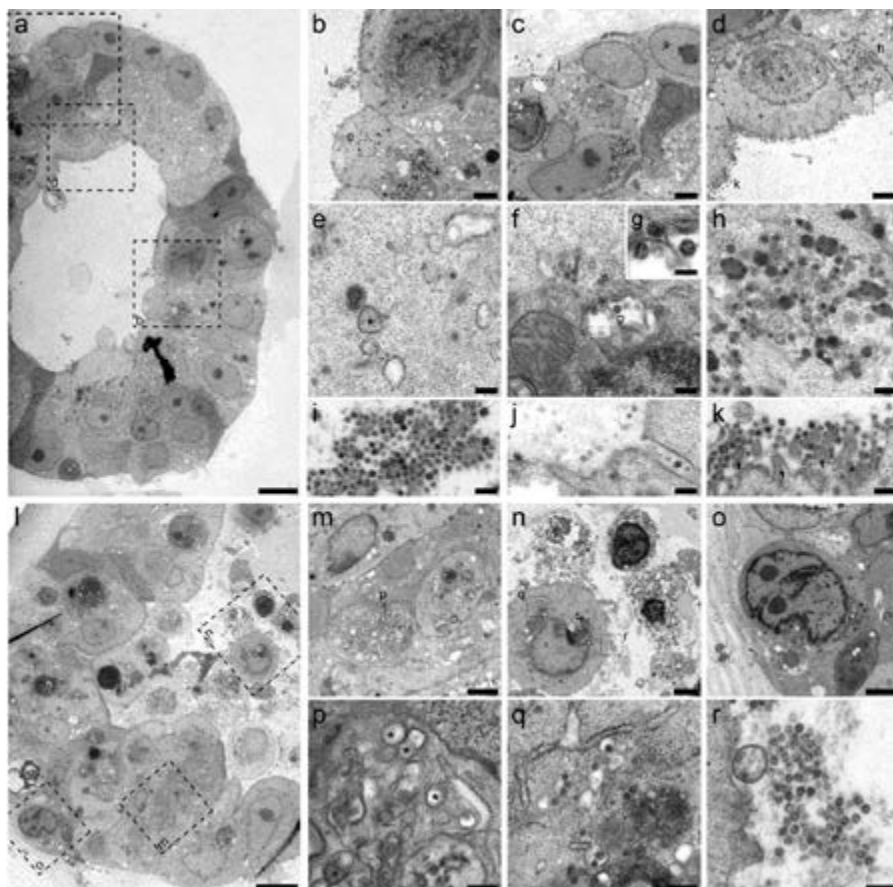


Figure 4. Transmission electron microscopy analysis of SARS-CoV-2 infected intestinal organoids. a) Overview of an intact organoid (a) showing the onset of virus infection (b-d) at different stages of the viral lifecycle, i.e. early double membrane vesicles (DMVs) (e; asterisk), initial viral production in the Golgi apparatus (f-g) and complete occupation of virus particles inside the endomembrane system (h). Extracellular viruses are observed in the lumen of the organoid (i), and are found at the basal (j) and apical side (k) alongside the microvilli (arrows). Scale bars represent 10 μm (a), 2.5 μm (b-d), 250 nm (e, f, h-k) & 100 nm (g). b) Overview of an organoid (l) showing severely infected cells (m,o), disintegrated cells (o) and stressed cells as evident from the atypical nucleoli (p). Intact cells reveal DMV areas of viral replication (p; asterisks) and infected Golgi apparatus (q). Extracellular clusters of viruses are shown in (r). Scale bars represent 10 μm (l), 2.5 μm (m-p) & 250 nm (p-r). Data was deposited to the Image Data Resource (<https://idr.openmicroscopy.org>) under accession number idr0083.

RNA EXPRESSION CHANGES IN INFECTED ENTEROCYTES

We then performed mRNA sequence analysis to determine gene expression changes induced by SARS-CoV and SARS-CoV-2-infection of hSIOs cultured continuously in EXP medium and hSIOs cultured in DIF medium. Infection with SARS-CoV-2 elicited a broad signature of cytokines and interferon stimulated genes (ISGs) attributed to type I and

1

2

3

4

5

6

7

8

9

&

III interferon responses (**Figure 5A, Supplementary table 1-2**), as confirmed by Gene Ontology analysis (**Figure 5B**). An overlapping list of genes appeared in SARS-CoV-2-infected DIF organoids (**Supplementary figure S6, Supplementary table 3**). RNA sequencing analysis confirmed differentiation of DIF organoids into multiple intestinal lineages, including ACE2 upregulation (**Supplementary figure S7**). SARS-CoV also induced ISGs, yet to a much lower level (**Supplementary table 4**). **Figure 5C** visualizes the regulation of SARS-CoV-2-induced genes in SARS-CoV infected organoids. This induction was similar to infections with other viruses like norovirus³¹, rotavirus³² and enteroviruses^{33,34}. A recent study³⁵ describes an antiviral signature induced in human cell lines after SARS-CoV-2 infection. Whereas the ISG response is broader in intestinal organoids, the induced gene sets are in close agreement between the two datasets (**Supplementary figure S8**). One striking similarity was the low expression of Type I and III interferons: we only noticed a small induction of the Type III interferon IFNL1 in SARS-CoV-2 infected organoids. In SARS-CoV-infected organoids, we did not observe any type I or type III interferon induction. We confirmed these findings by ELISA on culture supernatant and qRT-PCR, which in addition to IFNL1 picked up low levels of type I interferon IFNB1 in SARS-CoV-2 but not in SARS-CoV infected organoids (**Supplementary figure S9**). The specific induction of IP-10/CXCL10 and ISG15 by SARS-CoV-2 was also confirmed by ELISA and qRT-PCR, respectively (**Supplementary figure S10**). As in Blanco-Melo *et al.*³⁵, a short list of cytokine genes was induced by both viruses albeit it to modest levels. For a comparison with³⁵, see **Supplementary figure S11**. Altogether these data indicate that SARS-CoV-2 induces a stronger interferon response than SARS-CoV in HIOs.

Finally, the infection was repeated in a second experiment in the same ileal HIO line and analyzed after 72 hours. Analysis involved viral titration (**Supplementary figure S12**), confocal imaging (**Supplementary figure S13**), and RNA sequencing (**Supplementary figure S14**). This experiment essentially confirmed the observations presented above. A limited, qualitative experiment applying confocal analysis demonstrated infectability of two other lines available in the lab (one ileal, one duodenal) from independent donors (**Supplementary figure S13**). This study shows that SARS-CoV and SARS-CoV-2 infect enterocyte lineage cells in a human intestinal organoid model. We observed similar infection rates of enterocyte-precursors and enterocytes whereas ACE2 expression increases ~1000-fold upon differentiation at the mRNA level (**Supplementary figure S2**). This suggests that low levels of ACE2 may be sufficient for viral entry.

SARS-CoV-2 is the third highly pathogenic coronavirus (after SARS-CoV and MERS-CoV) to jump to humans within less than 20 years suggesting that novel zoonotic coronavirus spillovers are likely to occur in the future. Despite this, limited information is available on coronavirus pathogenesis and transmission. This is in part due to the lack of *in vitro* cell models that accurately model host tissues. Very recently, it was shown that human iPS cells differentiated towards a kidney fate support replication of SARS-CoV-2¹³. Our data imply that human organoids represent faithful experimental models to study the biology of coronaviruses.

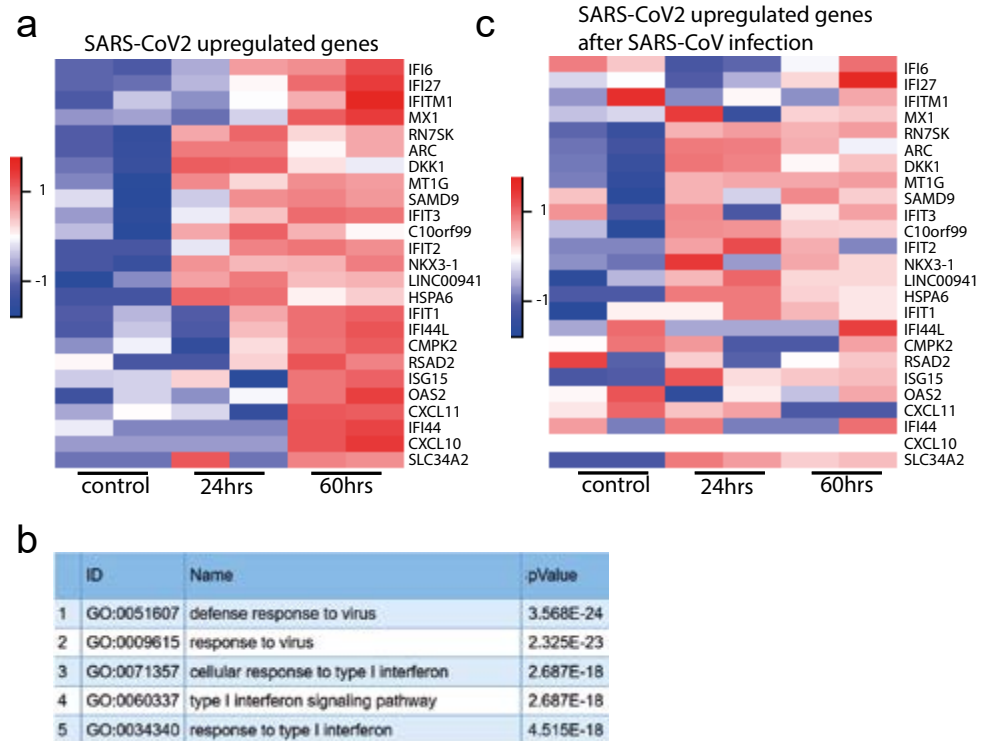


Figure 5. Transcriptomic analysis of SARS-CoV-2 infected intestinal organoids. a) Heatmaps depicting the 25 most significantly enriched genes upon SARS-CoV-2 infection in expanding intestinal organoids. Colored bar represents Z-score of log₂ transformed values. b) GO term enrichment analysis for biological processes of the 50 most significantly upregulated genes upon SARS-CoV-2 infected in intestinal organoids. c) Heatmaps depicting the genes from (a) in SARS-CoV infected expanding organoids. Colored bar represents Z-score of log₂ transformed values.

ACKNOWLEDGEMENTS

We thank E. Eenjes and R. Rottier for providing human lung material, A. de Graaff and Hubrecht Imaging Centre (HIC) for microscopy assistance and Single Cell Discoveries for RNA library preparation, and the Utrecht Sequencing Facility (subsidized by the University Medical Center Utrecht, Hubrecht Institute, Utrecht University and NWO project 184.034.019).

FUNDING

This work was supported by ERC Advanced Grant 67013 and by Lung Foundation Netherlands to HC, and by NWO Grant 022.005.032. KK, JQD, PJP & RBGR received funding from the Dutch Technology Foundation STW (UPON 14207) and from European Union's Horizon 2020 Programme, Grant Agreement No 766970 Q-SORT.

1
2
3
4
5
6
7
8
9
&

AUTHOR CONTRIBUTIONS

ML, JB and JV performed experiments and designed the study. KK & JQD prepared samples. KK & RBGR performed imaging. KK, JPvS, PJP & RGBR interpreted results. TB, AM, SR, DS and MG measured virus titers. JP analyzed RNAseq data. EC performed sequencing. MK, BH and HC supervised.

DATA AND REAGENT AVAILABILITY

Organoid lines could be requested directly from the non-profit HUB (<https://huborganoids.nl/>), who do not directly benefit from this research. RNA sequence data can be accessed through GEO: GSE149312

COMPETING INTERESTS

H.C. is inventor on patents held by the Royal Netherlands Academy of Arts and Sciences that cover organoid technology.: PCT/NL2008/050543, WO2009/022907; PCT/NL2010/000017, WO2010/090513; PCT/IB2011/002167, WO2012/014076; PCT/IB2012/052950, WO2012/168930;PCT/EP2015/060815, WO2015/173425; PCT/EP2015/077990, WO2016/083613; PCT/EP2015/077988, WO2016/083612; PCT/EP2017/054797,WO2017/149025; PCT/EP2017/065101, WO2017/220586; PCT/EP2018/086716,; and GB1819224.5,

HC's full disclosure is given at <https://www.uu.nl/staff/JCClevers/>

MATERIALS AND METHODS

Viruses and cell lines

Vero E6 cells were maintained in Dulbecco's modified Eagle's medium (DMEM, Gibco) supplemented with 10% fetal calf serum (FCS), HEPES, sodium bicarbonate, penicillin (10,000 IU/mL) and streptomycin (10,000 IU/mL) at 37°C in a humidified CO₂ incubator. SARS-CoV (isolate HKU 39849, accession no. AY278491) and SARS-CoV-2 (isolate BetaCoV/Munich/BavPat1/2020; European Virus Archive Global #026V-03883; kindly provided by Dr. C. Drosten) were propagated on Vero E6 (ATCC® CRL 1586™) cells in Opti- MEM I (1X) + GlutaMAX (Gibco), supplemented with penicillin (10,000 IU/mL) and streptomycin (10,000 IU/mL) at 37°C in a humidified CO₂ incubator. The SARS-CoV-2 isolate was obtained from a clinical case in Germany, diagnosed after returning from China. Stocks were produced by infecting Vero E6 cells at a multiplicity of infection (MOI) of 0.01 and incubating the cells for 72 hours. The culture supernatant was cleared by centrifugation and stored in aliquots at -80°C. Stock titers were determined by preparing 10-fold serial dilutions in Opti-MEM I (1X) + GlutaMAX. Aliquots of each dilution were added to monolayers of 2 × 10⁴ Vero E6 cells in the same medium in a 96-well plate. Twenty-four replicates were performed per virus stock. Plates were incubated at 37°C for 5 days and then examined for cytopathic effect. The TCID₅₀ was calculated according

to the method of Spearman & Kärber. All work with infectious SARS-CoV and SARS-CoV-2 was performed in a Class II Biosafety Cabinet under BSL-3 conditions at Erasmus Medical Center.

Cell culture of human intestinal organoids

Tissues from the duodenum and ileum was obtained from the UMC Utrecht with informed consent of the patient. All patients were males that were operated for resection of an intestinal tumor. A sample from non-transformed, normal mucosa was taken for this study. The study was approved by the UMC Utrecht (Utrecht, The Netherlands) ethical committee and was in accordance with the Declaration of Helsinki and according to Dutch law. This study is compliant with all relevant ethical regulations regarding research involving human participants.

Human small intestinal cells were isolated, processed and cultured as described previously (23, 25). Instead of Wnt conditioned media, the medium was supplemented with Wnt surrogate (0,15nM, U-Protein Express). This was termed expansion (EXP) medium. To generate human EECs in organoids, NEUROG3-P2A sequence was cloned into a previously published pLX-NS2 vector (36). Resulting constructs were transduced into small clumps of cells (2-10 cells). EEC differentiation was induced by treating with 1 µg/ml doxycycline (Sigma) in 'ENR' medium (23) for 48 hours, followed by 3 days of incubation in ENR without doxycycline. General differentiation (termed DIF) was achieved in 'ENR'. BMP activation was achieved by withdrawing Noggin from 'ENR' and addition of BMP-2 (Peprotech, 50 ng/ml) and BMP-4 (Peprotech, 50 ng/ml) (termed DIF+BMP).

Human airway organoid culture and differentiation

Adult human lung stem cells were derived from non-tumour lung tissue obtained from patients undergoing lung resection. Lung tissue was obtained from residual, tumor-free, material obtained at lung resection surgery for lung cancer. The Medical Ethical Committee of the Erasmus MC Rotterdam granted permission for this study (METC 2012-512). Isolation of human bronchial airway stem cells was performed using a protocol adapted from Sachs and colleagues (2019). Bronchial tissues of adult lungs were cut into ~4mm sections, washed in Advanced DMEM supplemented with GlutaMax (Thermo Fisher), HEPES, penicillin (10,000 IU/mL) and streptomycin (10,000 IU/mL) (AdDF+++), and incubated with dispase (Corning) mixed with airway organoid (AO) medium (36) at a 1:1 ratio for 1 hour at 37°C. The digested tissue suspension was sequentially sheared using 10- and 5-ml plastic and flamed glass Pasteur pipettes. After shearing and filtering, lung cell pellets were then resuspended in 200 µL of growth factor reduced Matrigel (Corning) and plated in ~30 µL droplets in a 48 well tissue culture plate. Plates were placed at 37 degrees Celsius with 5% CO₂ for 20 min to solidify the Matrigel droplets upon which 250µL of media was added to each well. Plates were incubated under standard tissue culture conditions.

1

2

3

4

5

6

7

8

9

&

To obtain differentiated organoid-derived cultures, organoids were dissociated into single cells using TrypLE express. Cells were seeded on Transwell membranes (Corning) coated with rat tail collagen type I (Fisher Scientific). Single cells were seeded in AO growth medium: complete base medium (CBM; Stemcell Pneumacult-ALI) at a 1:1 ratio. After 2-4 days, confluent monolayers were cultured at air-liquid interphase in CBM. Medium was changed every 5 days. After 4 weeks of differentiation, cultures were used for infection experiments.

SARS-CoV and SARS-CoV-2 Infection

Organoids were harvested in cold AdDF+++, washed once to remove BME, and sheared using a flamed Pasteur pipette in AdDF+++ or TrypLE express, for undifferentiated and differentiated organoids, respectively. After shearing, organoids were washed once in AdDF+++ before infection at a multiplicity of infection (MOI) of 1 in expansion or differentiation medium. After 2 hours of virus adsorption at 37°C 5% CO₂, cultures were washed twice with excess AdDF+++ to remove unbound virus. Organoids were re-embedded into 30 µL BME in 24-well tissue culture plates and cultured in 500 µL expansion or differentiation medium at 37°C with 5% CO₂. Each well contained ~100,000 cells per well. Samples were taken at indicated timepoints by harvesting the medium in the well (supernatant) and the cells by resuspending the BME droplet containing organoids into 500 µL AdDF+++. Samples were stored at -80°C, a process which lysed the organoids, releasing their contents into the medium. 2D differentiated airway cultures were washed twice with 200 µL AdDF+++ before inoculation from the apical side at a MOI of 0.1 in 200 µL AdDF+++ per well. Next, cultures were incubated at 37°C 5% CO₂ for 2 hours before washing 3 times in 200 µL AdDF+++. At the indicated timepoints, virus was collected from the cells by adding 200 µL AdDF+++ apically, incubating 10 min at 37°C 5% CO₂, and storing the supernatant at -80°C. Prior to determining the viral titer, all samples were centrifuged at 2,000 g for 5 min. Live virus titers were determined using the Spearman & Kärber TCID₅₀ method on VeroE6 cells. All work was performed in a Class II Biosafety Cabinet under BSL-3 conditions at Erasmus Medical Center.

Determination of virus titers using qRT-PCR

Supernatant and organoid samples were thawed and centrifuged at 2,000 g for 5 min. Sixty µL supernatant was lysed in 90 µL MagnaPure LC Lysis buffer (Roche) at RT for 10 min. RNA was extracted by incubating samples with 50 µL Agencourt AMPure XP beads (Beckman Coulter) for 15 min at RT, washing beads twice with 70% ethanol on a DynaMag-96 magnet (Invitrogen) and eluting in 30 µL MagnaPure LC elution buffer (Roche). Viral titers (TCID₅₀ equivalents per mL) were determined by qRT-PCR using primers targeting the E gene (37) and comparing the Ct values to a standard curve derived from a virus stock titrated on VeroE6 cells.

Fixed immunofluorescence microscopy on differentiated human airway

Transwell inserts were fixed in 4% paraformaldehyde for 20 min, permeabilized in 70% ethanol, and blocked for 60 min in 10% normal goat serum in PBS (blocking buffer). Cells were incubated with primary antibodies overnight at 4°C in blocking buffer, washed twice with PBS, incubated with corresponding secondary antibodies Alexa350-, 488- and 594-conjugated anti-rabbit and anti-mouse (1:400; Invitrogen) in blocking buffer for 2 h at room temperature, washed two times with PBS, incubated with indicated additional stains (TO-PRO3), washed twice with PBS, and mounted in Prolong Antifade (Invitrogen) mounting medium. Viral nucleocapsid was stained with anti-NP (1:200; Sino biological), ciliated cells were stained with anti-ActUB (1:100; Santa Cruz, 6-11B-1) and goblet cells with anti-MUC5AC (1:100; Invitrogen, 45M1). Samples were imaged on a LSM700 confocal microscope using ZEN software (Zeiss).

Immunostaining of hSIOs

Organoids were stained as described before (25). Primary antibodies used were goat antichromogranin A (1:500; Santa Cruz), mouse anti-nucleoprotein (1:200; Sino Biological), mouse anti-dsRNA (1:200; Scicons), mouse anti-APOA1 (1:100; ThermoFisher, PA5-88109), rabbit anti-cleaved caspase 3 (1:200; Cell Signaling Technology, 9661), goat anti-ACE2 (1:100; R&D Systems, AF933) and rabbit anti-KI67 (1:200; Abcam, ab16667). Organoids were incubated with the corresponding secondary antibodies Alexa488, 568- and 647-conjugated anti-rabbit and anti-mouse (1:1,000; Molecular Probes) in blocking buffer containing 4',6-diamidino-2-phenylindole (DAPI; 1;1,000, Invitrogen) and Phalloidin-Alexa488 (ThermoFisher). Sections were embedded in Vectashield (Vector Labs) and imaged using a Sp8 confocal microscope (Leica). Image analysis was performed using ImageJ software.

Quantitative PCR

Quantitative PCR (qPCR) analysis was performed using biological and technical duplicates as described before (38). Primers were designed using the NCBI primer design tool, tested using a standard curve, and include:

```
ACE2_fw CGAAGCCGAAGACCTGTTCTA
ACE2_rev GGGCAAGTGTGGACTGTTCC
GAPDH_fw GGAGCGAGATCCCTCCAAAAT
GAPDH_rev GGCTGTTGTCATACTTCTCATGG
```

For qPCR analysis of IFNB1, IFNL1 and ISG15 we used RNA extracted from lysed organoids as described above. We used the following ThermoFisher TaqMan primer-probe mixes:

```
IFNB1: Hs00277188-s1
IFNL1: Hs00601677-g1
```

1

2

3

4

5

6

7

8

9

&

ISG15: Hs01921425-s1

Beta actin was amplified using the following primer set:

Bact_fw GGCATCCACGAAACTACCTT,

Bact_rev AGCACTGTGTTGGCGTACAG

Bact_probe FAM-ATCATGAAGTGTGACGTGGACATCCG-BHQ1.

Bulk RNA sequencing

Library preparation was performed at Single Cell Discoveries (Utrecht, The Netherlands), using an adapted version of the CEL-seq protocol. In brief: Total RNA was extracted using the standard TRIzol (Invitrogen) protocol and used for library preparation and sequencing. mRNA was processed as described previously, following an adapted version of the single-cell mRNA seq protocol of CEL-Seq (39, 40). In brief, samples were barcoded with CEL-seq primers during a reverse transcription and pooled after second strand synthesis. The resulting cDNA was amplified with an overnight *In vitro* transcription reaction. From this amplified RNA, sequencing libraries were prepared with Illumina Truseq small RNA primers. Paired-end sequencing was performed on the Illumina Nextseq500 platform using barcoded 1 x 75 nt read setup. Read 1 was used to identify the Illumina library index and CELSeq sample barcode. Read 2 was aligned to the CRCh38 human RefSeq transcriptome, with the addition of SARS-CoV1 (HKU-39849) and SARS-CoV-2 (Ref-SKU: 026V-03883) genomes, using BWA using standard settings (41). Reads that mapped equally well to multiple locations were discarded. Mapping and generation of count tables was done using the MapAndGo script. Samples were normalized using RPM normalization. Differential gene expression analysis was performed using the DESeq2 package (42). SARSmapping reads were removed before analyzing the different datasets. After filtering for an adjusted p-value < 0.05, the row z-score for the 25 genes with the highest upregulation after 60 hours of exposure to SARS-CoV-2 was calculated. Data will be deposited in GEO. The 50 genes which were most strongly induced in response to SARS-CoV-2 (padj < 0.05, ranked by fold change) were subjected to functional enrichment analysis for a biological process using TopFun on the TopGene Suite (<https://toppgene.cchmc.org/enrichment.jsp>) as described before (43). The 5 biological processes with highest enrichment (after FDR correction and a pvalue cutoff of 0.05) for each virus are displayed with the corresponding GO term and corrected p value.

Transmission electron microscopy

Organoids were chemically fixed for 3 hours at room temperature with 1.5% glutaraldehyde in 0.067 M cacodylate buffered to pH 7.4 and 1 % sucrose. Samples were washed once with 0.1 M cacodylate (pH 7.4), 1 % sucrose and 3x with 0.1 M cacodylate (pH 7.4), followed by incubation in 1% osmium tetroxide and 1.5% K₄Fe(CN)₆ in 0.1 M sodium cacodylate (pH 7.4) for 1 hour at 4 °C. After rinsing with MQ, organoids were dehydrated at RT in a graded ethanol series (70, 90, up to 100%) and embedded in epon. Epon was

polymerized for 48h at 60 °C. 60nm Ultrathin sections were cut using a diamond knife (Diatome) on a Leica UC7 ultramicrotome, and transferred onto 50 Mesh copper grids covered with a formvar and carbon film. Sections were post-stained with uranyl acetate and lead citrate.

All TEM data were collected autonomously as virtual nanoscopy slides (28) on FEI Tecnai T12 microscopes at 120kV using an Eagle camera. Data were stitched, uploaded, shared and annotated using Omero (44) and PathViewer. Data was deposited to the Image Data Resource (<https://idr.openmicroscopy.org>) under accession number idr0083.

Multiplex cytokine ELISA

Organoid supernatant samples, stored at -80 °C, were thawed and centrifuged at 2,000 g for 5 min. The Anti-virus response panel multiplex ELISA kit (BioLegend) was used to determine cytokine concentrations in the samples using a FACSLyric (BD biosciences) flow cytometer. The procedure was performed according to the manufacturer's instructions with the addition that capture beads were inactivated in 4% paraformaldehyde for 15 min at room temperature and washed once in wash buffer after completion of the staining protocol in a Class II Biosafety Cabinet under BSL-3 conditions.

Statistical analysis

Statistical analysis was performed with the GraphPad Prism 8 software. We compared differences in cytokine levels and log₁₀ transformed viral titers by a two-way ANOVA followed by a Sidak multiple-comparison test.

1

2

3

4

5

6

7

8

9

&

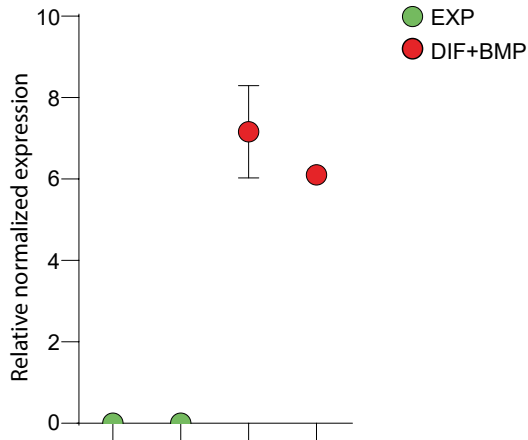
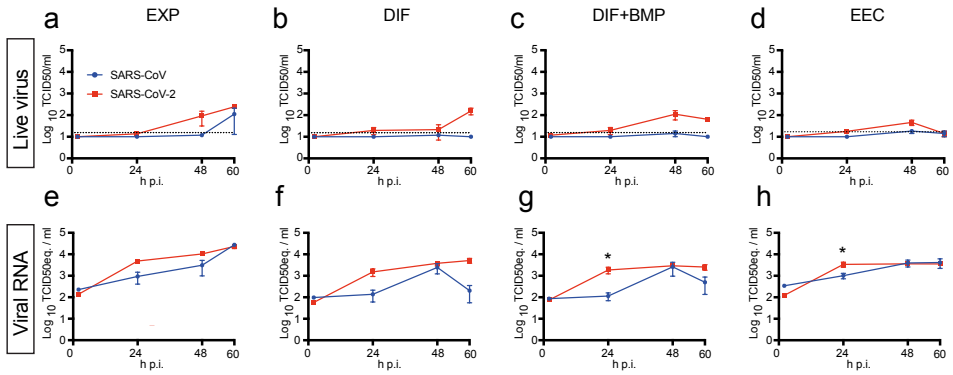
REFERENCES

1. Drosten, C. et al. Identification of a Novel Coronavirus in Patients with Severe Acute Respiratory Syndrome. *N. Engl. J. Med.* **348**, 1967–1976 (2003).
2. Guan, W. et al. Clinical Characteristics of Coronavirus Disease 2019 in China. *N. Engl. J. Med.* (2020). doi:10.1056/nejmoa2002032
3. Jiang, S., Du, L. & Shi, Z. An emerging coronavirus causing pneumonia outbreak in Wuhan, China: calling for developing therapeutic and prophylactic strategies. *Emerg. Microbes Infect.* **9**, 275–277 (2020).
4. Zhu, N. et al. A novel coronavirus from patients with pneumonia in China, 2019. *N. Engl. J. Med.* **382**, 727–733 (2020).
5. Andersen, K. G., Rambaur, A., Lipkin, W. I., Holmes, E. C. & Garry, R. F. The proximal origin of SARS-CoV-2. *Nat. Med.* (2020). doi:10.1038/s41591-020-0820-9
6. Lu, R. et al. Genomic characterisation and epidemiology of 2019 novel coronavirus: implications for virus origins and receptor binding. *Lancet* **395**, 565–574 (2020).
7. Gorbalenya, A. E. et al. The species Severe acute respiratory syndrome-related coronavirus: classifying 2019-nCoV and naming it SARS-CoV-2. *Nat. Microbiol.* (2020). doi:10.1038/s41564-020-0695-z
8. Imai, Y. et al. Angiotensin-converting enzyme 2 protects from severe acute lung failure. *Nature* **436**, 112–116 (2005).
9. Kuba, K. et al. A crucial role of angiotensin converting enzyme 2 (ACE2) in SARS coronavirus-induced lung injury. *Nat. Med.* **11**, 875–879 (2005).
10. Walls, A. C. et al. Structure, Function, and Antigenicity of the SARS-CoV-2 Spike Glycoprotein. *Cell* **0**, (2020).
11. Wan, Y., Shang, J., Graham, R., Baric, R. S. & Li, F. Receptor Recognition by the Novel Coronavirus from Wuhan: an Analysis Based on Decade-Long Structural Studies of SARS Coronavirus. *J. Virol.* **94**, (2020).
12. Wrapp, D. et al. Cryo-EM structure of the 2019-nCoV spike in the prefusion conformation. *Science (80-.).* **367**, 1260–1263 (2020).
13. Monteil, V. et al. Inhibition of SARS-CoV-2 infections in engineered human tissues using clinical-grade soluble human ACE2. *Cell* **181**, 905-913.e7 (2020).
14. Qi, F., Qian, S., Zhang, S. & Zhang, Z. Single cell RNA sequencing of 13 human tissues identify cell types and receptors of human coronaviruses. (2020). doi:10.1016/j.bbrc.2020.03.044
15. Zhao, Y. et al. Single-cell RNA expression profiling of ACE2, the putative receptor of Wuhan 2019-nCoV. *bioRxiv* 2020.01.26.919985 (2020). doi:10.1101/2020.01.26.919985
16. Jia, H. P. et al. ACE2 receptor expression and severe acute respiratory syndrome coronavirus infection depend on differentiation of human airway epithelia. *J. Virol.* **79**, 14614–21 (2005).
17. ACE2 protein expression summary - The Human Protein Atlas. Available at: <https://www.proteinatlas.org/ENSG00000130234-ACE2>. (Accessed: 7th April 2020)
18. Gu, J., Han, B. & Wang, J. COVID-19: Gastrointestinal manifestations and potential fecal-oral transmission. *Gastroenterology* (2020). doi:10.1053/j.gastro.2020.02.054
19. Cholankeril, G. et al. High Prevalence of Concurrent Gastrointestinal Manifestations in Patients with SARS-CoV-2: Early Experience from California. *Gastroenterology* **0**, (2020).
20. Wang, W. et al. Detection of SARS-CoV-2 in Different Types of Clinical Specimens. *JAMA - J. Am. Med. Assoc.* 2–3 (2020). doi:10.1001/jama.2020.3786
21. Holshue, M. L. et al. First case of 2019 novel coronavirus in the United States. *N. Engl. J. Med.* **382**, 929–936 (2020).
22. Xiao, F. et al. Evidence for gastrointestinal infection of SARS-CoV-2. *Gastroenterology* (2020). doi:10.1053/j.gastro.2020.02.055
23. Sato, T. et al. Long-term Expansion of Epithelial Organoids From Human Colon, Adenoma, Adenocarcinoma, and Barrett's Epithelium. *Gastroenterology* **141**, 1762–1772 (2011).

24. Ettayebi, K. et al. Replication of human noroviruses in stem cell-derived human enteroids. *Science (80-.)*. **353**, 1387–1393 (2016).
25. Beumer, J. et al. Enteroendocrine cells switch hormone expression along the crypt-to-villus BMP signalling gradient. *Nature Cell Biology* **20**, 909–916 (2018).
26. Leung, W. K. et al. Enteric involvement of severe acute respiratory syndrome-associated coronavirus infection. *Gastroenterology* **125**, 1011–1017 (2003).
27. Chan, W. S. et al. Coronaviral hypothetical and structural proteins were found in the intestinal surface enterocytes and pneumocytes of severe acute respiratory syndrome (SARS). *Mod. Pathol.* **18**, 1432–1439 (2005).
28. Faas, F. G. A. et al. Virtual nanoscopy: Generation of ultra-large high resolution electron microscopy maps. *J. Cell Biol.* **198**, 457–469 (2012).
29. Knoops, K. et al. SARS-coronavirus replication is supported by a reticulovesicular network of modified endoplasmic reticulum. *PLoS Biol.* **6**, 1957–1974 (2008).
30. McNutt, N. S. & Crain, W. R. Quantitative electron microscopic comparison of lymphocyte nuclear contours in mycosis fungoides and in benign infiltrates in skin. *Cancer* **47**, 698–709 (1981).
31. Hosmillo, M. et al. Norovirus Replication in Human Intestinal Epithelial Cells Is Restricted by the Interferon-Induced JAK/STAT Signaling Pathway and RNA Polymerase II-Mediated Transcriptional Responses. *MBio* **11**, (2020).
32. Saxena, K. et al. A paradox of transcriptional and functional innate interferon responses of human intestinal enteroids to enteric virus infection. *Proc. Natl. Acad. Sci. U. S. A.* **114**, E570–E579 (2017).
33. Drummond, C. G. et al. Enteroviruses infect human enteroids and induce antiviral signaling in a cell lineage-specific manner. *Proc. Natl. Acad. Sci. U. S. A.* **114**, 1672–1677 (2017).
34. Good, C., Wells, A. I. & Coyne, C. B. Type III interferon signaling restricts enterovirus 71 infection of goblet cells. *Sci. Adv.* **5**, eaau4255 (2019).
35. Blanco-Melo, D. et al. Imbalanced host response to SARS-CoV-2 drives development of COVID-19. *Cell* (2020). doi:10.1016/j.cell.2020.04.026
36. N. Sachs, A. Papaspyropoulos, D. D. Zomer-van Ommen, I. Heo, L. Böttinger, D. Klay, F. Weeber, G. Huelsz-Prince, N. Iakobachvili, G. D. Amatngalim, J. de Ligt, A. van Hoeck, N. Proost, M. C. Viveen, A. Lyubimova, L. Teeven, S. Derakhshan, J. Korving, H. Begthel, J. F. Dekkers, K. Kumawat, E. Ramos, M. F. van Oosterhout, G. J. Offerhaus, D. J. Wiener, E. P. Olimpio, K. K. Dijkstra, E. F. Smit, M. van der Linden, S. Jaksani, M. van de Ven, J. Jonkers, A. C. Rios, E. E. Voest, C. H. van Moorsel, C. K. van der Ent, E. Cuppen, A. van Oudenaarden, F. E. Coenjaerts, L. Meyaard, L. J. Bont, P. J. Peters, S. J. Tans, J. S. van Zon, S. F. Boj, R. G. Vries, J. M. Beekman, H. Clevers, Long-term expanding human airway organoids for disease modeling. *EMBO J.*, e100300 (2019).
37. V. M. Corman, O. Landt, M. Kaiser, R. Molenkamp, A. Meijer, D. K. Chu, T. Bleicker, S. Brünink, J. Schneider, M. L. Schmidt, D. G. Mulders, B. L. Haagmans, B. van der Veer, S. van den Brink, L. Wijsman, G. Goderski, J. L. Romette, J. Ellis, M. Zambon, M. Peiris, H. Goossens, C. Reusken, M. P. Koopmans, C. Drosten, Detection of 2019 novel coronavirus (2019-nCoV) by real-time RT-PCR. *Euro Surveill.* **25** (2020), doi:10.2807/1560-7917.ES.2020.25.3.2000045.
38. J. Muñoz, D. E. Stange, A. G. Schepers, M. van de Wetering, B.-K. Koo, S. Itzkovitz, R. Volckmann, K. S. Kung, J. Koster, S. Radulescu, K. Myant, R. Versteeg, O. J. Sansom, J. H. van Es, N. Barker, A. van Oudenaarden, S. Mohammed, A. J. R. Heck, H. Clevers, The Lgr5 intestinal stem cell signature: robust expression of proposed quiescent “+4” cell markers. Muñoz, J., Stange, D. E., Schepers, A. G., van de Wetering, M., Koo, B.-K., Itzkovitz, S., ... Clevers, H. (2012). The Lgr5 intestinal stem cell signature: ro. *EMBO J.* **31**, 3079–91 (2012).

39. T. Hashimshony, N. Senderovich, G. Avital, A. Klochendler, Y. de Leeuw, L. Anavy, D. Gennert, S. Li, K. J. Livak, O. Rozenblatt-Rosen, Y. Dor, A. Regev, I. Yanai, CEL-Seq2: Sensitive highly-multiplexed single-cell RNA-Seq. *Genome Biol.* **17** (2016), doi:10.1186/s13059-016-0938-8.
40. S. Simmini, M. Bialecka, M. Huch, L. Kester, M. Van De Wetering, T. Sato, F. Beck, A. Van Oudenaarden, H. Clevers, J. Deschamps, Transformation of intestinal stem cells into gastric stem cells on loss of transcription factor Cdx2. *Nat. Commun.* **5** (2014), doi:10.1038/ncomms6728.
41. H. Li, R. Durbin, Fast and accurate long-read alignment with Burrows-Wheeler transform. *Bioinformatics* **26**, 589–595 (2010). *Journal?*
42. M. I. Love, W. Huber, S. Anders, Moderated estimation of fold change and dispersion for RNA-seq data with DESeq2. *Genome Biol.* **15** (2014), doi:10.1186/s13059-014-0550-8.
43. V. Kaimal, E.E. Bardes, S.C. Tabar, A. G. Jegga, B.J. Aronow, ToppCluster: a multiple gene list feature analyzer for comparative enrichment clustering and network-based dissection of biological systems. *Nucleic acids research*, **38** W96-W102 (2010).
44. J.-M. Burel, S. Besson, C. Blackburn, M. Carroll, R. K. Ferguson, H. Flynn, K. Gillen, R. Leigh, S. Li, D. Lindner, M. Linkert, W. J. Moore, B. Ramalingam, E. Rozbicki, A. Tarkowska, P. Walczysko, C. Allan, J. Moore, J. R. Swedlow, Publishing and sharing multi-dimensional image data with OMERO. *Mamm. Genome.* **26**, 441–7 (2015).

SUPPLEMENTARY FIGURES



1

2

3

4

5

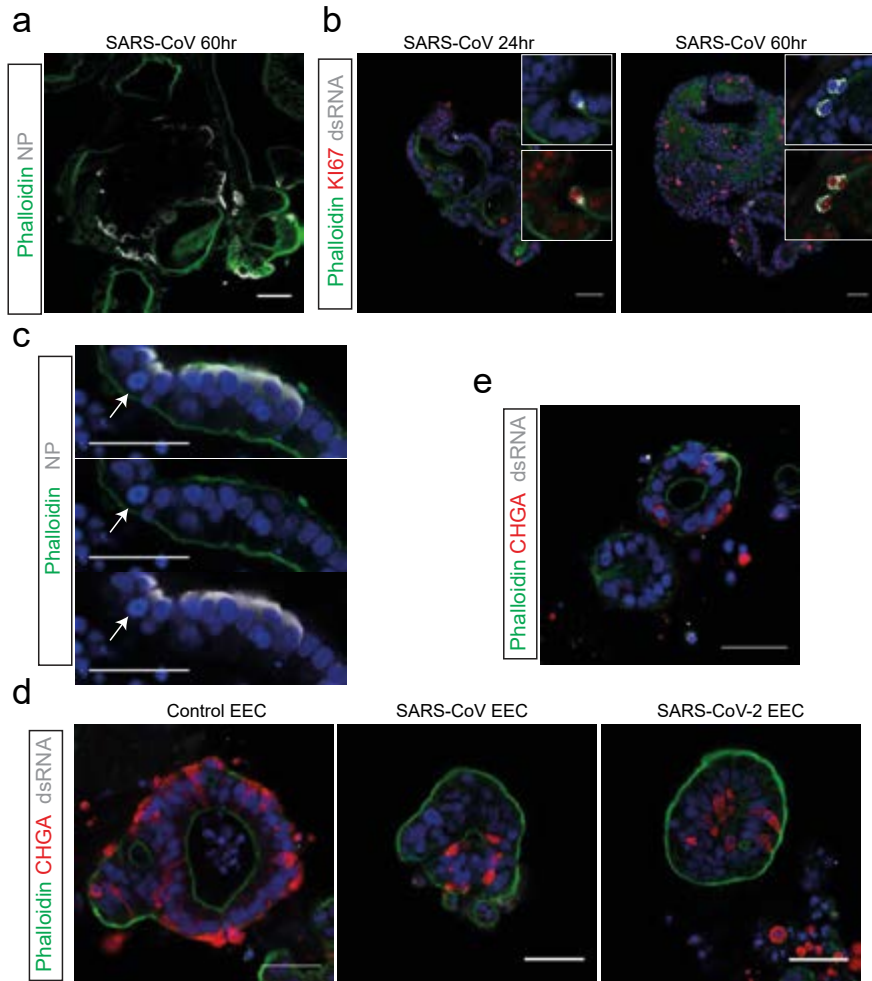
6

7

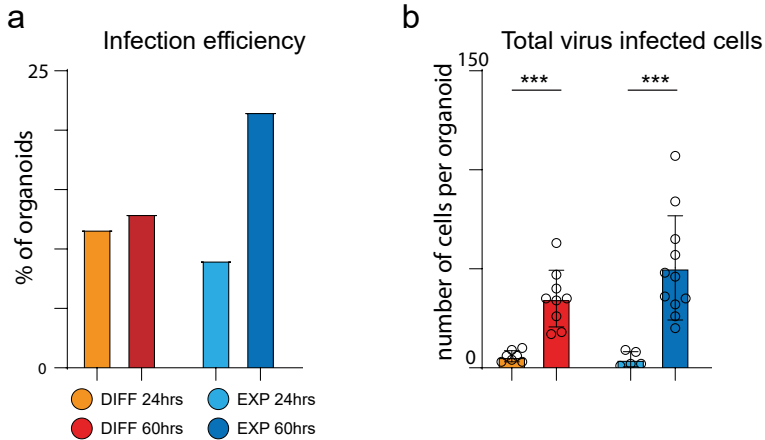
8

9

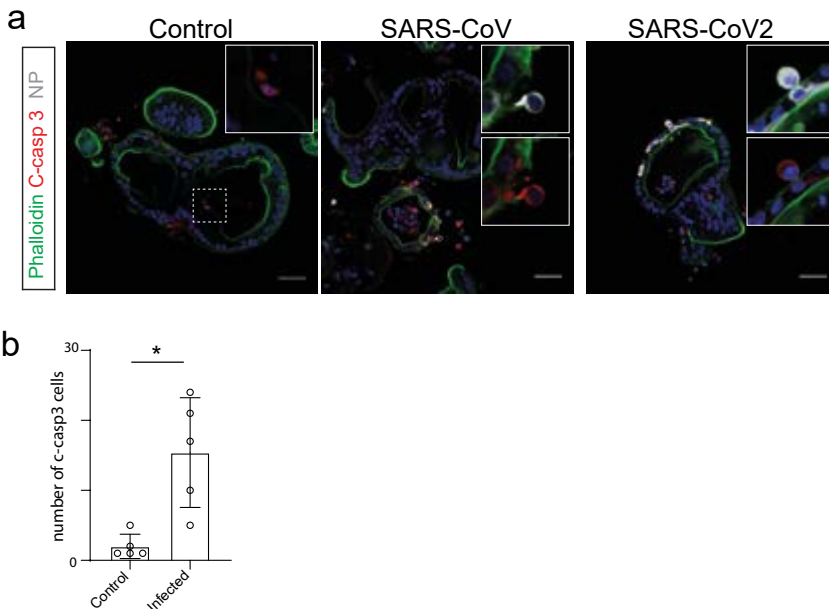
&



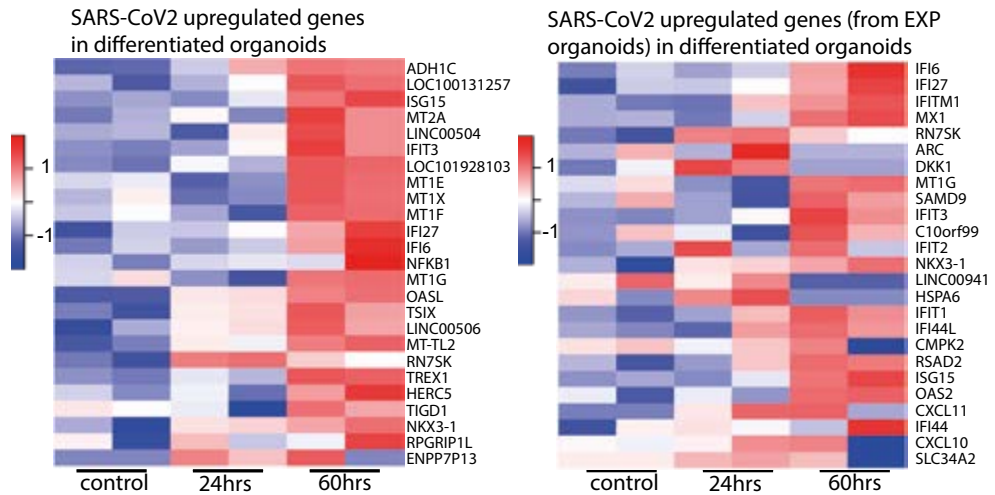
Supplementary figure S3. SARS-CoV infects proliferating cells but not secretory endocrine cells.
 a) Immunofluorescent staining of SARS-CoV-infected intestinal organoids in expansion conditions. Nucleoprotein (NP) stains viral capsid. Infected organoids contain large clusters of virus-containing cells at 60 hours after infection. b) SARS-CoV infects dividing cells that are KI67-positive. c) Example of a mitotic infected cell (arrow). d) Enteroendocrine cell (EEC) differentiated organoids do not facilitate viral infection. EECs are marked by Chromogranin A (CHGA). An average of $7 \pm 5,2$ CHGA+ EECs were observed per organoid section (n= 9 sections). e) Example of an EEC-differentiated organoid with a virus infected cell. All scale bars are 50 μ m.



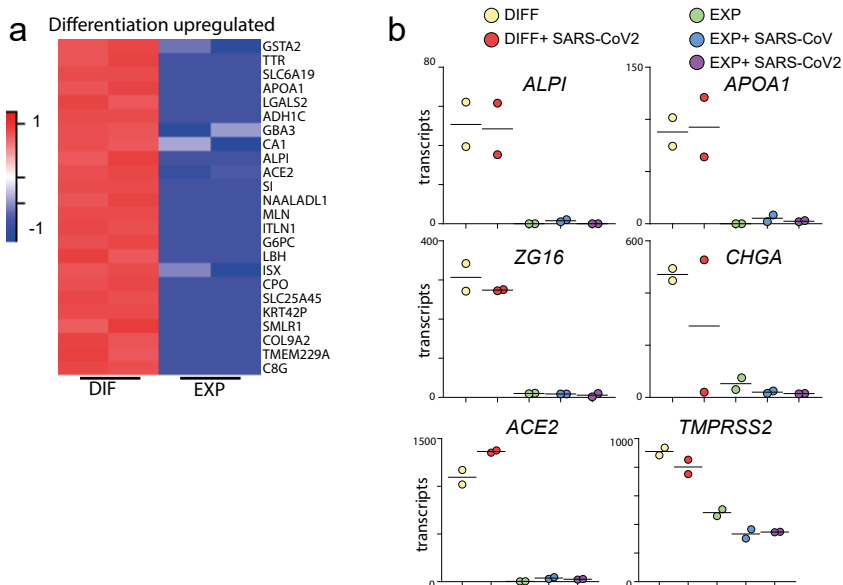
Supplementary figure S4. Quantification of SARS-CoV-2 infection spreading in organoids. a) Percentage of organoids harboring at least 1 SARS-CoV2 infected cell are depicted in the different culture conditions and at different timepoints. At least 50 different organoids were counted per condition. 60 hours infection in EXP medium was performed in n=2 independent experiments (see Figure S13), the other conditions as single experiment. b) The total number of infected cells per organoid (from a) were counted. 60 hours infection in EXP medium was performed in n=2 independent experiments (see Figure S13). *P<0.05, **P<0.01, ***P<0.001.



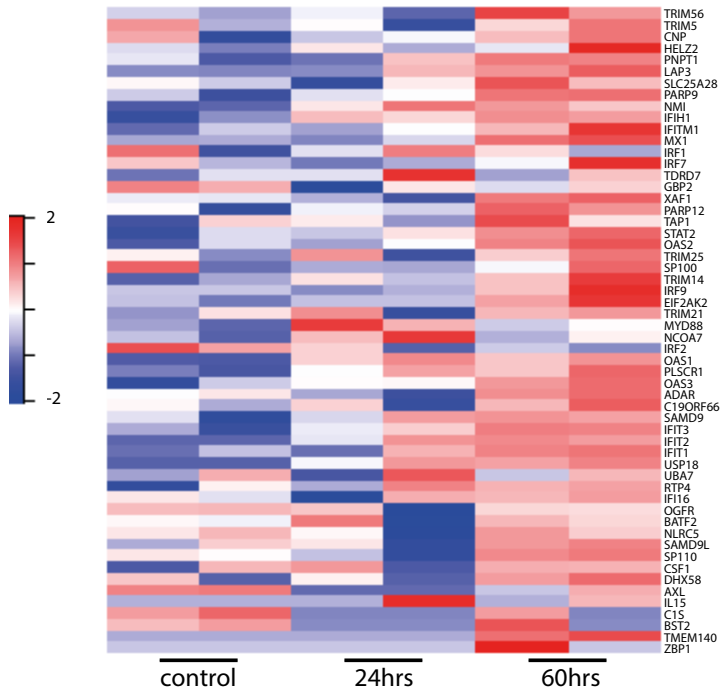
Supplementary figure S5. Increased apoptosis in organoids infected with SARS-CoV and SARS-CoV-2. a) SARS-CoV and -2-infected organoids show hallmarks of cell death, including detachment from the epithelial layer and cleaved-caspase 3 positivity. All scale bars are 50 μ m. b) Number of cleaved-caspase 3 positive cells in control and SARS-CoV2 infected organoids were counted. n= 5 organoids per condition. *P<0.05, **P<0.01, ***P<0.001.



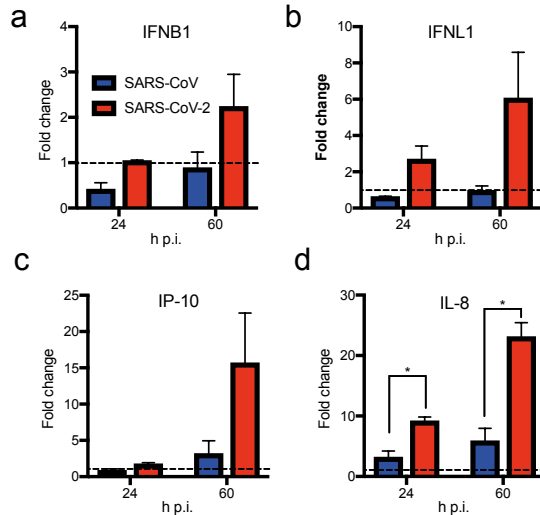
Supplementary figure S6. Transcriptomic analysis of SARS-CoV-2 infected differentiated organoids. Heatmaps depicting the 25 most significantly enriched genes upon SARS-CoV-2 infection in differentiated intestinal organoids (left). Right heatmap shows the top 25 signature genes from SARS-CoV2 infected EXP organoids (Figure 2a) upon SARS-CoV2 infection in differentiated intestinal organoids. Colored bar represents Z-score of \log_2 transformed values.



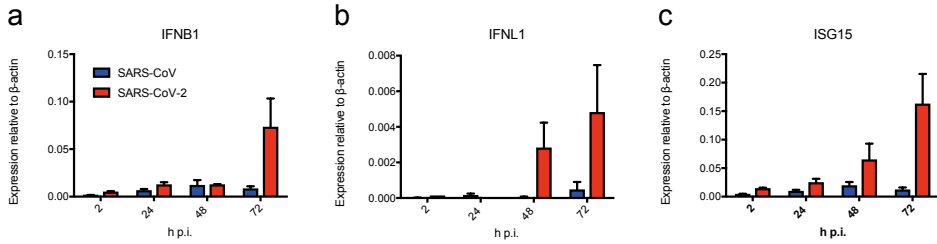
Supplementary figure S7. Differentiated organoids upregulate markers of mature intestinal lineages. a) Heatmaps depicting the 25 most significantly enriched genes upon differentiation compared to expansion condition. Colored bar represents Z-score of \log_2 transformed values. b) Graphs depicting the transcript counts of different genes enriched in mature lineages. Enterocytes (*ALPI* and *APOA1*), Goblet cells (*ZG16*) and Enteroendocrine cells (*CHGA*) increase upon differentiation. Genes required for viral entry (*ACE2* and *TMPRSS2*) are enriched in differentiated organoids.



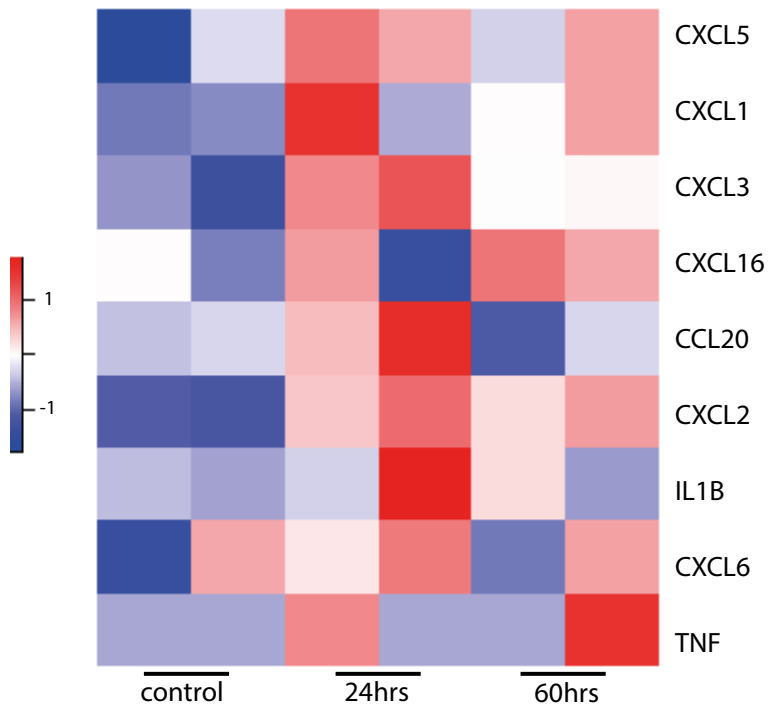
Supplementary figure S8. Interferon stimulated genes after SARS-CoV2 infection in intestinal organoids. Heatmaps depicting ISGs reported in (33) upon SARS-CoV2 infection in intestinal organoids. Colored bar represents Z-score of log₂ transformed values.



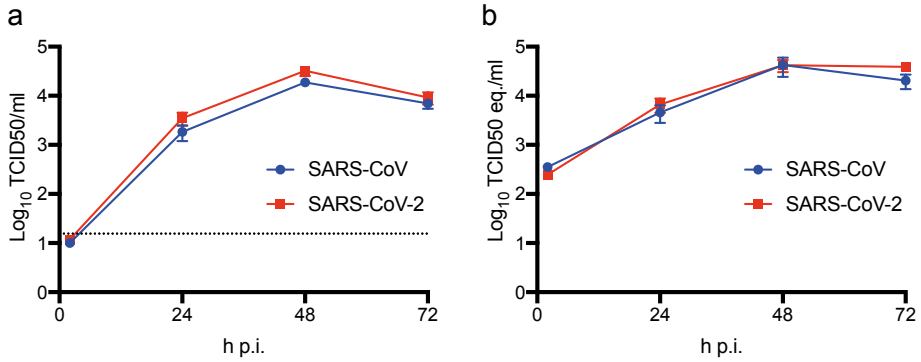
Supplementary figure S9 SARS-CoV-2 elicits cytokine responses in intestinal organoids. IFNB1 (a), IFNL1 (b), IP-10 (c) and IL-8 (d) levels in organoid culture supernatants were determined using Legendplex multiplex ELISA. Values were normalized to the 2h timepoint post infection. The dotted line indicates a fold change of 1. Error bars indicate SEM. N=3. *P<0.05, **P<0.01, ***P<0.001.



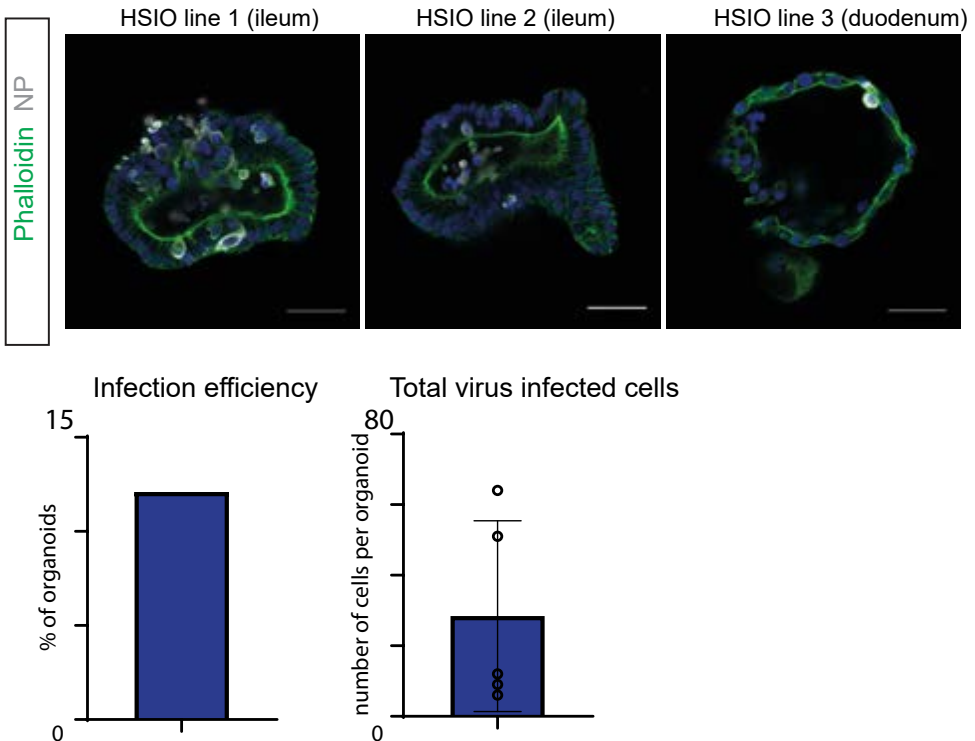
Supplementary figure S10. SARS-CoV-2 elicits cytokine responses in intestinal organoids as determined by qRT-PCR. IFNB1 (a), IFNL1 (b) and ISG15 (c) mRNA expression in organoids was determined by qRT-PCR. Values were normalized to β -actin expression. Error bars indicate SEM. N=3. *P<0.05, **P<0.01, ***P<0.001.



Supplementary figure S11. Cytokines after SARS-CoV2 infection in intestinal organoids. Heatmaps depicting virally regulated cytokines reported in (33) upon SARS-CoV2 infection in intestinal organoids. Colored bar represents Z-score of log2 transformed values.



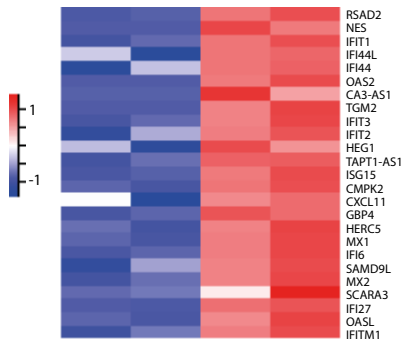
Supplementary figure S12. SARS-CoV and SARS-CoV-2 replicate in hSIOs in expansion medium. (a) Live virus and viral RNA (b) titers can be observed by virus titrations on VeroE6 cells of lysed organoids at 2, 24, 48 and 72h after infection with SARS-CoV (blue) and SARSCoV- 2 (red). The dotted line indicates the lower limit of detection. Error bars represent SEM. N=3.



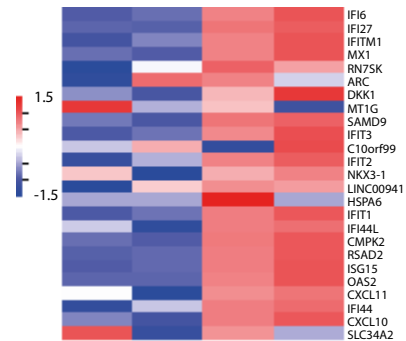
Supplementary figure S13. Human intestinal organoids from multiple donors are infected by SARS-CoV2. Immunofluorescent staining of SARS-CoV2-infected intestinal organoids in expansion conditions 72 hours after infection. Nucleoprotein (NP) stains viral capsid. The left panel is the same human small intestinal organoid (HSIO) line as used throughout the study, the middle panel a second line from a human ileum, and the right panel a line from a human duodenum. All scale bars are 50 μ m.

1
2
3
4
5
6
7
8
9
&

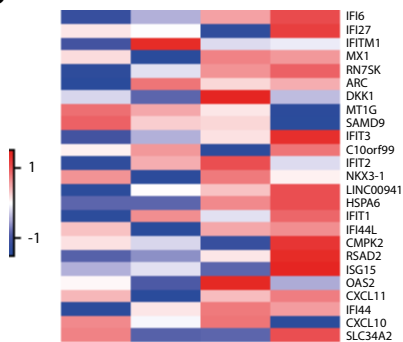
a Replicate SARS-CoV2 upregulated genes



b SARS-CoV2 upregulated genes from Fig2a



c SARS-CoV2 upregulated genes from Fig2a after replicate SARS-CoV infection



d

ID	Name	p-value
1	GO:0051607 defense response to virus	9.118E-32
2	GO:0071357 cellular response to type I interferon	6.109E-31
3	GO:0060337 type I interferon signaling pathway	6.109E-31
4	GO:0034340 response to type I interferon	1.375E-30
5	GO:0009615 response to virus	1.445E-30

Supplementary figure S14. Transcriptomic analysis of a replicate SARS-CoV-2 infection in intestinal organoids. a) Heatmaps depicting the 25 most significantly enriched genes upon the replicate SARS-CoV-2 infection in expanding intestinal organoids. Colored bar represents Z - Score of log2 transformed values. b) Heatmaps depicting the 25 genes from Figure 2a in the replicate SARS-CoV-2 infected expanding organoids. Colored bar represents Z-score of log2 transformed values. c) Heatmaps depicting the 25 genes from Figure 2a in the replicate SARS-CoV infected expanding organoids. Colored bar represents Z-score of log2 transformed values. d) GO term enrichment analysis for biological processes of the 50 most significantly upregulated genes upon SARS-CoV-2 infected in intestinal organoids.

CHAPTER

ADVANCING LUNG ORGANIDS FOR COVID-19 RESEARCH

Jelte van der Vaart¹, Mart M Lamers²,
Bart L. Haagmans² and Hans Clevers^{1*}

¹ Oncode Institute, Hubrecht Institute, Royal Netherlands Academy of
Arts and Sciences and University Medical Centre, Uppsalalaan 8,
Utrecht, 3584 CT, Netherlands.

² Viroscience Department, Erasmus University Medical Centre,
Rotterdam, the Netherlands.

5

ABSTRACT

The COVID-19 pandemic has emphasized the need to develop effective treatments to combat emerging viruses. Model systems that poorly represent a virus' cellular environment, however, may impede research and waste resources. Collaborations between cell biologists and virologists have led to the rapid development of representative organoid model systems to study SARS-CoV-2. We believe that lung organoids, in particular, have advanced our understanding of SARS-CoV-2 pathogenesis and have laid a foundation to study future pandemic viruses and develop effective treatments.

INTRODUCTION

First emerged at the end of 2019, SARS-CoV-2 has caused a pandemic of unprecedented scale and societal impact. The resulting disease, COVID-19, is characterised by pulmonary symptoms ranging from mild upper airway disease to life-threatening acute respiratory distress syndrome (ARDS). With over three and a half million deaths attributable to COVID-19 at the time of publication, this pandemic has underlined the importance of studying zoonotic viruses, preferably before they emerge as human pathogens. An important requirement to better understand the pathogenesis of infectious diseases is the establishment of representative model systems. Since many of the viruses considered pandemic threats cause pulmonary disease, experimental platforms to study pulmonary infections are crucial. Historically, most *in vitro* coronavirus studies have been performed on 2D cell lines like VeroE6, Caco-2 and Calu-3 cells¹. While these cell lines are often highly susceptible to these viruses, they may fail to model key aspects of the viral life cycle and antiviral compounds that work *in vitro* may fail in patients^{2,3}. Cell lines are known for intrinsic abnormalities which might influence the viral replication cycle. For example, in VeroE6 cells SARS-CoV-2 enters through the endosomal route after cleavage by cathepsins, whereas in primary airway cells SARS-CoV-2 enters the cell at the plasma membrane after serine protease mediated cleavage⁴. As a consequence, propagation of SARS-CoV-2 leads to the introduction of cell culture adaptive mutations in the spike protein multibasic cleavage site⁵⁻⁹. These adapted viruses do not behave like authentic SARS-CoV-2, as they are less pathogenic^{6,10} and they do not transmit¹¹. Apart from cell lines, multiple animal models have been used to study COVID-19. While mice are not susceptible to wild type SARS-CoV-2 infection¹², animals that overexpress the human variant of angiotensin converting enzyme 2 (ACE2) show high viral loads not only in the lungs but also in the brain¹³. In golden Syrian hamster SARS-CoV-2 can use hamster ACE2 for entry, although the animals do not develop severe lung disease upon viral infection as seen in hospitalized COVID-19 patients¹⁴. Similarly, in ferrets the disease is relatively mild and virus replication is mainly observed in the upper respiratory tract¹⁵. In addition, SARS-CoV-2 rapidly acquires spike protein mutations in ferrets as a result of critical species specific differences in ACE2 receptor interactions¹⁶ showing the complexity of the response to viral infection in different animal hosts^{17,18}. In addition, all these models are costly and require specialised animal BSL-3 facilities. Over the past year, human stem cell-derived organoids have emerged as powerful tools for COVID-19 research bridging the gap between cell lines and *in vivo* animal models.

RECAP OF CURRENT AIRWAY ORGANOID TECHNOLOGIES

Organoids are three-dimensional (3D) *in vitro* structures grown from stem cells which consist of organ-specific cell types that self-organise through cell sorting and spatially restricted lineage commitment^{19,20}. Organoids can be established from two distinct stem

1

2

3

4

5

6

7

8

9

&

cell populations: adult stem cells (ASCs) derived from adult or foetal tissue, or pluripotent stem cells (induced PSCs (iPSCs) and embryonic stem cells (ESCs)). Under optimal conditions, a comprehensive set of cell types from the tissue of interest is generated. Both stem cell types have been employed to generate lung organoids. Yet, the derivation of airway organoids and their subsequent characteristics differ greatly between the two stem cell types. iPSC-derived organoids are formed by generating 3D aggregates from the pertinent iPSCs. The subsequent lung fate specification is accomplished by culturing the aggregates in a series of growth factor-enriched media designed to mimic the journey of an embryonic stem cell on its way to build lung tissues in a developing embryo. In contrast, ASC-derived organoids are generated by isolation of resident stem cells from the airways by providing a 3D matrix as well as a single growth factor cocktail²¹.

Differentiation of iPSCs to airway epithelium generates structures that comprise of multiple airway cell types including basal, club and ciliated cells²²⁻²⁹ as well as alveolar cell types: alveolar type I and II (ATI and ATII) cells³⁰. These iPSC models may also contain non-epithelial/non-endodermal elements including mesenchyme and endothelium. While iPSC-derived lung progenitors can be induced to form 3D alveolar structures with ATI and ATII cells³¹, the combination of airway and alveoli has yet to be achieved. Similar challenges existed for ASC-derived human lung organoids with initial cultures containing the major airway cell types, while alveolar cells were absent³². Against this backdrop, we highlight that the COVID-19 pandemic has fuelled the development of multiple novel, long-term lung culture systems.

AIRWAY ORGANOID AS TOOLS FOR STUDYING COVID-19

Organoids have been used as models of a multitude of pathologies, including infectious diseases^{19,33}. Human intestinal organoids from ASCs were the first to allow successful *in vitro* propagation of human noroviruses³⁴⁻³⁶. During the Zika virus outbreak, iPSC-derived cerebral organoids allowed fast discovery of viral replication in dividing neural progenitors and the subsequent demise of the latter, explaining how foetal, but not adult, brains could be affected by the virus^{37,38}. Furthermore, ASC-derived human oral mucosal organoids were infectible by herpes simplex virus and human papilloma virus³⁹.

Importantly, airway organoids have been used to study a broad range of viruses, including respiratory syncytial virus and influenza virus^{32,40}.

When SARS-CoV-2 emerged in December 2019 in Wuhan, China, respiratory models were rapidly employed to study the infection of this newly identified coronavirus. ASC-derived airway organoids were infected as air-liquid interface (ALI) cultures^{9,41} and as 3D structures^{42,43}. Lamers and colleagues showed essential viral life cycle stages which include intracellular double vesicle membranes. Studies on 2D ALI cultures identified ciliated cells as a primary target of SARS-CoV-2 but also noted occasional infection of club cells^{41,44}. 3D cultures, however, showed primary infection in club cells⁴² or basal

cells⁴³, indicating that growth conditions, differentiation status, or perhaps differences between donors affect viral tropism. Infection of 2D ALI airway organoids with SARS-CoV-2 elicited a broad signature of interferon-stimulated genes (ISGs) attributed to type I/III interferon responses⁴¹. The potential of using ASC-derived airway cultures for virus propagation of SARS-CoV-2 was shown by Lamers *et al.*⁹. Most importantly, cell culture-adaptive mutations in the multibasic cleavage site of the spike protein of SARS-CoV-2, which mediates viral entry into the host cell, typically seen upon propagation of the virus in cell lines, did not occur in viruses propagated on these ALI cultures of airway organoids. This indicated that this culture system accurately models viral target cells *in vivo*⁹. Moreover, fundamental virology studies can be aided by the use of this representative model system. This is evidenced by the discovery that SARS-CoV-2 enters human airway cells via serine protease-mediated entry and not via endocytosis/cathepsin-mediated entry, as is the case in Vero cells and other cell lines commonly used in virology labs^{4,45}. The latter observation explains why the endocytosis pathway inhibitor (hydroxy-)chloroquine emerged from cell line screens, yet was ineffective in the clinic². A limitation however remains that these ALI cultures do not allow modelling of the immune system as the basal side of the cells is attached to plastic and therefore inaccessible to immune cells. 3D models that can be exposed to direct cell-cell interaction at their basal side, might overcome this limitation. These future models will be valuable in studying immune responses towards virally infected cells and could potentially be used to find new immune modulators that limit disease severity in patients.

ALVEOLAR ORGANOID SYSTEMS AS POTENTIAL MODELS FOR ARDS

While these airway models recapitulate some findings in COVID-19 patients, the search for genuine alveolar model systems remained. Studying alveolar response to SARS-CoV-2 infection is critical as most COVID-19 patients are hospitalized due to ARDS, but freshly isolated primary alveolar cultures from healthy individuals were found only minimally susceptible to SARS-CoV-2⁴⁶. In addition, human ATII cells rapidly differentiate to ATI-like cells in 2D cell culture, limiting the possibilities to study ATII biology⁴⁷. Several studies used existing iPSC-derived cells, first described in 2017⁴⁸, to generate alveolar epithelium⁴⁹. This differentiation was extended to specific ATII cells by Abo and colleagues. These authors induced iPSCs to differentiate towards ATII (iATII) cells which led to the comparable expression of the main SARS-CoV-2 viral entry factors ACE2 and transmembrane serine protease 2 (TMPRSS2) compared to freshly isolated ATII cells⁵⁰, which were thereafter permissive to SARS-CoV-2 infection in ALI cultures. The expression of these vital viral entry factors was in line with the expression *in vivo* in ATII and ciliated cells in the lung⁵¹⁻⁵³. The infection could be blocked by antiviral drug remdesivir and by TMPRSS2 inhibition while a cathepsin B/L inhibitor, that showed effect in VeroE6 cells, did not block virus replication in iATII cells⁵⁴. iPSC-derived alveolar model systems also

1

2

3

4

5

6

7

8

9

&

revealed other FDA-approved drugs to have potential in inhibiting SARS-CoV-2 infection, including the tyrosine kinase inhibitor imatinib, the immunosuppressant mycophenolic acid and the antimalarial agent quinacrine dihydrochloride⁵⁵. Although the effect of these drugs remain to be investigated in patients, these studies show the potential of iPSC-derived alveolar model systems as pre-clinical models over standardised immortalised cell lines.

Lamers and colleagues (2021a) used a different approach using human foetal lung epithelial stem cells to achieve alveolar differentiation by Lamers and colleagues⁴⁴ using lung bud tip organoids described earlier⁵⁶. These foetal lung bud tip organoids displayed alveolar differentiation potential in 3D⁵⁶ and were used to establish ALI cultures in combination with foetal fibroblasts to differentiate into bronchioalveolar-like cultures. These cultures were comprised of both alveolar-like and bronchiolar-like areas⁴⁴. This mix of cell types allows studying interactions between multiple areas in the airways, thereby providing a more complete view compared to studying a single area. A similar combinatorial culture system was recently established by using iPSCs^{57,58}. The susceptibility of these optimized foetal or iPSC-derived ALI cultures to SARS-CoV-2 infection appears to be higher than that of the ASC 3D systems, which could be related to the facile access of the virus to the apical side of the cells or their differentiation status.

COVID-19 also motivated the development of several alveolar model systems derived from ASCs. These studies used primary ATII cells as starting material to generate 3D spheres that were comprised of ATII cells only, while maintaining the potential to differentiate to ATI cells. Growth conditions and susceptibility to SARS-CoV-2 infection varied between studies^{42,59,60}. The system of Youk and colleagues appears to be most permissive to SARS-CoV-2 infection, achieving infectious virus titers up to 10^4 infectious units per ml (10^3 fold change compared with input). Very similar AT2 culture conditions were recently used by Lamers et al⁶¹, resulting in similar infectious virus titers (using 3D and 2D ATII cultures). Katsura, Youk and Lamers et al all report the induction of ISG responses, attributed to type I and III IFNs, and a decrease in the expression of surfactant proteins (e.g. SFTPB, SFTPC and SFTPD). Other AT2 markers did not decrease in expression upon SARS-CoV-2 infection⁵⁹⁻⁶¹. Lower levels of surfactant proteins are detrimental for oxygen exchange, as these proteins are crucial to preventing alveolar collapse. They are also involved in innate and adaptive immune responses^{62,63}. In addition, Katsura reports the prominent expression of chemokines (CXCL10, CXCL11, and CXCL17) and cell death-related genes (TNFSF10, CASP1, CASP4, CASP5, and CASP7)⁵⁹. Overall, it seems that alveolar infection is characterized by type I/III IFN responses, proinflammatory responses (e.g. chemokines), apoptosis, and low surfactant production. These responses are induced solely by epithelial cells and future studies may investigate the influence of other lung cell types on these responses.

Together, the toolbox of pulmonary organoid model systems has increased rapidly over the past year. In our opinion, it now provides a more physiological experimental setting to study SARS-CoV-2 and other pathogens that target the lungs, be it airways or alveoli.

FUTURE PERSPECTIVES

As discussed above, the emergence of COVID-19 has boosted the establishment of many new lung organoid models, as well as reviving older approaches. The extensive variation in protocols indicates that there may exist multiple ways to achieve our common goal and further improvements to the current technologies are to be expected. Combining cell biology and virology expertise has already led to the development of applicable, representative and easily infectable model systems. Knowledge of stem cell biology combined with that of pulmonary development thus allows the generation of multiple organoid-based respiratory cell cultures of airways and alveoli (**Figure 1**).

Organoid cultures originating from different parts of the respiratory tract could allow further insight into virus tropism, not only of SARS-CoV-2 but also other respiratory viruses. Cells of the upper airway could be used to study virus shedding or the role of host factors in the context of virus transmission, but might be less relevant when studying severe COVID-19, where infection of alveolar cells or inflammation in the distal lung can lead to potentially fatal ARDS^{64–66}. Alveolar models can be used to study the latter complication, either alone or in combination with other cell types such as endothelial, stromal or immune cells (**Figure 1**). Airway cells of the bronchus and bronchiole could be used to study local host responses and dissemination to the alveolus. It is vitally important to understand regional differences by using multiple model systems, which will further pinpoint the direct causes of disease severity and potentially elucidate effective therapies to alleviate this.

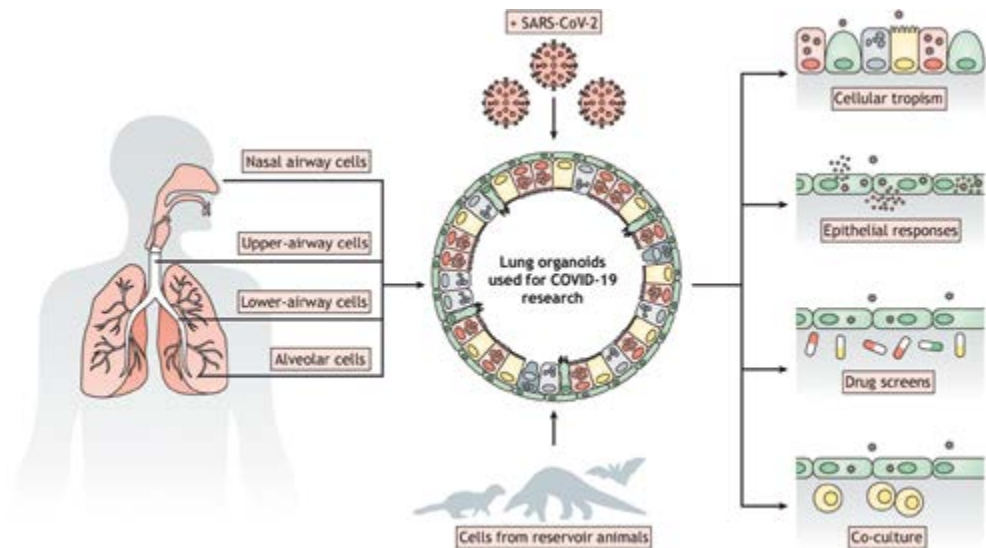


Figure 1. Overview of the potential of region-restricted lung organoids in virology.

1
2
3
4
5
6
7
8
9
&

SARS-CoV-2, like many other human viruses, originates from animals and has presumably undergone adaptations when infecting humans. Organoids derived from reservoir animals could be used to culture and study viruses that have not yet been shown to infect humans but may do so in the future. The potential of these organoids has already been shown using bat- and feline-derived intestinal organoids to study coronaviruses^{67,68}. Expanding these studies may reveal the adaptations required when viruses adapt to other species (**Figure 1**).

Several reports have shown the relationship between host genetic variants and susceptibility for SARS-CoV-2 and disease severity⁶⁹. The underlying biology can be studied in relevant organoid models derived from individuals with representative genetic backgrounds. The use of sophisticated genetic editing tools can also increase understanding of SARS-CoV-2 biology (**Figure 1**). Genome-wide CRISPR-Cas9 screens have already identified a number of host factors like ACE2 that play a crucial role in SARS-CoV-2 infection^{70,71}. These studies were performed on classical cell lines (and have revealed a role for endocytosis in VeroE6 cells; see above) but we emphasize that these finding should be confirmed in more physiologically relevant models.

Contrarily, variants of SARS-CoV-2 that may transmit better or escape from immunity are increasingly identified⁷². Organoids can potentially be used to identify the differences between these strains of SARS-CoV-2. Infection of the British variant in airway, alveolar and intestinal organoids produced higher levels of viral particles late in infection compared to the ancestral strain⁶¹, identifying extended shedding as an in vitro correlate of viral fitness. The British variant also outcompeted the ancestor in airway organoids when both viruses were added to the same culture. The rapid comparison of SARS-CoV-2 variants in organoid systems may ultimately inform public health decision making.

Organoids have also emerged as a promising tool for predicting drug efficacy through high-throughput screens (**Figure 1**). Norovirus infection in intestinal organoids could be blocked by a variety of antibodies⁷³. Moreover, iPSC-derived cerebral organoids have provided a platform for identifying treatments that limit neural progenitor cell death after Zika-virus infection^{37,38}. In the past year, intestinal and airway organoid models have been implicated in predicting SARS-CoV-2 treatment discovery. Application of 25-hydroxycholesterol, remdesivir, interferon- λ or camostat decrease SARS-CoV-2 spread in the organoids^{4,43,44,74,75}. While these studies used known antiviral drugs or drugs based on known SARS-CoV-2 biology, a recent study employed iPSC-derived airway organoids in a 384-well format to uncover FDA-approved drugs that effectively lower viral replication⁷⁶. A separate study used human iPSC-derived colorectal infected with SARS-CoV-2 organoids in a similar set-up and tested more than 1,000 drugs⁷⁷. Many of these hits overlapped with those in lung organoids, indicating effective viral blockade in at least two epithelial tissues.

It is evident that advancing the development of pulmonary organoid culture models has contributed to understanding pathogenesis and advancing drug development for SARS-CoV-2. Continuing this progress will be essential to prepare for future pandemics.

REFERENCES

1. Takayama, K. In Vitro and Animal Models for SARS-CoV-2 research. *Trends in Pharmacological Sciences* **41**, 513–517 (2020).
2. Hernandez, A. V., Roman, Y. M., Pasupuleti, V., Barboza, J. J. & White, C. M. Hydroxychloroquine or Chloroquine for Treatment or Prophylaxis of COVID-19: A Living Systematic Review. *Ann. Intern. Med.* **173**, 287–296 (2020).
3. Wang, M. et al. Remdesivir and chloroquine effectively inhibit the recently emerged novel coronavirus (2019-nCoV) in vitro. *Cell Res.* **30**, 269–271 (2020).
4. Mykytyn, A. Z. et al. Sars-cov-2 entry into human airway organoids is serine protease-mediated and facilitated by the multibasic cleavage site. *Elife* **10**, 1–23 (2021).
5. Klimstra, W. B. et al. SARS-CoV-2 growth, furin-cleavage-site adaptation and neutralization using serum from acutely infected hospitalized COVID-19 patients. *J. Gen. Virol.* **101**, 1156–1169 (2020).
6. Lau, S. Y. et al. Attenuated SARS-CoV-2 variants with deletions at the S1/S2 junction. *Emerg. Microbes Infect.* **9**, 837–842 (2020).
7. Liu, Z. et al. Identification of Common Deletions in the Spike Protein of Severe Acute Respiratory Syndrome Coronavirus 2. *J. Virol.* **94**, (2020).
8. Ogando, N. S. et al. SARS-coronavirus-2 replication in Vero E6 cells: Replication kinetics, rapid adaptation and cytopathology. *J. Gen. Virol.* **101**, 925–940 (2020).
9. Lamers, M. M. et al. Human airway cells prevent SARS-CoV-2 multibasic cleavage site cell culture adaptation. *Elife* **10**, 2021.01.22.427802 (2021).
10. Johnson, B. A. et al. Loss of furin cleavage site attenuates SARS-CoV-2 pathogenesis. *Nature* **591**, 293–299 (2021).
11. Peacock, T. P. et al. The furin cleavage site in the SARS-CoV-2 spike protein is required for transmission in ferrets. *Nat. Microbiol.* (2021). doi:10.1038/s41564-021-00908-w
12. Zhou, P. et al. A pneumonia outbreak associated with a new coronavirus of probable bat origin. *Nature* **579**, 270–273 (2020).
13. Sun, S. H. et al. A Mouse Model of SARS-CoV-2 Infection and Pathogenesis. *Cell Host Microbe* **28**, 124–133.e4 (2020).
14. Chan, J. F. W. et al. Simulation of the Clinical and Pathological Manifestations of Coronavirus Disease 2019 (COVID-19) in a Golden Syrian Hamster Model: Implications for Disease Pathogenesis and Transmissibility. *Clin. Infect. Dis.* **71**, 2428–2446 (2020).
15. Shi, J. et al. Susceptibility of ferrets, cats, dogs, and other domesticated animals to SARS-coronavirus 2. *Science (80-.).* **368**, 1016–1020 (2020).
16. Richard, M. et al. SARS-CoV-2 is transmitted via contact and via the air between ferrets. *Nat. Commun.* **11**, 1–6 (2020).
17. Rosa, R. B. et al. In Vitro and In Vivo Models for Studying SARS-CoV-2, the Etiological Agent Responsible for COVID-19 Pandemic. *Viruses* **13**, 379 (2021).
18. Leist, S. R., Schäfer, A. & Martinez, D. R. Cell and animal models of SARS-CoV-2 pathogenesis and immunity. *DMM Dis. Model. Mech.* **13**, (2020).
19. Clevers, H. Modeling Development and Disease with Organoids. *Cell* **165**, 1586–1597 (2016).
20. Lancaster, M. A. & Knoblich, J. A. Organogenesis in a dish: Modeling development and disease using organoid technologies. *Science (80-.).* **345**, (2014).
21. van der Vaart, J. & Clevers, H. Airway organoids as models of human disease. *Journal of Internal Medicine* (2020). doi:10.1111/joim.13075
22. Wilkinson, D. C. et al. Development of a Three-Dimensional Bioengineering Technology to Generate Lung Tissue for Personalized Disease Modeling. *Stem Cells Transl. Med.* **6**, 622–633 (2017).
23. Huang, S. X. L. et al. Efficient generation of lung and airway epithelial cells from

- human pluripotent stem cells. *Nat. Biotechnol.* **32**, 84–91 (2014).
24. Mou, H. et al. Generation of Multipotent Lung and Airway Progenitors from Mouse ESCs and Patient-Specific Cystic Fibrosis iPSCs. *Cell Stem Cell* **10**, 385–397 (2012).
 25. Firth, A. L. et al. Generation of multiciliated cells in functional airway epithelia from human induced pluripotent stem cells. *Proc. Natl. Acad. Sci. U. S. A.* **111**, E1723-30 (2014).
 26. McIntyre, B. A. S. et al. Expansive Generation of Functional Airway Epithelium From Human Embryonic Stem Cells. *Stem Cells Transl. Med.* **3**, 7–17 (2014).
 27. Konishi, S. et al. Directed Induction of Functional Multi-ciliated Cells in Proximal Airway Epithelial Spheroids from Human Pluripotent Stem Cells. *Stem cell reports* **6**, 18–25 (2016).
 28. Dye, B. R. et al. In vitro generation of human pluripotent stem cell derived lung organoids. *Elife* **4**, (2015).
 29. McCauley, K. B. et al. Efficient Derivation of Functional Human Airway Epithelium from Pluripotent Stem Cells via Temporal Regulation of Wnt Signaling. *Cell Stem Cell* **20**, 844-857.e6 (2017).
 30. van Riet, S. et al. In vitro modelling of alveolar repair at the air-liquid interface using alveolar epithelial cells derived from human induced pluripotent stem cells. *Sci. Rep.* **10**, (2020).
 31. de Carvalho, A. L. R. T. et al. Glycogen synthase kinase 3 induces multilineage maturation of human pluripotent stem cell-derived lung progenitors in 3D culture. *Dev.* **146**, (2019).
 32. Sachs, N. et al. Long-term expanding human airway organoids for disease modeling. *EMBO J.* **38**, e100300 (2019).
 33. Lancaster, M. A. & Huch, M. Disease modelling in human organoids. *DMM Dis. Model. Mech.* **12**, (2019).
 34. Ettayebi, K. et al. Replication of human noroviruses in stem cell-derived human enteroids. *Science (80-.).* **353**, 1387–1394 (2016).
 35. Haga, K. et al. Genetic manipulation of human intestinal enteroids demonstrates the necessity of a functional fucosyltransferase 2 gene for secretor-dependent human norovirus infection. *MBio* **11**, 1–10 (2020).
 36. Estes, M. K. et al. Human Norovirus Cultivation in Nontransformed Stem Cell-Derived Human Intestinal Enteroid Cultures: Success and Challenges. *Viruses* **11**, 9–11 (2019).
 37. Qian, X., Nguyen, H. N., Jacob, F., Song, H. & Ming, G. L. Using brain organoids to understand Zika virus-induced microcephaly. *Dev.* **144**, 952–957 (2017).
 38. Watanabe, M. et al. Self-Organized Cerebral Organoids with Human-Specific Features Predict Effective Drugs to Combat Zika Virus Infection. *Cell Rep.* **21**, 517–532 (2017).
 39. Driehuis, E. et al. Oral Mucosal Organoids as a Potential Platform for Personalized Cancer Therapy. *Cancer Discov.* **9**, 852–871 (2019).
 40. Zhou, J. et al. Differentiated human airway organoids to assess infectivity of emerging influenza virus. *Proc. Natl. Acad. Sci.* **115**, 6822–6827 (2018).
 41. Lamers, M. M. et al. SARS-CoV-2 productively infects human gut enterocytes. *Science (80-.).* **369**, 50–54 (2020).
 42. Salahudeen, A. A. et al. Progenitor identification and SARS-CoV-2 infection in human distal lung organoids. *Nature* **588**, 670–675 (2020).
 43. Suzuki, T. et al. Generation of human bronchial organoids for SARS-CoV-2 research. *bioRxiv* **4**, 2020.05.25.115600 (2020).
 44. Lamers, M. M. et al. An organoid-derived bronchioalveolar model for SARS-CoV-2 infection of human alveolar type II-like cells. *EMBO J.* (2021). doi:10.15252/embj.2020105912
 45. Hoffmann, M. et al. SARS-CoV-2 Cell Entry Depends on ACE2 and TMPRSS2 and Is Blocked by a Clinically Proven Protease Inhibitor. *Cell* **181**, 271-280.e8 (2020).
 46. Hou, Y. J. et al. SARS-CoV-2 Reverse Genetics Reveals a Variable Infection Gradient in the Respiratory Tract. *Cell* **182**, 429-446.e14 (2020).

47. Bove, P. F. et al. Breaking the in vitro alveolar type II cell proliferation barrier while retaining ion transport properties. *Am. J. Respir. Cell Mol. Biol.* **50**, 767–776 (2014).
48. Jacob, A. et al. Differentiation of Human Pluripotent Stem Cells into Functional Lung Alveolar Epithelial Cells. *Cell Stem Cell* **21**, 472–488.e10 (2017).
49. Jacob, A. et al. Derivation of self-renewing lung alveolar epithelial type II cells from human pluripotent stem cells. *Nat. Protoc.* **14**, 3303–3332 (2019).
50. Abo, K. M. et al. Human iPSC-derived alveolar and airway epithelial cells can be cultured at air-liquid interface and express SARS-CoV-2 host factors. *bioRxiv* (2020). doi:10.1101/2020.06.03.132639
51. Jia, H. P. et al. ACE2 receptor expression and severe acute respiratory syndrome coronavirus infection depend on differentiation of human airway epithelia. *J. Virol.* **79**, 14614–21 (2005).
52. Qi, F., Qian, S., Zhang, S. & Zhang, Z. Single cell RNA sequencing of 13 human tissues identify cell types and receptors of human coronaviruses. (2020). doi:10.1016/j.bbr.2020.03.044
53. Hikmet, F. et al. The protein expression profile of ACE2 in human tissues. *Mol. Syst. Biol.* **16**, e9610 (2020).
54. Huang, J. et al. SARS-CoV-2 Infection of Pluripotent Stem Cell-Derived Human Lung Alveolar Type 2 Cells Elicits a Rapid Epithelial-Intrinsic Inflammatory Response. *Cell Stem Cell* **27**, 962–973.e7 (2020).
55. Han, Y. et al. Identification of SARS-CoV-2 inhibitors using lung and colonic organoids. *Nature* **589**, 270–275 (2021).
56. Nikolić, M. Z. et al. Human embryonic lung epithelial tips are multipotent progenitors that can be expanded in vitro as long-term self-renewing organoids. *Elife* **6**, (2017).
57. Tiwari, S. K., Wang, S., Smith, D., Carlin, A. & Rana, T. M. Revealing tissue-specific SARS-CoV-2 infection and host responses using human stem cell derived lung and cerebral organoids. *Stem Cell Reports* (2021). doi:10.1016/j.stemcr.2021.02.005
58. Rodrigues Toste de Carvalho, A. L. et al. The in vitro multilineage differentiation and maturation of lung and airway cells from human pluripotent stem cell-derived lung progenitors in 3D. *Nat. Protoc.* 1–28 (2021). doi:10.1038/s41596-020-00476-z
59. Katsura, H. et al. Human Lung Stem Cell-Based Alveolospheres Provide Insights into SARS-CoV-2-Mediated Interferon Responses and Pneumocyte Dysfunction. *Cell Stem Cell* **27**, 890–904.e8 (2020).
60. Youk, J. et al. Three-Dimensional Human Alveolar Stem Cell Culture Models Reveal Infection Response to SARS-CoV-2. *Cell Stem Cell* **27**, 905–919.e10 (2020).
61. Lamers, M. M. et al. Human organoid systems reveal in vitro correlates of fitness for SARS-CoV-2. B.1.1.7. *bioRxiv* 2021.05.03.441080 (2021). doi:10.1101/2021.05.03.441080
62. Crouch, E. & Wright, J. R. Surfactant proteins A and D and pulmonary host defense. *Annual Review of Physiology* **63**, 521–554 (2001).
63. McCormack, F. X. & Whitsett, J. A. The pulmonary collectins, SP-A and SP-D, orchestrate innate immunity in the lung. *J. Clin. Invest.* **109**, 707–712 (2002).
64. Ackermann, M. et al. Pulmonary Vascular Endothelialitis, Thrombosis, and Angiogenesis in Covid-19. *N. Engl. J. Med.* **383**, 120–128 (2020).
65. McGonagle, D., Bridgewood, C., Ramanan, A. V., Meaney, J. F. M. & Watad, A. COVID-19 vasculitis and novel vasculitis mimics. *The Lancet Rheumatology* **3**, (2021).
66. Menter, T. et al. Postmortem examination of COVID-19 patients reveals diffuse alveolar damage with severe capillary congestion and variegated findings in lungs and other organs suggesting vascular dysfunction. *Histopathology* **77**, 198–209 (2020).
67. Zhou, J. et al. Infection of bat and human intestinal organoids by SARS-CoV-2. *Nat. Med.* **26**, 1077–1083 (2020).
68. Tekes, G., Ehmann, R., Boulant, S. & Stanifer, M. L. Development of Feline Ileum- and Colon-Derived Organoids

1
2
3
4
5
6
7
8
9
&

- and Their Potential Use to Support Feline Coronavirus Infection. *Cells* **9**, (2020).
69. Mohammadpour, S., Torshizi Esfahani, A., Halaji, M., Lak, M. & Ranjbar, R. An updated review of the association of host genetic factors with susceptibility and resistance to COVID-19. *Journal of Cellular Physiology* **236**, 49–54 (2021).
70. Wei, J. et al. Genome-wide CRISPR Screens Reveal Host Factors Critical for SARS-CoV-2 Infection. *Cell* **184**, 76-91.e13 (2021).
71. Wang, R. et al. Genetic Screens Identify Host Factors for SARS-CoV-2 and Common Cold Coronaviruses. *Cell* **184**, 106-119.e14 (2021).
72. Plante, J. A. et al. The variant gambit: COVID-19's next move. (2021). doi:10.1016/j.chom.2021.02.020
73. Alvarado, G. et al. Human Monoclonal Antibodies That Neutralize Pandemic GII.4 Noroviruses. *Gastroenterology* **155**, 1898–1907 (2018).
74. Krüger, J. et al. Drug Inhibition of SARS-CoV-2 Replication in Human Pluripotent Stem Cell-Derived Intestinal Organoids. *CMGH* **11**, 935–948 (2021).
75. Zu, S. et al. 25-Hydroxycholesterol is a potent SARS-CoV-2 inhibitor. *Cell Res.* 1–3 (2020). doi:10.1038/s41422-020-00398-1
76. Han, Y. et al. Identification of Candidate COVID-19 Therapeutics using hPSC-derived Lung Organoids. 16–19 (2020).
77. Duan, X. et al. Identification of Drugs Blocking SARS-CoV-2 Infection using Human Pluripotent Stem Cell-derived Colonic Organoids. (2020). doi:10.1101/2020.05.02.073320

CHAPTER

AN ORGANOID-DERIVED BRONCHIOALVEOLAR MODEL FOR SARS-COV-2 INFECTION OF HUMAN ALVEOLAR-TYPE II-LIKE CELLS

Mart M. Lamers*¹, Jelte van der Vaart*², Kèvin Knoops³,
Samra Riesebosch¹, Tim I. Breugem¹, Anna Z. Mykytyn¹,
Joep Beumer², Debby Schipper¹, Karel Bezstarosti⁴,
Charlotte D. Koopman⁵, Nathalie Groen⁵, Raimond B.G. Ravelli³,
Hans Q. Duimel³, Jeroen A.A. Demmers⁴, Georges M.G.M. Verjans¹,
Marion P.G. Koopmans¹, Mauro J. Muraro⁵, Peter J. Peters³,
Hans Clevers², Bart L. Haagmans¹

¹Viroscience Department, Erasmus University Medical Center,
Rotterdam, the Netherlands.

²Oncode Institute, Hubrecht Institute, Royal Netherlands Academy of
Arts and Sciences and University Medical Center, Uppsalalaan 8, Utrecht,
3584 CT, Netherlands.

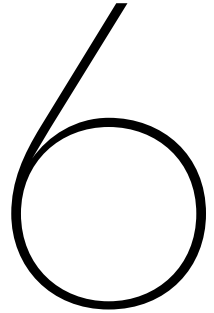
³The Maastricht Multimodal Molecular Imaging Institute, Maastricht
University, 6229 ER Maastricht, the Netherlands.

⁴Proteomics Center, Erasmus University Medical Center,
Rotterdam, the Netherlands.

⁵Single Cell Discoveries, Utrecht, the Netherlands.

*These authors contributed equally to this work.

*Published in The EMBO Journal (2021);
doi: 10.15252/embj.2020105912*



ABSTRACT

Severe acute respiratory syndrome coronavirus 2 (SARS-CoV-2), which causes coronavirus disease 2019 (COVID-19), may result in acute respiratory distress syndrome (ARDS), multi-organ failure and death. The alveolar epithelium is a major target of the virus, but representative models to study virus host interactions in more detail are currently lacking. Here, we describe a human 2D air-liquid interface culture system which was characterized by confocal-, electron-microscopy and single cell mRNA expression analysis. In this model, alveolar cells, but also basal cells and rare neuroendocrine cells, are grown from 3D self-renewing fetal lung bud tip organoids. These cultures were readily infected by SARS-CoV-2 with mainly surfactant protein C-positive alveolar type II-like cells being targeted. Consequently, significant viral titers were detected and mRNA expression analysis revealed induction of type I/III interferon response program. Treatment of these cultures with a low dose of interferon lambda 1 reduced viral replication. Hence, these cultures represent an experimental model for SARS-CoV-2 infection and can be applied for drug screens.

INTRODUCTION

The severe acute respiratory syndrome coronavirus 2 (SARS-CoV-2) has spread globally within several months after an initial outbreak in Wuhan, China, in December 2019¹. The World Health Organization (WHO) declared SARS-CoV-2 a pandemic on March 11, 2020. As of November 1, 2020, >46,000,000 patients were confirmed including >1,200,000 deaths². SARS-CoV-2 belongs to the Sarbecovirus subgenus (genus Betacoronavirus, family Coronaviridae), together with SARS-CoV³⁻⁵. SARS-CoV-2 causes coronavirus disease 2019 (COVID-19), an influenza-like illness associated with a broad spectrum of clinical respiratory syndromes, ranging from mild upper airway symptoms to a life-threatening viral pneumonia⁶⁻⁹. This pneumonia fulfils the radiographic and histological criteria for acute respiratory distress syndrome (ARDS). Classically, ARDS is caused by damage to the alveoli, more specifically to the alveolar type I cells that are critical in the oxygen transport from the alveoli to the blood, triggered through an inflammatory response to pathogens or toxins¹⁰⁻¹⁵.

The early events that lead to respiratory failure as a result of coronavirus infection are initiated following virus replication¹⁶. After virus entry, which is determined by receptor availability, viral replication generates pathogen-associated molecular patterns, specifically RNA structures, that can be detected by pattern recognition receptors (PRRs). PRR signalling subsequently leads to the transcription of antiviral genes; the response triggered varies between pulmonary cell types¹⁷. Therefore, disease outcome can be greatly influenced by the viral target cell, which is determined largely by the presence of CoV entry receptor. In the lungs, angiotensin-converting enzyme 2 (ACE2), the SARS-CoV-2 receptor¹⁸⁻²¹, is expressed mainly in ciliated cells and alveolar type II cells²²⁻²⁴. Ciliated cells, alveolar type II cells, but also alveolar type I cells, have been identified as SARS-CoV-2 target cells in animal models and in COVID-19 patients^{8,25,26}. In previous work, we confirmed ciliated cells as a viral target cell using organoid-derived bronchial airway cultures²⁷. In contrast to ciliated cells, alveolar cells are notoriously difficult to culture, thus limiting our understanding of COVID-19, but also of other respiratory virus infections. Currently, standardized methods use immortal cell lines or primary alveolar cells to study disease²⁸. Immortal cell lines, however, do not fully recapitulate the complexity of the alveolar space and epithelium. Primary alveolar cells partially capture this complexity but remain incapable of undergoing passaging and quickly lose their *in vivo* phenotype which restricts the model by the availability of donor material^{29,30}. Importantly, primary adult alveolar cultures were recently shown to be poorly permissive to SARS-CoV-2 infection, emphasizing the urgent need to develop a susceptible SARS-CoV-2 alveolar infection model^{26,31}. Some induced pluripotent stem cell-derived models have been able to show alveolar differentiation³²⁻³⁷, yet differentiation from primary lung cells has remained challenging.

Here, we describe a bronchioalveolar-like 2D air-liquid interface cell system by confocal-, electron-microscopy and mRNA expression analysis. In this model, alveolar

1

2

3

4

5

6

7

8

9

&

cells, but also basal cells, and rare neuroendocrine cells, are grown from 3D self-renewing lung bud tip progenitor organoids. In this system, SARS-CoV-2 replication competence, tropism and induced host responses were determined and compared to 2D differentiated small airway epithelium.

REPLICATION COMPETENCE AND TROPISM OF SARS-COV-2 IN 2D DIFFERENTIATED SMALL AIRWAY EPITHELIUM

Human bronchial airway epithelial (HAE) cell cultures are an established primary epithelial lung cell model to study respiratory virus infections. In these cultures, primary basal cells can be differentiated at air-liquid interface into mature airway cell types. It has already been shown that 3D self-renewing airway organoids can also be used as a source of basal cells in this culture system^{27,38,39}. We first established this system using small airway basal cells (**Supplementary figure S1A-C**) and demonstrated that SARS-CoV-2 readily infects human small airway organoid-derived epithelium cultured in 2D at air-liquid interface (ALI) (**Figure 1**). SARS-CoV-2 grew to relatively high titers on these cells, as shown by titration of VeroE6 cells (**Figure 1A-B**) and viral RNA quantification (**Supplementary figure S1D**). Shedding of virus occurred predominantly apically (**Supplementary figure S1E-F**). As we have previously shown for large airway (bronchial) cultures²⁷, ciliated cells were extensively targeted by SARS-CoV-2 (**Figure 1C**). In addition, we noted rare infection of CC10⁺ club cells (**Figure 1D**), but no infection of MUC5AC⁺ goblet cells (**Figure 1E**).

ESTABLISHMENT OF A 2D DIFFERENTIATED BRONCHIOALVEOLAR-LIKE MODEL

Another 3D lung organoid system was developed by Nikolic and colleagues in 2017⁴⁰, but this system has not yet been applied in virology. In this system, culture conditions were established to support long term self-renewal of multipotent SOX2⁺SOX9⁺ lung bud tip progenitor cells which *in vivo* differentiate into both airway and alveolar cells. We grew these lung bud tip organoids (LBT) from canalicular stage human fetal lungs 16-17 pcw (post-conception weeks). In expansion medium, which activates EGF, FGF and WNT signaling, and inhibits BMP and TGF β , the vast majority of cells were SOX2⁺SOX9⁺ (**Figure 2A**), but rare ATII-L were also detected in a subpopulation of organoids using the HTII-280 antibody which exclusively stains ATII cells in the human lung⁴¹ (**Figure 2B**). Organoid lines were maintained for >14 passages without apparent change in morphology, or SOX2 and SOX9 expression. Next, we established a model that contains alveolar-like cells, which could be accessed from the apical side for infection experiments. We plated SOX2⁺SOX9⁺ progenitor cells in Transwell inserts in differentiation medium. Based on recent literature, we reasoned that addition of human canalicular stage mesenchyme would provide cues for the survival of ATII-L cells and differentiation

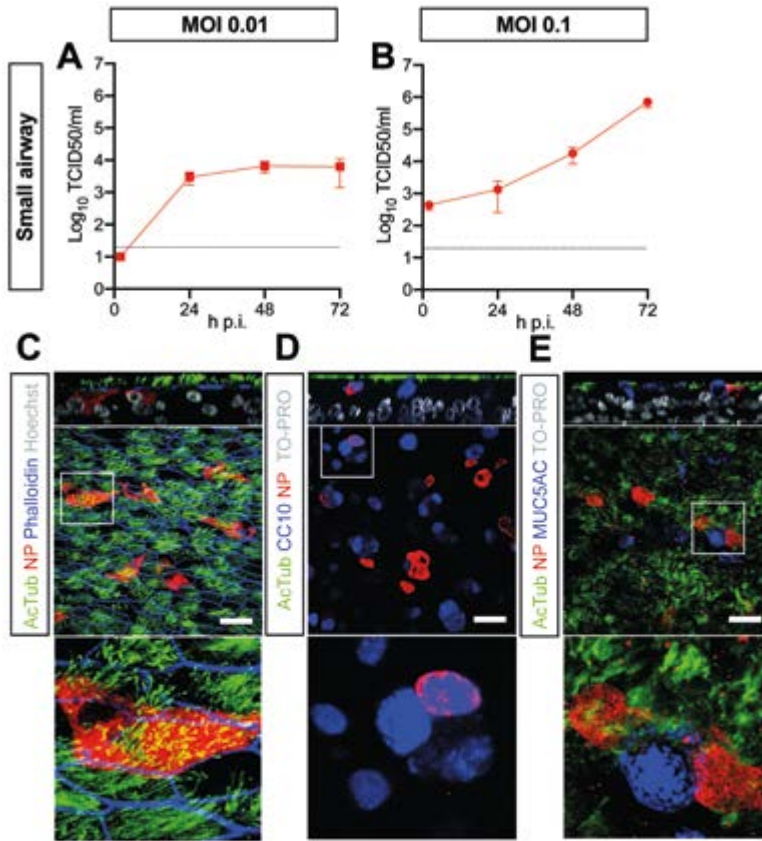


Figure 1. SARS-CoV-2 infects human organoid-derived 2D small airway cultures. A, B) Infectious virus titers can be observed by virus titrations on VeroE6 cells of apical washes at 2, 24, 48, and 72h after infection at MOI 0.01 (A) or 0.1 (B) with SARS-CoV-2 (red). The dotted line indicates the lower limit of detection. Error bars represent SEM. N=4. H p.i. = hours post infection. C-E) Immunofluorescent staining of SARS-CoV-2 infected differentiated small airway cultures. Nucleoprotein (NP) stains viral capsid (red), which colocalized with the ciliated cell marker AcTUB (green; (C, D, E) and club cell marker CC10 (blue; (D)). Phalloidin was included to stain actin (blue; (C)). Goblet cells are identified by MUC5AC (blue; (E)). Scale bars indicate 50 μ m.

towards an alveolar fate^{40,42-44}. After reaching confluency, cells were differentiated for at least 14 days at ALI (**Figure 2C**). The addition of canalicular stage mesenchymal cells in the bottom compartment of the Transwell increased the frequency of HTII-280+ cells (**Supplementary figure S2A-B**). After 14 days of differentiation at ALI, cultures consisted of both multi-layered and single-layered squamous epithelium. The areas with a single layer of mostly thin epithelium contained cells expressing the ATI markers HOPX (**Figure 2D**) and HTI-56 (**Figure 2E**), as well as the mature ATII marker HTII-280 (**Figure 2F**) and LPCAT1 (**Figure 2G**)^{41,45,46}. SFTPC+ cells were present in the single layered epithelium and the top layer of the multilayered areas (**Figure 2H**). The multilayered areas contained TP63+ basal

1
2
3
4
5
6
7
8
9
&

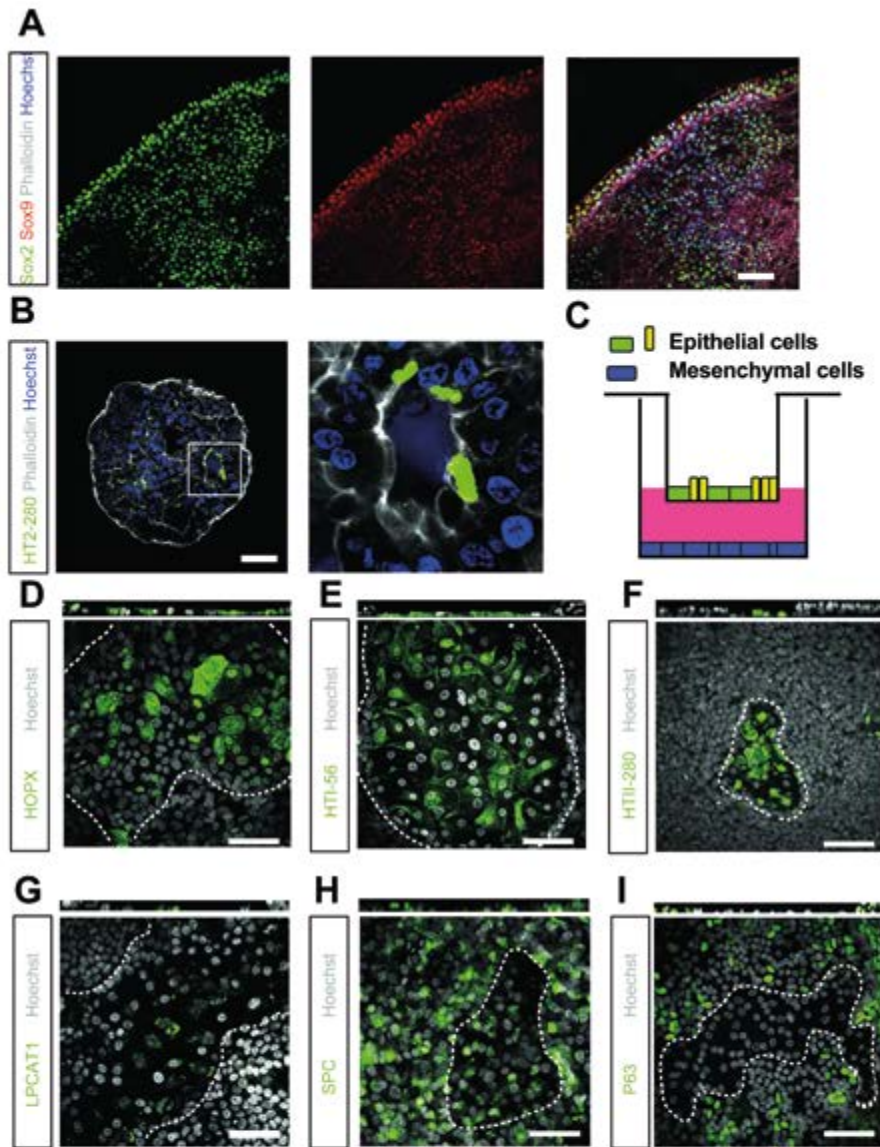


Figure 2. Self-renewing human fetal lung bud tip progenitor organoids differentiate at air-liquid interface to alveolar type I- and II-like cells. A) Immunofluorescent staining of fetal lung bud tip progenitor organoids in expansion medium coexpressing stem cell markers Sox2 (green) and Sox9 (red). Phalloidin (white) was used to stain actin. B) Immunofluorescent staining of rare HTII-280+ type II pneumocytes (green) in a subpopulation of fetal lung bud tip progenitor organoids grown in expansion medium. C) Schematic of the 2D air-liquid interface bronchioalveolar-like model. D-I) Differentiated lung bud tip organoids at air-liquid interface in co-culture with donor-specific human fetal lung fibroblasts. After 14 days of differentiation at air-liquid interface, cells express alveolar type I (HOPX, green, (D); HTI-56, green, (E)), type II cells (HTII-280, green, (F); LPCAT1, green, (G); SFTPC (SPC), green, (H)) and basal cell (TP63 (P63), green, (I)) markers in areas containing one cell layer. Dotted lines indicate the barrier between multilayered and single layered epithelium. Data information: Nuclei are stained with Hoechst (blue in (A, B) or white in (D-I)). Scale bars indicate 50µm.

cells as a bottom layer (**Figure 2I**). Canalicular stage mesenchyme from different donors resulted in similar expression of alveolar markers (**Figure EV1A-H**), whereas some variation was observed in basal cell proliferation (**Figure EV1I-J**). Using mass spectrometry on apical washes we also detected secreted surfactant proteins SFTPA1, SFTPA2, SFTPB

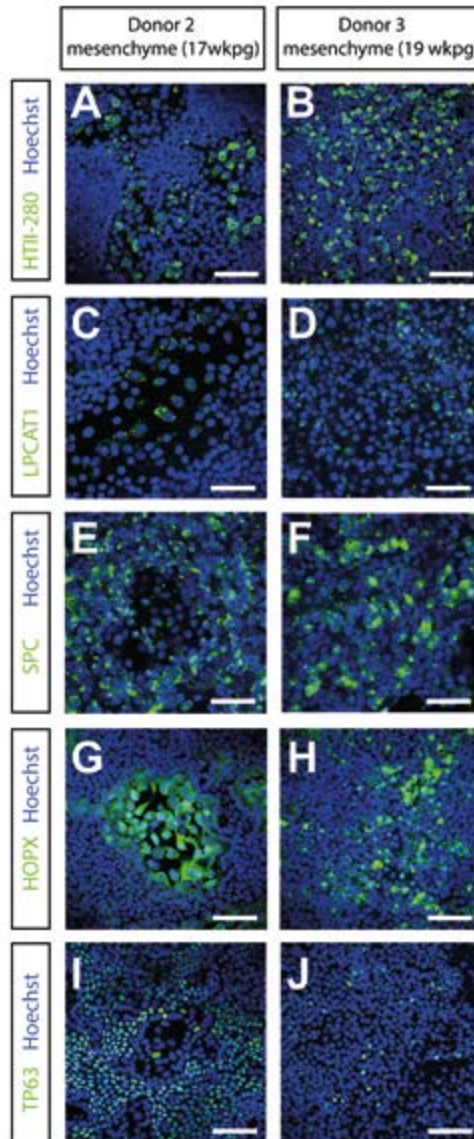


Figure EV1. A comparison of different mesenchymal donors on 2D bronchioalveolar-like differentiation. (A-J) Immunofluorescent staining of HTII-280 (A, B), LPCAT1 (C, D), SPC (E, F), HOPX (G H) and TP63 (I J) after two weeks of differentiation at air-liquid interface in the presence of mesenchyme in the basal compartment of the Transwell. Nuclei are stained with Hoechts (blue). Scale bars represent 50 μ m.

1
2
3
4
5
6
7
8
9
&

and SFTPD (**Supplementary figure S3**). mRNA expression analysis of 3D LBT, confluent 2D cultures before (2D non ALI) and after (2D ALI) exposure to air indicated that lung bud tip progenitor markers SOX9 and SOX2 were decreased during differentiation (**Figure EV2A-B**) while alveolar cell markers SFTPA2, SFTPB and HOPX gradually increased during differentiation (**Figure EV2C-E**). A general increase in ATI- and ATII-related genes from 3D LBT to 2D ALI cells was observed with intermediate levels at 2D non-ALI (**Figure EV2F, Table EV1-2**). The composition of cells in 2D ALI cultures was different from small airway ALI cultures, as indicated in differential expression analysis (**Figure 3A**,

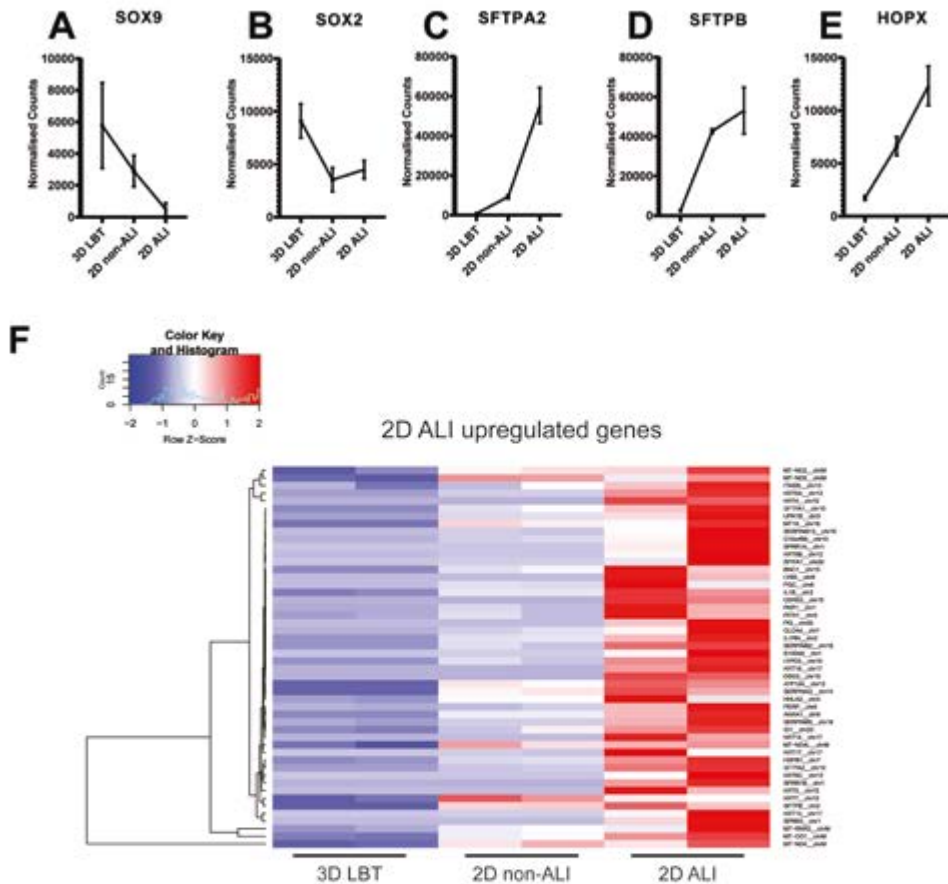


Figure EV2. Transcriptomic analysis of differentiation towards bronchioalveolar-like cells from lung bud tip organoids. A-E) Line graphs indicating normalised read count of 3D lung bud tip organoids (3D LBT), airway organoids on transwell system with apical medium (2D non-ALI) and 2D bronchioalveolar-like air-liquid cultures (2D ALI). n=2 and error bars represent stdev. (A, B) Graphs depicting fetal bud tip progenitor markers SOX9 and SOX2. (C, D) Graphs depicting ATII markers SFTPA2 and SFTPB. (E) Graphs depicting ATI marker HOPX. F) Heatmaps depicting top 50 enriched genes in 2D bronchioalveolar-like air-liquid cultures (2D ALI) compared to 3D lung bud tip organoids (3D LBT). N=2 of 3D LBT, airway organoids on transwell system with apical medium (2D non-ALI) and 2D ALI. Colored bars represent Z-scores of log₂ transformed values.

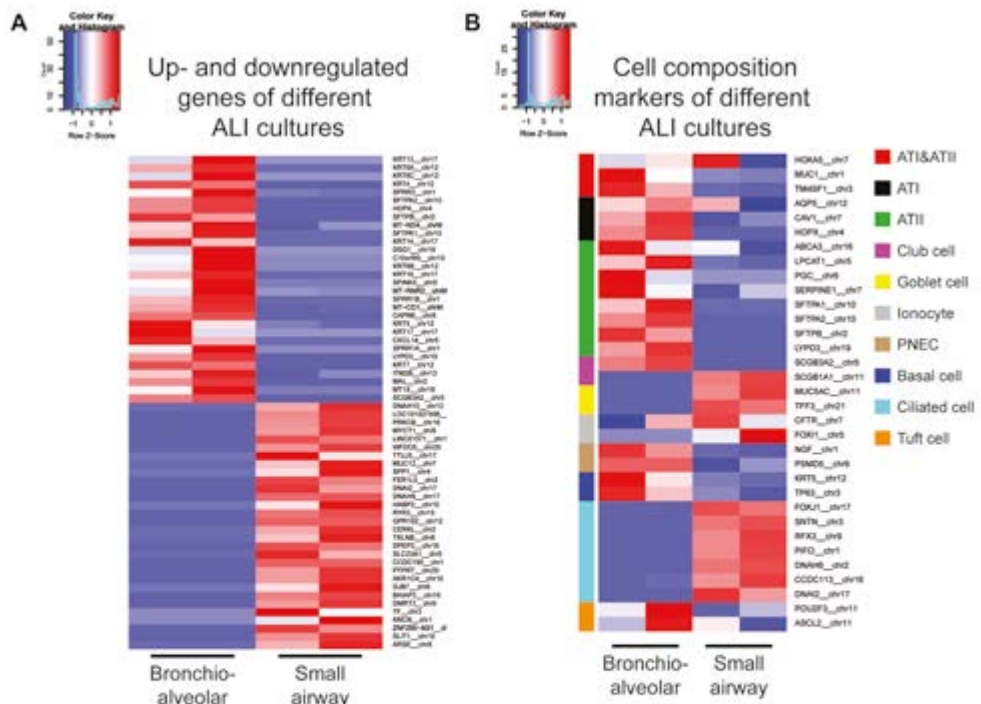


Figure 3. Transcriptomic analysis of bronchioalveolar-like and small airway air-liquid interface cultures. A) Heatmaps depicting top 30 up- and downregulated genes in 2D bronchioalveolar-like air-liquid cultures (Bronchioalveolar) compared to small airway air-liquid interface cultures (Small airway). Colored bars represent Z-scores of log2 transformed values. B) Heatmaps depicting pulmonary cell type marker genes in 2D bronchioalveolar-like air-liquid cultures (Bronchioalveolar) and small airway air-liquid interface cultures (Small airway). Color coded bars indicate which cell type is marked by the presented gene. Colored bars represent Z-scores of log2 transformed values.

Table EV3. While small airway ALI cultures were mainly expressing ciliated cell markers like DNAH10 (**Figure 3A**), FOXJ1 and SNTN (**Figure 3B**), alveolar like ALI-cultures were enriched in ATI&II makers like HOPX and SFTPA1 (**Figure 3**). Moreover, 2D ALI cultures were enriched in markers for pulmonary neuroendocrine, tuft and basal cells, while small airway cultures were enriched in goblet and ciliated cell markers (**Figure 3B**). All together, these data indicate that the 2D ALI cultures contain both alveolar-like as well as bronchiolar-like cells. These cultures could therefore be characterized as bronchioalveolar-like by confocal microscopy and mRNA expression analysis. The presence of pulmonary neuroendocrine cells (PNEC) was confirmed by confocal imaging (**Supplementary figure S6B**). The club and ATII cell marker SCGB3A2 was also detected in both single and multilayered areas (**Supplementary figure S6C**).

To further investigate the diversity and frequency of the cell types in the bronchioalveolar system we performed single-cell mRNA sequencing (**Figure 4**). This revealed a large alveolar-like cluster (94,3% of cells), a smaller basal cell cluster (4,9% of

1
2
3
4
5
6
7
8
9
&

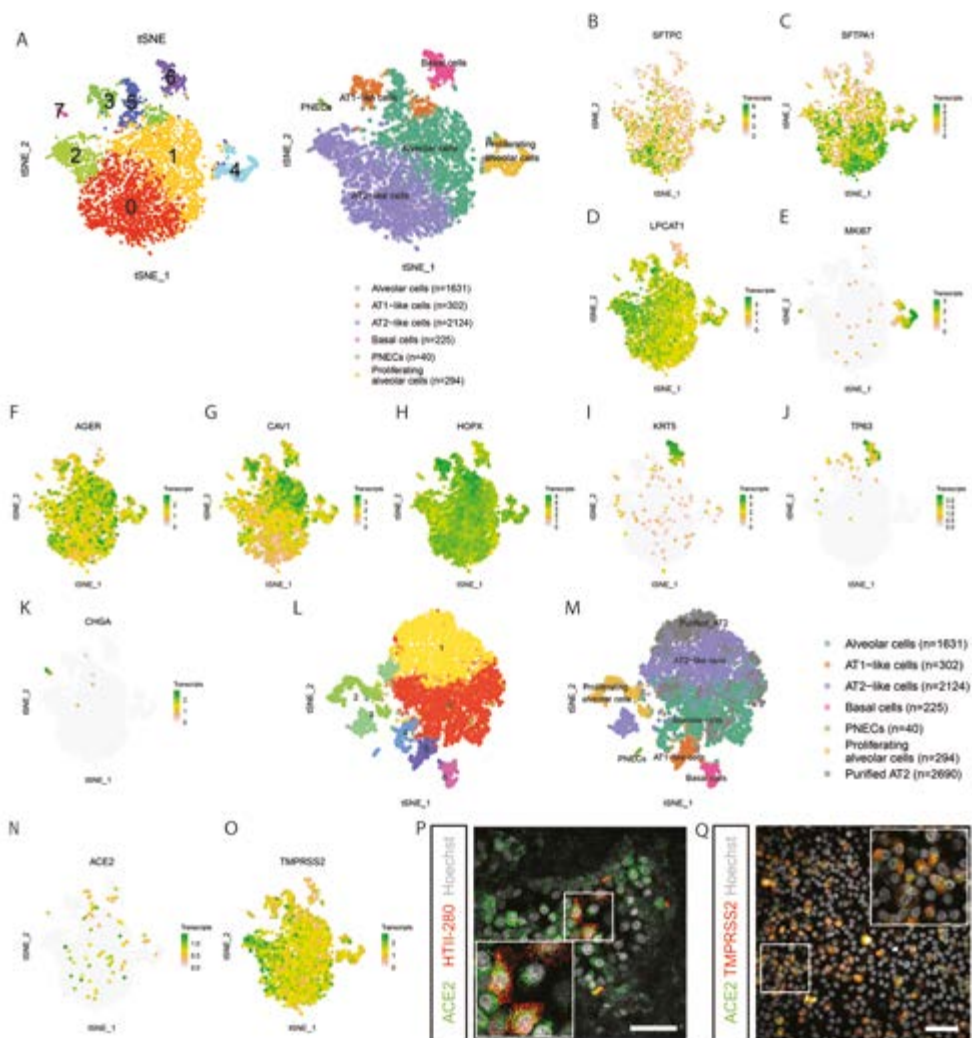


Figure 4. Single cell analysis of bronchioalveolar cultures. A) t-SNE maps showing clustering based on differentially expression analysis and highlighting cell type identification of bronchioalveolar cultures based on cell makers. Each color represents a cluster or different cell type. Number indicates number of cells in cluster identified as cell type presented. B-K) t-SNE maps highlighting the expression of marker genes for each of the cell types. Transcript counts are given in a Log2 scale. L) t-SNE map showing clustering based on differentially expression analysis including dataset from A) and published dataset of GSM2855485. Each color represents a single cluster. M) t-SNE map showing clustering of L) with annotation of cell types. Cell type annotation are transferred from A) and published dataset GSM2855485 is annotated as "Purified AT2". Number indicates number of cells in cluster identified as cell type presented. N, O) t-SNE maps highlighting the expression of SARS-CoV-2 entry receptors ACE2 (N) and TMPRSS2 (O). Transcript counts are given in a Log2 scale. P) Differentiated bronchioalveolar cultures express SARS-CoV-2 entry receptor ACE2 (green) on ATII-like cells marked by HTII-280 (red). Scale bar indicates 50µm. Q) Bronchioalveolar cultures co-express both entry receptors ACE2 (green) and TMPRSS2 (red). Scale bar indicates 50µm.

cells), and a rare population of PNECs (0,9% of cells) (**Figure 4A**). The alveolar cluster contained ATII-like cells (46,0% of cells, clusters 0 and 2) (**Figure 4B-D**; SFTPC, SFTPA1, LPCAT1; **Supplementary figure S4A**), proliferating ATII-like cells (6,4% of alveolar cells, cluster 4) (**Figure 4E**), and alveolar cells that showed an increased expression of several ATI markers (6,5% of alveolar-like cells, cluster 3) (**Figure 4 F-H**; AGER, CAV1, HOPX; **Supplementary figure S4B**). The basal cell cluster (cluster 5) was characterized by KRT5 and TP63 expression (**Figure 4I-J**; **Supplementary figure S4C**). A rare PNEC population (cluster 7) expressed CHGA (**Figure 4K**; **Supplementary figure S4D**). To investigate whether the cultured cells were representative of adult alveolar cells, we compared our

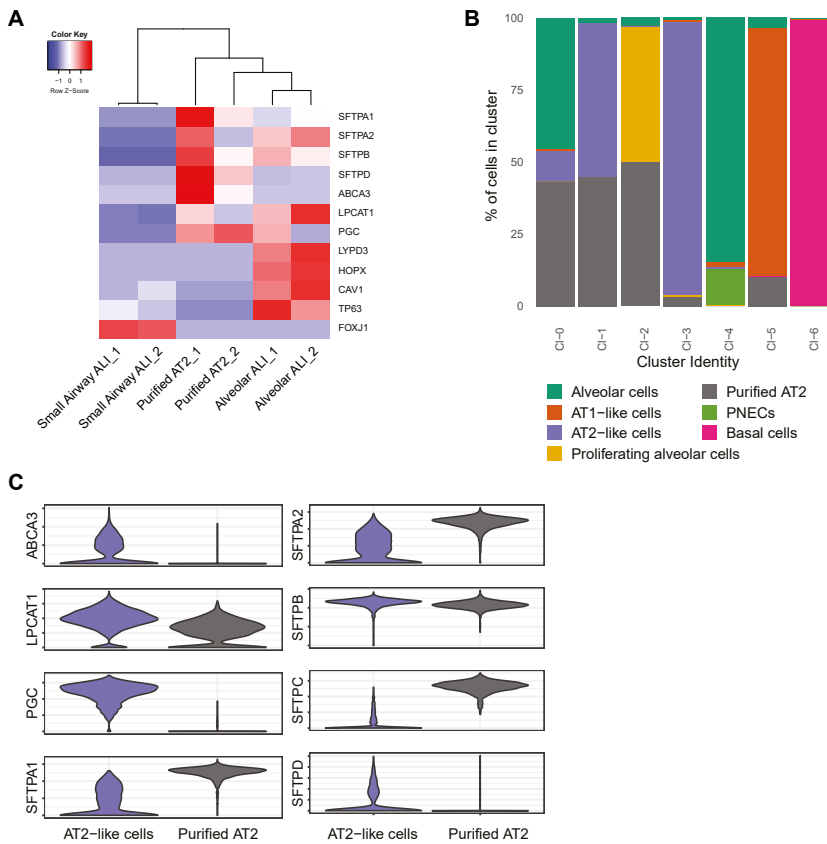


Figure EV3. Comparison of bronchioalveolar culture to published datasets of AT2 cells. A) Heatmaps depicting marker genes in 2D small airway air-liquid cultures (Small Airway ALI), bronchioalveolar-like air-liquid cultures (Alveolar ALI) and published dataset of purified AT2 cells (Purified AT2). Colored bars represent Z-scores of log2 transformed values. B) Barplot indicating percentage of annotated cells within a cluster. Color represent annotated cell identity. Combined current dataset and of GSM2855485 are presented. Indicated annotation is based on separate clustering. Published dataset GSM2855485 is annotated as "Purified AT2". C) Violin plots visualizing expression levels of marker genes for AT2 cells. AT2-like cells comprise cells annotated as AT2-like cells in current dataset (cluster 0 and 2). Purified AT2 cells are from published dataset GSM2855485.

1
2
3
4
5
6
7
8
9
&

bulk RNA sequencing and single cell RNA sequencing dataset to previously published bulk (Figure EV3A) and single cell sequencing datasets (Figure 4L-M; Figure EV3B-C) of freshly isolated adult ATII cells of freshly isolated HTII-280+ ATII cells. The freshly isolated adult ATII cells did not form a separate cluster in the tSNE map (Figure 4L-M), and overlapped with cultured alveolar, proliferating alveolar and ATII-like cells (Figure 4M; Figure EV3B). The expression of a set of ATII marker genes was also compared between the cultured ATII-like cluster and the freshly purified ATII cells (Figure EV3C). The SARS-CoV-2 entry receptor ACE2 was detected at low levels in the alveolar cluster (Figure 4N, Supplementary figure S5A), and ACE2 expression in ATII-like cells was confirmed by immunofluorescent imaging (Figure 4P). The activating protease TMPRSS2 was detected in all clusters with a higher expression in ATII-like cells (Figure 4O).

In addition, there was a slight trend towards a correlation between ACE2 and TMPRSS2 expression (Supplementary figure S5A-D). At the protein level, both ACE2 and TMPRSS2 were readily detected and often coexpressed (Figure 4Q). Other TMPRSS-family members were detected in lower levels (Supplementary figure S5E-H). These data show that the bronchioalveolar model consists mainly of ATII-like cells and potentially is susceptible to SARS-CoV-2 infection.

REPLICATION COMPETENCE AND TROPISM OF SARS-COV-2 IN 2D DIFFERENTIATED BRONCHIOALVEOLAR-LIKE CULTURES

In order to also assess the replication competence and tropism of SARS-CoV-2 in bronchioalveolar-like cells, we infected these cultures with SARS-CoV-2. SARS-CoV-2 readily infected the cells at a low multiplicity of infection (MOI) of 0.01 and reached slightly higher titers at a MOI of 0.1, as shown by titration of VeroE6 cells (Figure 5 A-B) and viral RNA quantification (Figure EV4A-B). Shedding of virus occurred predominantly apically (Figure EV4C-D). In these cultures, we observed infection of alveolar cells (Figure 5C-E) as evidenced by staining against HOPX, HTII-280 and SFTPC. Most infected cells appeared to be SFTPC+ (Figure 5E). Using a marker for dividing cells (Ki67), we showed that infected cells were not dividing (Supplementary figure S6C). We did not detect infected PNEC in the top compartment, nor infected mesenchymal cells in the basal compartment.

TRANSMISSION ELECTRON MICROSCOPY ANALYSIS OF SARS-COV-2 INFECTED BRONCHIOALVEOLAR-LIKE CELLS AND SMALL AIRWAY EPITHELIAL CELLS

Next, we performed transmission electron microscopy (TEM) to confirm SARS-CoV-2 infection inside the 2D bronchioalveolar-like (Figure EV4A-F) and 2D small airway (Figure EV5G-K) cultures at high magnification. Upon inspection of the 2D bronchioalveolar-

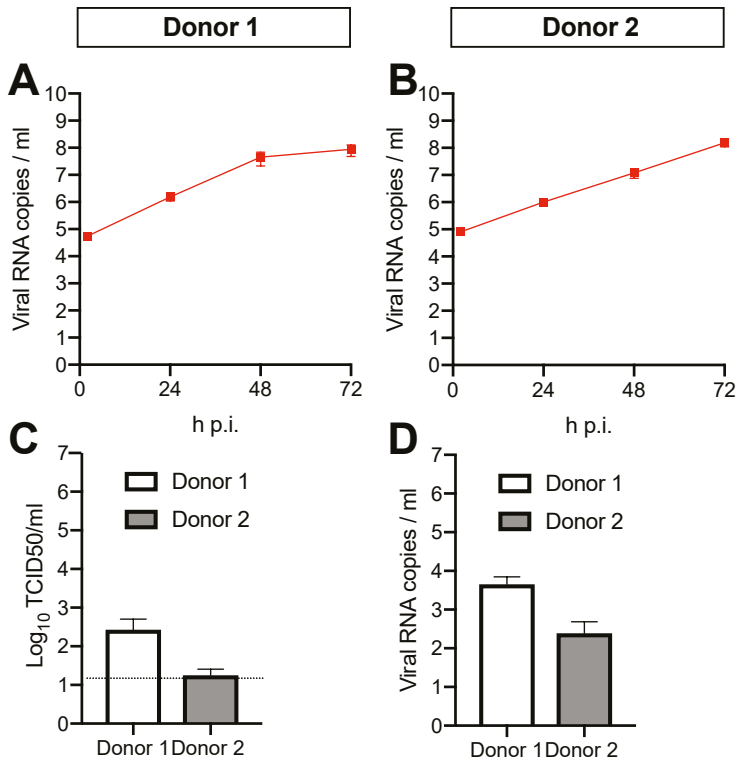


Figure EV4. Apical viral RNA and basal shedding in differentiated 2D bronchioalveolar-like cultures. A, B) Viral SARS-CoV-2 RNA titers of apical washes at 2, 24, 48, and 72h after infection at MOI 0.1 for donor 1 (A) and donor 2 (B). C, D) Infectious virus titers as observed by virus titrations on VeroE6 cells (C) and qRT-PCR (D) in basal compartments. The dotted line indicates the lower limit of detection. Data information: Error bars represent SEM. N=4 for donor 1 and N=3 for donor 2. H p.i. = hours post infection.

like culture, ATII-L were readily classified (**Figure EV5A-B**) based on the presence of lamellar bodies (**Figure EV5D**). SARS-CoV-2 infection was found in ATII-L cells (**Figure EV5C-D**) and showed the early infection onset with few double membrane vesicles and both electron dense- (**Figure EV5D**) and lucent (**Figure EV5C**) compartments harboring virus particles. Interestingly, next to the ATII-L cell, a fragmented dead cell is visible (**Figure EV5F**) with many extracellular virus particles still attached to the apical side and only few particles present on the basal side. This suggests that virus shedding mainly occurs on the air-faced side inside lung tissue. Nonetheless, also in between the ATII-L cells and an adjacent cell, some virus particles were detected, although it is not clear whether these sites are also the place of virion secretion or whether virions can diffuse between the cell layers. The latter is implausible due to the lack of detectable infectious virus in the basal compartment of the culture. Similarly, also the 2D small airway cultures (**Figure EV5G-K**) were examined with TEM and contained a confluent layer consisting mainly of ciliated cells

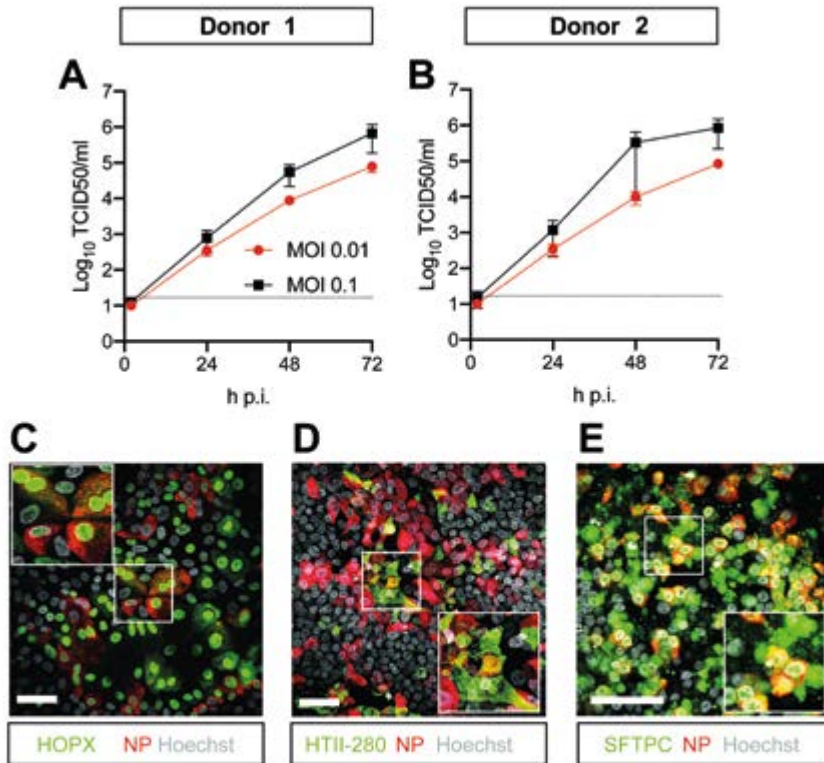


Figure 5. SARS-CoV-2 infects human organoid-derived 2D bronchioalveolar-like cultures. A, B) Infectious virus titers can be observed by virus titrations on VeroE6 cells of apical washes at 2, 24, 48, and 72h after infection of bronchioalveolar-like cells from donor 1 (A) and donor 2 (B) at MOI 0.01 (red) or 0.1 (black) with SARS-CoV-2. The dotted line indicates the lower limit of detection. Error bars represent SEM. N=4 for all except donor 2 MOI 0.1, which is N=3. H p.i. = hours post infection. C-E) Immunofluorescent staining of SARS-CoV-2 infected differentiated bronchioalveolar-like cultures. Nucleoprotein (NP) stains viral capsid (red), which colocalized with HOPX (C), HTII- 280 (D) and SFTPC (E). Scale bars indicate 50 μ m.

(**Figure EV5H-J**) along with club cells and goblet cells (**Figure EV5K**). In accordance with confocal microscopy findings, at 72 hours post infection, morphological evidence of SARS-CoV-2 infection, replication and assembly was found inside ciliated cells (**Figure EV5I**). Secreted virions were again found at the apical side next to the still intact cilia (**Figure EV5J**), whereas no viruses were found at the basal side. Using confocal microscopy, we also detected rare infection of club cells (**Figure 1D**), but these rare events could not be visualized by TEM thus far.

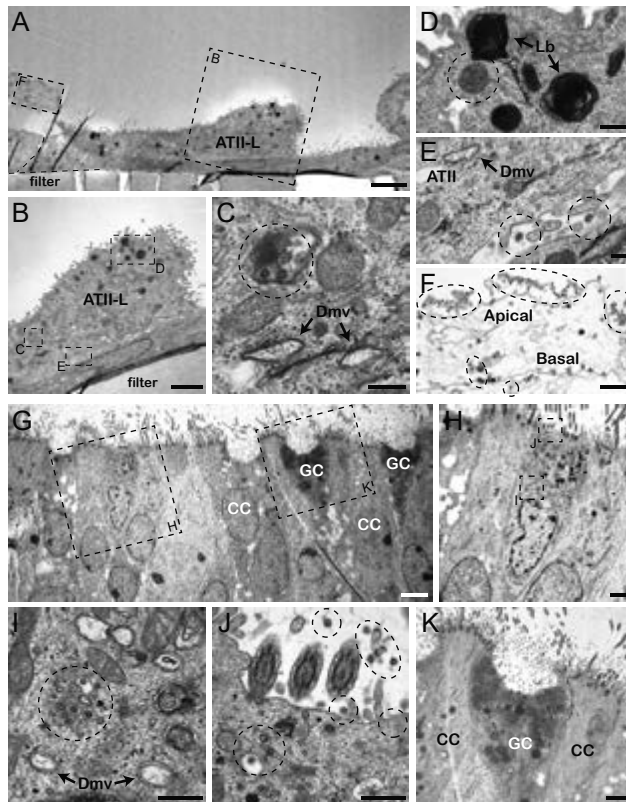


Figure EV5. Transmission electron microscopy analysis of 2D bronchioalveolar-like (A-F) and 2D small airway (G-K) cultures after 72h of SARS-CoV-2 infection. A-F Pulmonary alveolar type II-like (ATII-L) cells were found in the 2D bronchioalveolar-like culture (A,B). The early infection of the ATII-L cell (C) is recognizable by the double-membranes vesicles (Dmv) and virus particles (circles). (D) Next to the Lamellar bodies (Lb), the ATII-L also contained a lysosomal compartment with internal virus particles (circle). Extracellular virus particles were found in the intercellular space between the ATII-L and ATII-L cells (E), albeit at low concentration. Dashed circles indicate viral particles outside of the cell. The remnants of a dead detached cell (F) mainly showed apical shed virus particles (in areas marked by dotted lines), whereas the basal side was relatively free of virus particles. G-K Ciliated cells (CC; (H)) and Goblet cells (GC; (K)) are visible in the cross-section through the 2D small airway culture after 8 weeks of differentiation. SARS-CoV-2 replication (I) and virus shedding (J) was found to be associated particularly with ciliated cells, whereas no infections were found in Goblet cells (K). Dashed circles indicate viral particles inside and outside the cell. Data information: Scale bars represent 5 μm (A,G), 2.5 μm (B,H,K), 1 μm (F), 500 nm (D,I,J) and 250 nm (C,E).

HOST RESPONSES INDUCED BY SARS-COV-2 IN BRONCHIOALVEOLAR-LIKE CELLS AND SMALL AIRWAY EPITHELIAL CELLS

To investigate the cellular response to infection, we stained bronchioalveolar-like and small airway cultures for phosphorylated STAT1 (pSTAT1) at 72 hours post infection.

1

2

3

4

5

6

7

8

9

&

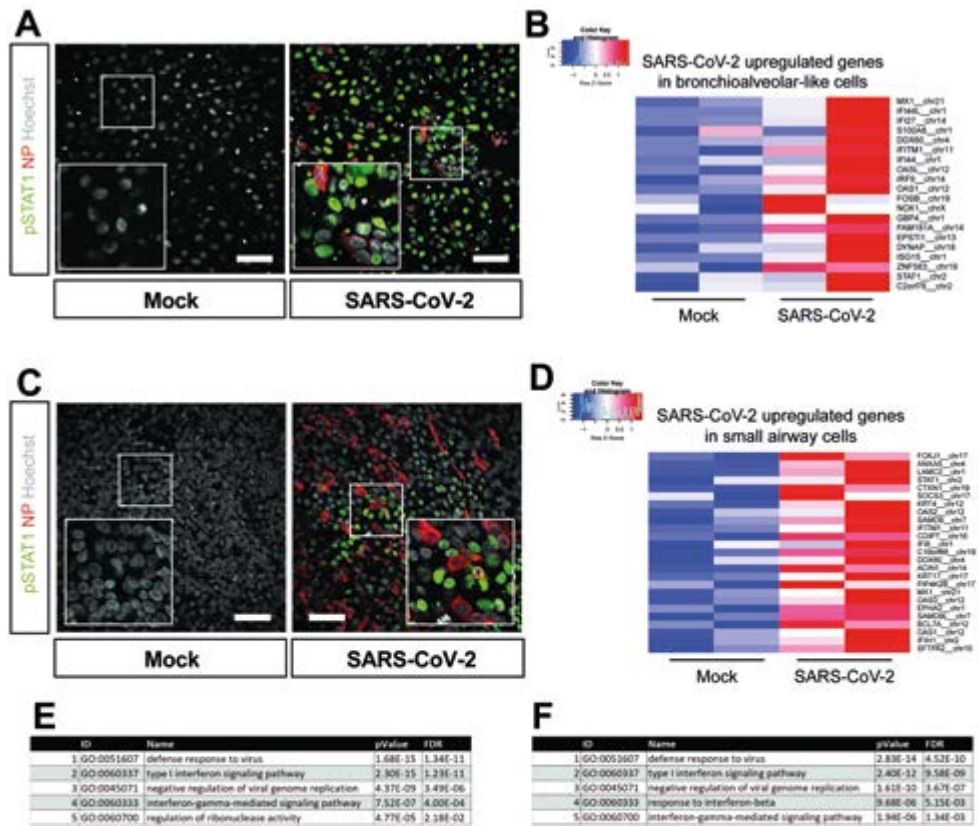


Figure 6. Host response analysis of SARS-CoV-2 infection in organoid-derived bronchioalveolar-like and small airway cells. A) pSTAT1 translocation in mock and SARS-CoV-2-infected bronchioalveolar-like cells visualized in green. Scale bars indicate 50 μ m. Nucleoprotein (NP) stains viral capsid (red). Nuclei are stained with Hoechst (white). B) Heatmaps depicting top 20 enriched genes based on adjusted pvalue in bronchioalveolar-like cells after SARS-CoV-2 infection. Colored bars represent Z-scores of log2 transformed values. C) pSTAT1 translocation in mock and SARS-CoV-2-infected small airway cells visualized in green. Nucleoprotein (NP) stains viral capsid (red). Nuclei are stained with Hoechst (white). Scale bars indicate 50 μ m. D) Heatmaps depicting top 25 enriched genes based on adjusted pvalue and log2 fold changes in small airway cells after SARS-CoV-2 infection. Colored bars represent Z-scores of log2 transformed values. E) GO term enrichment analysis for biological processes of the 20 most significantly up-regulated genes upon SARS-CoV-2 infected in bronchioalveolar-like cells. P-values were determined using PANTHER Overrepresentation Test. F) GO term enrichment analysis for biological processes of the 25 most significantly up-regulated genes upon SARS-CoV-2 infected in small airway cells. P-values were determined using PANTHER Overrepresentation Test.

STAT1 is phosphorylated in response to interferon (IFN) receptor signaling, which promotes translocation of STAT1 to the nucleus where it stimulates the expression of interferon stimulated genes (ISG). We observed STAT1 phosphorylation and nuclear translocation in bystander cells of SARS-CoV-2 infected cultures in both bronchioalveolar-

like (**Figure 6A**) and small airway (**Figure 6C**) cultures, but not in infected cells, indicating potentially active blocking of the JAK/STAT pathway in infected cells. Active blocking of STAT1 nuclear import has been reported for SARS-CoV. SARS-CoV ORF6 antagonizes STAT1 function by sequestering nuclear import factors on the rough endoplasmic reticulum/Golgi membrane^{47,48}. Whether SARS-CoV-2 ORF6 has similar functions remains to be investigated, but recently the SARS-CoV-2 N protein was shown to suppress the translocation of STAT1 and STAT2⁴⁹.

Next, we performed mRNA sequencing analysis to determine gene expression changes induced by SARS-CoV-2-infection of bronchioalveolar-like cultures. As suggested by pSTAT1 translocation, infection with SARS-CoV-2 elicited a broad signature of interferon-stimulated genes (ISGs) attributed to type I/III interferon responses (**Figure 6B,D**), which was confirmed by Gene Ontology analysis (**Figure 6E-F**) in both bronchioalveolar-like (**Figure 6B,E, Table EV4**) and small airway cultures (**Figure 6D,F, Table EV5**). This induction was similar to earlier reported SARS-CoV-2 infection in human bronchial epithelial cells⁵⁰ and indicated induction of strong chemotactic and inflammatory responses. Generally, the responses to SARS-CoV-2 appeared similar between the two pulmonary systems.

To test the suitability of the bronchioalveolar model for SARS-CoV-2 drug screens, we analysed the effect of IFN- λ 1 on viral replication. For this experiment, cultures were treated with IFN- λ 1 (50 ng/ml) two hours prior to infection at an MOI of 0.1, or 24 hours after infection. In the untreated control, SARS-CoV-2 replicated to high titers, approaching 10⁶ TCID50 or 10⁸ viral copies per ml (**Figure 7A-B**). Pre-treatment with IFN- λ 1 abrogated viral replication entirely and treatment at 24 hours post infection reduced infectious virus and RNA copies by ~5 logs and ~3 logs, respectively. These differences were also apparent by confocal imaging at 72 hours post infection (**Figure 7C**). This bronchioalveolar culture system can therefore be applied to test COVID-19 therapeutics.

DISCUSSION

In COVID-19 patients, alveolar injury can trigger a cascade of events that leads to ARDS, limiting the transport of oxygen into the blood. A plethora of models are currently being developed to study this. In vivo models can be very useful, but are often extremely difficult and expensive to establish and may not represent conditions in humans. Most in vitro models utilize cell lines or primary cells that are often limited by the availability of donor materials and show donor-donor variation. In addition, primary human alveolar cultures are poorly susceptible to SARS-CoV-2 infection^{26,31}. Self-renewing organoid models that contain stem cells which can differentiate into relevant cell types offer an elegant solution to develop human models that can be standardized. While a robust self-renewing organoid model exists for the airway epithelium, the alveolar epithelium has proven very difficult to establish. As the alveolar epithelium is thought to play a major role in the disease progression of COVID-19, the lack of an in vitro model greatly limits our understanding of this disease, but also of other respiratory virus infections.

1
2
3
4
5
6
7
8
9
&

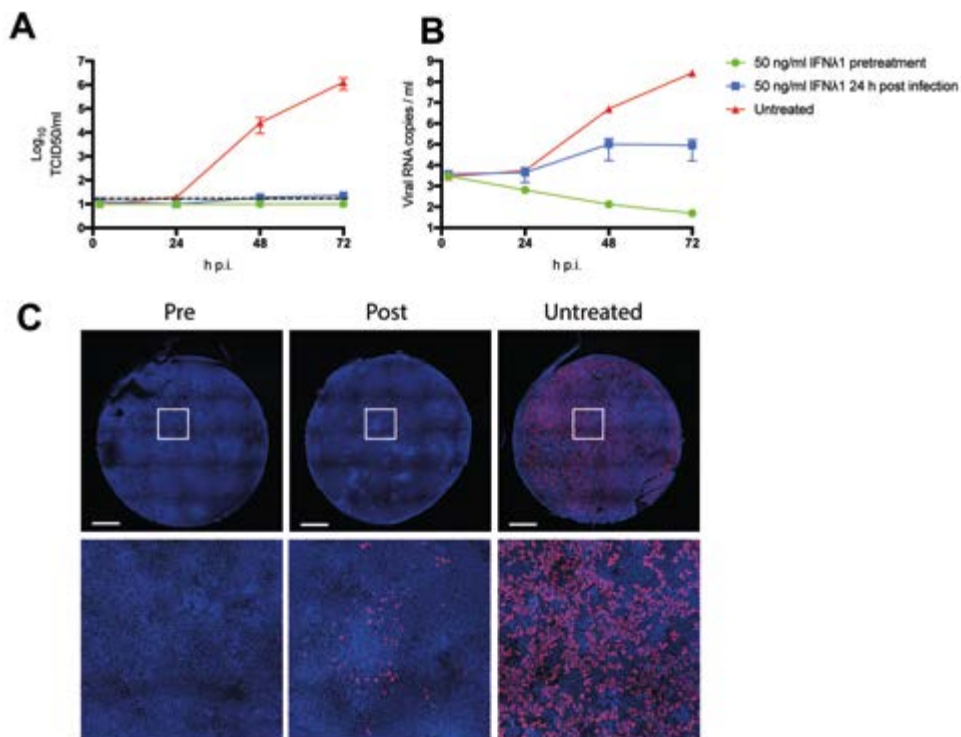


Figure 7. Low dose interferon lambda 1 treatment dramatically reduces SARS-CoV-2 replication in bronchioalveolar-like cultures. (A, B) SARS-CoV-2 replication shown as infectious virus titers (A) and viral RNA copies (B) in apical washes at 2, 24, 48, and 72h after infection at MOI 0.1. Cultures were either pretreated with 50 ng/ml IFN lambda 1 in the basal compartment two hours prior to the infection (green), at 24 h p.i. or left untreated. The dotted line indicates the lower limit of detection. Error bars represent SEM. N=2. H p.i. = hours post infection. C) Whole well immunofluorescent staining of representative cultures in (A) and (B) using an anti-NP antibody (red). Nuclei are stained with Hoechst (blue). Scale bar indicates 1mm.

This study shows that SARS-CoV-2 efficiently replicates in a human bronchioalveolar-like model, targeting ATII-L cells. This study is in accordance with clinical findings that SARS-CoV-2 infects alveolar cells in COVID-19 patients. However, the variable incidence and severity of lower lung disease, and recent findings that alveolar cells have low levels of ACE2 expression in health, indicates that alveolar cells are unlikely to be the first cells infected through microaerosol inhalation of virus particles²⁶. Ciliated cells in the airways seem to express ACE2 more constitutively, with increasing expression towards the proximal part of the airway^{24,26}. Using an organoid-derived small airway model we show that ciliated cells are indeed the main target cell in the small airways, as was observed recently for primary small airway cells²⁶. Therefore, ciliated cells could be infected prior to the alveoli, with inflammatory or antiviral signals possibly leading to increased ACE2 expression as this gene was recently shown to be induced by interferon⁵¹.

Treatment of the bronchioalveolar cultures with a low dose of interferon lambda 1 was highly effective in reducing viral replication and dissemination, underscoring the high interferon sensitivity of this virus and indicating that interferons are a viable treatment option. Organoid-derived alveolar-like and airway models are ideal models to study these aspects of COVID-19.

This model has several limitations. In human fetal development alveolar cells are derived from bipotent progenitor cells whereas in adults ATI cells are derived from a rare self-renewing population of ATII cells^{40,43}. In adult mice an additional cell type, the bronchioalveolar stem cell (BASC)⁵², differentiates into both bronchiolar and alveolar cells, but in adult humans such bipotent progenitors have not been identified yet. Fetal and adult alveolar cells may therefore be phenotypically distinct, and may respond differentially to infections. In addition, mesenchymal cells improved alveolar development in 2D and future work should focus on identifying which mesenchymal cues drive this. On the other hand, the presence of mesenchymal cells could offer an interesting opportunity to study differential expression of genes involved in lung fibrosis as well in these cells.

This model also has several advantages. The bronchioalveolar-like model presented here shows a robust increase in infectious virus titers over time of ~5 logs, whereas other recently developed adult-derived 3D alveolar organoid models show a more limited increase in viral titers (~1-2 logs)⁵³⁻⁵⁵. This allows for a larger window to observe antiviral effects of potential drugs. In addition, in our model pulmonary epithelial cells are infected from and shed virus apically while, in most 3D organoid models the apical side of the cells is facing the inside of the organoid. In the bronchioalveolar-like model presented here, the apical side of the cells is exposed to the air, which makes it is easily accessible, physiologically relevant and highly suitable for (high-throughput) virology studies. Similar results may be obtained with the recently developed iPSC-derived 2D ATII-like cultures⁵⁶. In addition, the modular Transwell setup allows the addition other cell types. For example, endothelial cells would be of interest, as the lungs of deceased COVID-19 patients were recently found to show distinctive vascular features, including endothelialitis, widespread thrombosis with microangiopathy, and angiogenesis¹⁴. In addition, immune cells could be added, which may be relevant as severe COVID-19 symptoms and hospitalization often occur ~8-15 days after disease onset⁵⁷ indicating that acute lung injury may be the result of an overreaction of the immune system, rather than a direct effect of virus replication. As this model is derived from self-renewing organoids, it is also amenable to genetic manipulation using CRISPR/Cas systems, which allows the study of specific host factors. Intrinsically, the model is also suitable for pulmonary cell- and developmental biology studies, especially for studies on the interaction between epithelial and mesenchymal cells without the need for physical interaction.

In conclusion, bronchioalveolar-like cells derived from self-renewing human fetal lung organoids give rise to a 2D human bronchioalveolar-like model with air-exposed apical side. In these cultures, alveolar type II-like cells are permissive to SARS-CoV-2 infection,

1

2

3

4

5

6

7

8

9

&

which induces a type-I/III interferon host response *in vitro*. SARS-CoV-2 replication is abrogated by low dose interferon lamda 1 treatment, showing that this model system can be used for COVID-19 drug screens.

DATA ACCESSIBILITY

Bulk RNA and 10x single cell RNA sequencing data are deposited at Gene Expression Omnibus under GSE153218 and GSE161934, respectively.

ACKNOWLEDGMENTS

We thank A de Graaff and Hubrecht Imaging Centre (HIC) for microscopy assistance and Single Cell Discoveries for single-cell sequencing and mRNA library preparation, and the Utrecht Sequencing Facility (subsidized by the University Medical Center Utrecht, Hubrecht Institute, Utrecht University and NWO project 184.034.019). KK, PJP & RBGR received funding from the Dutch Technology Foundation STW under project name UPON, number 14207. We acknowledge the Maastricht M4I Microscopy CORE Lab for their scientific and technological support. This work was supported by NWO Grant 022.005.032. We thank Evelien Eenjes and Robbert Rottier for providing human adult lung material.

AUTHOR CONTRIBUTIONS

Conceptualization, M.M.L., J.V.D.V., J.B., H.C., B.L.H.;

Methodology, M.M.L., J.V.D.V., K.K., S.R., J.A.A.D., M.J.M., P.J.P., H.C., B.L.H.;

Investigation, M.M.L., J.V.D.V., K.K., S.R., T.I.B., A.Z.M., D.S., K.B., L.K., C.D.K., N.G., R.R., H.Q.D., J.A.A.D.;

Resources, G.M.G.M.V., M.P.G.K., H.C.;

Writing-Original Draft, M.M.L., J.V.D.V., B.L.H.;

Writing-Review & Editing, P.J.P., H.C., B.L.H.;

Funding acquisition, P.J.P., H.C., B.L.H.,

CONFLICT OF INTEREST

H.C. is inventor on patents held by the Royal Netherlands Academy of Arts and Sciences that cover organoid technology. H.C.'s full disclosure is given at <https://www.uu.nl/staff/JCClevers/>.

MATERIALS AND METHODS

Viruses and cells

Vero E6 cells were maintained in Dulbecco's modified Eagle's medium (DMEM, Gibco) supplemented with 10% fetal calf serum (FCS), HEPES, sodium bicarbonate, penicillin (100

IU/mL) and streptomycin (100 IU/mL) at 37°C in a humidified CO₂ incubator. SARS-CoV-2 (isolate BetaCoV/Munich/BavPat1/2020; European Virus Archive Global #026V-03883; kindly provided by Dr. C. Drosten) was propagated on VeroE6 (ATCC® CRL 1586TM) cells in Opti- MEM I (1X) + GlutaMAX (Gibco), supplemented with penicillin (100 IU/mL) and streptomycin (100 IU/mL) at 37°C in a humidified CO₂ incubator. The SARS-CoV-2 isolate was obtained from a clinical case in Germany, diagnosed after returning from China. Stocks were produced by infecting VeroE6 cells at a multiplicity of infection (MOI) of 0.01 and incubating the cells for 72 hours. The culture supernatant was cleared by centrifugation and stored in aliquots at -80°C. Stock titers were determined by preparing 10-fold serial dilutions in Opti-MEM I (1X) + GlutaMAX. Aliquots of each dilution were added to monolayers of 2×10^4 Vero E6 cells in the same medium in a 96-well plate. Twenty-four replicates were performed per virus stock. Plates were incubated at 37°C for 5 days and then examined for cytopathic effect. The TCID₅₀ was calculated according to the method of Spearman & Kärber. All work with infectious SARS-CoV and SARS-CoV-2 was performed in a Class II Biosafety Cabinet under BSL-3 conditions at Erasmus Medical Center.

SARS-CoV-2 Infection

2D differentiated cultures were washed twice with 200 μ l Advanced DMEM/F12 (Gibco) with Glutamax (Gibco), HEPES (Lonza), penicillin (100 IU/mL) and streptomycin (100 IU/mL) (Lonza) (AdDF+++)) before inoculation from the apical side at a MOI of 0.01 or 0.1 (as indicated) in 200 μ L AdDF+++ per well. The number of cells in each culture was calculated by trypsinizing and counting the cells from 1 well. Next, cultures were incubated at 37°C 5% CO₂ for 2 hours before washing 3 times in 200 μ L AdDF+++ . At the indicated timepoints, virus was collected from the cells by adding 200 μ L AdDF+++ apically, incubating 10 min at 37°C 5% CO₂, and storing the supernatant at -80°C. Where indicated, cultures were treated basally with 50 ng/ml IFN-L1 (Peprotech) at the indicated time pre- or post-infection. Prior to determining the viral titer, all samples were centrifuged at 2,000 g for 5 min. Infectious virus titers were determined using the Spearman & Kärber TCID₅₀ method on VeroE6 cells. All work was performed in a Class II Biosafety Cabinet under BSL-3 conditions at Erasmus Medical Center.

Fixed immunofluorescence microscopy

Organoids and Transwell inserts were fixed in 4% paraformaldehyde for 20 min, permeabilized in 70% ethanol or 0.1% Triton X-100 in PBS, and blocked for 60 min in 10% normal goat serum or 3% bovine serum albumin (BSA) in PBS (blocking buffer). For organoids 0.1% triton X-100 was added to the blocking buffer to increase antibody penetration. Cells were incubated with primary antibodies overnight at 4°C in blocking buffer, washed twice with PBS, incubated with corresponding secondary antibodies Alexa 488 and 594 conjugated secondary antibodies (1:200; Invitrogen) in blocking buffer for 2

1

2

3

4

5

6

7

8

9

&

h at room temperature, washed two times with PBS, incubated with indicated additional stains (TO-PRO3, phalloidin-633 (Santa Cruz, sc-363796), Hoechst, DAPI), washed twice with PBS, and mounted in Prolong Antifade (Invitrogen) mounting medium.

Viral nucleocapsid was stained with mouse-anti-SARS-CoV NP (40143-MM05, 1:1000, Sino Biological) or rabbit-anti-SARS-CoV NP (40143-T62, 1:1000, Sino biological), alveolar type 2 cells with anti-HTII-280 (TB-27AHT2-280, 1:150, Terrace Biotech), anti-SFTPC (FL-197, 1:200, Santa Cruz), anti-LPCAT1 (HPA012501, 1:200, Sigma), alveolar type 1 cells with anti-HTI-56 (TB-29 AHTI-56, 1:30, Terrace Biotech) and anti-HOPX (sc-30216, 1:200, Santa Cruz Biotechnology), goblet cells with anti-MUC5AC (MA5-12178, 1:100, Invitrogen), club cells with anti-CC10 (sc-390313 AF594, 1:100, Santa Cruz Biotechnology) or anti-SCGB3A2 (AF3545, 1:100, R&D systems), ciliated cells with anti-AcTUB (sc-23950 AF488, 1:100, Santa Cruz Biotechnology), STAT1 translocation anti-pSTAT1 (MA5-15071, 1:100, Thermo Fisher), proliferating cells with anti-Ki67 (MIB-1, GAG2661-2, 1:100, DAKO), tight junctions with anti-ZO-1 (ZO1-1A12, 1:100, Invitrogen), multipotent lung bud tip stem cells with anti-SOX2 (sc-365823 AF488, 1:100, Santa Cruz Biotechnology) and anti-SOX9 (sc-166505 AF594, 1:100, Santa Cruz Biotechnology), basal cells with anti-TP63 (ab735, 1:500, Abcam), and pulmonary neuroendocrine cells with anti-SYP (sc-17750, 1:100, Santa Cruz Biotechnology). ACE2 was stained with anti-ACE2 (HPA000288, 1:200, Atlas antibodies) and TMPRSS2 was stained with anti-TMPRSS2 (sc-515727, 1:200, Santa Cruz). Samples were imaged on a LSM700 confocal microscope using ZEN software (Zeiss). Representative images were acquired and shown as Z-projections, single slices or XZ cross sections.

Procurement of human material and informed consent

Adult lung tissue was obtained from residual, tumor-free, material obtained at lung resection surgery for lung cancer. The Medical Ethical Committee of the Erasmus MC Rotterdam granted permission for this study (METC 2012-512). Human fetal lung tissue was obtained from legally terminated second trimester pregnancies (15–20 weeks) by the HIS-Mouse Facility of Academic Medical Center (AMC; Amsterdam, The Netherlands), after written informed consent of the mother for the tissue's use in research and with approval of the Medical Ethical Review Board of the AMC (MEC: 03/038). Study procedures were performed according to the Declaration of Helsinki, and in compliance with relevant Dutch laws and institutional guidelines. The tissues obtained were anonymized and non-traceable to the donor. On request by the researchers, only gender and gestational age is provided.

Isolation, culture and differentiation of human small airway stem cells

Isolation of human small airway stem cells was performed using a protocol adapted from Sachs and colleagues (2018). One adult small airway donor was used in this study. Distal regions of adult lungs (lung parenchyma) were cut into ~2mm sections, washed in

AdDF+++ , and incubated with dispase (Corning; #354235) mixed with airway organoid (AO) medium ³⁸ at a 1:1 ratio for 1 h at 37°C. The digested tissue suspension was sequentially sheared using 10- and 5-ml plastic and flamed glass Pasteur pipettes. After shearing, the suspension was strained over a 100-µm filter. Two percent FCS was added to the strained suspension before centrifugation at 400 g. The pellet was resuspended in 10 ml AdDF+++ and centrifuged again at 400 x g. In case of a visible red pellet, erythrocytes were lysed in 2 ml red blood cell lysis buffer (Roche-11814389001) for 5 min at room temperature before the addition of 10 ml AdDF+++ and centrifugation at 400 g. Lung cell pellets were then resuspended in 200 µL of growth factor reduced Matrigel (Corning; #356231) and plated in ~30 µL droplets in a 48 well tissue culture plate. Plates were placed at 37 degrees Celsius with 5% CO2 for 10 minutes to solidify the Matrigel droplets upon which 250 µL of media was added to each well. Plates were incubated under standard tissue culture conditions (37°C, 5% CO2).

Airway organoids were passaged by mechanical disruption at 1:2 to 1:4 ratios after 10–14 days of culture. Medium was aspirated and ice-cold AdDF+++ added to each well. The Matrigel in each well was disrupted by pipetting and sucked into a P1000 pipette tip and transferred into a 15 ml tube. Ice-cold AdDF+++ was added up to 10 ml after which the sample was centrifuged at 100 g for 5 min. The medium was aspirated and replaced by 1 ml TrypLE express (Gibco). Next, organoids were incubated at 37°C for 5 min after which they were triturated using a flame-polished glass Pasteur pipette. Cold AdDF+++ containing 2% FCS was added up to 10 ml and the sample was centrifuged at 400 g for 3 minutes. Medium was aspirated, washed once in cold AdDF+++ and the pellet incubated on ice for 2 minutes before being resuspended in Matrigel and plated in ~30 µL droplets in a 48 well tissue culture. Plates were placed at 37°C with 5% CO2 for 20 minutes to solidify the Matrigel droplets, upon which 250 µl AO medium was added per well. Medium was changed every 4 days.

Organoids were frozen for long-term storage using CellBanker I (11888; AMSBIO Europe B.V.) following manufacturers protocol. In short, organoids were grown for 2-5 days after splitting. Organoids were removed from BME using DMEM+P/S and spun down. Pellet was resuspended in CellBanker I and immediately transferred to -80°C. For storage over 2 months, vials were moved to liquid nitrogen storage boxes.

To obtain differentiated organoid-derived cultures, organoids were dissociated into single cells using TrypLE express. Cells were seeded on Transwell membranes (Corning) coated with rat tail collagen type I (Fisher Scientific). Single cells were seeded in AO growth medium : complete base medium (CBM; Stemcell Pneumacult-ALI; #05001) at a 1:1 ratio. After 2-4 days, confluent monolayers were cultured at air-liquid interface in CBM. Medium was changed every 5 days. After 8 weeks of differentiation, cultures were used for infection experiments.

1
2
3
4
5
6
7
8
9
&

Isolation, culture and differentiation of human fetal lung bud tips

Isolation of human fetal lung epithelial bud tips was performed using a protocol adapted from Miller and colleagues (2018). Fetal lung donors were 16-19 weeks post-conception (pcw). Tissues were shipped in Hibernate A (Gibco; #A1247501) on ice before processing on the day the specimen was obtained. Distal regions of fetal lungs were cut into ~2mm sections and incubated with dispase on ice for 30-60 minutes. Tissue pieces were then incubated in 100% FBS on ice for 15 minutes, after which they were transferred to a 10% FBS solution in AdDF+++. Lung bud tips were separated from mesenchymal cells through repeated pipetting and washing in AdDF+++ until mesenchymal cells were no longer visible. From each donor, donor-specific mesenchymal cells were isolated by plating single cells present in the supernatant from the first wash. Mesenchymal cells were maintained in AdDF+++ supplemented with 10% FCS. After washing, bud tips were then resuspended in 200 μ L of growth factor reduced Matrigel and plated in ~30 μ L droplets in a 48 well tissue culture plate. Plates were placed at 37 degrees Celsius with 5% CO₂ for 20 minutes to solidify the Matrigel droplets upon which 250 μ L of fetal lung (FL) medium (Nikolic et al., 2017) was added to each well. Plates were incubated under standard tissue culture conditions (37°C, 5% CO₂).

Fetal lung bud tip organoids were passaged by mechanical disruption at 1:2 to 1:4 ratios after 10–14 days of culture. Medium was aspirated and ice-cold AdDF+++ added to each well. The Matrigel in each well was disrupted by pipetting and sucked into a P1000 pipette tip and transferred into a 15 ml tube. Ice-cold AdDF+++ was added up to 10 ml after which the sample was centrifuged at 100 g for 5 min. The medium was aspirated and replaced by 1 ml AdDF+++. Next, organoids were triturated using a flame-polished glass Pasteur pipette. Cold AdDF+++ was added up to 10 ml and the sample was centrifuged at 400 g for 3 minutes. Medium was aspirated and the pellet incubated on ice for 2 minutes before being resuspended in Matrigel and plated in ~30 μ L droplets in a 48 well tissue culture. Plates were placed at 37°C with 5% CO₂ for 20 minutes to solidify the Matrigel droplets, upon which 250 μ L FL medium was added per well. Medium was changed every 4 days.

To obtain differentiated organoid-derived cultures, 10⁵ donor-specific fetal lung mesenchymal cells were seeded in 12-well plates in AdDF+++ containing 10% FCS. The next day, organoids were dissociated into small clumps using TrypLE express. Cells were seeded on Transwell membranes (Corning-3460). Clumps were seeded in FL : BEpiCM (bronchial epithelial cell growth medium; Sciencell; Cat. No. 3211) at a 1:1 ratio. BEpiCM was made by mixing basal medium (Sciencell; Cat. No. 3211-b) and DMEM at a 1:1 ratio and adding bronchial epithelial cell growth supplement (BEpiCGS, Sciencell; Cat. No. 3262), penicillin (100 IU/mL), streptomycin (100 IU/mL) and 0.001 μ M retinoic acid (Sigma). ROCK inhibitor was added for the first 5 days to prevent apoptosis (Y-27632; Sigma; Y0503; 10 μ M). After 4-7 days, confluent monolayers were cultured at air-liquid interface in BEpiCM. Eighty percent of the medium was changed every 4-5 days. After 14 days of differentiation, cultures were used for infection experiments.

Determination of virus titers using qRT-PCR

Supernatant and organoid samples were thawed and centrifuged at 2,000 g for 5 min. Sixty μL supernatant was lysed in 90 μL MagnaPure LC Lysis buffer (Roche) at room temperature for 10 min. RNA was extracted by incubating samples with 50 μL Agencourt AMPure XP beads (Beckman Coulter) for 15 min at RT, washing beads twice with 70% ethanol on a DynaMag-96 magnet (Invitrogen) and eluting in 30 μL MagnaPure LC elution buffer (Roche). Viral titers (Viral RNA copies per mL) were determined by qRT-PCR using primers targeting the E gene (35) and compared to a counted RNA standard curve.

Mass spectrometry

Proteins were digested with trypsin using the SP3 method⁵⁸ with minor modifications. Briefly, proteins secreted by alveolar-like cultures were collected from the cells by adding 200 μL AdDF+++ apically, incubating 10 min at 37°C 5% CO₂, and storing the supernatant at -80°C in Laemmli buffer (BioRad). Proteins in 30 μL Laemmli buffer (Bio Rad) were reduced with 5 mM dithiothreitol (Sigma, D8255) for 30 minutes at 50 °C and alkylated with 10 mM iodoacetamide (Sigma, I6125) for 10 minutes in the dark. Ten μg Sera-Mag SpeedBeads (Fisher Scientific) in 20 μL milli-Q and ethanol were added to a final concentration of 50 % and the solution was mixed for 10 minutes at RT. Beads were immobilized using a magnetic rack the and washed three times with 100 μL 80 % ethanol. One 1 μg trypsin and 0.5 μg Lys-C in 100 μL 50 mM Tris/HCl pH 8.3 were added to the beads and the sample was incubated overnight at 37 °C. The tryptic digest was acidified with TFA and desalted using a StageTip. Peptides were eluted with 100 μL 40 % Acetonitrile and 0.1 % formic acid and dried in a Speedvac. Before analysis by LC-MS peptides were dissolved in 20 μL 2 % acetonitrile and 0.1 % formic acid.

Nanoflow liquid chromatography tandem mass spectrometry (nLC-MS/MS) was performed on an EASY-nLC 1200 coupled to an Orbitrap Eclipse Tribrid mass spectrometer (ThermoFisher Scientific) operating in positive mode. Peptide mixtures were trapped on a 2 cm x 100 μm Pepmap C18 column (Thermo Fisher 164564) and then separated on an in-house packed 50 cm x 75 μm capillary column with 1.9 μm Reprosil-Pur C18 beads (Dr. Maisch) at a flowrate of 250 nL/min, using a linear gradient of 0–32 % acetonitrile (in 0.1 % formic acid) during 90 min. The eluate was directly sprayed into the electrospray ionization (ESI) source of the mass spectrometer. Spectra were acquired in continuum mode; fragmentation of the peptides was performed in data-dependent mode by HCD. Mass spectrometry data were analyzed with Proteome Discoverer 2.4 with Mascot version 2.6.2 as the search engine. The target FDR for both PSMs and peptides was set to 0.01. MS/MS spectra were searched against a combined database composed of all UniProt entries taxonomy *Homo Sapiens* (release October 2019) and all SARS-CoV-2 protein sequences (<https://covid-19.uniprot.org/>) concatenated with the reversed versions of all sequences. For precursor ion quantification based on the Minora algorithm in Proteome Discoverer only unique and razor peptides were used. Normalization was done on total peptide amounts for all samples.

1

2

3

4

5

6

7

8

9

&

Bulk RNA sequencing

Library preparation was performed at Single Cell Discoveries (Utrecht, The Netherlands), using an adapted version of the CEL-seq protocol. In brief:

Total RNA was extracted using the standard TRIzol (Invitrogen) protocol and used for library preparation and sequencing. mRNA was processed as described previously, following an adapted version of the single-cell mRNA seq protocol of CEL-Seq^{59,60}. In brief, samples were barcoded with CEL-seq primers during a reverse transcription and pooled after second strand synthesis. The resulting cDNA was amplified with an overnight *In vitro* transcription reaction. From this amplified RNA, sequencing libraries were prepared with Illumina Truseq small RNA primers. Paired-end sequencing was performed on the Illumina Nextseq500 platform using barcoded 1 x 75 nt read setup. Read 1 was used to identify the Illumina library index and CEL-Seq sample barcode. Read 2 was aligned to the CRCh38 human RefSeq transcriptome, with the addition of the SARS-CoV-2 (Ref-SKU: 026V-03883) genome, similar to earlier study²⁷, using BWA using standard settings⁶¹. Reads that mapped equally well to multiple locations were discarded. Mapping and generation of count tables was done using the MapAndGo script. Samples were normalized using RPM normalization.

Differential gene expression analysis was performed using the DESeq2 package⁶². SARS-mapping reads were removed before analyzing the different datasets.

For bronchioalveolar-like samples, two donors were sequenced twice as technical replicates which were combined in the DESeq2 methods when comparing to the remaining datasets. We compared the bulk mRNA sequencing of the bronchioalveolar culture system to freshly purified adult ATII cells. Previously published profiles of purified human ATII cultures were downloaded from NCBI GEO (Accession No GSM3818009 and GSM3818010). Normalized counts were used in generating heatmaps.

The top genes which were most strongly induced in response to SARS-CoV-2 ($\text{padj} < 0.05$, ranked by fold change) were subjected to functional enrichment analysis for a biological process using ToppFun on the ToppGene Suite (<https://toppgene.cchmc.org/enrichment.jsp>) as described before⁶³. The 5 biological processes with highest enrichment (after FDR correction and a p -value cutoff of 0.05) for each virus are displayed with the corresponding GO term, corrected p value and FDR.

10x Single cell sequencing - library preparation

Single-cell mRNA sequencing was performed at Single Cell Discoveries according to standard 10x Genomics 3' V3.1 chemistry protocol. In short, single cells suspensions were methanol fixed in 80% methanol and frozen at -80°C . Prior to loading the cells on the 10x Chromium controller, cells were rehydrated in rehydration buffer and counted to assess cell concentration. Cells were loaded and the resulting sequencing libraries were prepared following standard 10x Genomics protocol. The DNA libraries was paired-end sequenced on an Illumina Novaseq S4, with a 2x150 bp Illumina kit.

10x Single cell sequencing - Mapping of sequencing data and clustering and differential gene expression analysis.

BCL files resulting from sequencing were transformed to FASTQ files with 10x Genomics Cell Ranger mkfastq. FASTQ files were mapped with Cell Ranger count. During sequencing, Read 1 was assigned 150 base pairs, but only the first 28 bp were used for identification of the Illumina library barcode, cell barcode and UMI. R2 was used to map to a custom made reference transcriptome of Hg38 with additional sequences for SARS-CoV-2 added. Filtering of empty barcodes was done Cell Ranger. In total, approximately 5015 cells were detected. Unsupervised clustering and differential gene expression analysis was done with the Seurat¹ R toolkit⁶⁴. We compared the ATII-L cells in the bronchioalveolar culture system to purified ATII cells. Previously published single-cell transcriptomic profiles of purified ATII cultures were downloaded from NCBI GEO (Accession No GSM2855485). Raw counts were normalized, integrated with the abovementioned single-cell dataset and further analyzed using the Seurat R toolkit.

Transmission electron microscopy

2D cultures were chemically fixed for 3 hours at room temperature and prepared for imaging within the transmission electron microscope as described in (Lamers et al., 2020). All TEM data were collected with an Eagle detector on a FEI Tecnai T12 microscope operated at 120kV.

Statistical analysis

For single-cell sequencing data, clustering and differential gene expression analysis was performed with Seurat version 3⁶⁴, following standard parameters.

1

2

3

4

5

6

7

8

9

&

REFERENCES

1. Zhu, N. et al. A Novel Coronavirus from Patients with Pneumonia in China, 2019. *N Engl J Med* **382**, 727-733, doi:10.1056/NEJMoa2001017 (2020).
2. WHO. Coronavirus disease (COVID-19). Situation Report – 132. (2020).
3. Andersen, K. G., Rambaut, A., Lipkin, W. I., Holmes, E. C. & Garry, R. F. The proximal origin of SARS-CoV-2. *Nat Med* **26**, 450-452, doi:10.1038/s41591-020-0820-9 (2020).
4. Lu, R. et al. Genomic characterisation and epidemiology of 2019 novel coronavirus: implications for virus origins and receptor binding. *Lancet* **395**, 565-574, doi:10.1016/S0140-6736(20)30251-8 (2020).
5. Coronaviridae Study Group of the International Committee on Taxonomy of, V. The species Severe acute respiratory syndrome-related coronavirus: classifying 2019-nCoV and naming it SARS-CoV-2. *Nat Microbiol* **5**, 536-544, doi:10.1038/s41564-020-0695-z (2020).
6. Chen, N. et al. Epidemiological and clinical characteristics of 99 cases of 2019 novel coronavirus pneumonia in Wuhan, China: a descriptive study. *Lancet* **395**, 507-513, doi:10.1016/S0140-6736(20)30211-7 (2020).
7. Wolfel, R. et al. Virological assessment of hospitalized patients with COVID-2019. *Nature*, doi:10.1038/s41586-020-2196-x (2020).
8. Xu, Z. et al. Pathological findings of COVID-19 associated with acute respiratory distress syndrome. *Lancet Respir Med* **8**, 420-422, doi:10.1016/S2213-2600(20)30076-X (2020).
9. Wang, D. et al. Clinical Characteristics of 138 Hospitalized Patients With 2019 Novel Coronavirus-Infected Pneumonia in Wuhan, China. *JAMA*, doi:10.1001/jama.2020.1585 (2020).
10. Barton, L. M., Duval, E. J., Stroberg, E., Ghosh, S. & Mukhopadhyay, S. COVID-19 Autopsies, Oklahoma, USA. *Am J Clin Pathol* **153**, 725-733, doi:10.1093/ajcp/aqaa062 (2020).
11. Menter, T. et al. Post-mortem examination of COVID19 patients reveals diffuse alveolar damage with severe capillary congestion and variegated findings of lungs and other organs suggesting vascular dysfunction. *Histopathology*, doi:10.1111/his.14134 (2020).
12. Raptis, C. A. et al. Chest CT and Coronavirus Disease (COVID-19): A Critical Review of the Literature to Date. *AJR Am J Roentgenol*, 1-4, doi:10.2214/AJR.20.23202 (2020).
13. Thompson, B. T., Chambers, R. C. & Liu, K. D. Acute Respiratory Distress Syndrome. *N Engl J Med* **377**, 562-572, doi:10.1056/NEJMra1608077 (2017).
14. Ackermann, M. et al. Pulmonary Vascular Endothelialitis, Thrombosis, and Angiogenesis in Covid-19. *N Engl J Med*, doi:10.1056/NEJMoa2015432 (2020).
15. Ware, L. B. & Matthay, M. A. The acute respiratory distress syndrome. *N Engl J Med* **342**, 1334-1349, doi:10.1056/NEJM200005043421806 (2000).
16. tenOever, B.R. The Evolution of Antiviral Defense Systems. *Cell Host Microbe* **19**, 142-149, doi:10.1016/j.chom.2016.01.006 (2016).
17. Ravindra, N. G., Alfajaro, M.M., Gasque, V., Wei, J., Filler, R.B., Huston, N.C., Wan, H., Szigeti-Buck, K., Wang, B., Montgomery, R.R., Eisenbarth, S.C., Williams, A., Pyle, A.M., Iwasaki, A., Horvath, T.L., Foxman, E.F., van Dijk, D., Wilen, C.B. Single-cell longitudinal analysis of SARS-CoV-2 infection in human bronchial epithelial cells. *BioRxiv In Press*, doi:https://doi.org/10.1101/2020.05.06.081695 (2020).
18. Zhou, P. et al. A pneumonia outbreak associated with a new coronavirus of probable bat origin. *Nature* **579**, 270-273, doi:10.1038/s41586-020-2012-7 (2020).
19. Walls, A. C. et al. Structure, Function, and Antigenicity of the SARS-CoV-2 Spike Glycoprotein. *Cell* **181**, 281-292 e286, doi:10.1016/j.cell.2020.02.058 (2020).
20. Wrapp, D. et al. Cryo-EM structure of the 2019-nCoV spike in the prefusion conformation. *Science* **367**, 1260-1263, doi:10.1126/science.abb2507 (2020).
21. Hoffmann, M. et al. SARS-CoV-2 Cell Entry Depends on ACE2 and TMPRSS2

- and Is Blocked by a Clinically Proven Protease Inhibitor. *Cell* **181**, 271-280 e278, doi:10.1016/j.cell.2020.02.052 (2020).
22. Jia, H. P. et al. ACE2 receptor expression and severe acute respiratory syndrome coronavirus infection depend on differentiation of human airway epithelia. *J Virol* **79**, 14614-14621, doi:10.1128/JVI.79.23.14614-14621.2005 (2005).
 23. Qi, F., Qian, S., Zhang, S. & Zhang, Z. Single cell RNA sequencing of 13 human tissues identify cell types and receptors of human coronaviruses. *Biochem Biophys Res Commun* **526**, 135-140, doi:10.1016/j.bbrc.2020.03.044 (2020).
 24. Hikmet, F., Mear, L., Edvinsson, A., Micke, P., Uhlen, M., Lindskog, C. The protein expression profile of ACE2 in human tissues. *BioRxiv In press*, doi:https://doi.org/10.1101/2020.03.31.016048 (2020).
 25. Rockx, B. et al. Comparative pathogenesis of COVID-19, MERS, and SARS in a nonhuman primate model. *Science*, doi:10.1126/science.abb7314 (2020).
 26. Hou, Y. J., Okuda, K., Edwards, C.E., Martinez, D.R., Asakura, T., Dinnon III., K.H., Kato, T., Lee, R.E., Yount, B.L., Mascenik, T.M., Chen, G., Olivier, K.N., Ghio, A., Tse, L.V., Leist, S.R., Gralinski, L.E., Schäfer, A., Dang, H., Gilmore, R., Nakano, S., Sun, L., Fulcher, M.L., Livraghi-Butrico, A., Nicely, N.I., Cameron, M., Cameron, C., Kelvin, D.J., de Silva, A., Margolis, D.M., Markmann, A., Bartelt, L., Zumwalt, R., Martinez, F.J., Salvatore, S.P., Borczuk, A., Tata, P.R., Sontake, V., Kimple, A., Jaspers, I., O'Neal, W.K., Randell, S.H., Boucher, R.C., Baric, R.S. SARS-CoV-2 Reverse Genetics Reveals a Variable Infection Gradient in the Respiratory Tract. *Cell In press*, doi:https://doi.org/10.1016/j.cell.2020.05.042. (2020).
 27. Lamers, M. M. et al. SARS-CoV-2 productively infects human gut enterocytes. *Science*, doi:10.1126/science.abc1669 (2020).
 28. van den Bogaard, E. H., Dailey, L. A., Thorley, A. J., Tetley, T. D. & Forbes, B. Inflammatory response and barrier properties of a new alveolar type 1-like cell line (TT1). *Pharm Res* **26**, 1172-1180, doi:10.1007/s11095-009-9838-x (2009).
 29. Logan, C. Y. & Desai, T. J. Keeping it together: Pulmonary alveoli are maintained by a hierarchy of cellular programs. *Bioessays* **37**, 1028-1037, doi:10.1002/bies.201500031 (2015).
 30. Zacharias, W. J. et al. Regeneration of the lung alveolus by an evolutionarily conserved epithelial progenitor. *Nature* **555**, 251-255, doi:10.1038/nature25786 (2018).
 31. Hui, K. P. Y. et al. Tropism, replication competence, and innate immune responses of the coronavirus SARS-CoV-2 in human respiratory tract and conjunctiva: an analysis in ex-vivo and in-vitro cultures. *Lancet Respir Med*, doi:10.1016/S2213-2600(20)30193-4 (2020).
 32. Gotoh, S. et al. Generation of alveolar epithelial spheroids via isolated progenitor cells from human pluripotent stem cells. *Stem Cell Reports* **3**, 394-403, doi:10.1016/j.stemcr.2014.07.005 (2014).
 33. van Riet, S. et al. In vitro modelling of alveolar repair at the air-liquid interface using alveolar epithelial cells derived from human induced pluripotent stem cells. *Sci Rep* **10**, 5499, doi:10.1038/s41598-020-62226-1 (2020).
 34. Dye, B. R. et al. In vitro generation of human pluripotent stem cell derived lung organoids. *Elife* **4**, doi:10.7554/eLife.05098 (2015).
 35. Yamamoto, Y. et al. Long-term expansion of alveolar stem cells derived from human iPSC cells in organoids. *Nat Methods* **14**, 1097-1106, doi:10.1038/nmeth.4448 (2017).
 36. Jacob, A. et al. Differentiation of Human Pluripotent Stem Cells into Functional Lung Alveolar Epithelial Cells. *Cell Stem Cell* **21**, 472-488 e410, doi:10.1016/j.stem.2017.08.014 (2017).
 37. de Carvalho, A. et al. Glycogen synthase kinase 3 induces multilineage maturation of human pluripotent stem cell-derived lung progenitors in 3D culture. *Development* **146**, doi:10.1242/dev.171652 (2019).
 38. Sachs, N. et al. Long-term expanding human airway organoids for disease modeling. *EMBO J* **38**, doi:10.15252/embj.2018100300 (2019).

1

2

3

4

5

6

7

8

9

&

39. Zhou, J. et al. Differentiated human airway organoids to assess infectivity of emerging influenza virus. *Proc Natl Acad Sci U S A* **115**, 6822-6827, doi:10.1073/pnas.1806308115 (2018).
40. Nikolic, M. Z. et al. Human embryonic lung epithelial tips are multipotent progenitors that can be expanded in vitro as long-term self-renewing organoids. *Elife* **6**, doi:10.7554/eLife.26575 (2017).
41. Gonzalez, R. F., Allen, L., Gonzales, L., Ballard, P. L. & Dobbs, L. G. HTII-280, a biomarker specific to the apical plasma membrane of human lung alveolar type II cells. *J Histochem Cytochem* **58**, 891-901, doi:10.1369/jhc.2010.956433 (2010).
42. Nikolic, M. Z. & Rawlins, E. L. Lung Organoids and Their Use To Study Cell-Cell Interaction. *Curr Pathobiol Rep* **5**, 223-231, doi:10.1007/s40139-017-0137-7 (2017).
43. Barkauskas, C. E. et al. Type 2 alveolar cells are stem cells in adult lung. *J Clin Invest* **123**, 3025-3036, doi:10.1172/JCI68782 (2013).
44. Leeman, K. T., Pessina, P., Lee, J. H. & Kim, C. F. Mesenchymal Stem Cells Increase Alveolar Differentiation in Lung Progenitor Organoid Cultures. *Sci Rep* **9**, 6479, doi:10.1038/s41598-019-42819-1 (2019).
45. Dobbs, L. G., Gonzalez, R. F., Allen, L. & Froh, D. K. HTI56, an integral membrane protein specific to human alveolar type I cells. *J Histochem Cytochem* **47**, 129-137, doi:10.1177/002215549904700202 (1999).
46. Gonzales, L. W. et al. Expression of Carcinoembryonic Cell Adhesion Molecule 6 and Alveolar Epithelial Cell Markers in Lungs of Human Infants with Chronic Lung Disease. *J Histochem Cytochem* **63**, 908-921, doi:10.1369/0022155415603768 (2015).
47. Frieman, M. et al. Severe acute respiratory syndrome coronavirus ORF6 antagonizes STAT1 function by sequestering nuclear import factors on the rough endoplasmic reticulum/Golgi membrane. *J Virol* **81**, 9812-9824, doi:10.1128/JVI.01012-07 (2007).
48. Kopecky-Bromberg, S. A., Martinez-Sobrido, L., Frieman, M., Baric, R. A. & Palese, P. Severe acute respiratory syndrome coronavirus open reading frame (ORF) 3b, ORF 6, and nucleocapsid proteins function as interferon antagonists. *J Virol* **81**, 548-557, doi:10.1128/JVI.01782-06 (2007).
49. Mu, J. et al. SARS-CoV-2 N protein antagonizes type I interferon signaling by suppressing phosphorylation and nuclear translocation of STAT1 and STAT2. *Cell Discov* **6**, 65, doi:10.1038/s41421-020-00208-3 (2020).
50. Blanco-Melo, D. et al. Imbalanced Host Response to SARS-CoV-2 Drives Development of COVID-19. *Cell*, doi:10.1016/j.cell.2020.04.026 (2020).
51. Ziegler, C. G. K. et al. SARS-CoV-2 Receptor ACE2 Is an Interferon-Stimulated Gene in Human Airway Epithelial Cells and Is Detected in Specific Cell Subsets across Tissues. *Cell*, doi:10.1016/j.cell.2020.04.035 (2020).
52. Kim, C. F. et al. Identification of bronchioalveolar stem cells in normal lung and lung cancer. *Cell* **121**, 823-835, doi:10.1016/j.cell.2005.03.032 (2005).
53. Youk, J. et al. Three-Dimensional Human Alveolar Stem Cell Culture Models Reveal Infection Response to SARS-CoV-2. *Cell Stem Cell*, doi:10.1016/j.stem.2020.10.004 (2020).
54. Katsura, H. et al. Human Lung Stem Cell-Based Alveolospheres Provide Insights into SARS-CoV-2-Mediated Interferon Responses and Pneumocyte Dysfunction. *Cell Stem Cell*, doi:10.1016/j.stem.2020.10.005 (2020).
55. Salahudeen, A. A. et al. Progenitor identification and SARS-CoV-2 infection in human distal lung organoids. *Nature*, doi:10.1038/s41586-020-3014-1 (2020).
56. Huang, J. et al. SARS-CoV-2 Infection of Pluripotent Stem Cell-Derived Human Lung Alveolar Type 2 Cells Elicits a Rapid Epithelial-Intrinsic Inflammatory Response. *Cell Stem Cell*, doi:10.1016/j.stem.2020.09.013 (2020).
57. Lauer, S. A. et al. The Incubation Period of Coronavirus Disease 2019 (COVID-19) From Publicly Reported Confirmed Cases: Estimation and Application. *Ann Intern Med* **172**, 577-582, doi:10.7326/M20-0504 (2020).
58. Hughes, C. S. et al. Single-pot, solid-phase-enhanced sample preparation for proteomics

- experiments. *Nat Protoc* **14**, 68-85, doi:10.1038/s41596-018-0082-x (2019).
59. Hashimshony, T. et al. CEL-Seq2: sensitive highly-multiplexed single-cell RNA-Seq. *Genome Biol* **17**, 77, doi:10.1186/s13059-016-0938-8 (2016).
60. Simmini, S. et al. Transformation of intestinal stem cells into gastric stem cells on loss of transcription factor Cdx2. *Nat Commun* **5**, 5728, doi:10.1038/ncomms6728 (2014).
61. Li, H. & Durbin, R. Fast and accurate long-read alignment with Burrows-Wheeler transform. *Bioinformatics* **26**, 589-595, doi:10.1093/bioinformatics/btp698 (2010).
62. Love, M. I., Huber, W. & Anders, S. Moderated estimation of fold change and dispersion for RNA-seq data with DESeq2. *Genome Biol* **15**, 550, doi:10.1186/s13059-014-0550-8 (2014).
63. Kaimal, V., Bardes, E. E., Tabar, S. C., Jegga, A. G. & Aronow, B. J. ToppCluster: a multiple gene list feature analyzer for comparative enrichment clustering and network-based dissection of biological systems. *Nucleic Acids Res* **38**, W96-102, doi:10.1093/nar/gkq418 (2010).
64. Butler, A., Hoffman, P., Smibert, P., Papalexi, E. & Satija, R. Integrating single-cell transcriptomic data across different conditions, technologies, and species. *Nat Biotechnol* **36**, 411-420, doi:10.1038/nbt.4096 (2018).

1

2

3

4

5

6

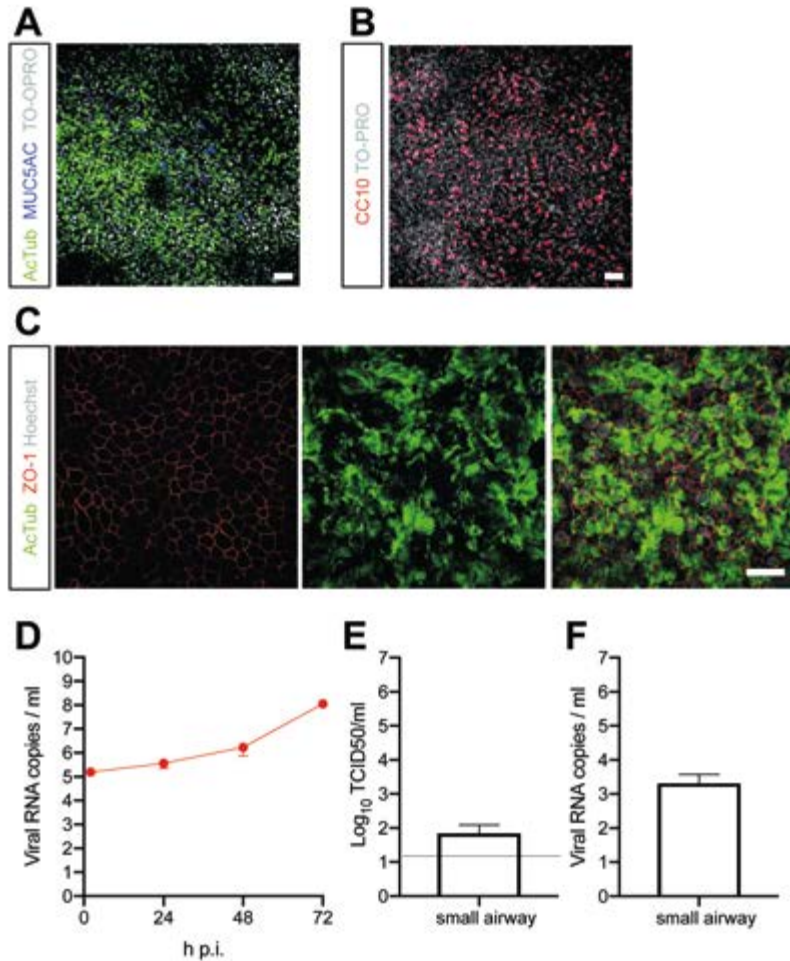
7

8

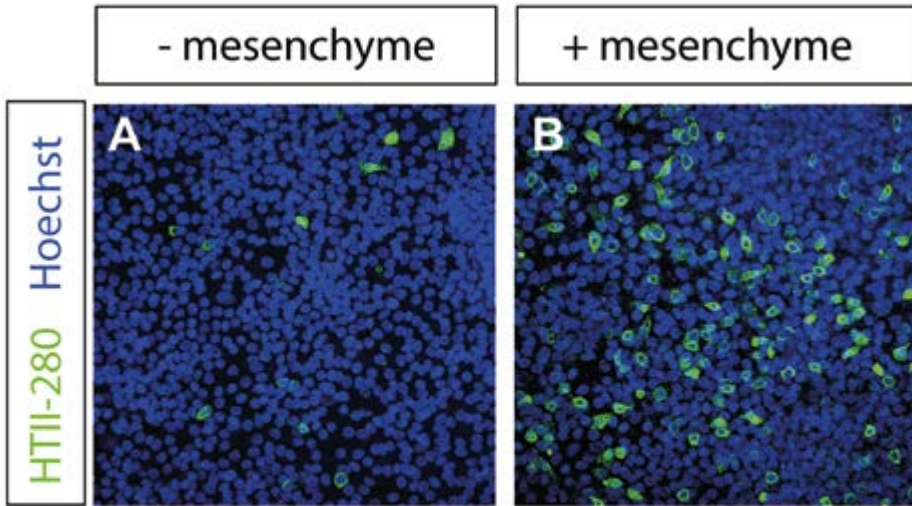
9

&

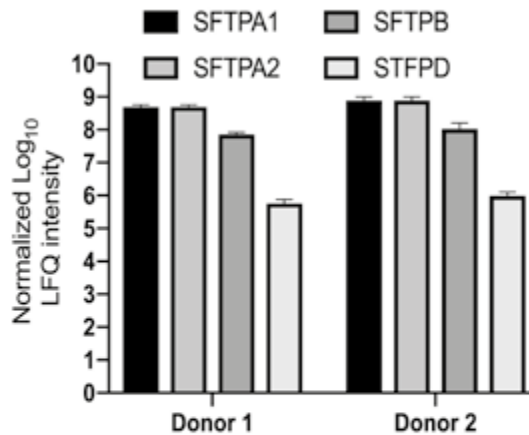
SUPPLEMENTARY FIGURE



Supplementary figure S1. Characterization of organoid-derived air-liquid interface differentiated small airway cultures. A) Immunofluorescent staining of small airway cultures after 8 weeks of differentiation at air-liquid inter- phase. Ciliated cells were stained with ActTUB (green), and goblet cells with MUC5AC (blue). B) Club cells were stained with CC10 (red). C) Tight junctions were stained with ZO-1 (red). Nuclei were visualized with TO-PRO or Hoechst (white). Scale bars represent 50 μ m. D) Viral SARS-CoV-2 RNA titers of apical washes at 2, 24, 48, and 72h after infection at MOI 0.1. E and F) Infectious virus titers as observed by virus titrations on VeroE6 cells (E) and qRT-PCR (F) in basal compartments. The dotted line indicates the lower limit of detection. Error bars represent SEM. N=4. H p.i. = hours post infection.

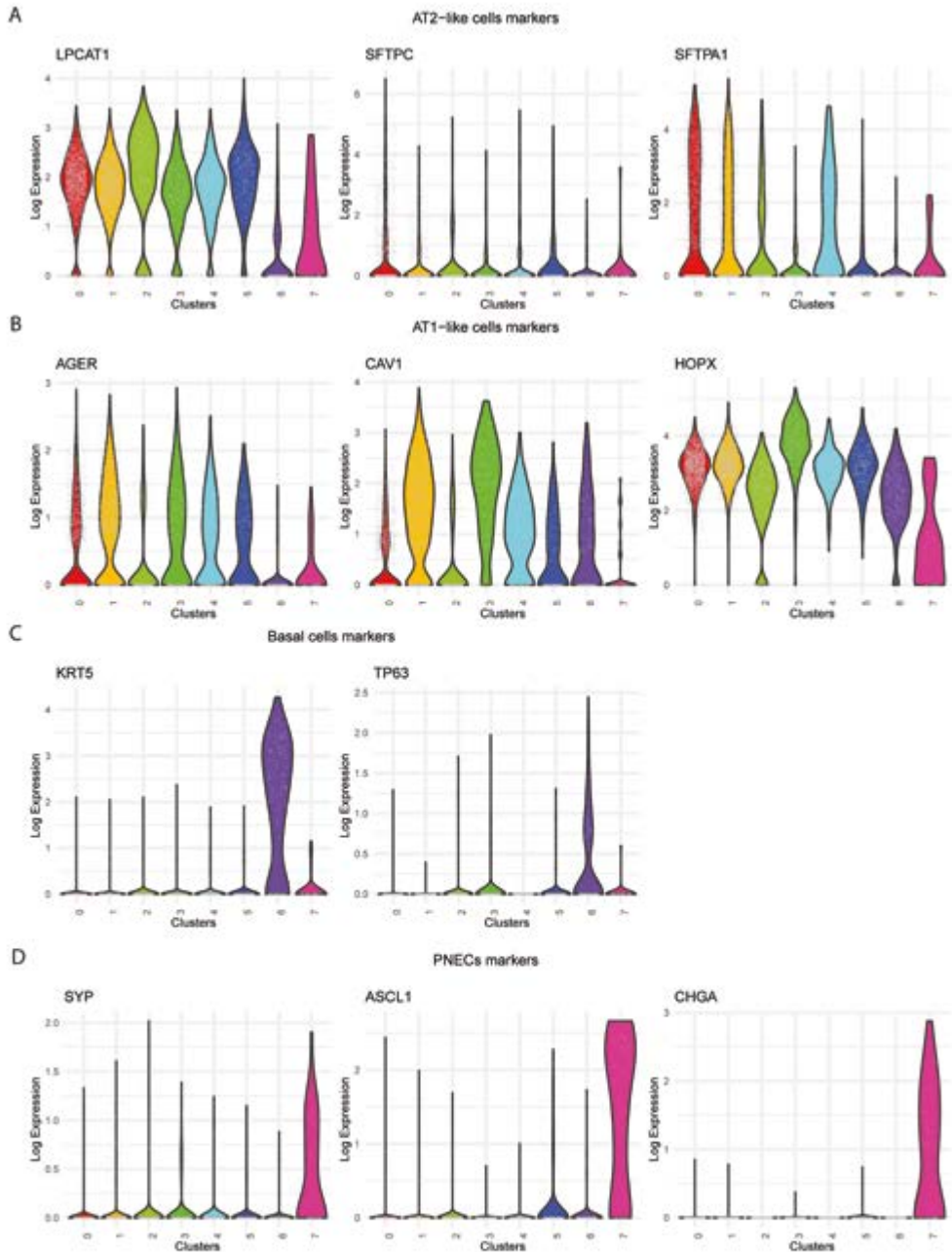


Supplementary figure S2. Mesenchymal cells increase HTII-280 expression. Immunofluorescent staining of HTII-280 (green) after two weeks of differentiation at air-liquid interface in the absence (A) or presence (B) of mesenchyme in the basal compartment of the Transwell. Nuclei are stained with Hoechts (blue). Scale bars represent 50 μ m.

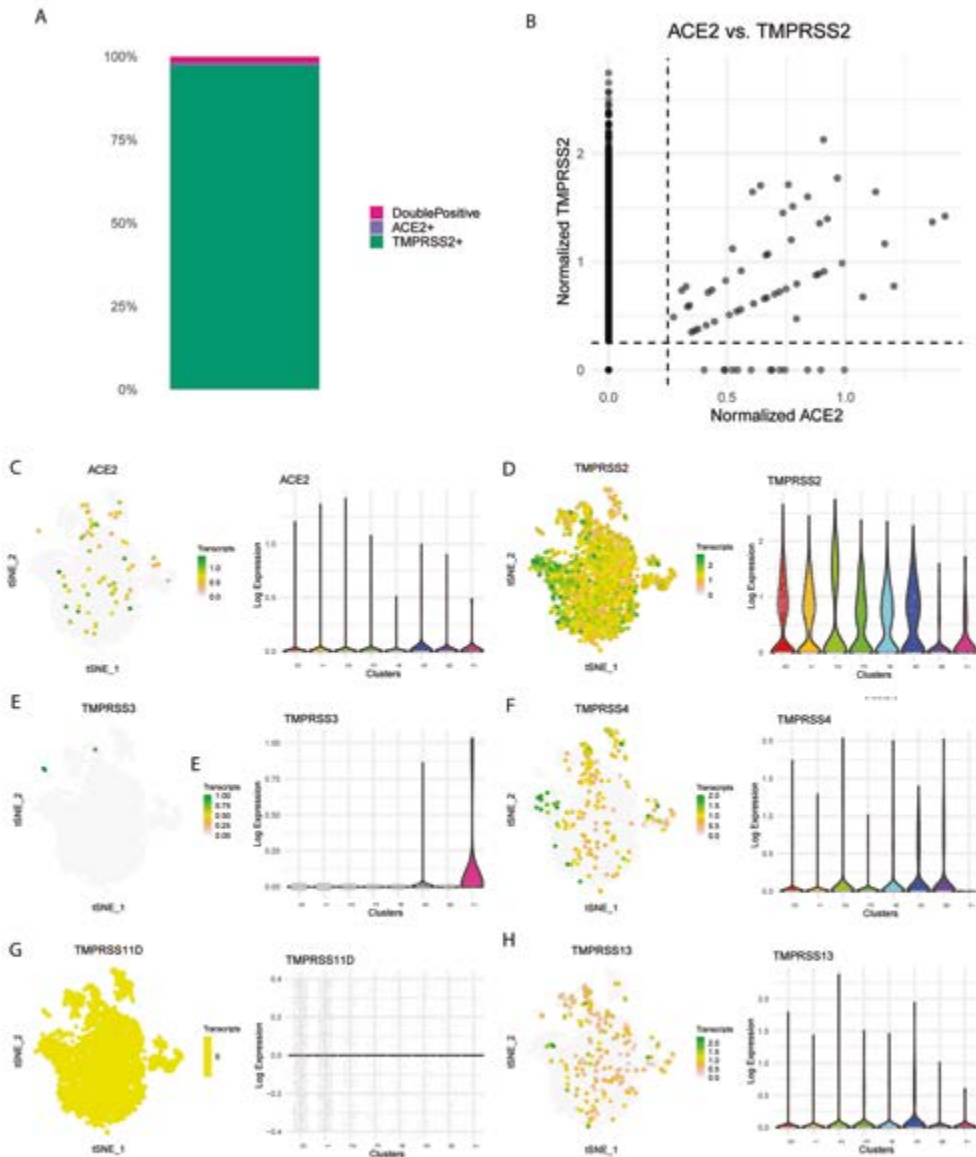


Supplementary figure S3. Mass spectrometric analysis of surfactant proteins collected from an apical washes of differentiated cultures. LFQ = label free quantification. Error bars represent SD.

1
2
3
4
5
6
7
8
9
&



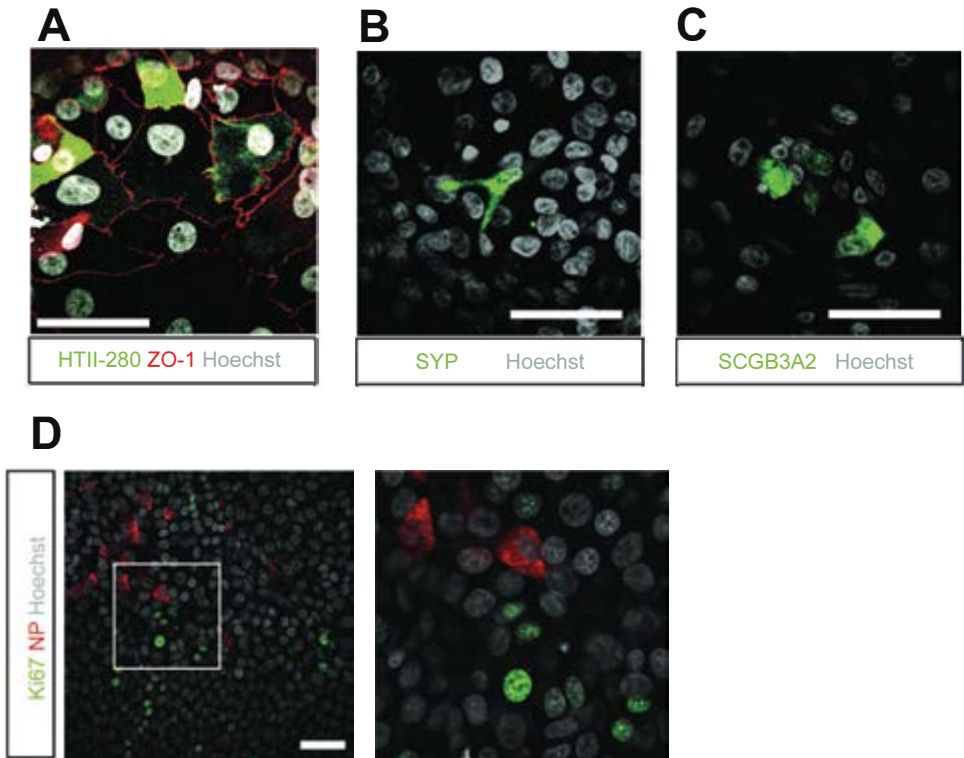
Supplementary figure S4. Expression analysis of cell type defining marker genes. A-D) Violin plots visualizing expression levels of marker genes for populations of cell types identified in bronchioalveolar cultures. A) AT2-like cell markers LPCAT1, SFTPC and SFTPA1 are enriched in clusters 0 and 2. B) AT1-like cell markers AGER, CAV1 and HOPX are enriched in cluster 3. C) Basal cell markers KRT5 and TP63 are highly enriched in cluster 6. D) Neuroendocrine cell markers SYP, ASCL1 and CHGA are highly enriched in cluster 7.



Supplementary figure S5. Expression levels of SARS-CoV-2 entry receptors and family members.

A) Bar graph indicating percentage of cells in data set with expression of TMPRSS2, ACE2 or both. Only very limited number of ACE2+ cells are not co-expressing TMPRSS2. B) Correlation plot indicating expression levels of ACE2 and TMPRSS2 in single cells C-H) Expression levels of entry receptors ACE2 (redisplay of Figure 4M) (C), TMPRSS2 (redisplay of Figure 4O) (D) and family members TMPRSS3 (E), TMPRSS4 (F), TMPRSS11D (G) and TMPRSS13 (H) in t-SNE map (color coded logarithmic scale of transcript expression) and violin plots visualizing expression levels.

1
2
3
4
5
6
7
8
9
&



Supplementary figure S6. Additional confocal images characterizing bronchioalveolar-like cultures. A) Differentiated bronchioalveolar cultures contain tight junctions (ZO1, red). HTII-280 stains ATII-like cells. B-C) Differentiated bronchioalveolar cultures contain pulmonary neuroendocrine cells (SYP, B, green) and SCGB3A2⁺ cells (C, green). D) SARS-CoV-2 infects Ki67-negative cells in differentiated 2D bronchioalveolar-like cultures. Dividing cells were stained with anti-Ki67 (green), and SARS-CoV-2 infected cells for NP (red). Nuclei were visualized with Hoechst (white). Scale bars represent 50 μ m.

CHAPTER

ADULT MOUSE AND HUMAN ORGANOIDS DERIVED FROM THYROID FOLLICULAR CELLS AND MODELLING OF GRAVES' HYPERTHYROIDISM

7

Jelte van der Vaart^{1,2}, Lynn Bosmans¹, Stijn F. Sijbesma¹,
Kèvin Knoops³, Willine J. van de Wetering³, Henny G. Otten⁴,
Harry Begthel^{1,2}, Inne H.M. Borel Rinkes⁵, Jeroen Korving^{1,2},
Eef G.W.M. Lentjes⁶, Carmen Lopez-Iglesias³, Peter J. Peters³,
Hanneke M. van Santen^{7,8}, Menno R. Vriens⁵, Hans Clevers^{1,2,7}

¹ Hubrecht Institute, Royal Netherlands Academy of Arts and Sciences
(KNAW) and University Medical Centre Utrecht, 3584 CT Utrecht,
the Netherlands

² Oncode Institute, Hubrecht Institute, 3584 CT Utrecht, the Netherlands

³ The Maastricht Multimodal Molecular Imaging Institute, Maastricht
University, 6229 ER Maastricht, the Netherlands

⁴ Central Diagnostic Laboratory (CDL) / Centre of Translational
Immunology (CTI), UMCU, The Netherlands

⁵ Department of Surgical Oncology, UMC Utrecht Cancer Center, Utrecht,
The Netherlands

⁶ Central Diagnostic Laboratory (CDL), University Medical Centre,
Utrecht, The Netherlands

⁷ Princess Máxima Center for Paediatric Oncology, Utrecht,
The Netherlands

⁸ Department of Paediatric Endocrinology, Wilhelmina Children Hospital,
University Medical Center Utrecht, Utrecht, The Netherlands

*Published in Proceedings of the National Academy of Sciences (2021);
doi: 10.1073/pnas.2117017118*

ABSTRACT

The thyroid maintains systemic homeostasis by regulating serum thyroid hormone concentrations. Here we report the establishment of three-dimensional (3D) organoids from adult thyroid tissue representing murine and human thyroid follicular cells (TFCs). The TFC organoids (TFCO) harbour the complete machinery of hormone production as visualised by the presence of colloid in the lumen and by the presence of essential transporters and enzymes in the polarised epithelial cells that surround a central lumen. Both the established murine as human thyroid organoids express canonical thyroid markers PAX8 and NKX2.1, while the thyroid hormone precursor thyroglobulin is expressed at comparable levels to tissue. Single cell RNA sequencing and transmission electron microscopy confirm that TFCOs phenocopy primary thyroid tissue. Thyroid hormones are readily detectable in conditioned medium of human TFCOs. We show clinically relevant responses (increased proliferation and hormone secretion) of human TFCOs towards a panel of Graves' disease patient sera, demonstrating that organoids can model human autoimmune disease.

INTRODUCTION

The thyroid gland is comprised of two histologically distinguishable cell types characterised by their representative hormone secretion: parafollicular cells, responsible for the secretion of calcitonin, and follicular cells which secrete the main thyroid hormones (TH) triiodothyronine (T3) and thyroxine (T4). Parafollicular cells (also known as clear-cells (C-cells) are relatively rare cells compared to the epithelial thyroid follicular cells (TFCs). TFCs line the follicles in which thyroid hormones are stored. This allows for a rapid release of thyroid hormones upon stimulation of the gland by thyroid stimulating hormone (TSH) secreted by the pituitary gland. A main component of TH, iodine, is transported from the circulation through TFCs into the follicle lumen. Transmembrane thyroid peroxidase (TPO) binds luminal iodine to tyrosine residues in the carrier protein thyroglobulin (TG). Upon stimulation by TSH T3 and T4 coupled TG are reabsorbed into TFCs. Through lysosomal degradation, T3 and T4 are released from TG and secreted into the blood stream. Negative T3/T4-driven feedback loops block secretion of TSH resulting in homeostasis¹. Both T3 and T4 affect many organ systems. The importance of maintaining thyroid hormone homeostasis is exemplified by the global incidence of thyroid-related diseases related to thyroid imbalance.

Graves' disease is a thyroid-specific autoimmune disorder resulting in increased levels of thyroid hormones with subsequent low levels of TSH. The incidence of Graves' hyperthyroidism in the Western world is around 20 cases per 100.000 individuals²⁻⁴. Graves' disease is characterised by the presence of anti-thyroid antibodies against the TSH receptor (TSHR) which activate downstream pathways, thus mimicking activation by TSH. This results in overproduction of T3 and T4 and subsequent low levels of TSH. Graves' disease patients suffer from a variety of symptoms due to thyrotoxicosis, including an enlarged thyroid, anxiety and tremor and may have bulging eyes due to swelling of the tissue in the orbit⁵. Current treatment consists of anti-thyroid therapy reducing the levels of T3 and T4 and normalising TSH levels⁶. Approximately half of the patients treated with anti-thyroid drugs ultimately require additional treatment such as radio-iodine or thyroidectomy often resulting in hypothyroidism for which patients have to take lifelong hormone replacement⁷. Generation of an *in vitro* model system that would allow for better understanding of thyroid-related diseases such as Graves' disease could potentially lead to the development of alternative treatment options. Moreover, the generation of a transplantable thyroid culture system could potentially restore normal thyroid function.

Several different model systems have been employed to study thyroid biology and Graves' disease. As early as in the 1950s, two-dimensional TFC layers were used as short-term thyroid cultures⁸. These 2D layers, however, do not form normal physiological follicles and can't be propagated. Submerging TFCs in suspension cultures including extracellular matrix components generates 3D polarised spheroids with a follicle architecture, but can still not be maintained long-term⁹. Alternatively, mouse models have shown potential as

1

2

3

4

5

6

7

8

9

&

model systems for thyroid biology and Graves' disease modelling. The cost- and time-effectiveness of these studies however remains a limiting factor¹⁰. These limitations can potentially be overcome by human adult stem cell-derived organoids. These three-dimensional cultures are representative *in vitro* model systems which recapitulate human physiology¹¹. While we were finalising the current study, Coppes and colleagues reported a first description of transplantable human (and mouse) thyroid organoids¹². In this study, we report similar findings and apply TFCOs to model Graves' diseases using patient sera.

MATERIALS AND METHODS

Patient samples

Human thyroid biopsies were anonymously obtained from the Department of Surgery at the University Medical Center Utrecht (UMCU) from waste material of patients undergoing surgery at the UMCU. The use of sample for research and informed consent procedures were approved by the medical ethical committee (TCBio) of the UMCU as protocol 12-093 and was in accordance with the Declaration of Helsinki and according to Dutch law. This study is compliant with all relevant ethical regulations regarding research involving human participants. Informed consent was obtained prior to surgery. Samples were de-identified for the researcher to keep patient data at the medical center.

Mice

All animal experiments were performed after institutional review by the Animal Ethics Committee of the Royal Netherlands Academy of Arts and Sciences (KNAW) with project license AVD8010020151. Surplus material from female C57BL/6 was used to derive organoids in this study.

Thyroid organoid culture

Organoid derivation and analysis is adapted from earlier described protocols⁵¹.

Human samples were kept in Advanced DMEM/F12 solution (GIBCO) with Pen/Strep (Thermo Fisher scientific) at 4°C until further processing. For both mouse and human, complete or part of the gland was chopped into small pieces of approximately 1 mm using a scalpel. Tissue pieces were enzymatically digested in digestion medium for about 25-30 minutes shaking (120 RPM) at 37°C. Composition of the medium is further described in the SI appendix. The homogeneous cell suspension was pelleted and washed with AdDMEM/F12. The tissue was resuspended in 1mL Red blood cell lysis buffer (Roche, 11814389001) and incubated at RT for 5 min. Fragments were mechanically dissociated using narrowed glass pipette. Cells from a single murine thyroid were plated in approximately 100 µL Cultrex Pathclear Reduced Growth Factor Basement Membrane Extract (BME) (3533-001, Amsbio). For human biopsies the volume of BME was determined based on the size of the final pellet. After BME solidification, complete expansion medium was added. Splitting procedures are further described in SI Appendix.

Organoids were frozen for long-term storage using CellBanker I (11888; AMSBIO Europe B.V.) following manufacturers protocol. In short, organoids were grown for 2-5 days after splitting. Organoids were removed from BME using DMEM+P/S and spun down. Pellet was resuspended in CellBanker I and immediately transferred to -80°C. For storage over 2 months, vials were moved to liquid nitrogen storage boxes.

Viability assays

Cell viability was determined using CellTiterGlo 3D (Promega) according to the manufacturer's instructions. More detailed protocol is discussed in SI Appendix.

Immunohistochemistry and imaging

Organoids were harvested in Cell Recovery solution (354253, Corning) and fixed in 4% paraformaldehyde (Sigma-Aldrich) for at least 2 hours at room temperature. Thyroid tissue used for immunohistochemistry was directly fixed in 4% paraformaldehyde upon dissection and incubated for at least 2 hours at room temperature or overnight at 4°C. Samples were washed and dehydrated by an increasing ethanol gradient and washed in xylene before embedding in paraffin. Sections were cut and hydrated before staining. Slides were imaged using a Leica DM4000 microscope.

For immunofluorescence, organoids were harvested, fixed and permeabilized using 0.2% Triton X-100. Whole-mount staining was performed overnight in 2% goat serum. Organoids were imaged on a Leica SP8X or SP8 microscope.

Antibodies used in this manuscript are listed in the SI Appendix.

qPCR analysis

RNA isolations of organoids and tissue for bulk RNA sequencing and qPCR were performed with RNeasy Mini Kit (QIAGEN) following the manufacturer's instructions. Quantitative PCR analysis was performed using the SYBR Green and Bio-Rad systems. Changes in expression relative to housekeeping gene and thyroid or lung tissue when indicated were calculated using CFX manager software (Bio-Rad). Primers were designed using NCBI primer design tool and are indicated in de SI Appendix.

Bulk mRNA sequencing

Bulk mRNA sequencing was performed by the Utrecht Sequencing Facility (USEQ) using the TruSeq stranded mRNA kit (Illumina). In short, polyA enriched RNA was reverse transcribed and paired-end reads mapped to the mouse genome. Expression data was analysed using DESeq2⁵².

Single-cell mRNA sequencing

For single-cell sequencing of the tissue, mouse thyroid was dissociated with collagenase I (Sigma-Aldrich) as described above and subsequently resuspended in TrypLE Express

1

2

3

4

5

6

7

8

9

&

(GIBCO) pre-heated to 37°C and dissociated under repeated pipetting. For single-cell sequencing of TFCOs, organoid droplets were incubated in Cell Recovery solution (354253, Corning) for 30 minutes in order to dissolve the BME. Then, organoids were pelleted and resuspended in TrypLE Express (GIBCO) pre-heated to 37°C and dissociated under repeated pipetting. When the gland and the organoids were fully dissociated into single cells, samples were pelleted, washed, resuspended in FACS buffer (advanced DMEM/F12, 10 µM Y-27632 and DAPI) and strained (35 µm).

DAPI-negative cells were immediately sorted into 384-well plates containing ERCC spike-ins (Agilent), RT primers and dNTPs (Promega) using a FACSFusion (BD Biosciences). Plates were prepared using Mosquito HTS (TTPlabtech). Single-cell RNA sequencing libraries were prepared following the SORT-seq protocol²⁶ which is based on the CEL-seq2 method⁵³. Extensive explanation of the protocol can be found in the SI Appendix.

Transmission electron microscopy

Organoids were chemically fixed for 3 hours at room temperature with 1.5% glutaraldehyde in 0.067 M cacodylate buffered to pH 7.4 and 1 % sucrose. Samples were washed once with 0.1 M cacodylate (pH 7.4), 1 % sucrose and 3x with 0.1 M cacodylate (pH 7.4), followed by incubation in 1% osmium tetroxide and 1.5% $K_4Fe(CN)_6$ in 0.1 M sodium cacodylate (pH 7.4) for 1 hour at 4 °C. After rinsing with MQ, organoids were dehydrated at RT in a graded ethanol series (70, 90, up to 100%) and embedded in epon. Epon was polymerized for 48h at 60 °C. 60nm Ultrathin sections were cut using a diamond knife (Diatome) on a Leica UC7 ultramicrotome, and transferred onto 50 Mesh copper grids covered with a formvar and carbon film. Sections were post-stained with uranyl acetate and lead citrate.

All TEM data were collected autonomously as virtual nanoscopy slides⁵⁴ on FEI Tecnai T12 microscopes at 120kV using an Eagle camera. Data were stitched, uploaded, shared and annotated using Omero⁵⁵ and PathViewer.

AITD patient serum

Patient serum were anonymously obtained from Henny Otten at the University Medical Center Utrecht (UMCU) from waste material of patients diagnosed at the UMCU. The use of sample for research was approved by the medical ethical committee (TCBio) of the UMCU as protocol 21-013 and was in accordance with the Declaration of Helsinki and according to Dutch law. This study is compliant with all relevant ethical regulations regarding research involving human participants.

TSHR autoantibodies were detected and quantified with the ELiA anti-TSH-R assay with sample processing by the Phadia 250 instrument, performed as specified by the manufacturer (ThermoFisher Scientific, Uppsala, Sweden) as described before⁵⁶. Serum was categorised as Graves' disease serum when TSHR-Ab titers were >3.3 IU/L and as normal serum when <3.3IU/L. Serum was aliquoted and stored at -20°C until use.

Free T3 analysis

Organoids were expanded as mentioned above. After organoids reached cystic morphology (4-6 days after splitting), medium was changed to experimental medium which included indicated supplements. Medium was harvested after 48h and kept at 4°C for maximum of two days or -20°C for extensive periods until analysis. For luminal content, medium was removed and organoids were spun down and resuspended in 800µl expansion medium. The organoids were broken using a narrowed glass pipette and spun down. Supernatant was collected and send for analysis. For intracellular content, organoids were harvested, broken using narrowed glass pipette and sonicated for 15 cycles 30sec and 30 sec pause using Branson sonicator SFX250. Samples were spun down and supernatant was sent for analysis.

Analysis was performed by Central Diagnostic Laboratory at UMCU. The FT3 measurements were performed, as specified by the manufacturer, on the Atellica® IM analyzer (Siemens Healthineers). Lowest concentration that can be measured with 95% confidence is 0.1pmol/L.

Statistical analysis

No statistical method was used beforehand to determine sample size. The investigators were not blinded and no data points was excluded. Data is represented as mean ± standard deviation. The number of duplicates as well as the type of test performed is indicated in each figure legend.

RESULTS

Based on our previously described 3D culturing conditions of long-term expansion of mouse and human organoids from a variety of other tissues, we dissected and minced thyroid tissue, incubated the fragments in digestion solution and plated thyroid cells in basement membrane extract (BME). We optimized mouse TFCO medium by trial and error, to define a medium containing cyclic AMP (cAMP) activator forskolin (FSK), the Wnt potentiator R-spondin (RSPO), transforming growth factor beta (TGFβ) inhibitor A83-01, epidermal growth factor (EGF) and fibroblast growth factor 10 (FGF10). Human samples required the addition of Wnt surrogate¹³, p38 inhibitor and TSH before significant growth could be observed (**Figure 1A**). Using these expansion media, organoids first formed after 4 days (mouse) or 1-2 weeks (human) and continued to grow over a 3-6 week period. Thereafter, organoids could be mechanically passaged at a ratio of 1:3-1:7 every two weeks. The organoids could be maintained over 24 passages without significant change in morphology (to date we have reached passage 35 for mouse and passage 24 for human) (**Figure 1B and D**). The organoids were polarised in an 'apical-in' orientation, as shown by the apical marker ZO-1 (**Supplementary figure S1A**). To confirm the cellular composition of the organoids, we used RT-qPCR, immunofluorescence and immunohistochemistry. We observed expression of the generic TFC markers *Pax8/PAX8* and *Nkx2.1/NKX2.1*

1

2

3

4

5

6

7

8

9

&

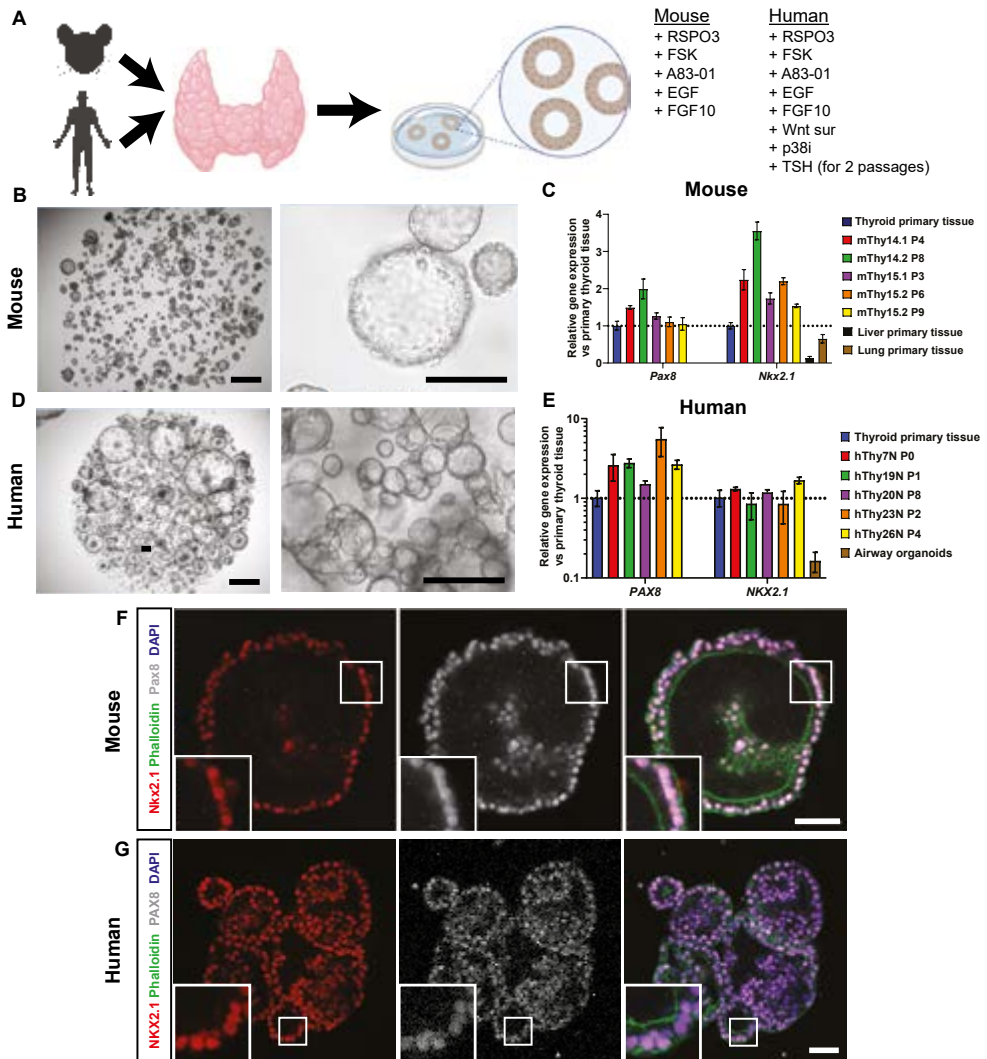


Figure 1. Establishment of thyroid follicular cell organoids from mouse and human origin. A) Schematic representation of organoid derivation of thyroid follicular cell organoids (TFCOs) including medium components required for the establishment of murine TFCOs. Human TFCOs require additional components for establishment. B) Brightfield images of murine TFCO cultures show cystic organoids grown in BME. Scale bars = 1mm (left panel), 100µm (right panel). C) RT-qPCR analysis reveals similar to increased levels of Pax8 and Nkx2.1 expression in mouse TFCOs compared to primary thyroid tissue in early (<4 passages) and late (>6 passages) TFCOs while lung and liver tissue shows lower expression levels. N=3. Error bars = stdev. D) Brightfield images of human TFCO cultures show cystic organoids grown in BME. Scale bars = 1mm (left panel), 250µm (right panel). E) RT-qPCR analysis reveals similar to increased levels of PAX8 and NKX2.1 expression in human TFCOs compared to primary thyroid tissue in early (<4 passages) and late (>6 passages) TFCOs while lung tissue shows lower expression levels. N=3. Error bars = stdev. F-G) Co-expression of thyroid transcription factors Nkx2.1/NKX2.1 (red) and Pax8/PAX8 (grey) in all cells in mouse (F) and human (G) TFCOs shows a pure population of TFCs in the organoids. Membrane staining using Phalloidin (green) and nucleus staining using DAPI shows a single cell layer surrounding the lumen. Scale bar = 100µm.

(formerly known as thyroid transcription factor-1 (TTF-1)), in murine and human organoids. The expression appeared to be increased compared to primary thyroid tissue. Primary thyroid tissue, however, includes stromal cell types which could explain this difference. The levels were comparable between different mouse and human donors (**Figure 1C and E**). By immunofluorescence, combinatorial nuclear expression of the two transcription factors (Nkx2.1/NKX2.1 and Pax8/PAX8) was confirmed in all cells in the organoids (**Figure 1F-G and Supplementary figure S2A-B**). While both transcription factors are expressed in other tissues including lung for *NKX2.1* and kidney for *PAX8*, co-expression of these transcription factors is unique to TFCs¹⁴. Since all analysed cells in the organoids were positive for both transcription factors, we concluded that the organoids mainly consisted of expanding populations of TFCs.

To further characterise the TFCOs, we performed bulk mRNA sequencing on organoids at early and late passages for comparison with thyroid tissue and airway tissue (**SI Appendix, Dataset S1-2**), the latter as unrelated control tissue. Hierarchical clustering of the samples based on known thyroid-expressed genes showed extensive overlap between organoid samples and thyroid tissue samples, while clustering away from the lung tissue (**Figure 2A and C**). Both murine and human TFCO samples showed comparable levels of i.e. *TPO*, *PAX8*, *DUOX2* to primary tissue. TFCOs were stable as deduced from early and late passage TFCO expression data. When single genes were extracted and compared to primary tissue data, we observed a slight decrease in levels of some thyroid maturation markers like *TG* in both mouse and human TFCOs (**Figure 2B and D**). This could be due to the proliferative nature of cells within organoids compared to the *in vivo* situation. This proliferative nature is confirmed by the expression of *MKI67* in a subset of cells within the organoids while being absent in the thyroid tissue (**Supplementary figure S1B/2C**). Thyroid stem-like cells have been discussed for decades without a general consensus^{15,16}; the proliferative cells in the TFCOs likely represent their *in vitro* counterparts. We analysed the presence of proposed stem cell markers in human TFCOs. Since we observed a gradually increasing growth rate from passage 5 onwards, we hypothesised that such stem cell markers would become evident when comparing tissue to early passage TFCOs and would increase in expression from early to late passage organoids. No significant change in expression was identified in the putative stem cell markers *SCA1*^{17,18}, *ABCG2*^{17,19}, *FUT4*¹², *GATA4*²⁰, *HNF4A*²⁰, *NANOG*²¹, *OCT4*^{12,17,20-22} and *HHEX*^{15,23} in human TFCOs (**Supplementary figure S3A-J**). Increased expression was noted for *NGFR* and *FOXE1* (TTF2)²⁴ while *SOX2*^{12,22} was enriched in late passage human TFCOs (**Supplementary figure S3K-M**). Of note, the latter three genes were not upregulated in mouse TFCOs compared to tissue (**Supplementary figure S3N-P**).

To further delve into cellular heterogeneity in the organoids, we performed single cell sequencing²⁵ on mouse primary tissue and early and late passage mouse TFCOs. We sorted and processed, using the SORT-seq method²⁶, a total of 747 primary tissue cells and 1,843 TFCO cells which passed quality control. Clustering of the cells revealed nine clusters which could be annotated using known marker genes (**Figure 3A**). Some clusters

1

2

3

4

5

6

7

8

9

&

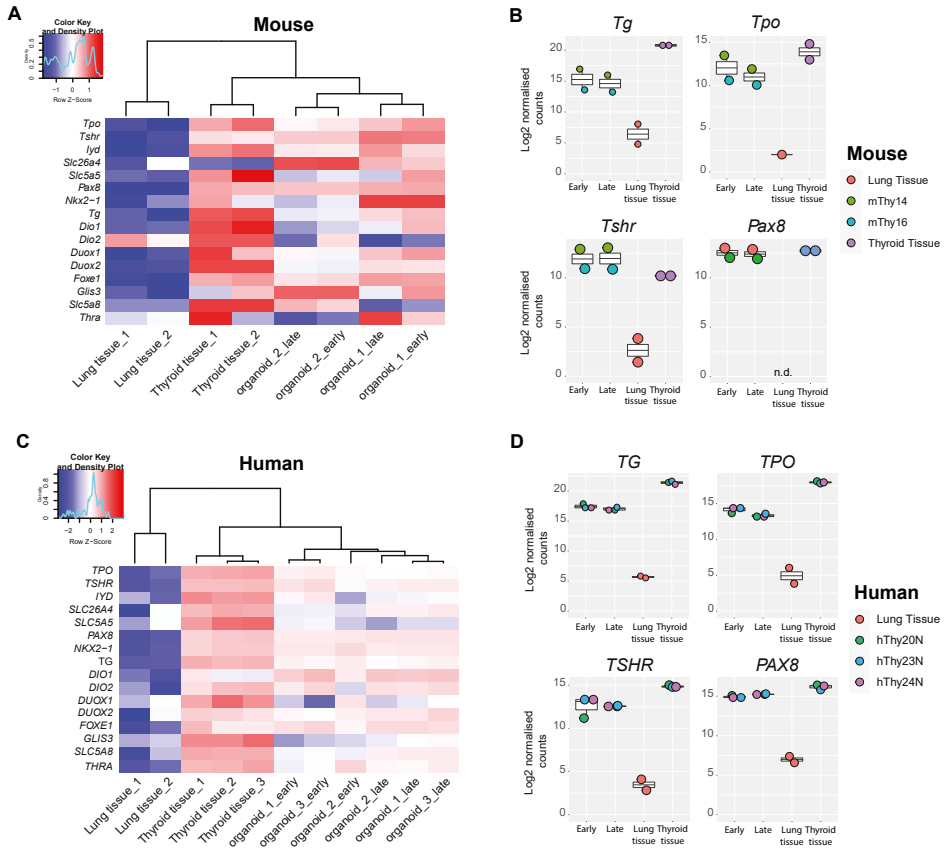


Figure 2. Bulk mRNA sequencing reveals limited differences between late and early passage TFCOs and primary thyroid tissue. A) Heatmap indicating the expression of thyroid follicular cell markers in mouse primary thyroid tissue, lung tissue and mouse TFCOs in early and late passages. TFCOs cluster with thyroid tissue in unsupervised hierarchical clustering and apart from lung tissue. Organoid 1 = mThy14, organoid 2 = mThy16. Coloured bar represents row z-scores of log₂ transformed normalised counts. Density plot indicates the fraction of genes with the given row z-score. B) Boxplots of mouse primary thyroid tissue (Thyroid tissue), early passage TFCOs (Early) and late passage TFCOs (Late) as well as primary lung tissue (Lung tissue) Log₂ transformed normalised counts of bulk mRNA sequencing. Expression levels of *Tg*, *Tpo*, *Tshr* and *Pax8* are comparable to thyroid tissue. Colour of the dots indicates donor visualised as described on the right. Boxplot shows median, two hinges (25th and 75th percentile) and two whiskers (largest and smallest value no further than 1.5x inter-quartile range). n.d. = not detected. C) Heatmap indicating the expression of thyroid follicular cell markers in human primary thyroid tissue, lung tissue (GSE148815) and human TFCOs in early and late passages. TFCOs cluster with thyroid tissue in unsupervised hierarchical clustering and apart from lung tissue. Organoid 1 = hThy20N, organoid 2 = hThy23N and organoid 3 = hThy24N. Coloured bar represents row z-scores of log₂ transformed normalised counts. Density plot indicates the fraction of genes with the given row z-score. D) Boxplots of human primary thyroid tissue (Thyroid tissue), early passage TFCOs (Early) and late passage TFCOs (Late) as well as primary lung tissue of GSE148815 (Lung tissue) Log₂ transformed normalised counts of bulk mRNA sequencing. Expression levels of *TG*, *TPO*, *TSHR* and *PAX8* are comparable to thyroid tissue. Colour of the dots indicates donor visualised as described on the right. Boxplot shows median, two hinges (25th and 75th percentile) and two whiskers (largest and smallest value no further than 1.5x inter-quartile range).

were only composed of cells originating from primary tissue, including 58 monocytes expressing *Ptprc* and *Lyz2*, 197 stromal cells expressing *Col3a1* and 216 endothelial cells expressing *Ly6a* (**Figure 3B and Supplementary figure S4**). Some *Calca*-expressing cells could be identified within the tissue cell sample, indicative of parafollicular/C-cells. A single *Calca* expressing cell was identified in the organoids underscoring the rapid loss of these neural crest-derived cells in the epithelial TFCOs (**Supplementary figure S4G-H**). This observation was confirmed by the loss of *Calca* expression as determined by RT-qPCR (**Supplementary figure S4I**). The majority of the cells (2,119 cells (276 cells from primary tissue and 1843 cells from TFCOs) expressed *Pax8*, *Tpo* and *Nkx2.1* and could therefore be annotated as TFCs (**Figure 3B-C**). Satisfyingly, TFCs from the primary tissue clustered with TFCs from TFCOs underscoring the high similarity between cultured and primary TFCs (**Figure 3D**). After reclustering of all TFCs, seven TFC clusters became evident (**Figure 3E**), while tissue TFCs continued to co-cluster with TFCO TFCs (**Figure 3F**). *Tg* levels between TFCs from organoids and primary tissue cells were similar, yet rare cells with high *Tg* levels were only seen in primary tissue (**Figure 3G**).

Differential expression analysis between the clusters revealed relatively minor differences between the clusters with the exception of cluster 5, which uniquely expressed multiple genes involved in cell cycling, including *Mki67*, *Ccnb2* and *Pcna* (**Figure 3H**). In agreement, cluster 5 only contained organoid-derived TFCs (**Figure 3E-F**) while expression levels of the TFC maturation marker *Tg* was slightly lower compared to the other clusters (**Figure 3I**). Thus, cluster 5 cells represented the proliferative TFC progenitors, also seen by immunofluorescence (**Supplementary figure S1B and S2C**). The relative proportion of proliferative cells (within cluster 5 of each line) ranged between 4-13%. Since this subpopulation could potentially contain the elusive thyroid stem cells, we performed differential expression analysis and identified 148 significantly ($p < 0.01$) enriched genes (**SI Appendix, Dataset S3**). None of the proposed stem cell markers (see above) were present in this list or were enriched in the proliferative TFC cluster with the exception of *Hhex*. *Hhex* was enriched in proliferative TFCs compared to other TFCs (**Supplementary figure S5A-B**) as well as in late passage TFCOs compared to early passage TFCOs and primary tissue (**Supplementary figure S5C**). Mouse *Hhex* expression was observed by bulk mRNA sequencing data to be higher in TFCO cultures than in primary tissue (**Supplementary figure S5D**) while *HHEX* levels in human TFCOs were similar to primary tissue (**Supplementary figure S3J**). It was therefore unlikely that *HHEX* performs similar functions in human and mouse TFCs. The lack of a single population and the high comparability between the populations might indicate that thyroid tissue and organoids do not harbour professional stem cells. The growth of organoids may therefore be due to the presence of a transient proliferative cell pool with high resemblance to mature TFCs. Moreover, we concluded that the single cell atlas of the mouse thyroid and TFCOs showed high similarity between TFCs derived from primary tissue and from TFCOs as well as within the TFC population.

1
2
3
4
5
6
7
8
9
&

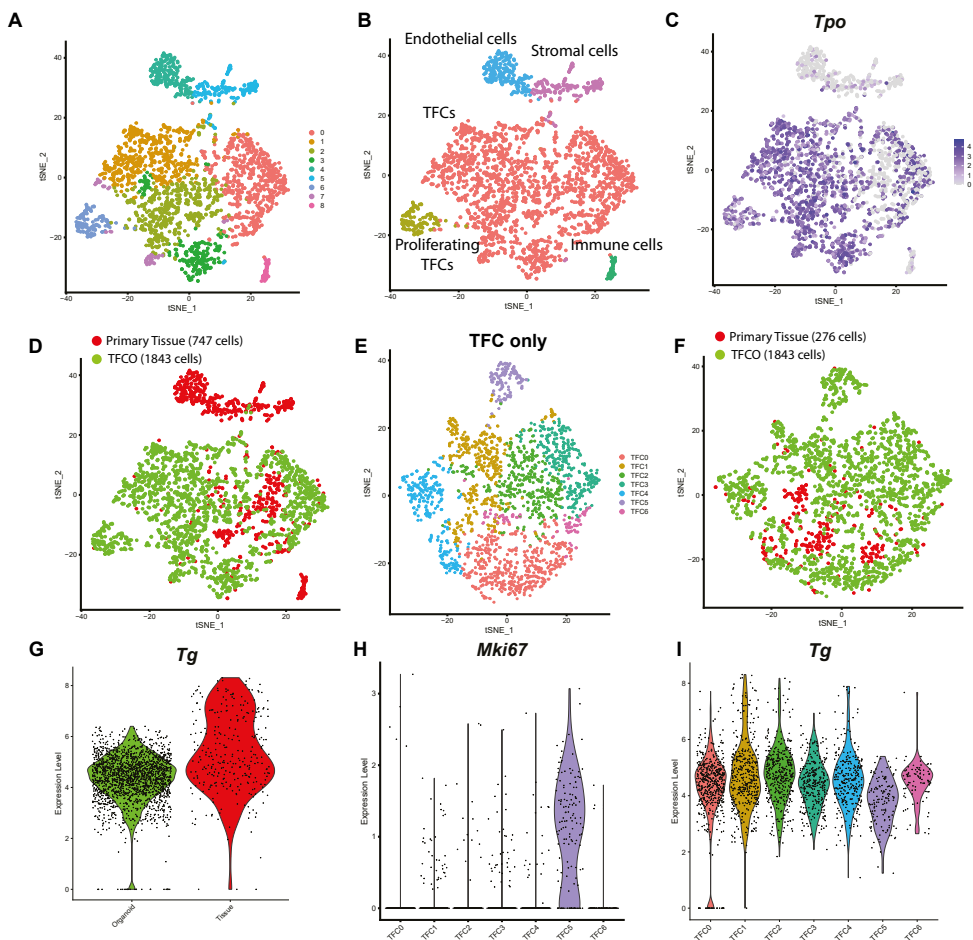


Figure 3. Single cell RNA sequencing of mouse TFCOs and primary tissue reveals limited differences between TFCs except for a proliferative population in organoids. A) tSNE representation of 9 clusters of mouse thyroid tissue cells (n = 747) and mouse TFCO cells (n=1843). B) tSNE representation of 5 cell types of mouse thyroid tissue cells (n = 747) and mouse TFCO cells (n=1843). B) tSNE representation of the expression of TFC-specific peroxidase *Tpo* (linear scale). D) tSNE representation of 2 origins of mouse thyroid tissue cells (n = 747) and mouse TFCO cells (n=1843) visualising overlap between tissue-derived and TFCO-derived TFCs. E) tSNE representation of 7 clusters of mouse thyroid tissue TFCs (n = 276) and mouse TFCO TFCs (n=1843) after reclustering. F) tSNE representation of 2 origins of mouse thyroid tissue TFCs (n = 276) and mouse TFCO TFCs (n=1843) after reclustering visualising the overlap between tissue-derived and TFCO-derived TFCs. G) Violin plots of the normalized expression level of *Tg* in TFCOs ("organoid", n = 1843 cells) and primary thyroid tissue ("Primary tissue", n = 276 cells) show similarity in expression levels with the exception of some more mature TFCs in thyroid tissue. H) Violin plots of the normalized expression level of *Mki67* in TFC clusters indicates the presence of a proliferative subpopulation of TFCs in cluster TFC5. I) Violin plots of the normalized expression level of *Tg* in TFC clusters indicates a less mature population of TFCs in cluster TFC5.

Since expression levels indicated maturity and functionality of the TFCOs, we examined the presence of the thyroid hormones machinery in murine and human TFCOs (**Figure 4**). In agreement with the sequencing data, TFCOs of murine and human origin both expressed high levels of *Tg/TG* and *Tpo/TPO*, essential for generation and storage of thyroid hormones (**Figure 4A-B**). Expression of *Tshr/TSHR* was similar between primary tissue and TFCOs from both species (**Figure 4A-B**). This indicated the potential of TFCOs to respond to TSH. TG is the carrier protein of thyroid hormones and allows for rapid hormone secretion without the need for transcription and translation; it is stored as colloid in the lumen of follicles. Five days after splitting, murine TFCOs contained a population of Tg-expressing cells (**Supplementary figure S1C**). When these TFCOs are maintained for 21 days without splitting, the lumens were filled with Tg, resembling the *in vivo* situation (**Figure 4C and Supplementary figure S2D**). Human TFCOs expressed cytoplasmic Tg in most if not all cells, while luminal TG was much less prominent (**Figure 4D**). This was likely due to the repeated swelling and bursting of human TFCOs (not observed in mouse TFCOs), potentially leading to continuous loss of luminal Tg. To document the potential of iodine transport and thyroid hormones production by human TFCOs, we analysed the expression of iodine transporters *SLC5A5* (sodium/iodine symporter (NIS)) and *SLC26A4* (Pendrin) as well as the T3 transporter *SLC16A2* (MCT8). All three transporters were expressed in human TFCOs (**Figure 4E**). Combined with the expression of *TPO* and *TG*, this indicated functionality of hormone production and secretion of human TFCOs. Secretion of thyroid hormones in the form of Free T3 (FT3) was successfully observed in medium collected from TFCOs 24h after replacing the medium by PBS (**Figure 4F**). Thus, TFCOs possessed the thyroid hormones machinery and could secrete thyroid hormones from their basal side.

We next performed transmission electron microscopy on both mouse and human TFCOs. Only follicular cells were identified in a typical thyroid gland organisation as a single layer of cells around the lumen. Colloid was identified in the lumen of most mouse and human TFCOs (**Figure 5A-B and F-G**). Moreover, abundant potential small secretory and endocytic vesicles transporting thyroglobulin to and from the lumen and hetero- or endolysosomal vesicles created by the fusion of lysosomes with the vesicles reabsorbing thyroglobulin could be detected (**Figure 5C and H-I**), indicative of active transport of Tg/TG and thyroid hormones. Underlining the active translation of carrier protein Tg and other thyroid hormones machinery, we observed typical swollen rough endoplasmic reticulum present in the follicular cells of the thyroid where thyroglobulin synthesis takes place (**Figure 5D**). Additionally, short microvilli were observed on the apical membrane projecting into the colloid of mouse and human TFCs (**Figure 5E and J**) and the follicle cell junctional complexes restricting colloid to the lumen (**Figure 5E**). All these features agree with earlier reports of transmission electron microscopic studies of rat thyroid²⁷⁻²⁹.

TSH stimulates the expression of iodine transporter *SLC5A5*, stimulates hormone formation and TG endocytosis and proteolysis and induces the secretion of thyroid hormones. Prolonged TSH stimulation of the thyroid gland induces hyperplasia^{30,31}.

1

2

3

4

5

6

7

8

9

&

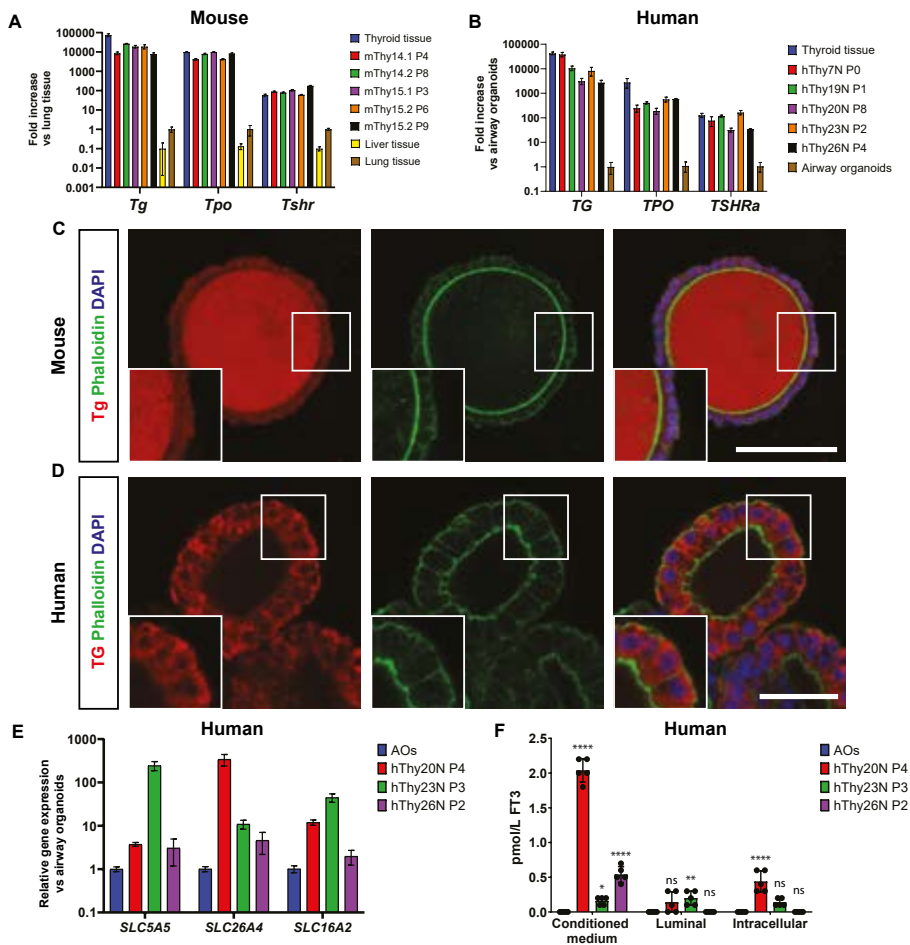


Figure 4. TFCOs express thyroid hormone machinery and secrete thyroid hormone basally. A) RT-qPCR analysis reveals similar levels of Tg, Tpo and Tshr expression in mouse TFCOs compared to primary thyroid tissue in early (<4 passages) and late (>6 passages) TFCOs while liver tissue shows lower expression levels. Expression levels are relative to lung tissue expression levels. N=3. Error bars = stdev. B) RT-qPCR analysis reveals slightly lower yet significant levels of TG and TPO and similar levels of TSHRa expression in human TFCOs compared to primary thyroid tissue in early (<4 passages) and late (>6 passages) TFCOs. Expression levels are relative to airway organoid expression levels. N=3. Error bars = stdev. C) Mouse TFCs secrete Tg (red) towards the lumen in TFCOs similar to TFCs in follicles in vivo. Membrane staining using Phalloidin (green) and nucleus staining using DAPI (blue). Scale bar = 100um. D) Human TFCs express TG (red) cytoplasmically in TFCOs. Membrane staining using Phalloidin (green) and nucleus staining using DAPI (blue). Scale bar = 50um. E) RT-qPCR analysis reveals expression of iodine transporters SLC5A5 and SLC26A4 and thyroid hormone transporter SLC16A2 in human TFCOs. Expression levels are relative to airway organoid (AOs) expression levels. N=3. Error bars = stdev. F) Human TFCOs in varying passages secrete variable yet measurable levels of free T3 (FT3) basally (conditioned medium) while apical secretion (luminal) is minimal or non-detectable. Some levels of FT3 are identified intracellularly (intracellular) yet at lower levels compared to basally. AOs = airway organoids. Each dot represents a separate expanded well of organoids measured. N=5. Error bars = stdev. ns = not significant, * = $p < 0.05$, ** = $p < 0.01$, **** = $p < 0.0001$ using two-way ANOVA with Tukey's multiple comparisons to AOs.

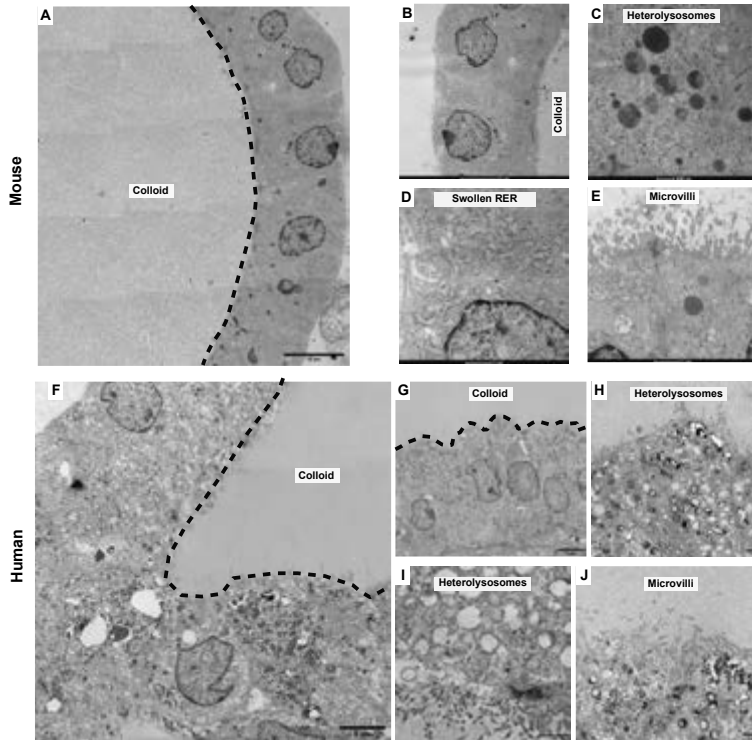


Figure 5. TFCs show short microvilli, swollen RER cisternae and heterolysosomes and electron-dense follicular lumens in TFCOs. A) Overview image of transmission electron microscopy image reveals a variable in density lumen like the thyroid follicles show filled with potential colloid (dashed line indicates boundary of lumen) in mouse TFCOs. Scale bar = 10 μ m. B) Detailed zoom-in reveals a single cell layer of TFCs with cubic to columnar cells containing the nucleus in the basal area in mouse TFCOs. Scale bar = 5 μ m. C) Extensive heterolysosomes can be observed in mouse TFCOs indicating active transport of thyroglobulin to and from the lumen. Scale bar = 500nm. D) Swollen rough endoplasmic reticulum (RER) is present in mouse TFCOs indicative of TFCs. Scale bar = 1 μ m. E) Finger-like extensions of the plasma membrane can be observed as microvilli on the apical membrane of TFCs in mouse TFCOs. Scale bar = 1 μ m. F) Overview image of transmission electron microscopy image reveals a variable in density lumen like the thyroid follicles show filled with potential colloid (dashed line indicates boundary of lumen) in human TFCOs. Scale bar = 5 μ m. G) Detailed zoom-in reveals a single cell layer with cubic to columnar cells containing the nucleus in the basal area of TFCs in human TFCOs. Scale bar = 5 μ m. H-I) Extensive heterolysosomes can be observed in human TFCOs indicating active transport of thyroglobulin to and from the lumen. Scale bars = 1 μ m. J) Finger-like extensions of the plasma membrane can be observed as microvilli on the apical membrane of TFCs in human TFCOs. Scale bar = 1 μ m

Given the expression at physiological levels of TSHR, which signal through cAMP^{32,33}, we performed growth assays upon addition of TSH. ATP-levels in the CellTiter Glo assay were used as surrogate for proliferation. Since Forskolin (FSK) also activates cAMP signalling, we removed FSK from the medium. Satisfyingly, growth of mouse TFCOs as well as human TFCOs was increased when assayed over a period of 7 days upon TSH stimulation

1

2

3

4

5

6

7

8

9

&

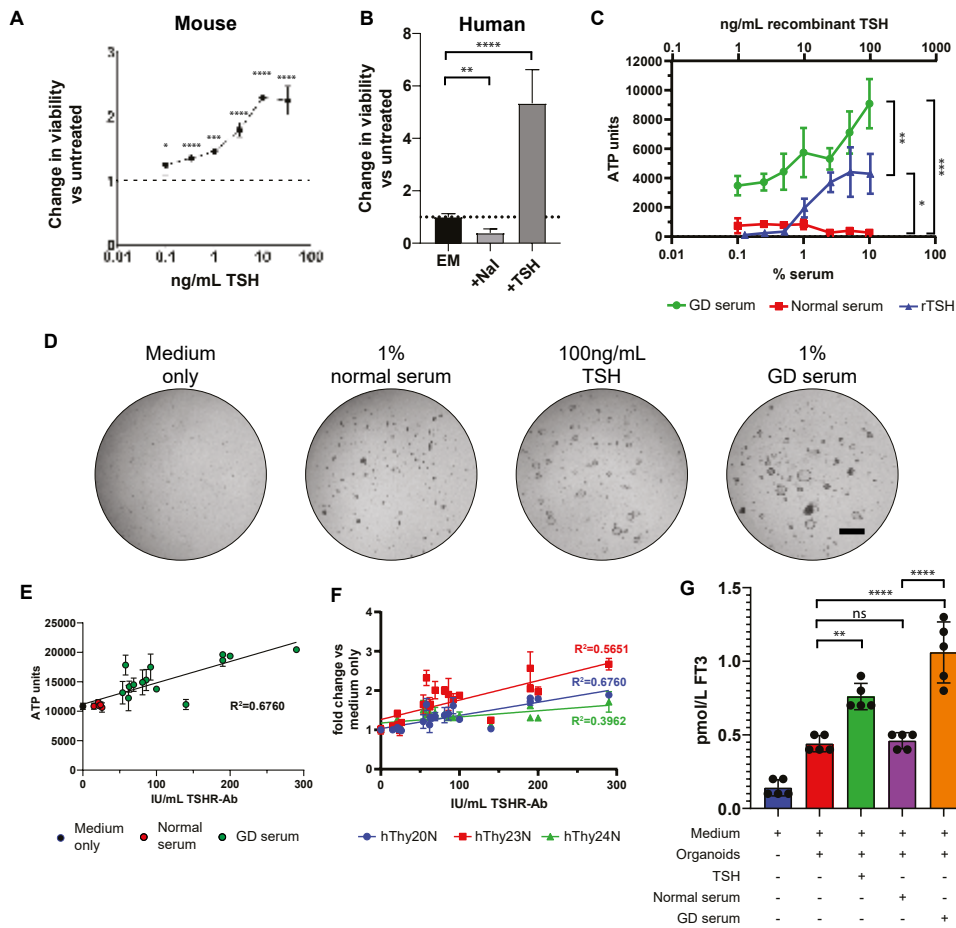


Figure 6 TFCOs model Graves' disease by increased proliferation and hormone secretion after TSHR-Ab stimulation. A) Addition of TSH increases viability of mouse TFCOs compared to TFCOs cultured without TSH after 7 days. All data points are relative to TFCOs grown in the absence of TSH and FSK. N=3 per datapoint. Error bars = stdev. * = $p < 0.05$, *** = $p < 0.001$, **** = $p < 0.0001$ using two-way ANOVA with Tukey's multiple comparisons to untreated samples. B) Human TFCOs increase viability upon addition of 100ng/mL TSH (+TSH) as compared to expansion medium (EM) after 7 days. Addition of sodium iodide (NaI) decreases viability of human TFCOs as compared to EM. N=3. Error bars = stdev. ** = $p < 0.01$, **** = $p < 0.0001$ using two-way ANOVA with Tukey's multiple comparisons. C) Increased viability is observed in human TFCOs when cultured for 10 days with 10-100ng/mL recombinant (rTSH) (top axis) compared to untreated TFCOs. More extensive increase in viability is observed when TFCOs are cultured for 10 days with serum of Graves' disease patients (TSHR-Ab >3.3IU/L) (lower axis). Incubation with normal serum (TSHR-Ab <3.3IU/L) did not show increased viability of TFCOs even when using 10% serum (lower axis). N=3. Error bars = stdev. * = $p < 0.05$, ** = $p < 0.01$, *** = $p < 0.001$ using two-way ANOVA with Tukey's multiple comparisons. D) Representative brightfield images shows limited outgrowth in expansion medium without FSK (medium only) and 1% normal serum (TSHR-Ab <3.3IU/L) after 10 days. Increased outgrowth is visible in cultures grown with 100ng/mL TSH after 10 days. More extensive outgrowth and organoid size is observed in cultures grown in 1% GD serum (TSHR-Ab >3.3IU/L). Scale bar = 1 mm. E) Incubation of TFCOs with 1% serum with varying TSHR-Ab titers reveals correlation between TFCO growth and

- TSHR-Ab titers. Each dot represents a single serum tested in triplicate. Colour of the dots indicate category of serum being medium only (black), normal serum (TSHR-Ab <3.3IU/L) (red) or GD serum (TSHR-Ab >3.3IU/L) (green). N=3 per datapoint. Error bars = stdev. R2 using Pearson correlation. F) Comparison between three different donors (indicated in different colours) in a similar assay as figure 6E shows correlation of TSHR-Ab titers and TFCO growth in all donors yet with variable slopes. N=3 per datapoint. Error bars = stdev. R2 using Pearson correlation. G) Stimulation with 100ng/mL recombinant TSH or 1% GD serum (TSHR-Ab >3.3IU/L) increases free T3 (FT3) levels in conditioned medium of human TFCOs after 48h. No significant increase in FT3 levels is observed when TFCOs are stimulated with 1% normal serum (TSHR-Ab <3.3IU/L) compared to medium in combination with organoids. Each dot represents a separate expanded well of organoids measured. N=5. Error bars = stdev. ns = not significant, ** = p<0.01, **** = p<0.0001 using two-way ANOVA with Tukey's multiple comparisons.

(Figure 6A-B) in a dose-dependent manner (Figure 6A). Contrarily, we observed reduced growth upon addition of iodine (sodium iodide (NaI)) in human TFCOs (Figure 6B). In patients with Graves' disease, the anti-TSHR autoantibodies overactivate the TSH-pathway resulting into hyperthyroidism. As shown above, TFCOs respond to TSH. To test if the TFCOs would also respond to TSHR-Abs, we incubated human TFCOs with sera from a Graves' disease patient (GD serum) (TSHR-Ab titers > 3.3 IU/L) at different dilutions for 10 days. The human TFCOs incubated with Graves' disease serum showed increased growth compared to TFCOs incubated with control sera (TSHR-Ab titers < 3.3 IU/L) (Figure 6C). In agreement, some expansion of TFCOs was observed in wells incubated with 1% control serum while extensive outgrowth of TSFO was observed in wells incubated with 100ng/mL TSH or 1% Graves' Disease sera (Figure 6D).

To further validate the use of TFCOs as *in vitro* models of Graves' disease, we tested 15 Graves' disease sera and 5 control sera in parallel at a 1% dilution and compared ATP units using the CellTiter Glo assay (see Methods). We observed a positive correlation between the anti-TSHR antibody titers and ATP levels in TFCOs ($R^2=0.6760$) (Figure 6E). Two independent donors showed similar correlations ($R^2=0.5651$ and 0.3962) underlining the robustness of TFCO culture (Figure 6F). Lastly, we measured FT3 levels in organoids after stimulation with TSH, a selected potent Graves' disease serum and control serum. TFCOs yielded background levels of 0.45 pmol/L FT3 in the conditioned medium after incubation of 48h. Incubation with 100ng/mL TSH or 1% Graves' disease serum increased FT3 levels to 0.75 and 1.05 pmol/L respectively, while TFCOs incubated with 1% normal serum yielded similar levels of FT3. (Figure 6G). In conclusion, TFCOs recapitulate characteristics of Graves' disease (growth and hormone release) when treated with Graves' disease serum.

DISCUSSION

In this study, we describe the generation of adult thyroid follicular cell organoids from mouse and human origin. The establishment of these TFCOs requires limited starting material and the resulting organoid lines can be stably expanded for >1 year.

1

2

3

4

5

6

7

8

9

&

The optimised protocol allowed the generation of 10 human organoid lines from 12 provided donor tissue samples ($\pm 83\%$). Several other groups have recently reported similar thyroid organoids derived from mouse³⁴, rat³⁵ and human tissue¹². Related approaches have resulted in the establishment of human thyroid cancer organoids^{36,37}. Our TCFO lines faithfully recapitulate TFC function and TSH responses. Our human TFCOs secrete thyroid hormone under expansion condition, which contrasts with the previously published human thyroid organoids where transfer to a maturation medium was required¹². Current expansion conditions showed stable expression of essential thyroid-related genes, even after >1 year of culture, while loss of thyroid differentiation was observed in organoids generated by Ogundipe et al over time in culture¹². These differences may result from differences in medium composition, yet we conclude that both studies provide definitive evidence that thyroid organoids can be established and that these faithfully recapitulate the primary tissue.

Using single cell mRNA sequencing, a proliferative population could be identified but -unlike the original Lgr5+ stem cell-driven gut organoids³⁸, we found no evidence for the existence of unique thyroid stem cells in our *in vitro* model system. It has emerged recently that many solid tissues don't rely on a 'professional' stem cell for their maintenance and repair, but rather temporarily recruit differentiated cells into a transient progenitor pool³⁹. The liver is likely the most explicit example of this phenomenon, where -depending on the type of damage- either fully differentiated cholangiocytes or hepatocytes transiently acquire proliferating progenitor phenotypes to regenerate lost tissue⁴⁰. We conclude that our current observations suggest that a similar phenomenon may play out in the thyroid. While adult thyroid turnover occurs in the order of 10 years, there are reports of thyroid regeneration after injury even though the gland does not tend to recover to its original size^{18,41-44}.

TFCOs could become a potential source of thyroid transplantation. Currently, radioiodine treatment or thyroidectomy are required to treat hyperthyroidism or thyroid carcinoma resulting in hypothyroidism followed by lifelong administration of thyroid hormones⁴⁵. Although thyroid hormone supplemental therapy can in theory "easily" be done by daily levothyroxine prescription, many patients complain of not being in optimal thyroid hormone balance. Autologous transplantation of TSH-responsive cultured TFCOs may in the future replace these external regulations and restore a physiological thyroid hormone balance with TSH-responsive thyroid tissue. Indeed, Coppes and colleagues have shown that their organoids (which are very similar to the ones described in the current study) can be transplanted to mice¹².

The requirement of TSH during the initial passages and FSK in further expansion of human TFCOs shows the dependence of TFC cells on the cAMP pathway. Activation of TSHR and thereby of the cAMP pathway by TSH has been shown to induce proliferation in TFCs^{30,31}. This activation is mimicked by TSHR binding antibodies⁵. These phenomena are readily recapitulated in our TFCOs. Recently, salivary gland organoids were generated from patients suffering from another autoimmune disorder, Sjögren's syndrome and

underlying biological mechanisms of salivary hypofunction were identified⁴⁶. Together, this indicates the promise of organoids as models for autoimmune disorders. Since organoids have been shown to predict patient responses for cystic fibrosis and cancer^{47–50}, TFCOs can potentially aid the development of new or repurposed drugs for Graves' disease.

In conclusion, we present adult mouse and human thyroid follicular cell organoids containing two populations of TFCs which are highly similar except for proliferation status. These TFCs recapitulate essential characteristics of the primary tissue and are responsive to external stimuli such as TSH and anti-TSHR antibodies.

ACKNOWLEDGEMENTS

We thank Stefan van der Elst for flow cytometry assistance; Anko de Graaff and the Hubrecht Imaging Centre (HIC) for microscopy assistance; Single Cell Discoveries for the provided single-cell sequencing service and support; Utrecht Sequencing (USEQ) for bulk RNA-sequencing services and Gijs van Son for help with bulk and single cell RNA-sequencing data mapping.

AUTHOR CONTRIBUTIONS

J.v.d.V and H.C. conceived and designed the project and H.C. supervised the study. J.v.d.V, L.B., S.S. performed experiments. J.v.d.V generated and analysed of bulk and single cell RNA-sequencing data. K.K. and W.v.d.W performed transmission electron microscopy supervised by C.L-I and P.J.P. H.O. provided human sera. H.B., and J.K. generated IHC slides analysed by J.v.d.V. E.L. analysed FT3 levels. I.B.R., H.v.S and M.V. provided access to human tissue and clinical feedback. J.v.d.V and H.C. wrote the manuscript, with input from all authors.

COMPETING INTEREST

H.C. is inventor on several patents related to organoid technology; his full disclosure is given at <https://www.uu.nl/staff/JCClevers/>.

DATA AVAILABILITY

Bulk and single cell mRNA sequencing data are deposited at GEO and are publicly available under SuperSeries GSE183964. Separately, mouse bulk mRNA sequencing data is available under GSE183962, human bulk mRNA sequencing data is available under GSE183961 and single cell mRNA sequencing data is available under GSE183963.

FUNDING

This work was supported by the gravitation program CancerGenomiCs.nl from the Netherlands Organisation for Scientific Research.

1

2

3

4

5

6

7

8

9

&

REFERENCES

1. Rousset, B., Dupuy, C., Miot, F. & Dumont, J. Chapter 2 *Thyroid Hormone Synthesis And Secretion*. *Endotext* (2000).
2. Smith, T. & Hegedüs, L. Graves' Disease. *N. Engl. J. Med.* **375**, 488–493 (2016).
3. Antonelli, A., Ferrari, S. M., Corrado, A., Di Domenicantonio, A. & Fallahi, P. Autoimmune thyroid disorders. *Autoimmun. Rev.* **14**, 174–180 (2015).
4. Antonelli, A. et al. Graves' disease: Epidemiology, genetic and environmental risk factors and viruses. *Best Pract. Res. Clin. Endocrinol. Metab.* **34**, 101387 (2020).
5. Kotwal, A. & Stan, M. Thyrotropin Receptor Antibodies-An Overview. *Ophthal. Plast. Reconstr. Surg.* **34**, S20–S27 (2018).
6. Corvilain, B. et al. Treatment of adult Graves' disease. *Ann. Endocrinol. (Paris)*. **79**, 618–635 (2018).
7. Sjölin, G. et al. The Long-Term Outcome of Treatment for Graves' Hyperthyroidism. *Thyroid* **29**, 1545–1557 (2019).
8. Pulvertaft, R. J., Davies, J. R., Weiss, L. & Wilkinson, J. H. Studies on tissue cultures of human pathological thyroids. *J. Pathol. Bacteriol.* **77**, 19–32 (1959).
9. Chew, D., Green, V., Riley, A., England, R. J. & Greenman, J. The Changing Face of in vitro Culture Models for Thyroid Cancer Research: A Systematic Literature Review. *Front. Surg.* **7**, 43 (2020).
10. Eckstein, A., Philipp, S., Goertz, G., Banga, J. P. & Berchner-Pfannschmidt, U. Lessons from mouse models of Graves' disease. *Endocrine* **68**, 265 (2020).
11. Schutgens, F. & Clevers, H. Human Organoids: Tools for Understanding Biology and Treating Diseases. *Annu. Rev. Pathol.* **15**, 211–234 (2020).
12. Ogundipe, V. M. L. et al. Generation and Differentiation of Adult Tissue-Derived Human Thyroid Organoids. *Stem Cell Reports* **16**, 913–925 (2021).
13. Miao, Y. et al. Next-Generation Surrogate Wnts Support Organoid Growth and Deconvolute Frizzled Pleiotropy In Vivo. *Cell Stem Cell* **27**, 840–851.e6 (2020).
14. Fernández, L. P., López-Márquez, A. & Santisteban, P. Thyroid transcription factors in development, differentiation and disease. *Nat. Rev. Endocrinol.* **2014 111 11**, 29–42 (2014).
15. Al-Suhaimi, E. A. & Al-Khater, K. Functions of stem cells of thyroid glands in health and disease. *Rev. Endocr. Metab. Disord.* **20**, 187–195 (2019).
16. Zito, G., Coppola, A., Pizzolanti, G. & Giordano, C. Heterogeneity of Stem Cells in the Thyroid. in 81–93 (2019). doi:10.1007/978-3-030-24108-7_5
17. Hoshi, N., Kusakabe, T., Taylor, B. J. & Kimura, S. Side Population Cells in the Mouse Thyroid Exhibit Stem/Progenitor Cell-Like Characteristics. *Endocrinology* **148**, 4251–4258 (2007).
18. Okamoto, M., Hayase, S., Miyakoshi, M., Murata, T. & Kimura, S. Stem Cell Antigen 1-Positive Mesenchymal Cells Are the Origin of Follicular Cells during Thyroid Regeneration. *PLoS One* **8**, e80801 (2013).
19. Lan, L., Cui, D., Nowka, K. & Derwahl, M. Stem Cells Derived from Goiters in Adults Form Spheres in Response to Intense Growth Stimulation and Require Thyrotropin for Differentiation into Thyrocytes. *J. Clin. Endocrinol. Metab.* **92**, 3681–3688 (2007).
20. Thomas, T., Nowka, K., Lan, L. & Derwahl, M. Expression of Endoderm Stem Cell Markers: Evidence for the Presence of Adult Stem Cells in Human Thyroid Glands. *Thyroid* **16**, 537–544 (2006).
21. Fierabracci, A., Puglisi, M. A., Giuliani, L., Mattarocci, S. & Gallinella-Muzi, M. Identification of an adult stem/progenitor cell-like population in the human thyroid. *J. Endocrinol.* **198**, 471–487 (2008).
22. Ma, R., Bonnefond, S., Morshed, S. A., Latif, R. & Davies, T. F. Stemness is Derived from Thyroid Cancer Cells. *Front. Endocrinol. (Lausanne)*. **5**, (2014).

23. Klonisch, T., Hoang-Vu, C. & Hombach-Klonisch, S. Thyroid Stem Cells and Cancer. *Thyroid* **19**, 1303–1315 (2009).
24. Dame, K. et al. Thyroid Progenitors Are Robustly Derived from Embryonic Stem Cells through Transient, Developmental Stage-Specific Overexpression of Nkx2-1. *Stem Cell Reports* **8**, 216–225 (2017).
25. Regev, A. et al. The Human Cell Atlas. *Elife* **6**, (2017).
26. Muraro, M. J. et al. A Single-Cell Transcriptome Atlas of the Human Pancreas. *Cell Syst.* **3**, 385-394.e3 (2016).
27. Wissig, S. L. The Anatomy of Secretion in the Follicular Cells of the Thyroid Gland. *J. Biophys. Biochem. Cytol.* **7**, 419–432 (1960).
28. BRAUNSTEINER, H., FELLINGER, K. & PAKESCH, F. ELECTRON MICROSCOPIC OBSERVATIONS ON THE THYROID. *Endocrinology* **53**, 123–133 (1953).
29. Monroe, B. G. Electron microscopy of the thyroid. *Anat. Rec.* **116**, 345–361 (1953).
30. Zaballos, M. A. & Santisteban, P. FOXO1 Controls Thyroid Cell Proliferation in Response to TSH and IGF-I and Is Involved in Thyroid Tumorigenesis. *Mol. Endocrinol.* **27**, 50–62 (2013).
31. Kimura, T. et al. Regulation of Thyroid Cell Proliferation by TSH and Other Factors: A Critical Evaluation of in Vitro Models. *Endocr. Rev.* **22**, 631–656 (2001).
32. Boutin, A. et al. TSH Receptor Homodimerization in Regulation of cAMP Production in Human Thyrocytes in vitro. *Front. Endocrinol. (Lausanne)*. **11**, (2020).
33. Vassart, G. A molecular dissection of the glycoprotein hormone receptors. *Trends Biochem. Sci.* **29**, 119–126 (2004).
34. Saito, Y. et al. Development of a functional thyroid model based on an organoid culture system. *Biochem. Biophys. Res. Commun.* **497**, 783–789 (2018).
35. Khoruzhenko, A. et al. Functional model of rat thyroid follicles cultured in Matrigel. *Endocr. Connect.* **10**, 570–578 (2021).
36. Chen, D. et al. Organoid Cultures Derived From Patients With Papillary Thyroid Cancer. *J. Clin. Endocrinol. Metab.* **106**, 1410–1426 (2021).
37. Sondorp, L. H. J. et al. Patient-Derived Papillary Thyroid Cancer Organoids for Radioactive Iodine Refractory Screening. *Cancers (Basel)*. **12**, 3212 (2020).
38. Sato, T. et al. Single Lgr5 stem cells build crypt-villus structures in vitro without a mesenchymal niche. *Nature* **459**, 262–265 (2009).
39. Post, Y. & Clevers, H. Defining Adult Stem Cell Function at Its Simplest: The Ability to Replace Lost Cells through Mitosis. *Cell Stem Cell* **25**, 174–183 (2019).
40. Gadd, V. L., Aleksieva, N. & Forbes, S. J. Epithelial Plasticity during Liver Injury and Regeneration. *Cell Stem Cell* **27**, 557–573 (2020).
41. Kimura, S. Thyroid Regeneration: How Stem Cells Play a Role? *Front. Endocrinol. (Lausanne)*. **5**, (2014).
42. Ozaki, T. et al. Thyroid Regeneration: Characterization of Clear Cells After Partial Thyroidectomy. *Endocrinology* **153**, 2514–2525 (2012).
43. Lee, J. et al. Regeneration of thyroid follicles from primordial cells in a murine thyroidectomized model. *Lab. Invest.* **97**, 478–489 (2017).
44. Iwadate, M., Takizawa, Y., Shirai, Y.-T. & Kimura, S. An in vivo model for thyroid regeneration and folliculogenesis. *Lab. Invest.* **98**, 1126–1132 (2018).
45. Alexander, E. K. et al. 2017 Guidelines of the American Thyroid Association for the Diagnosis and Management of Thyroid Disease During Pregnancy and the Postpartum. *Thyroid* **27**, 315–389 (2017).
46. Pringle, S. et al. Salivary Gland Stem Cells Age Prematurely in Primary Sjögren's Syndrome. *Arthritis Rheumatol.* **71**, 133–142 (2019).
47. Putker, M. et al. Medium-Throughput Drug- and Radiotherapy Screening Assay using Patient-Derived Organoids. *J. Vis. Exp.* (2021). doi:10.3791/62495
48. Driehuis, E., Kretzschmar, K. & Clevers, H. Establishment of patient-derived cancer organoids for drug-screening applications. *Nat. Protoc.* **15**, 3380–3409 (2020).

1

2

3

4

5

6

7

8

9

&

49. Driehuis, E. et al. Oral Mucosal Organoids as a Potential Platform for Personalized Cancer Therapy. *Cancer Discov.* **9**, 852–871 (2019).
50. Dekkers, J. F. et al. Characterizing responses to CFTR-modulating drugs using rectal organoids derived from subjects with cystic fibrosis. *Sci. Transl. Med.* **8**, 344ra84-344ra84 (2016).
51. Bannier-Hélaouët, M. et al. Exploring the human lacrimal gland using organoids and single-cell sequencing. *Cell Stem Cell* (2021). doi:10.1016/j.stem.2021.02.024
52. Love, M. I., Huber, W. & Anders, S. Moderated estimation of fold change and dispersion for RNA-seq data with DESeq2. *Genome Biol.* **15**, (2014).
53. Grün, D. et al. Single-cell messenger RNA sequencing reveals rare intestinal cell types. *Nature* **525**, 251–255 (2015).
54. Faas, F. G. A. et al. Virtual nanoscopy: Generation of ultra-large high resolution electron microscopy maps. *J. Cell Biol.* **198**, 457–469 (2012).
55. Burel, J.-M. et al. Publishing and sharing multi-dimensional image data with OMERO. *Mamm. Genome* **26**, 441–7 (2015).
56. Villalta, D. et al. Diagnostic accuracy of a new fluoroenzyme immunoassay for the detection of TSH receptor autoantibodies in Graves' disease. *Autoimmun. Highlights* **9**, 3 (2018).

SUPPLEMENTARY MATERIALS AND METHODS

Thyroid organoid cultures

Digestion medium consisted of 1 mg/mL collagenase (Sigma-Aldrich, C9407) with 10 μ M ROCK inhibitor Y-27632 (Abmole, M1817) and 100 μ g/mL Primocin (Invivogen, ant-pm-1) in AdDMEM/F12 (GIBCO)

Mouse expansion medium consisted of AdDMEM/F12 (GIBCO) supplemented with B27 supplement (Gibco, 17504044), Glutamax, HEPES, 100 U/mL Penicillin-Streptomycin (all Thermo Fisher scientific), 1.25 mM N-acetylcysteine (Sigma-Aldrich, A9165), 10 mM nicotinamide (Sigma-Aldrich, N0636) and the following growth factors: 1% R-spondin 3 conditioned medium (U-Protein Express), 0.5 μ M A83-01 (Tocris, 2939), 1 μ M FSK (Tocris, 1099), 500ng/mL EGF (Peprotech, AF-100-15-1mg) and 100 ng/mL FGF10 (Peprotech, 100-26).

Human expansion medium contained AdDMEM/F12 (GIBCO) supplemented with B27 supplement (Gibco, 17504044), Glutamax, HEPES, 100 U/mL Penicillin-Streptomycin (all Thermo Fisher scientific), 100 μ g/mL Primocin (Invivogen), 1.25 mM N-acetylcysteine (Sigma-Aldrich, A9165), 10 mM nicotinamide (Sigma-Aldrich, N0636) and the following growth factors: 1% R-spondin 3 conditioned medium (U-Protein Express), 0.5 μ M A83-01 (Tocris, 2939), 1 μ M FSK (Tocris, 1099), 500ng/mL EGF (Peprotech, AF-100-15-1mg), 100 ng/mL FGF10 (Peprotech, 100-26), 3mM p38 inhibitor (Sigma-Aldrich, S7067), 1:1000 Wnt surrogate (U-Protein Express) and 100ng/mL TSH (Sigma-Aldrich, T8931).

21-40 days after seeding, human and mouse organoids were removed from the BME, mechanically dissociated into small fragments using a narrowed Pasteur pipette and re-seeded in fresh BME. Passage was performed in 1:3 – 1:5 split ratio once every 7 - 14 days for >1 year. During culturing, medium was refreshed at most every three days. Images of organoid cultures were taken on EVOS FL Cell Imaging System (Thermo Fisher scientific).

Viability assays

Cell viability was determined using CellTiterGlo 3D (Promega) according to the manufacturer's instructions. In short, organoids were seeded using the same protocol as mentioned before. Two hours after seeding, medium was removed from organoid plates and 200 μ l CellTiterGlo 3D solution was added. Solution was incubated for 20min at RT while shaking (300rpm). 20 μ l solution, without touching BME dome was transferred to black 96-well plate. Luminescence was acquired with Berthold XS3 LB 960 within 5 min.

Immunohistochemistry and imaging

Antibodies used for immunohistochemistry included PAX8 (Abcam, ab124445), NKX2.1 (Abcam, ab76013), anti-TG (Abcam, ab156008) and KI67 (eBiosciences, 14-5698-82). Antibodies used for immunofluorescence included anti-PAX8 (Abcam, ab124445), anti-NKX2.1 (Abcam, ab76013), anti-TG (Abcam, ab156008), anti-ZO-1

1

2

3

4

5

6

7

8

9

&

(Life Technologies, 40-2200), anti-Ki67 (eBiosciences, 14-5698-82), Phalloidin–Alexa488 (Life Technologies, A12379) and DAPI (Invitrogen). Secondary antibodies included Alexa Fluor 568 goat anti-rabbit IgG (Life Technologies, A11036), Alexa Fluor 647 goat anti-rabbit IgG (Life Technologies, A21245) and Alexa Fluor 647 goat anti-mouse IgG (Life Technologies, A21236)

qPCR analysis

Primers used for qPCR analysis were designed using NCBI primer design.

Single-cell mRNA sequencing

After sorting as indicated in material and methods, cells were first lysed for 5 minutes at 65 °C, and RT and second-strand mixes were dispensed by the Nanodrop II liquid handling platform (GC Biotech). Single-cell double-stranded cDNAs were pooled together and in vitro transcribed for linear amplification. Illumina sequencing libraries were prepared using the TruSeq small RNA primers (Illumina) and these DNA libraries were sequenced paired-end, respectively, on the Illumina NextSeq.

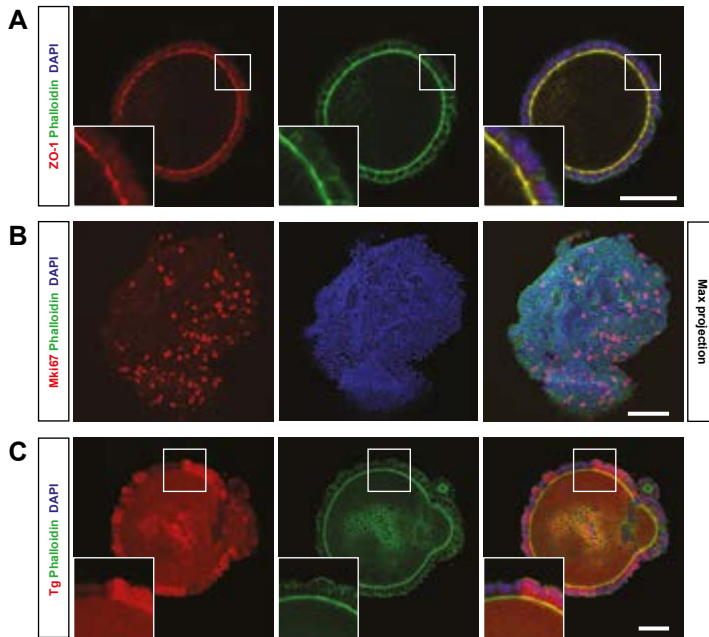
Fastq files were trimmed with TrimGalore-0.4.3 and mapped with STAR-2.5.3a to the mouse reference genome (GRCm38). Introns and exons were extracted from the corresponding annotation files. Cells with raw transcript counts higher than 1.5 times the interquartile range above the upper quartile of the rest of the population were removed as potential doublets. Subsequently, clustering and single-cell analysis were performed with Seurat package. To directly compare organoid and tissue cells in the violin plots, cells identified in the above-mentioned analysis were retrieved from

Table S1. Primer list for RT-qPCR analysis

Gene	Species	Forward	Reverse
Pax8	Mouse	CAGCCTGCTGAGTTCTCCAT	CTGTCTCAGCCAAGTCTCTC
Nkx2.1	Mouse	CAGTTCCACTCTGCAACGGA	TGATTCGGCGTCGGCTGG
Tg	Mouse	TCCGGAGGAAAGTTGTGCTG	GCCGCTCACACTCAAAGAAC
Tpo	Mouse	TGGATAGTAATTTGCAGGTGGACA	CCTCTATTCGCACAGGAGGAC
Tshr	Mouse	ATGACACGGAAGTGGCTCTG	ACTCTGCACTTCTCTCTCCTTC
Calca	Mouse	AGGATCAAGAGTCACCGCTTC	CATGATGCCTTCCTGGTGAG
PAX8	Human	CATTTGAGCGGCAGCACTAC	AAGGGTGAGTGAGGATCTGC
NKX2.1	Human	CTCGCTCGCTCATTTGTTGG	TCGGCGGCGGCTGAG
TG	Human	GCCTGTGGCTTGTCTGTCA	GCGTAGTCCCCTGAATCCTG
TPO	Human	AGTGCAAGTGGCTGAGAAGA	TCCCTCTCGAGATGAAGGGG
TSHRa	Human	GCTTGCTGGACGTGTCTCAA	CCCGTGTGAGGTGAAGGAAA
SLC5A5	Human	ATGTCGGCCGTGCAGGT	CGCATCTCCAGGTACTIONTAGG
SLC26A4	Human	GCGAGCAGAGACAGGTCAT	CTCGTGCTGTTGCTGGAAAG
SLC16A2	Human	CCCCAAGCAAGAGAGGTGTC	CCTCCACATACTTCATCAGGTG

another analysis containing both tissue and organoid cells ran with mintrans = 1500. Then, normalized expression (ndata) was plotted.

SUPPLEMENTARY FIGURES



Supplementary figure S1. TFCOs are comprised of polarised TFCs subdivided into proliferative and Tg-expressing TFCs. A) Mouse TFCOs have apical-in morphology based on apical membrane marker ZO-1 (red). Overlap of ZO-1 and membrane stain Phalloidin (green) is only observed on inner surface of TFCOs. DAPI = nuclear stain (blue). Representative image of mouse TFCOs in passage 5 (mThy15). Scale bar = 50um. B) Proliferative cells are observed in mouse TFCOs as indicated by Mki67-positivity (red). Only a subpopulation of TFCs are proliferative per TFCO. Representative image of mouse TFCOs in passage 8 (mThy14). Image shows max projection of z-stack. Phalloidin = membrane stain (green), DAPI = nuclear stain (blue). Scale bar = 100um. C) Subpopulations of mature TFCs can be identified in TFCOs in early days after organoid formation (day 5 after passaging) based on Tg. Representative image of mouse TFCOs in passage 5 (mThy16). Phalloidin = membrane stain (green), DAPI = nuclear stain (blue). Scale bar = 50um.

1

2

3

4

5

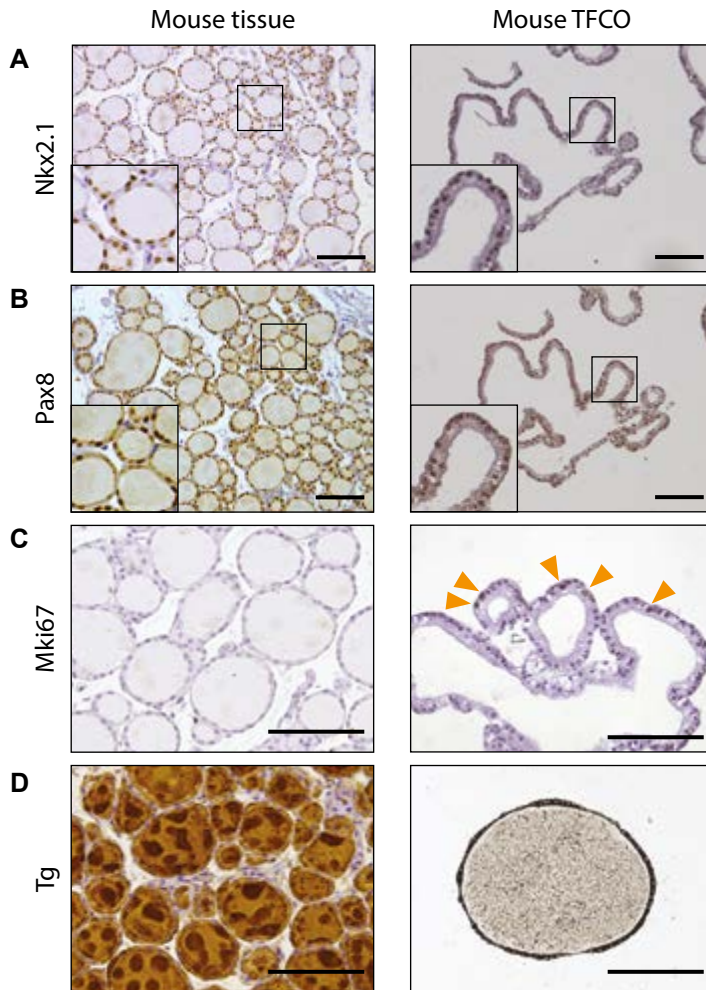
6

7

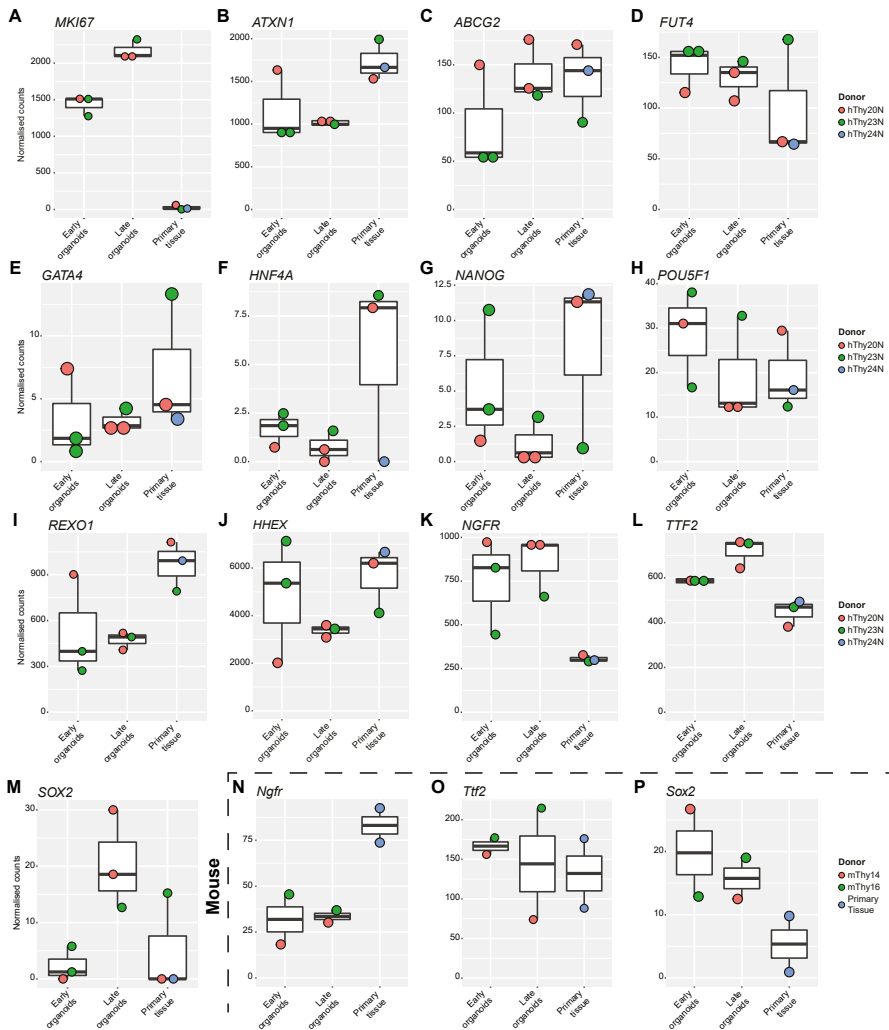
8

9

&

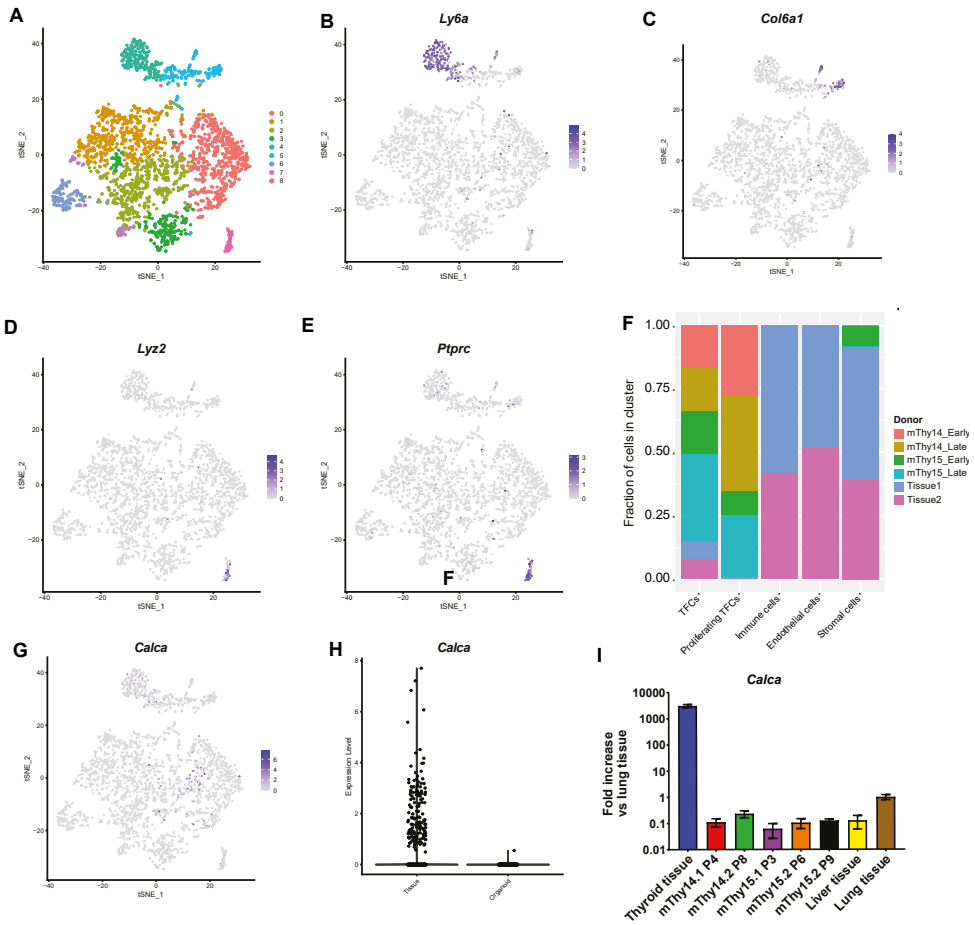


Supplementary figure S2. Mouse TFCs express nuclear thyroid transcription factors in both tissue and TFCOs while proliferation is limited to TFCOs. A-D) Representative images of mouse primary thyroid tissue and TFCOs stained for thyroid transcription factors Nkx2.1 (A), Pax8 (B), Mki67 (C) and Tg (D). Both transcription factors show nuclear expression in both mouse tissue as mouse TFCOs. Proliferation marker Mki67 is only observed in some cells in TFCOs and not observed in mouse primary thyroid tissue. Tg expression is observed in colloid follicles in tissue samples and similar in the lumen of TFCOs. Scale bar = 100um.

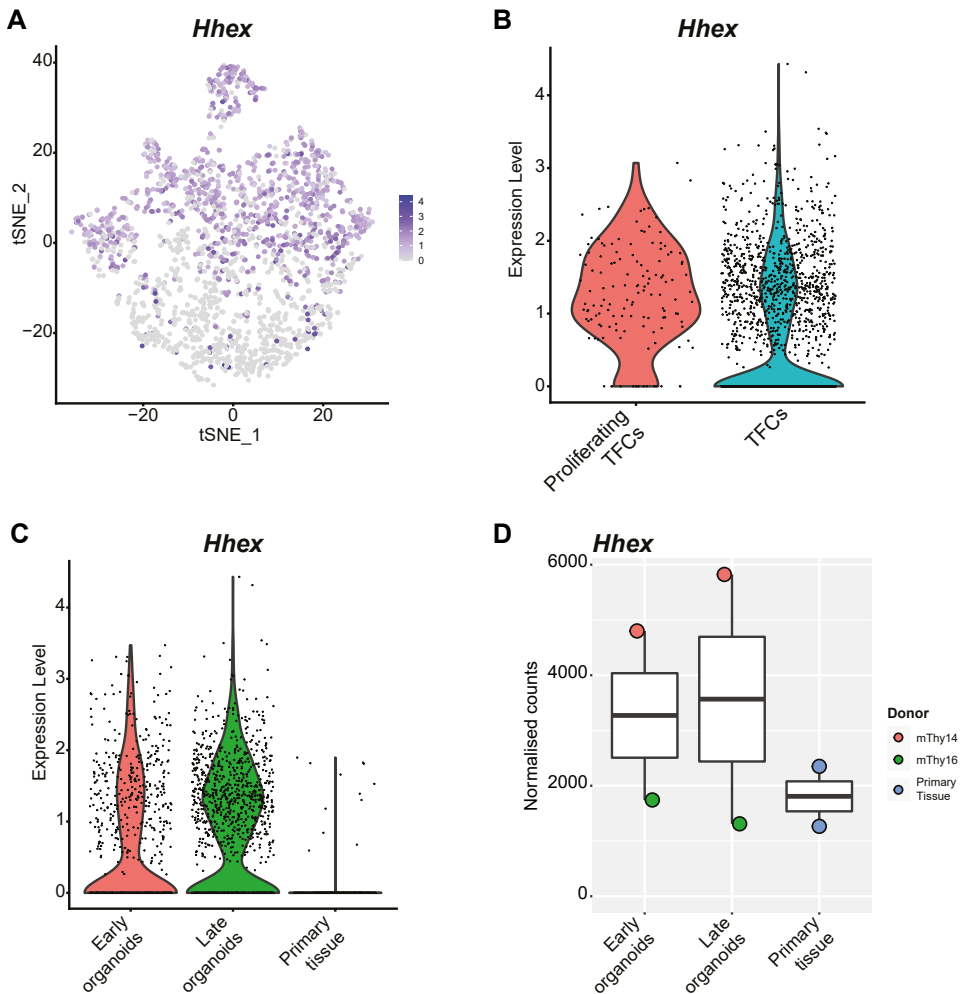


Supplementary figure S3. Most proposed stem cell markers show no enrichment in human TFCOs in early and late passages except for NGFR, TTF2 and SOX2 which are not enriched in mouse TFCOs. A-P) Boxplots of human (A-M) and mouse (N-P) primary thyroid tissue (Primary tissue, early passage TFCOs (Early organoids) and late passage TFCOs (Late organoids) normalised counts of bulk mRNA sequencing. Colour of the dots indicates donor visualised as described on the right of the row of graphs. Boxplot shows median, two hinges (25th and 75th percentile) and two whiskers (largest and smallest value no further than 1.5x inter-quartile range). A) Increased proliferation is observed over time from primary thyroid tissue to early and late organoids by normalised counts of MKI67 in line with observed increase in TFCO growth over passages. B-I) Proposed stem cell markers ATXN1 (B), ABCG2 (C), FUT4 (D), GATA4 (E), HNF4A (F), NANOG (G), POU5F1 (H), REXO1 (I) and HHEX (J) are not enriched in correlation with MKI67 and time in human tissue and TFCOs. K-M) Proposed stem cell markers NGFR (K) and TTF2 (L) are enriched in TFCOs compared to human tissue and increased over time and SOX2 (M) is enriched in late passage TFCOs. NGFR, TTF2 and SOX2 expression is therefore correlated to increased proliferation. N-P) Potential human stem cell markers Ngfr (N), Ttf2 (O) and Sox2 (P) are not enriched in mouse TFCOs compared to primary tissue and increased over time in culture.

1
2
3
4
5
6
7
8
9
&



Supplementary figure S4. Single cell sequencing of mouse primary tissue and TFCOs. A) tSNE representation of 9 clusters of mouse thyroid tissue cells (n = 747) and mouse TFCO cells (n=1843). B) tSNE representation of the expression of the endothelial cell marker *Ly6a* (linear scale). C) tSNE representation of the expression of the stromal cell marker *Col3a1* (linear scale). D) tSNE representation of the expression of the immune cell marker *Lyz2* (linear scale). E) tSNE representation of the expression of the immune cell marker *Ptprc* (linear scale). F) Clusters marked as endothelial, immune and stromal cells after single cell mRNA sequencing are comprised of cells originating from both primary tissues but not from TFCOs. The TFC cluster contains cells from all samples: primary tissue, early passage TFCOs and late passage TFCOs. Proliferative TFCs are only identified in cells from early and late passage TFCOs. Colour indicates donor. G) tSNE representation of the expression of the C-cell hormone calcitonin *Calca* (linear scale). H) Violin plots of the normalized expression level of *Calca* indicates potential presence of C-cells in tissue but absence in TFCOs. I) RT-qPCR analysis reveals loss of *Calca* expression in mouse TFCOs compared to primary thyroid tissue in early (<4 passages) and late (>6 passages) TFCOs. Expression levels are relative to lung tissue expression levels. N=3. Error bars = stdev.



Supplementary figure S5. Single cell sequencing of mouse primary tissue and TFCOs reveals *Hhex* as potential mouse thyroid stem cell marker.

A) tSNE representation of the expression of the potential stem cell markers *Hhex* enriched in proliferative TFCs (linear scale). B) Violin plots of the normalized expression level of *Hhex* in proliferative TFCs (n = 136 cells) and TFCs (n = 1,983 cells) shows increased expression in proliferative TFCs compared to other TFCs. C) Violin plots of the normalized expression level of *Hhex* in early passage TFCOs ("Early organoids", n = 725 cells), late passage TFCOs ("Late organoids", n = 1101 cells) and primary thyroid tissue ("Primary tissue", n = 293 cells) show presence of *Hhex* expression only in TFCOs and increased expression over time. D) Boxplot of *Hhex* expression in mouse primary thyroid tissue and early, and late passage TFCOs using bulk mRNA sequencing. A trend can be observed of increased expression from tissue to TFCOs and increased expression over time in TFCOs. Boxplot shows median, two hinges (25th and 75th percentile) and two whiskers (largest and smallest value no further than 1.5x inter-quartile range).

1

2

3

4

5

6

7

8

9

&

CHAPTER

BACTERIALLY PRODUCED R-SPONDIN3 INCREASES HEPATOCYTE PROLIFERATION INDEPENDENT OF LIVER ZONATION

Jelte van der Vaart^{1,2}, Johan van Es^{1,2}, Wim de Lau^{1,2},
Laura Zeinstra^{1,2}, Harry Begthel^{1,2}, Henner F. Farin³,
Jeroen Korving^{1,2}, Helmuth Gehart⁴, Hans Clevers^{1,2,5}

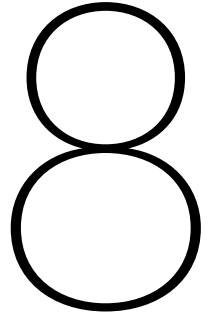
¹ Hubrecht Institute, Royal Netherlands Academy of Arts and Sciences
(KNAW) and University Medical Centre Utrecht, 3584 CT
Utrecht, the Netherlands

² Oncode Institute, Hubrecht Institute, 3584 CT Utrecht, the Netherlands

³ Hubrecht Institute, Royal Netherlands Academy of Arts and Sciences
(KNAW) and University Medical Centre Utrecht, 3584 CT Utrecht,
the Netherlands; Current address: Georg-Speyer-Haus, Institute for
Tumor Biology and Experimental Therapy, Frankfurt am Main, Germany

⁴ Hubrecht Institute, Royal Netherlands Academy of Arts and Sciences
(KNAW) and University Medical Centre Utrecht, 3584 CT Utrecht,
the Netherlands; Current address: Institute for Molecular Health
Sciences, ETH Zurich, 8093 Zurich, Switzerland.

⁵ Princess Máxima Center for Paediatric Oncology, 3584 CS
Utrecht, The Netherlands



ABSTRACT

Wnt signalling is essential for epithelial stem cell homeostasis and proliferation. Its many feedback mechanisms make Wnt signalling one of the main determinants of liver zonation. Wnt activation leads to expression of negative regulators, which are themselves regulated by secreted ligands RSPO1-4. The role of RSPO signalling in liver proliferation, however, remains poorly understood. We produced RSPO3 using bacterial expression (bacRSPO3) which is effective in potentiating Wnt signalling in vitro. Moreover, systemic injection of bacRSPO3 induces proliferation in the liver as well as in the Wnt-dependent small intestine. Proliferation is observed in two waves, with respective peaks at day 2 and 4 after bacRSPO3 injection. The first wave involves proliferating stellate cells, while proliferating hepatocytes are only observed at day 4 post-injection. The proliferation of hepatocytes occurred in all three liver zones and appeared independent of active Wnt-signalling. An extension of the Wnt-active zone was, however, observed after bacRSPO3 administration. In conclusion, we describe the production of bacRSPO3 that allows for both in vitro as in vivo RSPO signalling studies including the induction of liver proliferation.

INTRODUCTION

The Wnt signalling pathway plays a key role in development, adult homeostasis and regeneration. Additionally, its role in stem cell maintenance has been widely described¹. The tight regulation of this pathway by several feedback loops underscores the importance of maintaining the right levels of activation at the right location. The main components of this regulation acting at the earliest point of pathway activation, i.e. the cell membrane, are E3-ubiquitin-ligases zinc and ring finger 3 (ZNF3) and ring finger protein 43 (RNF43). These transmembrane proteins control Wnt receptor Frizzled (FZD) levels by marking the receptor complex for internalisation and degradation via ubiquitination^{2,3}. Since both ZNF3 and RNF43 are themselves target genes of the Wnt pathway, excessive Wnt signalling is prevented, potentially creating a slightly fluctuating yet stable activation of the pathway. R-spondins 1-4 (RSPO1-4) are a family of secreted proteins with the ability to potentiate Wnt activation by removing the negative regulators ZNF3 and RNF43 from the membrane. After binding of RSPO1-4 to either ZNF3 or RNF43 and simultaneously to a transmembrane protein of the leucine-rich repeat-containing G-protein coupled receptors family (LGR4-6), the complex is internalised and the downregulation of FZD blocked. The available level of FZDs at the cellular membrane is thereby increased which potentiates Wnt signalling activity. Since pathway activation still requires Wnt ligands to bind the receptor, RSPO1-4 are seen as potentiators (rather than initiators) of the Wnt signalling cascade⁴⁻⁶. There are additional reports of LGR-independent signalling of RSPOs by binding to heparin sulphate proteoglycans⁷. The exact mechanism and its consequences, however, remain inconclusive.

The role of Wnt signalling and the importance of Wnt activation in liver homeostasis and regeneration has been widely described. Due to its unique regenerative capacity, stem cell biologists have extensively studied the liver. Since Wnt signalling and stem cells have been shown to go hand-in-hand, researchers have been keen to establish the role of Wnt activation in liver regeneration. The liver is comprised of hexagonal liver lobules comprised of a single central vein surrounded by six portal triads consisting of a portal vein, portal artery and bile duct. Sinusoids connect these two areas and are lined by plates of hepatocytes. While these hepatocytes are characterised by expression of pan-hepatocyte markers, the precise function of a hepatocyte is determined by the location among the central-to-portal axis. Portal hepatocytes (zone 1) perform gluconeogenesis while central hepatocytes (zone 3) break down glucose by glycolysis. This zonation is established and maintained by several signalling cascades including differences in Wnt activity. While the central zone is characterised by the expression of Wnt target genes like AXIN2, the portal triad zone expresses Wnt inhibitory proteins like adenomatous polyposis coli (APC)⁸⁻¹². Accordingly, Wnt target genes such as Axin2, RNF43 and LGR5 are only expressed in central vein hepatocytes. This limits the Wnt potentiation function of RSPOs to the central vein hepatocytes. In contrast, RSPO-binding partners ZNF3 and LGR4/6 are observed throughout the lobules⁹. This raises the question whether RSPO

1

2

3

4

5

6

7

8

9

&

signalling is restricted to the Wnt active central zone of the liver or is able to signal independently from Wnt in other zones.

The essence of RSPO presence to stimulate hepatocyte zonation and proliferation has been described previously⁸⁻¹². Upon removal of RSPO receptors LGR4 and 5, liver size is reduced during homeostasis but more evident reduction is observed during regeneration⁹. Vice versa, stimulation of RSPO signalling might improve liver regeneration.

In this study, we present an optimised protocol for the production of functional RSPO3 in *E. coli*. We injected recombinant RSPO3 into mice to study the effect on proliferation in the liver. We observed proliferation of stellate cells followed by hepatocyte proliferation in all liver zones as well as in the intestine. The induction of proliferation was independent of Wnt activation indicating a potential secondary role for RSPO in the liver.

METHODS AND MATERIALS

Plasmids and Plasmid Construction

Protein expression plasmids were constructed using standard polymerase chain reaction-based and endonuclease-based restriction cloning techniques. The construct encodes maltose binding protein (MBP), tobacco etch virus (TEV) protease cleavage site, thrombin protease cleavage site, gene fragment and histidine (HIS) tag. The coding regions were verified by automated DNA sequencing by Macrogen Europe, Amsterdam.

Protein Expression and Purification

Bacterial protein expression was performed as previously described¹³. In short, SHuffle® Express Competent *E. coli* (New England Biolabs) were transfected with expression cassette and grown in liquid culture. Inductions were performed overnight at 16°C with 0.5 mM Isopropyl β -D-1-thiogalactopyranoside (IPTG). All purification steps were conducted at 4°C unless otherwise indicated. Cultures were spun down and resuspended in 50 mM Tris-HCl (pH 7.5), 150 mM NaCl, 20 mM imidazole, 8 M urea and 10% glycerol. Suspension was lysed for 1.5 h at 30°C with 1 mg/mL lysozyme (Sigma-Aldrich) and then sonicated (5x30 seconds with 45sec pauses). The lysate was clarified by centrifuging for 30 min at 25000g. Supernatant was loaded on HisTrap HP 5 mL nickel column on the ÄKTA purifier (GE Healthcare). HisTrap column was washed with 50 mM Tris-HCl (pH 7.5), 150 mM NaCl, 20 mM imidazole, 8 M urea and 10% glycerol until UV_{280nm} was at a stable background level. Column was washed with at least 5 column volumes. A gradient to 100% 50mM Tris-HCl (pH 7.5), 150mM NaCl, 600 mM imidazole and 10% glycerol was established to purify the protein. Eluted fractions were collected and validated by SDS-PAGE electrophoresis followed by Coomassie Brilliant Blue staining or Western Blot. Peak fractions were pooled and concentrated to 1 mg/mL using vivaspin 20 (MWCO 10000) or 15R (MWCO 2000). Solution was dialysed to PBS using Slide-A-Lyzer™ Dialysis Cassettes (Thermo Scientific) and stored at 4°C or -20°C for longer storage.

Western Blot

For every sample, 50µg of total protein, as determined by Bradford Protein Assay (BioRad), was loaded onto a 4-12% SDS-polyacrylamide gel (BioRad). Subsequently, protein was transferred on Immobilon-P PVDF membrane (Millipore). Blots were blocked in 5% bovine serum albumin (BSA) in PBS with 0.1% Tween-20 (PBST) for 1 hour and incubated overnight with primary antibody (mouse anti-HIStag, Abcam; rabbit anti-FLAGtag, Cell Signalling Technologies). Blots were incubated for 1 hour with HRP-conjugated anti-mouse or anti-rabbit antibody, which was detected using ECL Prime Western Blotting Detection Reagent (GE Healthcare).

TOPFLASH luciferase reporter assay

HEK293 SuperTopFlash cells were ordered from ATCC and grown in DMEM, 10% FCS, 50 units/mL penicillin and 50 µg/mL streptomycin. 24h prior to measurement cells were split to white 96-well plates (Corning) at a 1:10 ratio. Cells were stimulated with Wnt and RSPO concentration in triplicate for 24h. 25µL of Promega Steady-Glo Luciferase Assay System (Promega) was added to each well and incubated at RT for 20min. Luminescence was determined using a Centro XS LB 960 Microplate Luminometer (Berthold Technologies).

Organoid cultures

Cholangiocyte organoids were maintained in standard expansion medium²² (AdDMEM/F12 (Invitrogen), 10 mM Hepes, 10 mM Glutamax, 1x N2 and 1x B27 (both Invitrogen), 1.25 mM N-Acetylcysteine (Sigma), 10 nM gastrin (Sigma), and the growth factors: 50 ng/mL EGF (Peprotech), 100 ng/mL FGF10 (Peprotech), 25 ng/mL HGF (Peprotech), 10 mM Nicotinamide (Sigma), 5 µM A83.01 (Tocris), and 10 µM FSK (Tocris) complemented with indicated RSPO proteins for 3 passages.

Airway organoids were grown in airway organoid medium, previously described²¹, which consists of AdDF+++ supplemented with 1× B27 supplement (Life Technologies; 17504-044), 1,25 mM N-acetyl-l-cysteine (Sigma-Aldrich; A9165), 10 mM nicotinamide (Sigma-Aldrich; N0636), 500 nM A83-01 (Tocris; 2939), 5µM Y-27632 (Abmole; Y-27632), 1µM SB202190 (Sigma-Aldrich; S7067), 100 ng/mL human FGF10 (PeproTech; 100-26), 25ng/mL FGF7 (Peprotech; 100-19) and 1% vol/vol Noggin (produced via the r-PEX protein expression platform at U-Protein Express BV) complemented with indicated RSPO proteins for 3 passages.

Mouse studies

All mouse experiments were conducted under a project license granted by the Central Committee Animal Experimentation (CCD) of the Dutch government and approved by the KNAW-Hubrecht Institute Animal Welfare Body (IvD). Both male and female mice were used for all experiments. 6-8 week-old WT C57Bl6 mice were IP or IV injected with bacRSPO3 or PBS.

1

2

3

4

5

6

7

8

9

&

The flanking arms of the RSPO2-^{LoxP} and RSPO3-^{LoxP} construct, surrounding the floxed exon 2, were generated by high-fidelity PCR reactions from male 129/Ola-derived BAC DNA and subsequently cloned into vector PL451. Detailed cloning information is available on request. The targeting construct (100µg) was linearized and transfected into male 129/Ola-derived IB10 embryonic stem cells by electroporation (800V, 3F). RSPO2-^{LoxP} and RSPO3-^{LoxP} mice were generated through homologous recombination in IB10 embryonic stem cells (129/Ola). Single recombinant embryonic stem cell clones were screened by Southern blotting. RSPO1-LoxP ES cells were obtained via EUCOM (clone ID: EPD)720_2_A03). Positive clones were selected and injected into C57BL/6 derived blastocysts using standard procedures. All injected clones gave germline transmission. The neomycin selection cassette was flanked by Frt recombination sites and excised *in vivo* by crossing the mice with the general FLP deleter strain (Jackson Lab.). The described experiments with the newly generated mice were performed with mice that were backcrossed with C57Bl6 mice for at least 3 generations. Mice were subsequently crossed with the Rosa-^{CreERT2} mice. The Cre enzyme was induced by a single intraperitoneal injection of Tamoxifen (5mg in 200µl/25gr)(Sigma Aldrich) dissolved in sunflower oil. The 6-16 weeks mice, as well as various genotypic controls, were sacrificed and the organs were isolated for further analysis.

Immunohistochemistry

Liver and intestines were fixed overnight in 4% formalin. The formalin was removed and the intestines washed twice in PBS at room temperature. The intestines were then transferred to a tissue cassette and dehydrated by serial immersion in 20-fold volumes of 70%, 96% and 100% EtOH for 2 hours each at 4°C. Excess ethanol was removed by incubation in xylene for 1.5 hours at room temperature and the cassettes then immersed in liquid paraffin (56°C) overnight. Paraffin blocks were prepared using standard methods. 4µm tissue sections were de-waxed by immersion in xylene (2 times 5min) and hydrated by serial immersion in 100% EtOH (2 times 1min), 96% EtOH (2 times 1min), 70% EtOH (2 times 1min) and distilled water (2 times 1min). Endogenous peroxidase activity was blocked by immersing the slides in peroxidase blocking buffer (0.040 M citric acid, 0.121M disodium hydrogen phosphate, 0.030M sodium azide, 1.5% hydrogen peroxide) for 15min at room temperature. Antigen retrieval was performed (see details below for each antibody), and blocking buffer (1% BSA in PBS) added to the slides for 30min at room temperature. Primary antibodies were then added and incubated as detailed below. The slides were then rinsed in PBS and secondary antibody added (polymer HRP-labelled anti-mouse/rabbit, Envision) for 30min at room temperature. Slides were again washed in PBS and bound peroxidase detected by adding DAB substrate for 10min at RT. Slides were then washed 2 times in PBS and nuclei counterstained with Mayer's haematoxylin for 2min, followed by two rinses in tapwater for 5 min. Sections were dehydrated by serial immersion for 1 min each in 50% EtOH and 60% EtOH, followed by 2min each in

70% EtOH, 96% EtOH, 100% EtOH and xylene. Slides were mounted in Pertex mounting medium and a cover slip placed over the tissue section.

Antigen retrieval was performed by boiling samples for 20min in 10mM sodium citrate buffer pH 6.0. Antibodies used were; rat anti-BrdU (Abcam) (1:250 dilution); rat anti-Ki67 (eBioscience) (1:1000 dilution). Incubation of antibodies was performed O/N in blocking buffer at 4°C for the antibody. In all cases, the Envision+ kit (Dako) was used as a secondary reagent. Stainings were developed with DAB. Slides were counterstained with haematoxylin and mounted in Pertex. Images were acquired using Leica DM4000 with fixed parameters.

Tile scan images merged by Leica software were quantified using ImageJ. Quantification was performed by randomly assigning new numbers to each image. Random numbers were recorded with corresponding condition. Liver BrdU quantification was performed by randomly selecting areas of at least 1 mm². Manual BrdU count was performed in 8 different areas. Area measures were retrieved from ImageJ. Small intestine quantification was performed by measuring crypt length with ImageJ. Images with crypt lengths of 0,75-0,85 inch were manually counted on BrdU positive and BrdU negative cells within the crypt. 46-69 crypts were counted per condition. Detailed images were processed using ImageJ.

Immunofluorescence

Slides with tissue sections were rehydrated and boiled in 10 mM trisodium citrate-2-hydrate (pH 6,0). Blocking buffer (5% normal goat serum in PBS or 1% BSA in PBS) was added and slides were blocked for at least 30min at RT. The buffer was removed and blocking buffer containing the primary antibody (mouse anti-glutamine synthase (Abcam), rat anti-BrdU (Abcam), rabbit anti-Desmin (Thermo Scientific) or rat anti-Ki67 (eBioscience)) was incubated overnight at 4°C. Blocking buffer containing the secondary antibody (Alexa Fluor 488-labeled goat anti-mouse or anti-rabbit (Molecular Probes) and Alexa Fluor 568-labeled goat anti-rat (Molecular Probes)) at a dilution of 1:250 was incubated for 2h at RT. For nuclear staining, 1x DAPI solution was added to secondary antibody solution. Slides were mounted in Prolong Gold with DAPI mounting medium. Images were acquired using Leica DM6000 with fixed parameters. Tile scan images merged by Leica software were quantified using ImageJ. Detailed images were processed using ImageJ.

Statistical analysis

Statistical analysis was performed with the GraphPad Prism 8 software.

RESULTS

To allow *in vivo* studies on RSPO signalling, we adapted a previously described protocol of bacterial production of RSPO3¹³ and optimised the production process. We used E.coli strains that allow for the production of disulphide bond-reliant proteins like RSPO1-4.

1

2

3

4

5

6

7

8

9

&

These bacteria produced a truncated RSPO3 protein consisting of the two furin-domains of RSPO3 which are essential and sufficient to allow for Wnt potentiation¹⁴⁻¹⁸. We fused maltose-binding protein to RSPO3 to create a soluble protein in the bacteria, a FLAG-tag for easy characterisation and 6xHIS-tag to purify the protein (**Figure 1A**). We observed efficient expression of MBP-FLAG-RSPO3-Fu1-Fu2-6xHIS protein (bacRSPO3) in the bacteria upon induction by isopropyl β -d-1-thiogalactopyranoside (IPTG) (**Figure 1B**). The bacterial lysate was loaded on nickel columns and bacRSPO3 was purified. While bacterial proteins washed through the columns, bacRSPO3, identified based on molecular size, could be collected during the elution phase (**Figure 1C**). Presence of the full protein was observed upon western blot analysis for N-terminal FLAG-tag and C-terminal 6xHIS-tag (**Figure 1D**). Endotoxins were removed and recombinant protein solutions were concentrated and quantified. A single production round yielded 5-10 mg of bacRSPO3. This method therefore allows for production of recombinant RSPO3 that circumvents the use of either expensive commercially available RSPO or undefined conditioned medium from RSPO1-producing cell lines.

To test the functionality of bacRSPO3, we incubated HEK293 cells with increasing concentrations of bacRSPO3 in combination with Wnt. Satisfyingly, we observed a dose-dependent effect of bacRSPO3 in potentiating Wnt signalling (**Figure 2A**). At a concentration of 500ng/mL bacRSPO3, similar levels of Wnt signalling was observed compared to 10% RSPO1 HEK293-conditioned medium (RSPO1 CM), which is commonly used for organoid culture¹⁹ (**Figure 2A-B**). This activation was only observed when bacRSPO3 was used in combination with Wnt since addition of 500ng/mL bacRSPO3 alone did not induce significant Wnt signalling (**Figure 2B**). Recently, synthetic Wnt activators, termed 'surrogate Wnts', have been shown to be highly effective in inducing Wnt signalling²⁰. We compared Wnt3a-conditioned medium (Wnt3a CM) and Wnt surrogate²⁰ in combination with available Wnt potentiators (RSPO1 CM, RSPO3 conditioned medium of Utrecht Protein Express (UPE) (UPE RSPO3) and bacRSPO3). Inductions of Wnt signalling were observed in all combinations yet with varying efficacy. In general, higher induction was observed in cells treated with Wnt surrogate in combination with RSPO compared to Wnt3a CM. Of the Wnt potentiators, bacRSPO3 showed the highest induction in both Wnt3a CM- and in surrogate Wnt-treated cells, as compared to RSPO1 CM and UPE RSPO3 (**Figure 2C**). Overall, bacRSPO3 potentiates Wnt signalling *in vitro* at least as well as other available RSPOs. To test the stability of the protein, we stored bacRSPO3 in the fridge (4°C) or at -80°C and tested its ability to potentiate Wnt signalling after 2 months compared to newly produced bacRSPO3. Very limited differences were observed, which indicated high stability of bacRSPO3 (**Figure 2D**). Since Wnt signalling is essential for maintaining adult stem cell-derived organoids, we used 500ng/mL bacRSPO3 as replacement of other Wnt potentiators in airway²¹ and cholangiocyte²² organoid cultures. Organoid cultures showed similar growth rate and morphology in medium comprising bacRSPO3, RSPO1 CM and UPE RSPO3 for at least three passages (**Figure 2E**). In

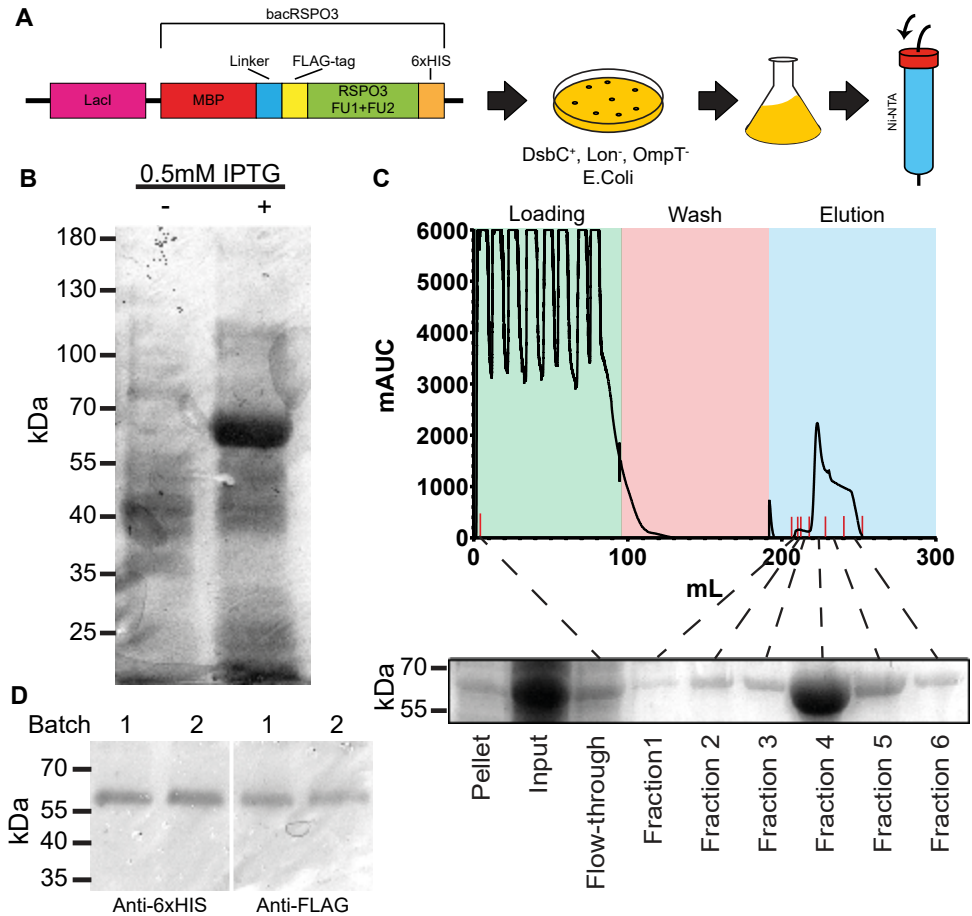


Figure 1. Efficient production of bacRSPO3 using bacterial expression. A) Schematic representation of the workflow of the production of bacRSPO3. The construct uses an inducible promoter (LacI), maltose-binding protein (MBP) for solubility, a short linker, FLAG-tag for visualisation, two furin-domains (FU1 and FU2) of RSPO3 and a 6xHIS for purification. The construct is expressed in E.Coli strain with expression of disulfide bond isomerase DsbC and loss of Lon and OmpT proteases. After bacterial culture expansion and bacterial lysis, the supernatant is purified over nickel-coated columns allowing purification of bacRSPO3. B) Coomassie stained polyacrylamide gel for analysing bacterial lysates of cultures containing bacRSPO3 construct incubated overnight in the absence (lane 1) or presence (lane 2) of 0.5mM isopropyl β - d-1-thiogalactopyranoside (IPTG). Addition of IPTG shows presence of a ± 65 kDa protein as expected from bacRSPO3. C) Representative absorbance plot of FPLC purification of bacRSPO3 with corresponding coomassie stained polyacrylamide gel. Initial loading phase (green) shows high absorbance peaks after the column including some potential bacRSPO3. The wash phase (red) shows limited absorbance. BacRSPO3 protein is identified in all fraction during elution phase (blue). Concentrations observed in coomassie stain is in line with absorbance measured. Red lines indicate start of new fractions collected. D) Western blot analysis on polyacrylamide gel loaded with endotoxin removed and concentrated bacRSPO3 fractions stained with anti-6xHIS (left panel) or Anti-FLAG-tag (right panel). Two independently produced batches (batch 1 and 2) show specific staining of bacRSPO3 N- and C-terminal tags at ± 65 kDa.

1

2

3

4

5

6

7

8

9

&

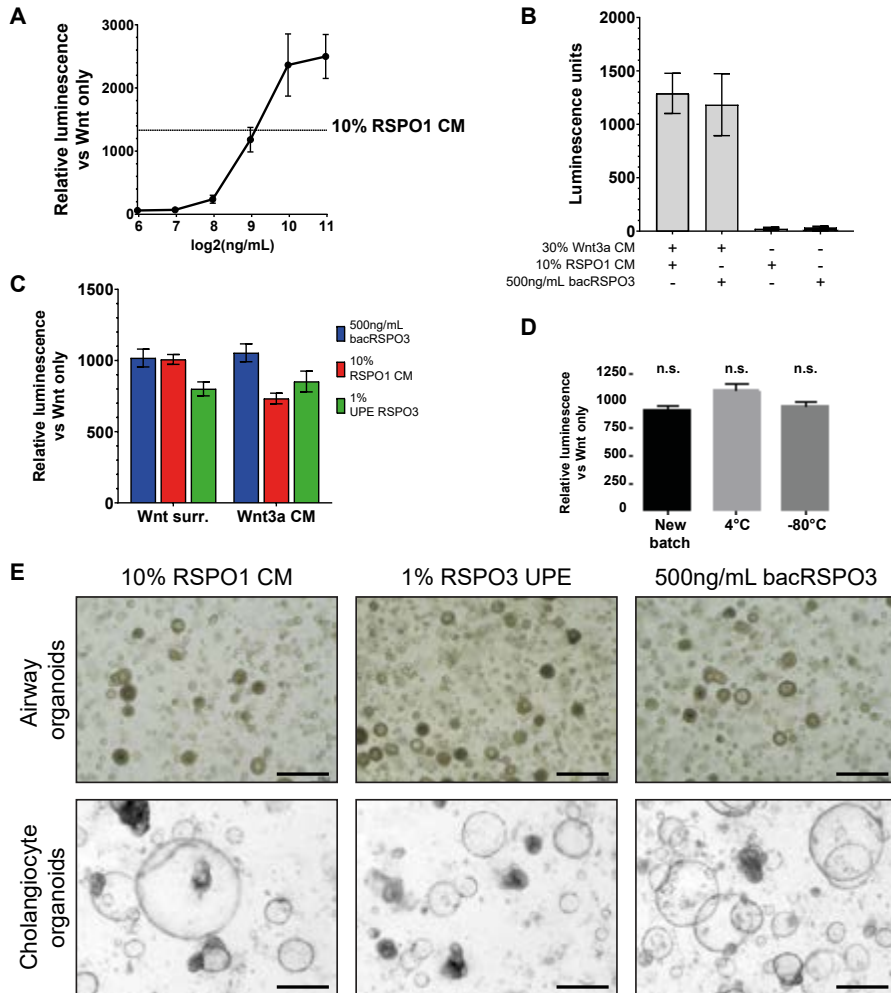


Figure 2. BacRSPO3 is efficient in potentiating Wnt signalling and maintaining organoid cultures in vitro. A) Line graph depicting relative luminescence of Super TOPFLASH (STF) assay of different concentrations of bacRSPO3 and 30% Wnt3a conditioned medium (Wnt3a CM). 500ng/mL bacRSPO3 shows similar luminescence as 10% RSPO1 conditioned medium (RSPO1 CM). Error bars = stdev. N=3. B) Bar graph depicting luminescence of STF assay. Similar Wnt activation is observed in 10% RSPO1 CM as 500ng/mL bacRSPO3 in combination with 30% Wnt3a CM. Limited luminescence is observed in HEK293 cells incubated in the absence of 30% Wnt CM indicating the potentiating role of RSPO. Error bars = stdev. N=3. C) Bar graph depicting luminescence of STF assay. Similar Wnt activation is observed in 10% RSPO1 CM as 500ng/mL bacRSPO3 in combination with Wnt surrogate (Wnt surr.). 1% UPE RSPO3 shows less Wnt activation in both Wnt surr as Wnt3a CM conditions. BacRSPO3 shows highest Wnt activation compared to RSPO1 CM and RSPO3 UPE when combined with Wnt3a CM. Error bars = stdev. N=3. D) Bar graph depicting luminescence of STF assay. Similar Wnt activation is observed in freshly produced bacRSPO3 and bacRSPO3 stored for 2 months at 4°C or -80°C showing high stability of the protein. Error bars = stdev. N=3. E) Representative brightfield images of airway (upper panel) and cholangiocyte organoids (lower panel) cultured in the presence of RSPO1 CM, RSPO3 UPE or bacRSPO3. No clear morphological differences can be observed. Scale bar = 200µm.

conclusion, bacRSPO3 is capable of potentiating Wnt signalling and thereby maintaining adult stem cell organoid cultures.

Since bacRSPO3 was able to potentiate Wnt signalling in vitro and maintain proliferation in organoid cultures, we injected bacRSPO3 in mice to study the role of RSPO in vivo. After two injections of 5mg/kg bacRSPO3 on consecutive days, we observed increased proliferation in the liver after 3 days based on Ki67 expression (**Figure 3A-B**). We also observed an enlarged area of proliferation in the small intestine, based on bromodeoxyuridine incorporation (**Figure 3C-D**). This increase is expected since the bacRSPO3 was given systemically using intraperitoneal (IP) injection and the intestinal epithelium is known to be Wnt-dependent²³. Since injection of bacterially produced RSPO3 might induce secondary effects independent of RSPO signalling, we verified our findings in RSPO1-3 KO mice. Limited effect on proliferation of RSPO KO was observed due to the limited baseline proliferation in livers of WT mice (**Supplementary figure S1A-B**). Satisfyingly, a more profound decrease of proliferation was observed in the small intestine (**Supplementary figure S1C-D**). To better define the optimal concentration of bacRSPO3, we injected between 0-10mg/kg bacRSPO3 and observed an increase in the number of proliferative cells in the liver with increasing concentrations of bacRSPO3; a plateau was reached at 7.5-10mg/kg bacRSPO3 (**Figure 3E**). We therefore determined 7.5mg/kg as optimal. To determine the optimal protocol, we injected mice via IP and intravenous (IV) injection and compared this to IV injection of PBS. An additional increase of proliferative cells in the liver was observed in mice injected using IV injections compared to IP injections while proliferation remained at background levels in PBS injected mice (**Figure 3F**). Since bacRSPO3 requires the presence of Wnt, we injected mice with both 7.5mg/kg bacRSPO3 and 5 mg/kg Wnt surrogate. This further increased the number of Ki67⁺ cells in the liver after 3 days post-injection (**Figure 3F**). Since hepatocytes are the main functional cell type in the liver, we quantified the number of proliferative hepatocytes after 3 days of bacRSPO3 injections. We observed a significant increase in the number of proliferative hepatocytes, based on nuclear morphology and Ki67 expression, in mice injected IV compared to IP injected mice and PBS injected mice (**Figure 3G**). Addition of Wnt surrogate further increased the number of proliferative hepatocytes (**Figure 3G**). Altogether, bacRSPO3 injected systemically upregulated proliferation in liver cells in a dose-dependent and administration-dependent manner while also increasing proliferation in other organs.

To better characterise the effect of bacRSPO3 over time, mice were given a single injection of 7.5mg/kg bacRSPO3 and tissue samples were collected over a period of 7 days. Two separate waves of proliferation were observed, with the first wave peaking at day 2 while the second wave peaked at day 4. Based on the nuclear morphology we could separate the waves based on the presence or absence of hepatocyte proliferation. On day 2, only small nuclei expressed Ki67 while larger rounded nuclei were Ki67⁺ from day 4 onwards (**Figure 4A**). Proliferation returned to homeostatic levels at day 7 (**Figure 4B**). The rounded nuclei were characteristic for hepatocytes while the cells with smaller nuclei

1
2
3
4
5
6
7
8
9
&

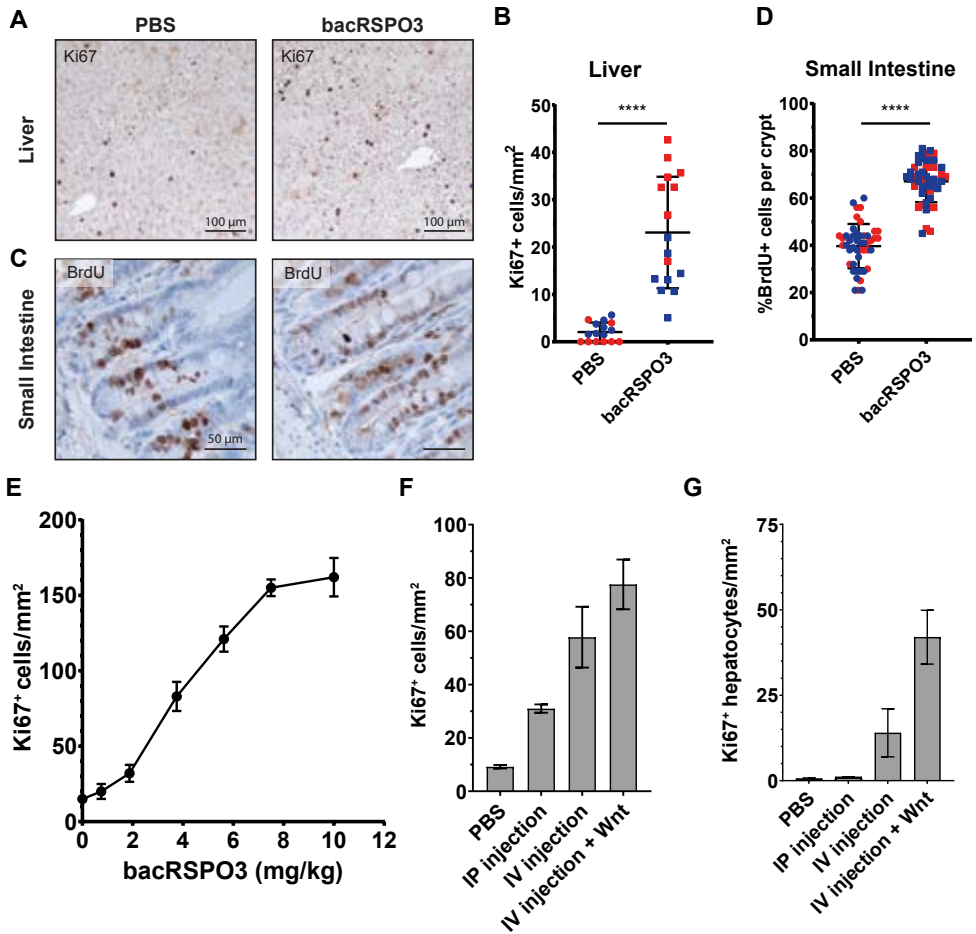


Figure 3. Systemic injection of bacRSPO3 induced proliferation in the liver in a dose- and method-dependent manner. A) Increased proliferation in the liver is observed in mice 3 days post-injection of 5mg/kg bacRSPO3 (right panel) compared to PBS injected mice as indicated by Ki67. Scale bars = 100um. B) Quantification of Ki67+ cells in the liver of mice injected with bacRSPO3 or PBS shows significant induction of proliferation in bacRSPO3 injected mice. Each colour represents a mouse. **** = $p < 0.0001$. Error bars = mean and stdev. C) Increased proliferation in the small intestine is observed in mice injected with 5mg/kg bacRSPO3 (right panel) compared to PBS injected mice as indicated by BrdU incorporation. Scale bars = 50um. D) Quantification of BrdU+ cells in the crypts of the small intestine of mice injected with bacRSPO3 or PBS shows significant induction of proliferation in bacRSPO3 injected mice. Each colour represents a mouse. **** = $p < 0.0001$. Error bars = mean and stdev. E) Line graph depicting the induction of proliferation in liver cells 3 days post-injection of different concentrations of bacRSPO3 by Ki67+ cells per mm². Error bars = stdev. N=2. F) Bar graph indicating the proliferation in liver cells by Ki67 per mm² based on the method of injection 3 days post-injection of PBS (1st bar) or bacRSPO3 (2nd and 3rd bar) or bacRSPO3 and Wnt surrogate (4th bar). Error bars = stdev. N=10. G) Bar graph indicating the proliferation in hepatocytes by Ki67 per mm² based on the method of injection 3 days post-injection of PBS (1st bar) or bacRSPO3 (2nd and 3rd bar) or bacRSPO3 and Wnt surrogate (4th bar). Hepatocytes were characterised based on nuclear morphology. Error bars = stdev. N=10.

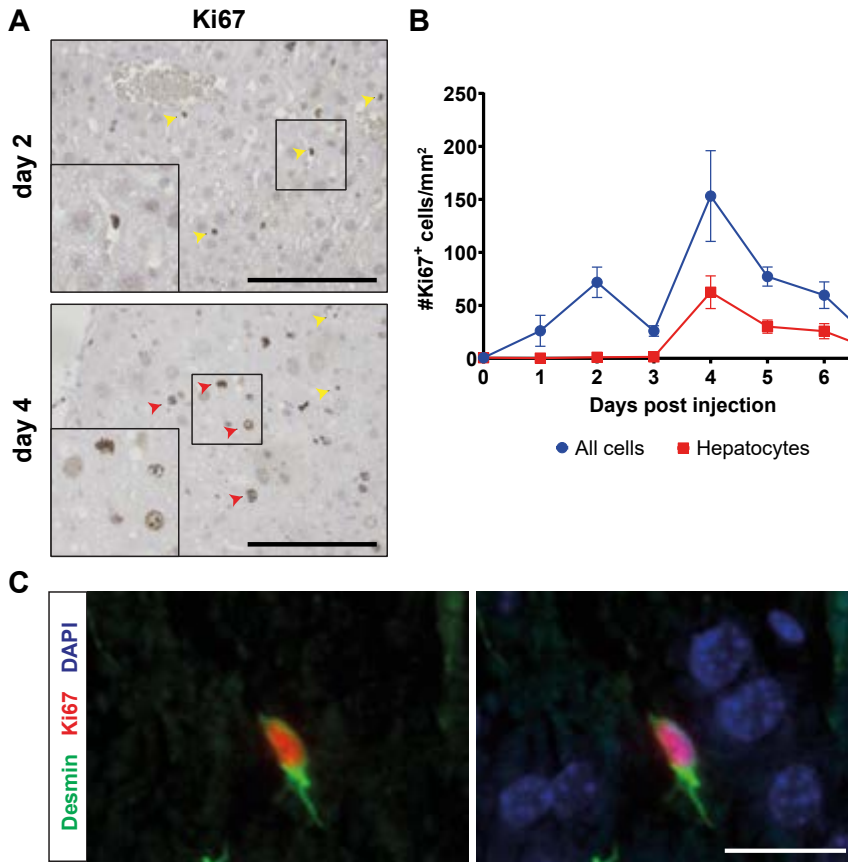


Figure 4. Proliferation after bacRSPO3 injection induces stellate cell proliferation before hepatocyte proliferation. A) Representative immunohistological stainings of liver of mice 2 days (upper panel) or 4 days (lower panel) post-injection of bacRSPO3 showing different nuclear morphologies with Ki67 expression. On day 1, only small nuclei show Ki67 positivity while day 4, larger rounded nuclei, characteristic for hepatocytes, are mainly identified in the Ki67⁺ population. Scale bar = 100µm. B) Line graph depicting the number of all Ki67⁺ cells (blue) and Ki67⁺ hepatocytes (red) per day after bacRSPO3 injection indicating two waves of proliferation peaking at day 2 and 4. Significant hepatocyte proliferation is only observed from day 4 onwards. Error bars = stdev. N=3. C) Representative images of Ki67⁺ stellate cell positive for Desmin on day 2 post-injection of bacRSPO3. Ki67 negative nuclei stained by DAPI can be characterised as hepatocytes based on size and circularity. Scale bar = 25µm.

showed Desmin-positivity indicative of stellate cells (**Figure 4C**). The initial proliferation wave therefore involved liver stellate cells instead of hepatocytes. RSPO has been shown to induce stellate cell proliferation²⁴. The second wave is mostly comprised of hepatocyte proliferation. To verify if the hepatocyte proliferation was a direct effect of the RSPO-furin domains in bacRSPO3, we visualised active Wnt signalling by expression of glutamine synthetase (GS), a bona fide Wnt target gene in the liver. We observed a gradual increase of GS⁺ hepatocytes surrounding the central vein over time after day 3 similar to

1

2

3

4

5

6

7

8

9

&

the hepatocyte proliferation curve (**Figure 5A-B**). When compared to PBS a significant increase in the number of GS⁺ cells was observed (**Figure 5C**). Similarly, a decrease in the number of GS⁺ cells surrounding the central vein was observed in the RSPO1-3 KO mice compared to WT mice (**Supplementary figure S1E-F**). This indicated that the enhanced Wnt activation by bacRSPO3 around day 4 induced proliferation of hepatocytes. To verify if active Wnt signalling was required for proliferation, we studied the combinatorial expression of the Wnt target GS and the proliferation marker Ki67. Both GS⁺Ki67⁺ as well as GS⁻ Ki67⁺ hepatocytes could be observed on day 4 post-injection (**Figure 5D**). When quantified, a larger proportion (78.34% ±5.417) was GS⁻ contrasted with canonical RSPO signalling (**Figure 5E**). Surprisingly, we observed the largest increase in proliferation in Wnt-inactive zone 1 and the smallest increase in proliferation in the Wnt-active zone 3 (all compared to PBS injected control mice) (**Figure 5F**). BacRSPO3 therefore induces an increase in Wnt signalling and proliferation in Wnt-active zone 3 but also induces proliferation in Wnt-inactive zone 1. RSPO signalling therefore seems independent of Wnt activity or liver zonation.

DISCUSSION

In this study, we present an optimised protocol for the generation of recombinant RSPO3 using bacterial expression. This bacRSPO3 was used to study the effect of RSPO administration on proliferation of the liver. We showed the existence of two waves of proliferation: initial proliferation of liver stellate cells and subsequent proliferation of hepatocytes. This latter proliferation wave induces an increase in Wnt-active zone 3 hepatocytes marked by GS, yet the highest induction of proliferation was identified in the Wnt-inactive portal triad zone 1. The origin of liver proliferation has been debated for years. While Wnt-active Axin2⁺ zone 3 hepatocytes were initially believed to be responsible for homeostatic turnover²⁵, later studies revealed evidence arguing against this hypothesis demonstrating that all hepatocytes, independent of their location, have similar proliferative potential^{9,26-30}. The current study underlines the equal proliferative potential and might even suggest that RSPO signalling induces more proliferation in zone 1 hepatocytes. Parallel studies suggested similarly that zone 2 hepatocytes have highest proliferative potential^{31,32}. The debate therefore remains unresolved.

The absence of an identifiable defined proliferative population in the liver does not, however, rule out Wnt signalling as essential component of hepatocyte proliferation. Many studies have shown the importance of Wnt signalling in liver homeostasis as well as regeneration^{9,33-35}. The direct relation between active Wnt signalling and the proliferative potential of the different liver zones remains elusive. The role of RSPO in this equation is even less clear. The current protocol enables the study of RSPO3 function in a variety of organs including the liver and its role in regeneration. Previous studies have shown the beneficial role of RSPO administration in enhancing regenerative capacity^{9,36}. This effect was ablated by knockout of RSPO-receptor Lgr4 but not by knockout of Wnt target

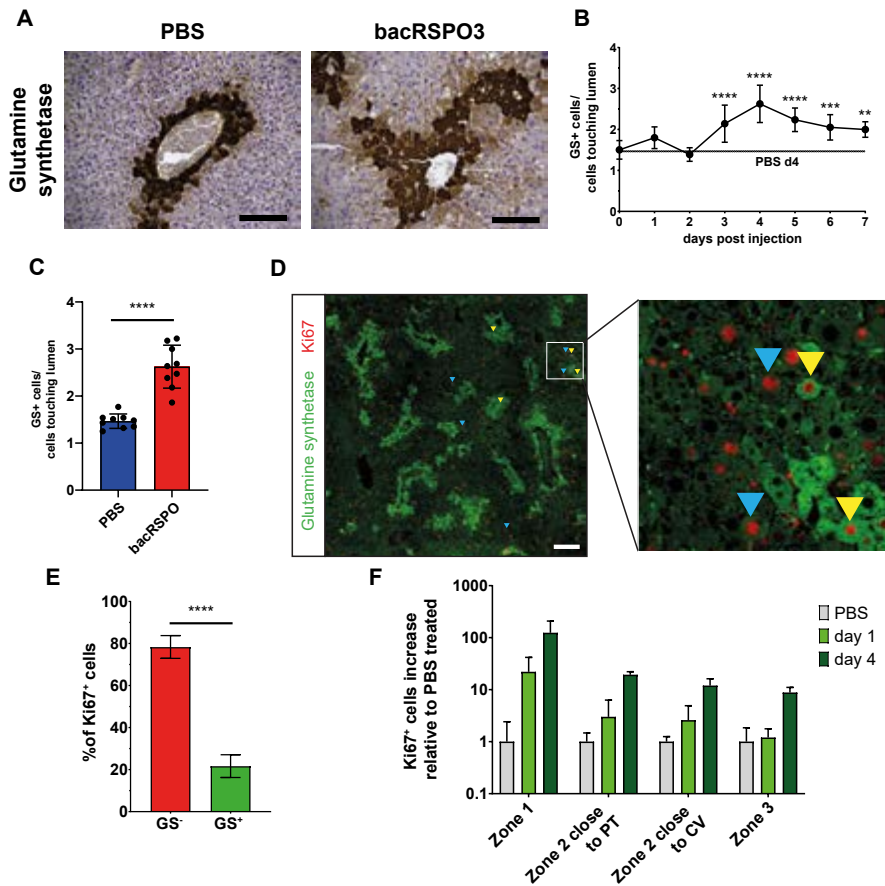


Figure 5. BacRSPO3 enhances Wnt signalling in central vein surroundings but also induces proliferation independently of Wnt activation. A) Representative images of bona fide Wnt target gene Glutamine synthetase (GS) on day 4 post-injection of PBS or bacRSPO3. An increase in cells surrounding the central vein expressed high levels of GS showing induction of Wnt activation by bacRSPO3. Scale bars = 100um. B) Line graph depicting the ratio between the number of GS+ cells and GS+ cells touching the lumen of the central vein. A slight peak is observed on day 1, yet significant increase is observed from day 3 post-injection up until day 7 compared to PBS treated mice (PBS d4). ** = $p \leq 0.01$, *** = $p \leq 0.001$ and **** = $p < 0.0001$. Error bars = stdev. N=12. C) Bar graph depicting the ratio between the number of GS+ cells and GS+ cells touching the lumen of the central vein in livers of mice after 4 days post-injection of PBS or bacRSPO3. A significant increase in GS+ cells underlines the Wnt activation by bacRSPO3. **** = $p < 0.0001$. Error bars =stdev. D) Representative image of proliferative cells marked by Ki67 and Wnt-active hepatocytes marked by GS on day 4 post-injection of bacRSPO3. GS+ proliferative cells (yellow arrow heads) as well as GS- negative cells (blue arrow heads) can be observed. Scale bar = 250um. E) Bar plot depicting the percentage of proliferative cells marked by Ki67 in Wnt-inactive cells (GS-) and Wnt-active cells (GS+). **** = $p < 0.0001$. Error bars = stdev. N=10. F) Bar plot depicting the relative increase of proliferative cells marked by Ki67 in the different zones of the liver on day 1 and 4 post-injection of bacRSPO3 compared to PBS injected mice. Cells are divided into their location along the central-to-portal axis. Zone 3 and Zone 1 cells touch the lumen of the vein or line a cell which touches a lumen. Zone 2 cells are not close to lumen and are divided based on the closest vein visible. Error bars = stdev. N=10.

1
2
3
4
5
6
7
8
9
&

gene and RSPO-receptor Lgr5⁹. Since Lgr4 is expressed throughout the liver lobule, even in Wnt-inactive areas, RSPO signalling could potentially signal independent of Wnt to enhance proliferation and liver regeneration. The discrepancy between Wnt signalling and RSPO function has been shown before in the maintenance of intestinal stem cells. Yan and colleagues even postulate a role for Wnt ligands to potentiate RSPO signalling by upregulating expression of RSPO receptors³⁷. This complicated interaction between RSPO and Wnt signalling requires further studies to better define the potential independent role of RSPO signalling.

To study signalling networks, a defined yet representative model system is required. The establishment of adult stem cell-derived organoid cultures allow for minimalistic stem cell dynamics while maintaining *in vivo* representation³⁸. Combinatorial supplementation of Wnt and RSPO to these cultures could potentially allow the disentangling of the Wnt-RSPO-axis. Recent development of Wnt surrogates²⁰ and the presented production of bacRSPO3 provide useful tools for controlled activation of both signalling pathways. (Current studies make use of Wnt3a and RSPO-conditioned medium generated by mammalian cell lines overexpressing the pertinent protein constructs). These media contain undefined other components which might interfere with functional studies. We here present a relatively cheap alternative for the production of functional RSPO that can be purified and used in defined concentrations as recombinant protein. In conclusion, while many aspects in RSPO signalling remain poorly understood, we provide bacterially produced RSPO3 as a tool to maintain stem cells *in vitro* and induce proliferation in the liver *in vivo*.

AUTHOR CONTRIBUTIONS

J.V. and H.G. designed and conceived the study. W.L. provided expression plasmids and helped designing and production of protein. J.V. wrote the manuscript. J.V. and H.G. performed purification and *in vitro* experiments. J.V. and H.G. analysed the data. J.V., J.K. and H.B. embedded tissue and performed immunohistochemistry staining. J.V. and H.G. performed mouse injections. L.Z. and J.E. generated RSPO1-LoxP and RSPO2-LoxP construct and analysed the floxed KO mice. H.F. generated the RSPO3-LoxP mice. J.K. and J.E. supervised mouse experiments. H.G. and J.E. wrote the mouse license. H.C. supervised the project.

ACKNOWLEDGEMENTS

We thank Anko de Graaff and the Hubrecht Imaging Centre (HIC) for microscopy assistance. We thank the Hubrecht Animal Facility for taking care of the experimental animals. We thank the Puck Knipscheer, Merlijn Witte and Francesca Mattioli for the use of and the help with the HPLC. This work was supported by the gravitation program CancerGenomiCs.nl from the Netherlands Organisation for Scientific Research.

CONFLICT OF INTEREST

H.C. is inventor on several patents related to organoid technology; his full disclosure is given at <https://www.uu.nl/staff/JCClevers/>.

1

2

3

4

5

6

7

8

9

&

REFERENCES

1. Clevers, H., Loh, K. M. & Nusse, R. An integral program for tissue renewal and regeneration: Wnt signaling and stem cell control. *Science* (80-.). **346**, 1248012 (2014).
2. Hao, H.-X. et al. ZNRF3 promotes Wnt receptor turnover in an R-spondin-sensitive manner. *Nature* **485**, 195–200 (2012).
3. Koo, B.-K. et al. Tumour suppressor RNF43 is a stem-cell E3 ligase that induces endocytosis of Wnt receptors. *Nature* **488**, 665–669 (2012).
4. de Lau, W. B., Snel, B. & Clevers, H. C. The R-spondin protein family. *Genome Biol.* **13**, 242 (2012).
5. de Lau, W. et al. Lgr5 homologues associate with Wnt receptors and mediate R-spondin signalling. *Nature* **476**, 293–297 (2011).
6. Glinka, A. et al. LGR4 and LGR5 are R-spondin receptors mediating Wnt/ β -catenin and Wnt/PCP signalling. *EMBO Rep.* **12**, 1055–1061 (2011).
7. Lebensohn, A. M. & Rohatgi, R. R-spondins can potentiate WNT signaling without LGRs. *Elife* **7**, (2018).
8. Rocha, A. S. et al. The Angiocrine Factor R-spondin3 Is a Key Determinant of Liver Zonation. *Cell Rep.* **13**, 1757–1764 (2015).
9. Planas-Paz, L. et al. The RSPO–LGR4/5–ZNRF3/RNF43 module controls liver zonation and size. *Nat. Cell Biol.* **18**, 467–479 (2016).
10. Burke, Z. D. et al. Liver Zonation Occurs Through a β -Catenin–Dependent, c-Myc–Independent Mechanism. *Gastroenterology* **136**, 2316–2324.e3 (2009).
11. Yang, J. et al. Beta-catenin signaling in murine liver zonation and regeneration: A Wnt–Wnt situation! *Hepatology* **60**, 964–976 (2014).
12. Benhamouche, S. et al. Apc Tumor Suppressor Gene Is the “Zonation-Keeper” of Mouse Liver. *Dev. Cell* **10**, 759–770 (2006).
13. Moad, H. E. & Pioszak, A. A. Reconstitution of R-Spondin:LGR4:ZNRF3 Adult Stem Cell Growth Factor Signaling Complexes with Recombinant Proteins Produced in Escherichia coli. *Biochemistry* **52**, 7295–7304 (2013).
14. Chen, P.-H., Chen, X., Lin, Z., Fang, D. & He, X. The structural basis of R-spondin recognition by LGR5 and RNF43. *Genes Dev.* **27**, 1345–1350 (2013).
15. Peng, W. C. et al. Structure of Stem Cell Growth Factor R-spondin 1 in Complex with the Ectodomain of Its Receptor LGR5. *Cell Rep.* **3**, 1885–1892 (2013).
16. Zebisch, M. et al. Structural and molecular basis of ZNRF3/RNF43 transmembrane ubiquitin ligase inhibition by the Wnt agonist R-spondin. *Nat. Commun.* **4**, 2787 (2013).
17. Wang, D. et al. Structural basis for R-spondin recognition by LGR4/5/6 receptors. *Genes Dev.* **27**, 1339–1344 (2013).
18. Xu, K., Xu, Y., Rajashankar, K. R., Robev, D. & Nikolov, D. B. Crystal Structures of Lgr4 and Its Complex with R-Spondin1. *Structure* **21**, 1683–1689 (2013).
19. Sugimoto, S. & Sato, T. Establishment of 3D Intestinal Organoid Cultures from Intestinal Stem Cells. in 97–105 (2017). doi:10.1007/978-1-4939-7021-6_7
20. Miao, Y. et al. Next-Generation Surrogate Wnts Support Organoid Growth and Deconvolute Frizzled Pleiotropy In Vivo. *Cell Stem Cell* **27**, 840–851.e6 (2020).
21. Sachs, N. et al. Long-term expanding human airway organoids for disease modeling. *EMBO J.* **38**, e100300 (2019).
22. Huch, M. et al. Long-term culture of genome-stable bipotent stem cells from adult human liver. *Cell* **160**, 299–312 (2015).
23. Hageman, J. H. et al. Intestinal Regeneration: Regulation by the Microenvironment. *Dev. Cell* **54**, 435–446 (2020).
24. Yin, X. et al. RSPOs facilitated HSC activation and promoted hepatic fibrogenesis. *Oncotarget* **7**, 63767–63778 (2016).
25. Wang, B., Zhao, L., Fish, M., Logan, C. Y. & Nusse, R. Self-renewing diploid Axin2+ cells fuel homeostatic renewal of the liver. *Nature* **524**, 180–185 (2015).
26. Sun, T. et al. AXIN2+ Pericentral Hepatocytes Have Limited Contributions to Liver Homeostasis and Regeneration. *Cell Stem Cell* **26**, 97–107.e6 (2020).

27. Matsumoto, T., Wakefield, L., Tarlow, B. D. & Grompe, M. In Vivo Lineage Tracing of Polyploid Hepatocytes Reveals Extensive Proliferation during Liver Regeneration. *Cell Stem Cell* **26**, 34-47.e3 (2020).
28. Chen, F. et al. Broad Distribution of Hepatocyte Proliferation in Liver Homeostasis and Regeneration. *Cell Stem Cell* **26**, 27-33.e4 (2020).
29. Lin, S. et al. Distributed hepatocytes expressing telomerase repopulate the liver in homeostasis and injury. *Nature* **556**, 244–248 (2018).
30. Kurosaki, S. et al. Cell fate analysis of zone 3 hepatocytes in liver injury and tumorigenesis. *JHEP Reports* **3**, 100315 (2021).
31. Wei, Y. et al. Liver homeostasis is maintained by midlobular zone 2 hepatocytes. *Science (80-.)*. **371**, (2021).
32. He, L. et al. Proliferation tracing reveals regional hepatocyte generation in liver homeostasis and repair. *Science (80-.)*. **371**, (2021).
33. Zhao, L. et al. Tissue Repair in the Mouse Liver Following Acute Carbon Tetrachloride Depends on Injury-Induced Wnt/ β -Catenin Signaling. *Hepatology* hep.30563 (2019). doi:10.1002/hep.30563
34. Huch, M. et al. In vitro expansion of single Lgr5+ liver stem cells induced by Wnt-driven regeneration. *Nature* **494**, 247–250 (2013).
35. Thompson, M. D. & Monga, S. P. S. WNT/ β -catenin signaling in liver health and disease. *Hepatology* **45**, 1298–1305 (2007).
36. Zhang, Z. et al. Tissue-targeted R-spondin mimetics for liver regeneration. *Sci. Rep.* **10**, 13951 (2020).
37. Yan, K. S. et al. Non-equivalence of Wnt and R-spondin ligands during Lgr5+ intestinal stem-cell self-renewal. *Nature* **545**, 238–242 (2017).
38. Schutgens, F. & Clevers, H. Human Organoids: Tools for Understanding Biology and Treating Diseases. *Annu. Rev. Pathol.* **15**, 211–234 (2020).

1

2

3

4

5

6

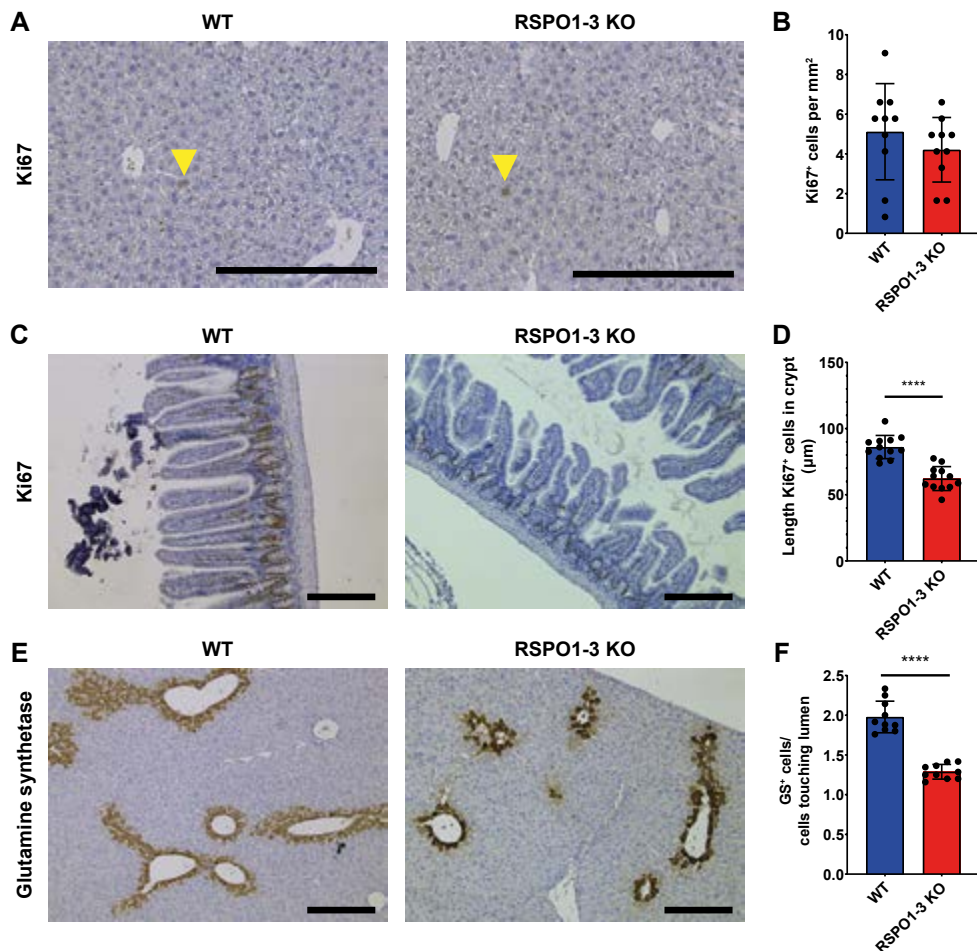
7

8

9

&

SUPPLEMENTARY FIGURES



Supplementary figure S1. RSPO1-3 knockout leads to decreased proliferation in the small intestine and loss of Wnt-active zones in the liver. A) Representative images of proliferative cells in the liver of wild-type (WT) and RSPO1-3 knockout (RSPO1-3 KO) mice marked by Ki67. Very limited proliferation is observed in WT mice and RSPO1-3 KO mice. Yellow arrow heads indicate proliferating hepatocytes. Scale bar = 200um. B) Bar graph depicting the number of proliferative cells in the liver of WT (blue) and RSPO1-3 KO (red) mice marked by Ki67. No significant differences can be identified. Error bars = stdev. C) Representative images of proliferative cells in the small intestine of wild-type (WT) and RSPO1-3 knockout (RSPO1-3 KO) mice marked by Ki67. Smaller areas of proliferation are observed in RSPO1-3 KO mice compared to WT mice. Scale bar = 200um. D) Bar graph depicting the length of proliferative crypts in the small intestine of WT (blue) and RSPO1-3 KO (red) mice marked by Ki67. **** = p < 0.0001. Error bars = stdev. E) Representative images of Wnt-active hepatocytes in the liver of wild-type (WT) and RSPO1-3 knockout (RSPO1-3 KO) mice marked by glutamine synthetase (GS). Scale bar = 200um. F) Bar graph depicting the number of GS+ cells relative to the number of GS+ cells touching the lumen of WT (blue) and RSPO1-3 KO (red) mice marked by GS. **** = p < 0.0001. Error bars = stdev.

CHAPTER

SUMMARISING DISCUSSION

9

In the eight chapters presented in this thesis, we have discussed a wide variety of model systems using adult stem cells. The establishment of the presented model systems relies on the insights generated in the past decades on adult stem cell signalling and organoid technology. This thesis builds upon current knowledge to extend the arsenal of model systems in the field of human diseases. While two studies presented here make use of previously developed organoid techniques of the small intestine¹ and airways² (chapter 2 and 4), two additional model systems are established by extending adult stem cell culture techniques (chapter 6 and 7). These model systems are utilised in a wide variety of human diseases including genetic (chapter 2), virological (chapter 4 and 6) and autoimmune diseases (chapter 7). Additionally, organoids have been used in an even broader spectrum of disease as summarised in chapter 1, 3 and 5. While chapters 1-7 describe adult stem cells *in vitro*, chapter 8 moves stem cell signalling *in vivo*.

AIRWAY ORGANOID AS MODELS OF DISEASE

The airway epithelium is a vital defensive barrier against pathogens yet also provides the essential processes of oxygen and carbon dioxide gas exchange. Malfunctioning of the pulmonary epithelium therefore causes a wide variety of diseases that could lead to systemic symptoms or even death. To improve both diagnostic and therapeutic abilities for airway-related diseases, it is important to better understand the biology of the disease. This requires either the use of human patients or representative model systems. In the initial establishment of airway organoids (AOs) in 2019, small patient biopsies were used to generate an avatar of this patient in the lab. These AOs are representative of the patients as well as the disease and shows susceptibility to known airway viruses². These and other related organoid technologies are then applied for both fundamental and clinical studies as summarised in chapter 1.

We extend on the potential of AOs in chapter 2. Here we present an example of a genetic disease called primary ciliary dyskinesia (PCD) that can be modelled using AOs. PCD affects the function of ciliated cells in the airways as well as other cells that require ciliary movement in other organs such as sperm cells. While the incidence of PCD is approximately one in 15,000–30,000, this condition is likely underdiagnosed due to suboptimal diagnostic parameters³. To date, therapeutic interventions can only alleviate PCD patients' symptoms. Most patients suffer from a lifelong chronic respiratory morbidity, with varying severity of the symptoms. Yet, the disease progresses and ultimately may lead to respiratory insufficiency and even the need for lung transplantation⁴. To overcome these challenges, a representative model system that allows long-term studying of the disease is needed. We therefore use AOs to model the most prominent symptoms of PCD. The use of nasal swaps to generate organoids, as performed in this study, limits patients discomfort due to a single non-invasive procedure. Current expansion conditions of the organoids, however, hamper visualisation of ciliated cells and thereby studying of the disease due to a lack of significant numbers of ciliated cells per organoid. To overcome

1

2

3

4

5

6

7

8

9

&

this problem, we developed, based on current literature⁵, a differentiation protocol which increases the number of ciliated cells, allowing modelling of PCD. Due to the many genes involved in ciliary motion, PCD is characterised by genetic heterogeneity and subsequent heterogeneity in disease phenotype and severity. To model the multiple aspects of PCD, we established four organoid lines of four patients with four different mutations leading to unique disease phenotypes. Extension on the number of patients included will help better understanding of the disease spectrum. Contrarily, since all patients are unique in their genetic background, establishment of organoid cultures from each individual patient would allow studies on patient-specific phenotypes and responses. The current patient-derived organoids are characterised using state-of-the-art techniques and show additional value to current diagnostic measures. It moreover provides a model system that can be established from small biopsy material that could be maintained in culture long-term. Future studies could reveal more insights into the biology of PCD but also disentangle the heterogeneity found in patients. On the road towards personalized medicine, these patient-specific phenotypes within PCD could subsequently be screened for potential therapeutics.

Current AOs generated by Sachs and colleagues show long-term expansion due to the presence of basal cells, the proposed stem cells of the lung⁶. To study diseases related to differentiated cell types of the airways, an additional protocol is required to differentiate cells in culture. The current protocols, however, only allow for the differentiation of one cell type of the lung. This limits the potential of the organoids to represent the complexity of the airways if the differentiation is unidirectional. For example, differentiation towards ciliated cells, as shown, leads to loss of secretory cells. Both cell types are however responsible for the mucociliary clearance⁷. Due to lack of the cellular diversity in the organoids, studies are currently restricted to cell type specific phenotypes.

The ciliated cell differentiation protocol in combination with the robust establishment of patient-derived organoids, however, is not only applicable for PCD. Many cilia-related diseases can be studied using the airway model system for airway-related symptoms but cilia are also present in other organs⁵. Adaptations of the presented differentiation protocol could be applied to organoids of other cilia-related organs like the endometrium. For instance, while human endometrial organoids show the presence of ciliated cells, the number is limited⁸⁻¹⁰. A differentiation protocol, similar to the one we describe, could reveal deeper insights in the cilia-related biology and diseases in the endometrium.

In conclusion, the development of AOs presents a toolbox that can be used for a broad spectrum of studies involving fundamental biology, disease modelling and potentially therapeutic screening. Moreover, the insights identified in ciliated cell differentiation could potentially open up new ways for other cilia-related organs.

ORGANOIDS TO MODEL COVID-19

While humanity might believe itself invincible, global pandemics like the current coronavirus disease 2019 (COVID-19) once more underline the reliance on medical care and science. In late 2019, Chinese researchers first described the existence of a new coronavirus that could infect humans and cause severe pulmonary distress¹¹. By March 2020, severe acute respiratory syndrome coronavirus-2 (SARS-CoV-2) had spread around the globe and was officially declared a pandemic¹². Due to the close resemblance to previously identified SARS-CoV virus, the angiotensin-converting enzyme 2 (ACE2) molecule was rapidly identified as entry receptor for SARS-CoV-2¹³⁻¹⁶. Expression of ACE2 is confirmed in multiple cell types in the lung including alveolar type II and ciliated cells¹⁷⁻¹⁹. Yet highest expression is identified in the intestinal lining^{18,19}. Additionally, viral particles are identified in sewage water and faeces indicating viral shedding in the gastrointestinal system²⁰⁻²². We therefore apply previously established intestinal organoids as potential model system of epithelial infection of SARS-CoV-2 as described in chapter 4. We reveal the susceptibility for SARS-CoV-2 in the intestinal lining and observe upregulation of viral infection-related interferon I and III pathways. The intestinal infection was, at that time, still postulated and therefore this study was one of the first to show scientific proof of infection. Since these organoids are a minimalistic model system of the epithelial layer, the exact mechanism of viral entry and replication can be identified without interference of other cell lineages²³. The advantage of using reductionistic, yet representative model systems is summarised in chapter 3 and 5. Epithelial organoids allow for translatable research on viral infections and potential preventative measures or treatments. While intestinal infection was already observed in the early pandemic^{24,25}, pulmonary manifestations are more heavily observed in patients suffering from SARS-CoV-2 infection leading to the disease COVID-19. To better understand the virological fundamentals of airway epithelial infection of SARS-CoV-2, many groups established organoid models that were susceptible to SARS-CoV-2 infection as summarised in chapter 5. Additionally, we established a new model system using airway organoids as cellular source. This two-dimensional culture system presents cells of both upper and lower airways. The presence of embryonic fibroblasts in culture as paracrine signalling of the fibroblasts is essential to differentiate the organoid cells to alveolar-like cells. Unravelling the signals secreted by the fibroblast, which are essential for this differentiation, would eventually lead to robust differentiation of alveolar cells *in vitro* using a defined medium. Infection of SARS-CoV-2 in these bronchioalveolar cultures reveals similar interferon responses as observed in small intestinal organoids and human COVID-19 patients. Besides COVID-19, these alveolar cells could be useful tools for understanding other alveolar diseases.

Apart from the papers presented in this thesis, many more studies revealed aspects of the pandemic as little as molecules involved in infection to as large as genome-wide screens. These studies implied repurposing of known model systems as well as generation of new model systems. While adult stem cell-derived organoids had been

1

2

3

4

5

6

7

8

9

&

used prior for infection studies^{2,26–30}, the technique was not around during previous pandemics. The strengths of a representative culture system speeds up new but most importantly translatable discoveries that could lead to useful therapeutics. The danger of a model system that does not represent human biology was illustrated in the discovery of hydroxychloroquine as SARS-CoV-2 treatment in African green monkey cells³¹. It was quickly implemented worldwide while limited effects were observed in humans and only caused severe side-effects³². This ineffectiveness in human cells was later confirmed using intestinal organoids²³. Recent developments in organoid technology as well as in genetic editing tools³³ and their combinatorial advantages^{34–37} holds great potential in prospect to future pandemics.

Apart from the current pandemic, organoids have been used widely for infection studies³⁸. Introduction of viruses, bacteria and helminth to a variety of adult stem cell cultures has revealed valuable insights in infection methods, epithelial responses and potential therapeutic targets. Further extension of the pathogen-organoid combinations will aid current understanding of infection diseases.

NOVEL ORGANOID MODEL OF THE THYROID

The thyroid maintains body homeostasis by secreting thyroid hormones into the blood stream. While this process is essential for everyday life, the processes involved in thyroid hormone secretion and regulation are understudied. This is mainly caused by the lack of a representative human thyroid model system. As elaborated before, the use of human adult stem cell-derived organoids could improve representability and thereby boost thyroid research. In chapter 7, we describe the generation of organoid cultures from murine and human adult thyroid follicular cells. These follicular cells can be expanded for more than a year while maintaining their thyroid follicular cell identity. Expression levels of thyroid hormone machinery genes is comparable to tissue level. Satisfyingly, basal secretion of thyroid hormones is observed which could be increased by stimulation of the organoids with thyroid stimulating hormone (TSH). Due to the polarised cell layer in a three-dimensional orientation in the organoids, thyroid hormone carrier protein is identified in the lumen (apical side) while free thyroid hormone is only detected on the basal side. The high resemblance of the organoids to the *in vivo* tissue in combination with the *in vitro* possibilities being genetic editing, drug discovery and much more makes these organoids an ideal model system to study thyroid biology and disease. To study this, we look at the effect of serum of Graves' disease patients on our thyroid organoids. We observe increased proliferation of our organoids after incubation with serum of Graves' disease patients while this is not the case for serum from non-patients. Since this stimulation is absent when using serum from non-patients, the effect can be accounted to the presence of TSH receptor (TSHR) activating antibodies. Additionally, the organoids secrete higher levels of thyroid hormone after stimulation, which is in line with clinical observations in patients suffering from Graves' disease³⁹. It is thereby the first reported organoid culture for the modelling of a human autoimmune disease.

In addition to fundamental thyroid biology and thyroid autoimmune diseases, the organoids could be employed for other clinical open questions. For example, childhood cancer survivors have shown increased risk on developing thyroid dysfunction or even cancer^{40,41}. Current treatment of neuroblastoma is based on administration norepinephrine analogue metaiodobenzylguanidine (MIBG). This is usually combined with radioactive iodine isotopes. Since iodine isotopes are mainly taken up by the thyroid, patients receive potassium iodide to saturate thyroid uptake and limit the radioactive iodide uptake⁴⁰. Unfortunately, the incidence of thyroid dysfunction after MIBG treatment remains. The thyroid organoids could be used as surrogates to model MIBG uptake by the thyroid gland and test interventions that limit this side effect. It could thereby aid the prevention of thyroid dysfunction or even thyroid cancer in adults.

Current organoid cultures only sustain the growth of thyroid follicular cells. Another important thyroid cell type responsible for maintaining body homeostasis, C-cells, are currently absent in the organoids. Due to its neural crest cell-origin, the growth is most likely not supported by the growth factors in the current medium. Future optimisation might allow the culture of C-cells in organoid cultures. This would further increase the potential of thyroid organoids to unravel thyroid biology and hormone regulations but also understand the communication between the two cell types.

Upon damage, the thyroid shows the potential to regenerate, however limited. This hints at the presence of thyroid adult stem cells. The identity of these stem cells to date however remains elusive. Organoid cultures are proliferative and could therefore be regarded as a regenerating organ. Additionally, the technique relies on the potential of cells to self-renew and differentiate, characteristics usually attributed to stem cells. The presence of thyroid stem cell-like cells in organoid cultures could therefore help the search for an adult thyroid stem cell population. In chapter 7, we briefly introduce the concept of less mature follicular cells, which are actively cycling. Whether these cells are bona fide thyroid stem cells is questionable. Recently, it has emerged that many solid tissues do not rely on a single stem cell population but rather temporarily recruit differentiated cells into a progenitor pool⁴². Deeper identification of this transient progenitor cell population in the thyroid organoids and the required signals to maintain or expand this population could potentially aid the recovery of thyroid cells after damage. Up until today, thyroid diseases are treated by removal of the diseased thyroid tissue^{43,44}. This results in patients taking life-long hormone replacements. Deeper understanding of thyroid regeneration using adult stem cells or transient progenitors might help recovery of patients after surgery and potentially even take the place of hormone replacement therapies. Transplantation of the healthy thyroid organoids in diseased patients could even circumvent the need for thyroid removal or at least replace removed tissue.

IN VIVO STEM CELL SIGNALLING IN THE LIVER

To establish adult stem cell-derived organoid cultures it is essential to understand stem cell signalling *in vivo*. Upon damage, adult stem cells are capable of replacing damaged

1

2

3

4

5

6

7

8

9

&

tissue by proliferation and subsequent differentiation. Similarly, hepatocyte proliferation is a common phenomenon upon liver damage. The hepatocytes replace damaged tissue which can be as large as two-thirds of the original size⁴⁵. Wnt signalling is essential for efficient liver regeneration⁴⁶. In line, ablation of R-spondin (RSPO) signalling by removal of LGR4 and LGR5 limits liver regeneration⁴⁷. Only addition of RSPO1 aided faster recovery in mice after partial hepatectomy⁴⁷. This hints at the potential of RSPO as therapeutic agent for patients suffering from liver damage or impaired liver repair. We therefore studied RSPO signalling in mouse livers using bacterially produced RSPO. Injection of the recombinant protein increases proliferation rates of hepatocytes up to a week post-injection. Interestingly, the proliferation is not limited to the liver zones known for active Wnt signalling but could also be observed in the Wnt inactive zones. Based on the role of RSPO as potentiator but not activator of Wnt signalling, a Wnt-independent role of RSPO, as shown before⁴⁸, could explain the observed zone-independent proliferation. This role is highly debated and further studies would be required to validate this independency.

Unfortunately, apart from the increased proliferation in the liver, we observe a systemic response to the presence of RSPO in the bloodstream or peritoneal cavity. The intestinal tract shows the most significant increase of proliferation in the crypts, the known adult stem cell niche of the intestine. Systemic administration of RSPO would therefore show severe side effects in patients. Targeted administration of the RSPO molecule would limit these side effects. By fusing a liver-specific binding partner to RSPO, the effects of RSPO can be limited to hepatocytes. Initial studies have shown the additive effect of using these fusion proteins^{49,50}. These targeted proteins could be administered after acute liver damage to limit the recovery period but also boost healthy hepatocytes in chronic liver diseases to replace tissue at a faster rate. Moreover, small biopsies could be transplanted and activated to grow into sufficient liver tissue, which would lower the requirement of liver donor material. Apart from biopsies, recent development of cholangiocytes organoids with the capacity of transdifferentiation⁵¹ and hepatocyte organoids⁵² could also be used as donor material. Since these organoids have limited cell numbers, addition of RSPO during transplantation could aid engraftment and further outgrowth.

Additionally, other essential stem cell signalling cascades might influence other or similar stem cell dynamics and could therefore aid recovery of patients. By using mouse models as well as culture systems like organoids, an organ-specific cocktail of stem cell signalling molecules could be developed and later implemented in the clinic.

FUTURE PERSPECTIVES ON ORGANOID MODEL SYSTEMS FOR DISEASE

The research presented in this thesis applies the general mechanism of adult stem cells in a wide variety of research fields within human homeostasis and disease. Individual chapters discuss the use of the current and our identified knowledge of adult stem cells to study a specific disease. The common denominator in each chapter, however, is using

fundamental biology to model clinically relevant data. The model systems presented limit current application of adult stem cells and organoid technology to primary ciliary dyskinesia, COVID-19, Graves' disease and liver damage but the options are much broader. The diseases presented cover multiple disease categories being hereditary or genetic, infection and autoimmune diseases. Within these fields, the organoids can be implemented as model systems for a variety of other diseases. Future developments might even further increase the scientific opportunities of adult stem cell research. The potential for the model systems presented in this thesis and their derivatives is therefore endless.

1

2

3

4

5

6

7

8

9

&

REFERENCES

1. Beumer, J. et al. High Resolution mRNA and Secretome Atlas of Human Enteroendocrine Cells. *Cell* **181**, 1291-1306.e19 (2020).
2. Sachs, N. et al. Long-term expanding human airway organoids for disease modeling. *EMBO J.* **38**, e100300 (2019).
3. Leigh, M. W., O'Callaghan, C. & Knowles, M. R. The challenges of diagnosing primary ciliary dyskinesia. in *Proceedings of the American Thoracic Society* vol. 8 434–437 (Proc Am Thorac Soc, 2011).
4. van der Vaart, J. et al. Modelling of primary ciliary dyskinesia using patient-derived airway organoids. *EMBO Rep.* (2021) doi:10.15252/embr.202052058.
5. Spassky, N. & Meunier, A. The development and functions of multiciliated epithelia. *Nature Reviews Molecular Cell Biology* vol. 18 423–436 (2017).
6. Rock, J. R., Randell, S. H. & Hogan, B. L. M. Airway basal stem cells: a perspective on their roles in epithelial homeostasis and remodeling. *Dis. Model. Mech.* **3**, 545–56 (2010).
7. Bustamante-Marin, X. M. & Ostrowski, L. E. Cilia and mucociliary clearance. *Cold Spring Harb. Perspect. Biol.* **9**, (2017).
8. Boretto, M. et al. Development of organoids from mouse and human endometrium showing endometrial epithelium physiology and long-term expandability. *Development* **144**, 1775–1786 (2017).
9. Boretto, M. et al. Patient-derived organoids from endometrial disease capture clinical heterogeneity and are amenable to drug screening. *Nat. Cell Biol.* **21**, 1041–1051 (2019).
10. Turco, M. Y. et al. Long-term, hormone-responsive organoid cultures of human endometrium in a chemically defined medium. *Nat. Cell Biol.* **19**, 568–577 (2017).
11. Huang, C. et al. Clinical features of patients infected with 2019 novel coronavirus in Wuhan, China. *Lancet* **395**, 497–506 (2020).
12. Carvalho, T., Krammer, F. & Iwasaki, A. The first 12 months of COVID-19: a timeline of immunological insights. *Nat. Rev. Immunol.* **21**, 245–256 (2021).
13. Zhou, P. et al. A pneumonia outbreak associated with a new coronavirus of probable bat origin. *Nature* **579**, 270–273 (2020).
14. Hoffmann, M. et al. SARS-CoV-2 Cell Entry Depends on ACE2 and TMPRSS2 and Is Blocked by a Clinically Proven Protease Inhibitor. *Cell* **181**, 271-280.e8 (2020).
15. Walls, A. C. et al. Structure, Function, and Antigenicity of the SARS-CoV-2 Spike Glycoprotein. *Cell* **0**, (2020).
16. Wrapp, D. et al. Cryo-EM structure of the 2019-nCoV spike in the prefusion conformation. *Science* (80-.). **367**, 1260–1263 (2020).
17. Hikmet, F. et al. The protein expression profile of ACE2 in human tissues. *Mol. Syst. Biol.* **16**, e9610 (2020).
18. Jia, H. P. et al. ACE2 receptor expression and severe acute respiratory syndrome coronavirus infection depend on differentiation of human airway epithelia. *J. Virol.* **79**, 14614–21 (2005).
19. Qi, F., Qian, S., Zhang, S. & Zhang, Z. Single cell RNA sequencing of 13 human tissues identify cell types and receptors of human coronaviruses. (2020) doi:10.1016/j.bbrc.2020.03.044.
20. Chen, Y. et al. The Presence of SARS-CoV-2 RNA in Feces of COVID-19 Patients. *J. Med. Virol.* (2020) doi:10.1002/jmv.25825.
21. Wang, W. et al. Detection of SARS-CoV-2 in Different Types of Clinical Specimens. *JAMA - J. Am. Med. Assoc.* 2–3 (2020) doi:10.1001/jama.2020.3786.
22. Xiao, F. et al. Evidence for gastrointestinal infection of SARS-CoV-2. *Gastroenterology* (2020) doi:10.1053/j.gastro.2020.02.055.
23. Beumer, J. et al. A CRISPR/Cas9 genetically engineered organoid biobank reveals essential host factors for coronaviruses. *Nat. Commun.* **12**, 5498 (2021).
24. Gu, J., Han, B. & Wang, J. COVID-19: Gastrointestinal manifestations and potential fecal-oral transmission. *Gastroenterology* (2020) doi:10.1053/j.gastro.2020.02.054.
25. Cholankeril, G. et al. High Prevalence of Concurrent Gastrointestinal

- Manifestations in Patients with SARS-CoV-2: Early Experience from California. *Gastroenterology* **0**, (2020).
26. Driehuis, E. et al. Oral Mucosal Organoids as a Potential Platform for Personalized Cancer Therapy. *Cancer Discov.* **9**, 852–871 (2019).
 27. Haga, K. et al. Genetic manipulation of human intestinal enteroids demonstrates the necessity of a functional fucosyltransferase 2 gene for secretor-dependent human norovirus infection. *MBio* **11**, 1–10 (2020).
 28. Ettayebi, K. et al. Replication of human noroviruses in stem cell-derived human enteroids. *Science (80-.)*. **353**, 1387–1393 (2016).
 29. Estes, M. K. et al. Human Norovirus Cultivation in Nontransformed Stem Cell-Derived Human Intestinal Enteroid Cultures: Success and Challenges. *Viruses* **11**, 9–11 (2019).
 30. Zhou, J. et al. Differentiated human airway organoids to assess infectivity of emerging influenza virus. *Proc. Natl. Acad. Sci.* **115**, 6822–6827 (2018).
 31. Wang, M. et al. Remdesivir and chloroquine effectively inhibit the recently emerged novel coronavirus (2019-nCoV) in vitro. *Cell Res.* **30**, 269–271 (2020).
 32. Hernandez, A. V., Roman, Y. M., Pasupuleti, V., Barboza, J. J. & White, C. M. Hydroxychloroquine or Chloroquine for Treatment or Prophylaxis of COVID-19: A Living Systematic Review. *Ann. Intern. Med.* **173**, 287–296 (2020).
 33. Anzalone, A. V., Koblan, L. W. & Liu, D. R. Genome editing with CRISPR–Cas nucleases, base editors, transposases and prime editors. *Nat. Biotechnol.* **38**, 824–844 (2020).
 34. Geurts, M. H. et al. CRISPR-Based Adenine Editors Correct Nonsense Mutations in a Cystic Fibrosis Organoid Biobank. *Cell Stem Cell* **26**, 503–510.e7 (2020).
 35. Geurts, M. H. et al. Evaluating CRISPR-based prime editing for cancer modeling and CFTR repair in organoids. *Life Sci. Alliance* **4**, e202000940 (2021).
 36. Schene, I. F. et al. Prime editing for functional repair in patient-derived disease models. *Nat. Commun.* **2020 111 11**, 1–8 (2020).
 37. Driehuis, E. & Clevers, H. *CRISPR/Cas 9 genome editing and its applications in organoids*. vol. 312 G257–G265 (American Physiological Society, 2017).
 38. Kim, J., Koo, B.-K. & Knoblich, J. A. Human organoids: model systems for human biology and medicine. *Nat. Rev. Mol. Cell Biol.* **21**, 571–584 (2020).
 39. Kotwal, A. & Stan, M. Thyrotropin Receptor Antibodies—An Overview. *Ophthal. Plast. Reconstr. Surg.* **34**, S20–S27 (2018).
 40. van Santen, H. M., de Kraker, J., van Eck, B. L. F., de Vijlder, J. J. M. & Vulsma, T. High incidence of thyroid dysfunction despite prophylaxis with potassium iodide during 131I-meta-iodobenzylguanidine treatment in children with neuroblastoma. *Cancer* **94**, 2081–2089 (2002).
 41. Lebbink, C. A., Waguespack, S. G. & van Santen, H. M. Thyroid Dysfunction and Thyroid Cancer in Childhood Cancer Survivors: Prevalence, Surveillance and Management. in 1–14 (2021). doi:10.1159/000513805.
 42. Post, Y. & Clevers, H. Defining Adult Stem Cell Function at Its Simplest: The Ability to Replace Lost Cells through Mitosis. *Cell Stem Cell* **25**, 174–183 (2019).
 43. Cabanillas, M. E., McFadden, D. G. & Durante, C. Thyroid cancer. *Lancet* **388**, 2783–2795 (2016).
 44. Corvilain, B. et al. Treatment of adult Graves' disease. (2018) doi:10.1016/j.ando.2018.08.003.
 45. Michalopoulos, G. K. & Bhushan, B. Liver regeneration: biological and pathological mechanisms and implications. *Nat. Rev. Gastroenterol. Hepatol.* **18**, 40–55 (2021).
 46. Hu, S. & Monga, S. P. Wnt/-Catenin Signaling and Liver Regeneration: Circuit, Biology, and Opportunities. *Gene Expr.* **20**, 189–199 (2021).
 47. Planas-Paz, L. et al. The RSPO–LGR4/5–ZNRF3/RNF43 module controls liver zonation and size. *Nat. Cell Biol.* **18**, 467–479 (2016).

1

2

3

4

5

6

7

8

9

&

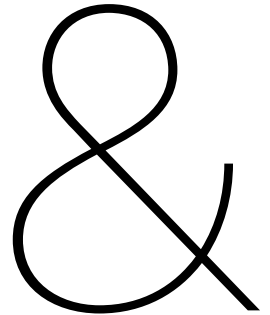
48. Yan, K. S. et al. Non-equivalence of Wnt and R-spondin ligands during Lgr5+ intestinal stem-cell self-renewal. *Nature* **545**, 238–242 (2017).
49. Zhang, Z. et al. Tissue-targeted R-spondin mimetics for liver regeneration. *Sci. Rep.* **10**, 13951 (2020).
50. Coulstock, E. et al. Liver-Targeting of Interferon-Alpha with Tissue-Specific Domain Antibodies. *PLoS One* **8**, e57263 (2013).
51. Huch, M. et al. Long-term culture of genome-stable bipotent stem cells from adult human liver. *Cell* **160**, 299–312 (2015).
52. Hu, H. et al. Long-Term Expansion of Functional Mouse and Human Hepatocytes as 3D Organoids. *Cell* **175**, 1591-1606.e19 (2018).

ADDENDUM

NEDERLANDSE SAMENVATTING

CURRICULUM VITAE AND
LIST OF PUBLICATIONS

DANKWOORD/ACKNOWLEDGEMENTS



NEDERLANDSE SAMENVATTING

Organoïden uit volwassen stamcellen als model voor een breed spectrum aan ziekten

(ook voor niet-ingewijden)

Dit proefschrift beschrijft de ontwikkeling van nieuwe modelsystemen om meer kennis te verkrijgen over de biologie rondom ziekten. Deze modelsystemen zijn ontwikkeld met behulp van volwassen stamcellen. Ons lichaam bestaat uit miljarden cellen die elk hun eigen functie uitvoeren. Al deze cellen zijn dochtercellen van stamcellen. Deze stamcellen kunnen worden onderverdeeld in embryonale en volwassen stamcellen. Embryonale stamcellen zijn enkel aanwezig tijdens de ontwikkeling en hebben de potentie om veel verschillende organen te worden. Volwassen stamcellen kunnen alleen in het volgroeide lichaam van het organisme worden geïdentificeerd en zijn gelimiteerd tot het orgaan waarin ze zich bevinden. De volwassen stamcellen zijn verantwoordelijk voor de vervanging van het weefsel waarin ze gelokaliseerd zijn met behulp van celdeling en opvolgende differentiatie in verschillende andere cel types. Deze vervanging is noodzakelijk als cellen verloren gaan door schade of bij natuurlijke weefselvernieuwing. Dit proces is essentieel voor de groei maar ook de homeostase van het lichaam. Door gebruik te maken van de potentie van stamcellen om epitheliale weefsels te vernieuwen, is het mogelijk om modelsystemen te ontwikkelen die sterk vergelijkbaar zijn met het orgaan waaruit de stamcellen zijn geïsoleerd. Als dit proces tot een driedimensionale structuur leidt die representatief is voor het weefsel en over langere tijd gekweekt kan worden, spreekt men van organoïden.

In dit proefschrift gebruiken wij volwassen stamcellen of organoïden uit volwassen stamcellen. Deze organoïden zijn sterk lijkend op het weefsel waaruit de stamcellen zijn geïsoleerd vanwege de vernieuwings- en differentiatie capaciteit van de volwassen stamcellen die aanwezig zijn in de kweek. Het kweken en vermenigvuldigen van epitheliale stamcel populaties leek voor lange tijd onmogelijk tot Sato en collega's de eerste dunne darm organoïden van muizen ontwikkelden. Door toepassing van vergelijkbare technieken werd het arsenaal aan organoïden uitgebreid met organoïden van onder andere de long, maag en lever van zowel muizen als humane origine. Door de sterke overeenkomst tussen organoïden en het orgaan in het lichaam zijn deze kweeksystemen bruikbaar als modelsystemen voor fundamentele biologie van gezond weefsel maar ook ziekten. Zowel fundamentele biologie als therapeutische interventies kunnen op deze manier bestudeerd worden zonder het gebruik van proefdieren of proefpersonen. De combinatie van recent ontwikkelde genetische modificatie technieken en organoïden opent daarbij de mogelijkheid om zowel bekende mutaties aan te brengen, en daarmee ziekten te veroorzaken en te bestuderen in de organoïden, als patiënt-specifieke mutaties te repareren in organoïden van patiënten. De gerepareerde organoïden zouden in de toekomst getransplanteerd kunnen worden ter vervanging van het zieke weefsel. Beschreven organoïden uit volwassen stamcellen hebben daardoor grote potentie om

1

2

3

4

5

6

7

8

9

&

gebruikt te worden als modelsystemen voor ziekte, maar ook als mogelijke nieuwe therapie. Het onderzoek in dit proefschrift maakt gebruik van eerder ontwikkelde organoïden technieken van de dunne darm en long, maar beschrijft ook de ontwikkeling van een nieuw organoïden kweekstelsel van de schildklier.

Verscheidene signalen zijn essentieel voor het behoud van volwassen stamcellen in het lichaam maar ook in kweeksystemen. Een van de meest bekende signaleringsroutes voor het onderhoud van stamcellen is de Wnt-signalering. Wnt-moleculen, liganden genoemd, worden uitgescheiden door omliggende cellen en binden aan receptoren die specifiek aanwezig zijn op stamcellen. Door binding van de liganden aan de juiste receptoren worden processen die noodzakelijk zijn voor het behoud van stamcellen geactiveerd. Verschillende niveaus van stimulatie leiden tot expansie, behoud of differentiatie van de stamcelpopulatie. Dit verklaart de strakke regulatie van Wnt-signalering die nodig is voor het functioneren van stamcellen en omliggend weefsel. Deze regulatie vindt plaats op het celmembraan waar de hoeveelheid receptoren gelijk staat aan de mate van potentiële activatie. Externe regulatoren zoals het molecuul R-spondin verhogen de potentie van Wnt-activatie door de afbraak van Wnt receptoren te verhinderen en daarmee receptor niveaus te verhogen. In de aanwezigheid van Wnt liganden leidt dit tot verhoogde Wnt-signalering en daarmee behoud en soms zelfs vergroting van de stamcelpopulatie. Het belang van R-spondin voor stamcelexpansie wordt benadrukt door de noodzaak van R-spondin in het medium van de volwassen stamcel organoïden. In parallel, manipulatie van de R-spondin-Wnt-signalering in het menselijk lichaam geeft mogelijkheden tot het stimuleren van regeneratie door expansie van de stamcelpopulatie.

In **hoofdstuk 1** beschrijven we de huidige stand van zaken omtrent luchtwegorganoïden en het gebruik ervan als modelsysteem voor ziekten. Hoewel de ontwikkelingen in luchtwegorganoïden elkaar snel opvolgen in het laatste decennium, blijven er hiaten in ons begrip en onze mogelijkheden om de juiste of complexere modelsystemen te ontwikkelen. Een voorbeeld van zo'n ontwikkeling van luchtwegmodelsystemen is beschreven in **hoofdstuk 2**. Met behulp van een nieuw differentiatieprotocol zijn wij in staat grotere aantallen trilhaarcellen waar te nemen in de luchtwegorganoïden. Dit protocol is toegepast op organoïden ontwikkeld uit patiëntenmateriaal met primaire ciliaire dyskinesie zodat deze organoïden gebruikt kunnen worden als modelsysteem voor de desbetreffende ziekte. Het gebruik van luchtwegorganoïden kan daarbij mogelijk bijdragen aan de huidige diagnostische onderzoeken.

In **hoofdstuk 3** beschrijven we het gebruik van organoïden als modelsysteem voor onderzoek naar COVID-19. We zetten niet alleen huidige technieken uiteen, maar kijken ook vooruit naar mogelijk nieuwe modelsystemen voor SARS-CoV-2 infectiestudies en potentieel komende pandemieën. **Hoofdstuk 4** illustreert de voordelen van het gebruik van zowel driedimensionale dunne darmorganoïden als tweedimensionale kweken afkomstig van luchtwegorganoïden voor het onderzoek naar SARS-CoV-2 infectie. Door het gebruik van de organoïden werd duidelijk dat ook delende enterocyten in de dunne darm geïnfecteerd kunnen worden door SARS-CoV-2. Aangezien COVID-19 vooral

gerelateerd is aan luchtwegproblemen, beschrijven we de ontwikkelingen binnen huidige- en nieuwe modelsystemen voor SARS-CoV-2 infectie in **hoofdstuk 5**. Een voorbeeld van een recent ontwikkeld modelsysteem met behulp van luchtwegorganoïden is beschreven in **hoofdstuk 6**. Hier beschrijven we de ontwikkeling van een bronchioalveolair kweekstelsel en de infectie van SARS-CoV-2 in deze cellen. Infectie van SARS-CoV-2 in deze celkweek stimuleert de interferon signaleringsroute die vergelijkbaar is met wat waarneembaar is in COVID-19 patiënten.

In **hoofdstuk 7** beschrijven we de ontwikkeling van een nieuw organoïdensysteem waarbij we mini-orgaantjes kweken van folliculaire cellen van de schildklier. Volwassen stamcellen uit muizen en humane schildklier werden gebruikt om dit nieuwe kweekstelsel op te zetten. De cellen in de organoïden brengen de genen verantwoordelijk voor schildklierhormoonproductie tot expressie en scheiden actief schildklierhormoon uit na stimulatie. Daarbij kunnen de organoïden gebruikt worden als modelsysteem voor de ziekte van Graves. Hiermee is dit het eerst beschreven organoïdensysteem voor het modelleren van auto-immuunziekten.

Hoofdstuk 8 trekt de ontdekkingen over volwassen stamcellen en de essentie van Wnt-signalering van organoïden naar het lichaam. We presenteren een geoptimaliseerd protocol voor het produceren van Wnt-potentiator R-spondin. Vervolgens gebruiken we dit recombinant R-spondin via systemische injectie om de rol van R-spondin in de lever te onderzoeken. We observeren verhoogde celdeling in hepatocyten tot zeven dagen na injectie. Deze proliferatie is niet beperkt tot de zones in de lever met actieve Wnt-signalering.

Hoofdstuk 9 vat de bevindingen van dit proefschrift samen en bediscussieert de implicaties. Daarbij ga ik in op de applicatie van de modelsystemen uit dit proefschrift en de toekomstige mogelijkheden voor nieuwe modelsystemen voor overige ziekten.

1

2

3

4

5

6

7

8

9

&

CURRICULUM VITAE

Jelte van der Vaart was born on the 2nd of January 1994 in Zwijndrecht, the Netherlands. He graduated from Walburg College in Zwijndrecht in 2012 majoring Nature and Health and Nature and Technology track at gymnasium level. He obtained his Bachelor of Science degree in Biomedical Sciences from the Utrecht University in 2015. During his bachelor 's degree, he conducted research at the Erasmus Medical Centre in Rotterdam, the Netherlands. In 2015, he enrolled in the Biomedical Sciences research Master's program Cancer, Stem Cells and Developmental Biology at the Utrecht University. His first internship was performed at the Hubrecht Institute working in R-spondin signalling in the liver in the laboratory of Prof. Hans Clevers. He spent his final internship at the Department of Oncology at the University of Oxford, Oxford, United Kingdom. He worked on the development of pancreatic ductal organoid systems to study the role of RASSF1A signalling in tumour development at the laboratory of Prof. Eric O'Neill. He graduated from the Master's program and obtained his Master of Science degree in 2017. In that same year, he started as PhD-student in the laboratory of Prof. Hans Clevers at the Hubrecht Institute in Utrecht, the Netherlands. The results of this work is presented in this thesis.

LIST OF PUBLICATIONS

(*: shared first author, †: shared corresponding author)

Laura Novellasdemunt, Anna Kucharska, Cara Jamieson, Maria Prange-Barczynska, Anna Baulies, Pedro Antas, **Jelte van der Vaart**, Helmuth Gehart, Madelon M Maurice & Vivian Sw Li (2020). NEDD4 and NEDD4L regulate Wnt signalling and intestinal stem cell priming by degrading LGR5 receptor. *The EMBO journal*, 39(3), e102771.

Mart M Lamers*, Joep Beumer*, **Jelte van der Vaart***, Kèvin Knoops, Jens Puschhof, Tim I Breugem, Raimond B G Ravelli, J Paul van Schayck, Anna Z Mykytyn, Hans Q Duimel, Elly van Donselaar, Samra Riesebosch, Helma J H Kuijpers, Debby Schipper, Willine J van de Wetering, Miranda de Graaf, Marion Koopmans, Edwin Cuppen, Peter J Peters, Bart L Haagmans† & Hans Clevers† (2020). SARS-CoV-2 productively infects human gut enterocytes. *Science*, 369(6499), 50-54.

Joris H Hageman, Maria C Heinz, Kai Kretzschmar, **Jelte van der Vaart**, Hans Clevers & Hugo J G Snippert (2020). Intestinal regeneration: regulation by the microenvironment. *Developmental Cell*, 54(4), 435-446.

Jelte van der Vaart & Hans Clevers (2021). Airway organoids as models of human disease. *Journal of Internal Medicine*, 289(5), 604-613.

Mart M Lamers*, **Jelte van der Vaart***, Kèvin Knoops, Samra Riesebosch, Tim I Breugem, Anna Z Mykytyn, Joep Beumer, Debby Schipper, Karel Bezstarosti, Charlotte D Koopman, Nathalie Groen, Raimond B G Ravelli, Hans Q Duimel, Jeroen A A Demmers, Georges M G M Verjans, Marion P G Koopmans, Mauro J Muraro, Peter J Peters, Hans Clevers[†] & Bart L Haagmans[†] (2021). An organoid-derived bronchioalveolar model for SARS-CoV-2 infection of human alveolar type II-like cells. *The EMBO journal*, 40(5), e105912.

Maarten H Geurts*, **Jelte van der Vaart***, Joep Beumer*[†] & Hans Clevers[†] (2021). The Organoid Platform: Promises and Challenges as Tools in the Fight against COVID-19. *Stem Cell Reports*, 16(3), 412-418.

Marie Bannier-Hélaouët*, Yorick Post*, Jeroen Korving, Marc Trani Bustos, Helmuth Gehart, Harry Begthel, Yotam E Bar-Ephraim, **Jelte van der Vaart**, Rachel Kalmann, Saskia M Imhoff & Hans Clevers (2021). Exploring the human lacrimal gland using organoids and single-cell sequencing. *Cell Stem Cell*, 28(7):1221-1232.e7.

Jelte van der Vaart, Mart M Lamers, Bart L Haagmans & Hans Clevers (2021) Advancing lung organoids for COVID-19 research. *Disease Models & Mechanisms*, 14(6):dmm049060

Joep Beumer*, Maarten H Geurts*, Mart M Lamers*, Jens Puschhof, Jingshu Zhang, **Jelte van der Vaart**, Anna Z Mykytyn, Tim I Breugem, Samra Riesebosch, Debby Schipper, Petra B van den Doel, Wim de Lau, Cayetano Pleguezuelos-Manzano, Georg Busslinger, Bart L Haagmans[†] & Hans Clevers[†] (2021). A CRISPR/Cas9 genetically engineered organoid biobank reveals essential host factors for coronaviruses. *Nature Communications*, 12(1):5498

Jelte van der Vaart, Lena Böttinger, Maarten H Geurts, Willine J van de Wetering, Kèvin Knoops, Norman Sachs, Harry Begthel, Jeroen Korving, Carmen Lopez-Iglesias, Peter J Peters, Kerem Eitan, Alex Gileles-Hillel & Hans Clevers (2021). Modelling of primary ciliary dyskinesia using patient-derived airway organoids. *EMBO Reports*, 22(12):e52058

Jelte van der Vaart, Lynn Bosmans, Stijn F. Sijbesma, Kèvin Knoops, Willine J. van de Wetering, Henny G. Otten, Harry Begthel, Inne H.M. Borel Rinkes, Jeroen Korving, Eef G.W.M. Lentjes, Carmen Lopez-Iglesias, Peter J. Peters, Hanneke M. van Santen, Menno R. Vriens & Hans Clevers (2021). Adult mouse and human organoids derived from thyroid follicular cells and modelling of Graves' hyperthyroidism. *Proceedings of the National Academy of Sciences*, 118(51):e2117017118

Jelte van der Vaart, Johan van Es, Wim de Lau, Laura Zeinstra, Harry Begthel, Henner F. Farin, Jeroen Korving, Helmuth Gehart & Hans Clevers. Bacterially produced R-spondin3 increases hepatocyte proliferation independent of liver zonation. (manuscript in preparation).

1

2

3

4

5

6

7

8

9

&

ACKNOWLEDGEMENTS/DANKWOORD

This thesis was established due to the direct and indirect involvement of many people. Projects always require scientific teamwork and motivation as well as sparring partners to generate relevant data. Over the past four years, I have not only grown professionally but also personally. Scientific achievements can only be collected when the right environment is created by those near to you. It is why I would like to highlight some amazing people to whom I owe a lot of gratitude and who deserve the recognition of their contribution to the thesis.

Als eerste wil ik natuurlijk **Hans** bedanken voor de mogelijkheid om dit traject te volbrengen binnen je groep. Onder jouw toezicht is de groep een ongelooflijk succesvol lab geworden waarbij de standaard van data hoog ligt en er altijd wordt gewerkt met een grote publicatie als doel. Dat dit tijd kost en dat daardoor kleinere groepen ons kunnen scoopen, hebben we gemerkt met het schildklierproject. Toch kon jij toen maar ook tijdens mijn gehele PhD-traject mijn projecten naar nieuwe hoogtes sturen. Je professionaliteit om binnen enkele minuten weer up-to-date te zijn met ieder project en de achtergrond verbaasd mij elke keer opnieuw. Het lab heeft zich uitgespreid over een heel divers veld waarbij jij als middelpunt altijd het overzicht houdt over alle projecten. Niet alleen professioneel, maar ook persoonlijk is er bij jou altijd een goed gesprek te halen. De laatste jaren werd je motto "Just because you can do it, does not mean you have to do it". Dit is een mantra voor mij geworden en hopelijk ook voor de rest van het lab. Hans, bedankt voor de geweldige tijd die ik mocht hebben in je groep!

De leden van de leescommissie, **Prof. Dr. Saskia van Mil**, **Prof. Dr. Gerlof Valk**, **Prof. Dr. Frank van Kuppeveld**, **Prof. Dr. Reinoud Gosens** en **Prof. Dr. Rob Coppes**, wil ik graag bedanken voor het kritisch lezen en het goedkeuren van het manuscript.

Frank en **Madelon**, mijn PhD commissie, wil ik bedanken voor de gesprekken die wij jaarlijks hebben gehad. Hoewel dit slechts 1x per jaar gebeurde heeft het altijd mij geholpen de juiste focus te houden in projecten en een fijn gevoel gegeven dat ik goed op weg was. In het specifiek wil ik **Frank** bedanken voor altijd de kritische vraag te stellen "Oké, en wat kunnen we ermee?". Hierdoor bleef ik de focus houden op wat belangrijk was en niet experimenten doen omdat het kon (zie ook motto van Hans hierboven). **Madelon**, jouw directe visie op projecten en je focus op het afronden van projecten voordat de leuke nieuwe projecten werden gestart, heeft een groot aandeel gehad aan de publicaties in dit proefschrift. Ik ben dan ook vereerd om aan de slag te gaan als postdoc in jouw lab.

Mijn trouwe rechterhanden de afgelopen tijd, paranymfen **Eline** en **Maarten**. Ondanks dat jullie een drukke periode zelf hadden met het afronden van jullie eigen PhD-traject,

hebben jullie mij de afgelopen maanden bijgestaan bij alles rondom de borrels en feesten. Al sinds onze bachelor, **Eline**, klikte het goed tussen jou, mij en natuurlijk de rest die verderop genoemd zal worden. Doordat wij samen redelijk gelijklieden in onze studie heb ik veel aan je inzichten en hulp gehad. Je directheid en eerlijkheid moet je zeker niet verliezen! Je was altijd in de buurt ook toen ik de gesprekken tussen ons nodig had en dat zal ik nooit vergeten. En dan **Maarten**, jongen we gaan jouw naam nog vaak in de komende stukken tegenkomen. Hoewel sommige mensen je uitgesproken mening als aanvallend aanvaren, heb ik altijd genoten van onze gesprekken en discussies. Je persoonlijkheid om altijd het onderste uit de kan te halen wanneer je je thuis voelt is bewonderingswaardig. Blijf kritisch want daar red je het wel mee!

Lieve **Ed** en **Elsa**, pap en mam, natuurlijk zijn jullie belangrijk geweest voor dit proefschrift. Het was niet altijd makkelijk om een drukke PhD-student als zoon te hebben en dit heeft ook zeker geleid tot (te) weinig keren op de koffie bij elkaar. Toch bleven jullie mij steunen. Jullie geduld wanneer ik weer eens even moest luchten over alles wat weer niet liep zoals het moest, heeft mij soms de rust gegeven die niet altijd makkelijk te vinden was. Ook mijn lieve zussen, **Tjitske** en **Nienke**, hebben mij altijd gesteund. Onze gezellige spelletjesmiddagen waren altijd een goed moment voor ontspanning. Hoewel Hendrik-Ido-Ambacht en Zwijndrecht toch een stukje van Houten liggen was het altijd heerlijk om de reis te maken.

Wat ben ik trots om ook jullie, **opa van der Vaart** en **oma Smit**, nog mijn proefschrift te kunnen overhandigen. Hoewel het misschien niet altijd duidelijk was wat ik nu precies in dat verre Utrecht deed, was u altijd geïnteresseerd in hoe het ging. Dat het jaren werk was en moeilijk, was een goede samenvatting. De vele kopjes thee en chocolaatjes hoop ik nog vaak met u te mogen delen. Op naar de 100!

Ook de rest van de **familie van der Vaart** en **familie Smit** wil ik bedanken voor de eeuwige interesse en gezelligheid.

Mijn grootste supporter, **Veerle**. Wat een gekke tijd hebben wij samen doorgemaakt. Hoewel je ook mijn collega was, konden we die zaken goed uit elkaar houden. Op de fiets naar ons mooie huis in Houten was het heerlijk om met jou nog even de dag door te nemen. Je realisme heeft mij vaak geholpen uit de stress te komen. Hoewel je het soms toestond dat ik thuis door werkte, was je gelukkig ook vaak streng genoeg om mij te laten genieten van alles buiten het werk. Mede daardoor ligt hier nu een mooi en effectief geschreven proefschrift. Inmiddels zijn ook Jip en Mauw helemaal blije katten bij ons thuis en dat komt vooral door je verzorgende en lieve karakter. Je enthousiasme steekt mij elke dag nog aan dus blijf vooral jezelf. Ik ben super trots op je!

Ook **Petra**, **Thijs** en **Merlijne** verdienen een plekje in dit dankwoord. Vanaf dag 1 heb ik mij op mijn gemak bij jullie gevoeld. Jullie hebben mij opgenomen in de familie en

1

2

3

4

5

6

7

8

9

&

daar ben ik enorm trots op. Hoewel we vanwege de afstand elkaar niet vaak zien, is het altijd de lange rit waard om weer in America aan te komen. Jullie kritische maar vooral geïnteresseerde blik op mijn projecten maar ook het onderzoek in het algemeen opende soms nieuwe mogelijkheden waarmee ik aan de slag kon. Ik hoop nog lang de ritjes Houten-America te mogen maken!

Members of the current and former Clevers lab. Thank you all for the amazing environment in which great science meets great people. Keep up the work and do not worry, Martina can moderate and organise lab meetings even better. The other side office deserves a top spot in this list: **Maarten**, as discussed before, your critical look on projects and extensive CRISPR knowledge makes you an amazing scientific addition to the lab and far more than just a handy person to get mutations in organoids. In addition, your sarcastic remarks and elaborate sense of humour lifts the spirit of the lab and office, so keep that alive. Our first Spanish office member: **Cayetano**. I will miss the unexpected Spanish curse words when the computer did not do what you wanted it to do. My Spanish vocabulary is therefore limited but very effective. You have an amazing view on science and in combination with your warm character and always willingness to play some games of darts, makes you a great person. It's a small step from Spain to Spain: **Carla**. I've always enjoyed our talks and your relaxed attitude towards our somewhat chaotic office. You are one of the best-organised scientists I know and always have your experiments on fleek with proper controls. Whenever we discussed each other's data, we always knew you had compared the right data to the right control. Keep up that attitude and you will do great! Apart from the scientific talks, I've always enjoyed your relaxed but hilarious comments and the great outings at your place. Our most senior office member: **Amanda**. As a postdoc, your experience was always highly valued in our office. Yet your gullibility also allowed for hilarious conversations. Thank you for all the kind words during the harder times and setting up many of our office outings (or well at least starting the conversation so someone else could organise). Don't forget to take some hours off outside of the lab to run or bike. Nevertheless, do not overdo sports since we know what comes from it. Honorary office member **Lisanne**. Even though you were often busy working, and not appreciating the chaotic basketball matches in our office, we could always find time to chat up about TV shows, Dutch policies or life itself. Thank you for listening when I kept talking and keeping our office in line when needed to. Our latest addition to the office: **Nella**. While initially you might have believed our office was more fun, you have now probably already labelled us as insane. Keeping the English as main language increased the general chat reputation of our office. We unfortunately only crossed paths for a few months but happy to see the amount of lung-interested people remain constant in the office. All in all, office for life!

All current and former PhD students: **Frans, Else, Joep, Jens, Kim, Yorick, Kadi, Margit, Maarten, Cayetano, Carla, Fjodor, Lulu, Evelyn, Marie, Adriana, Seok-Young, Joost,**

Martina, Emma, Laurens, Ninouk and Sam. Frans, hoewel we elkaar niet zo vaak op het lab zijn tegen gekomen, heb ik erg gezellige herinneringen aan onze gesprekjes tijdens de PhD-outings. Houd die gezelligheid vast en ik weet zeker dat alles goed komt. **Else**, aangezien jij mijn voorbeeld was als eerst promovende PhD tijdens mijn PhD-tijd, ben ik altijd erg onder de indruk geweest van je wetenschappelijke adviezen. Naast deze gouden tips was er ook altijd veel lol te beleven met jou. Die goedwerkende combi van gezelligheid en wetenschap moet je koesteren. Onze expert en vast aanspreekpunt van het lab wanneer er foto's achter de confocal gemaakt moeten worden, **Joep**. Niet alleen je bezoeken aan onze office waren altijd een genot, maar ook onze tripjes van en naar Rotterdam op een verlaten snelweg met achterin de eerste corona samples zal ik nooit vergeten. Je staat altijd open voor een goede discussie over wetenschap maar ook voor een gesprek over compleet random onderwerpen ga je niet uit de weg. Mochten ze ooit een MRI-scan maken van jouw geheugen, zou je die dan willen opsturen want volgens mij vergeet jij nooit iets, hoe onzinnig ook. Kom maar door met al die feitjes! **Jens**, what a guy, what a guy. We have had some serious subjects changing to random while talking, but I've always enjoyed our little conversations about anything. Your scientific input and out-of-the-box thinking has advanced many of the current projects in the Clevers lab and will spark some great projects in your own lab. Go get them! Mijn reismaatje naar Boston, **Kim**. Onze reis samen in Boston en omgeving was een geweldige ervaring. Niet alleen tijdens het congres maar ook de dagen eromheen had je altijd top onder controle. Hoewel je vroeg wakker was, respecteerde je mijn nachtrust en zat er als ik bij het ontbijt aankwam altijd een gezellige Kim op mij te wachten. **Yorick**, hoewel je onderdeel uitmaakte van de wicked 3Js (hoewel Yorick niet met een J begon), denk ik wel dat onze karakters op elkaar lijken. Je bedachtzaamheid die soms omsloeg naar complete wanorde heeft altijd veel sfeer gebracht in de PhD-groep. De mooie positie in het verre Amerika onderstreept daarbij de waarde die je bent voor de wetenschap. Estonian representative **Kadi**. Starting together in the corridor as students has really ignited a true friendship. After my year of absence, I returned to a warm nest since you were my bench neighbour. Our, or mostly your, what-is-yours-is-mine policy worked perfectly and this efficiency has led to this thesis of course. While you wouldn't always agree on the music played in TC, I could always cheer you up with some Bruno Mars or ABBA. I will definitely visit you soon in Copenhagen since it has been a too long time no see. Mede-Houtenaar en collega vanaf het eerste moment **Margit**. Net als Kadi begonnen wij op de gang van het Clevers lab. Toen was al duidelijk dat met jou wel een feestje te bouwen is. Dat idee heb je altijd onderstreept wanneer het kon, maar ook onze diepgaande gesprekken hebben mij altijd goed gedaan. Je enthousiasme en gezelligheid zijn aanstekelijk en neem die dan ook mee naar je huidige baan. We gaan elkaar vaak nog zien want Houten is niet zo heel groot. **Maarten, Cayetano and Carla**, see above :P. Hoogachtende **Fjodor**, je niet uit te putten interesse in de medemens zorgden er altijd voor dat gesprekken met jou nooit stilvielen. Daarbij is jouw oneindige culinaire kennis wel een vervelende bijkomstigheid rond lunch of dinertijd. Ik krijg altijd trek als je weer eens verteld hoe jij een heel kruidenrek toevoegt

1

2

3

4

5

6

7

8

9

&

aan de bekende bolognaise saus. Ook je medische kennis was handig om eens te peilen wanneer ik in mijn project weer een nieuw ziektebeeld of medicijn tegenkwam. Het gaat een aderlating worden je niet meer elke dag te spreken. **Lulu**, you started as a shy PhD-student but as soon as you compared me to Sheldon Cooper during one of the PhD outings, I knew there was a lot more to you. You have developed into a cosy co-PhD-student with whom I definitely shared many funny moments, especially when you were the only colleague at the Hubrecht during lockdown. **Evelyn**, it is a shame that you and the others were all the way over at the PMC, which made our interactions few. It has however always been a pleasure when we had a little chat whenever I visited the PMC. I wish you all the best! Bonjour **Marie**, my fellow badminton player. Up until this point, we have never crossed rackets, however. Being part of the wave of new PhD-students together with Caye, Maarten and me does create a somewhat special bond in four years. Your sarcasm and to-the-point character has sometimes left me speechless, yet these moments are overshadowed by the jokes and laughs we shared. **Adriana**, starting in the EEC-team is not easy when there are two older PhD-students already highly involved but you have shown that it definitely is possible to establish yourself in this situation. You have grown from a somewhat insecure master student to a talkative, scientifically brilliant PhD-student. I've really enjoyed our conversations during lunch but also our short science discussions. Keep up the good work! By the way, you should move apartments since the stories that you tell are not very promising. Thyroid buddy **Seok-Young**, we have only met early 2020, which definitely is unfortunate since I needed your fresh view on the thyroid carcinoma efforts. I wish you all the best with the remainder of the projects and keep that smile up! **Joost**, een heerlijke Nederlandse additie aan het PhD-team, maar wat voor een. We kennen elkaar nog maar kort helaas, maar ik kan nu al zien dat je een mooie toevoeging gaat vormen aan de groep. Ook je projecten zijn misschien wat nieuw voor de groep maar net zo interessant en belangrijk! **Martina**, our conversations were always hilarious. Whether it was about the teratoma project or just general conversation, it always ended with a good laugh. It's a shame we won't be able to work together on the teratoma project because I think you will become a great scientist. **Emma**, your enthusiasm has made my mood several times. I hope you will enjoy your time at the Hubrecht and PMC combined. And don't stop practicing Mario Kart. **Laurens**. Ook wij hebben maar kort kennis mogen maken tijdens de laatste BBQ bij Hans. Je zit volgens mij helemaal op je plek in het PMC en ik wens je dan ook heel veel succes en vooral plezier de komende jaren! Last but not least, **Ninouk** en **Sam**. Begonnen net voor of net na dat ik het lab verliet, heb ik jullie natuurlijk wel meegemaakt als student. Jullie drive om terug te komen bij het Clevers lab zal je zeker geluk brengen in het onderzoek wat je als PhD gaat uitvoeren in de groep.

All the current and former Postdocs: **Rosie, Lin, Daniel, Daisong, Delilah, Chris, Guiwei, Elena, Talya, Matteo, Sangho, Jochem, Nella, Tomo, Amanda, Karin, Oded, Yoshi, Benedetta, Kai, Yotam, Helmuth, Georg, Marrit, Huili** and **Lena**. My master supervisor

and early PhD mentor, **Helmuth**. I remember my first days in the lab were slightly delayed because you just became a father. A few years and kids later, we have worked together on the RSPO project and spend quite some time figuring out where that project would end up. Sleep deprived mouse surgeries because of your kids, long days at the RNA sequencing bench looking at magnetic beads drying and the great discussions about the scRNAseq data really encouraged me to stay in science. You've taught me most of the techniques used in this thesis so you can be proud! Your critical and overthought remarks on our project but also science in general really pushed me into always thinking about the main question of the project. Unfortunately, the RSPO project has not found its way to a journal but it could not be missed from my thesis. **Lena**, what started as maybe a little bit of help with cloning plasmids, turned into a full collaboration on ciliated cells. It's a shame we could not finish the paper together but I wish you all the best with your career.

Alle huidige en voormalige research analisten, lab managers, senior researchers en PA's van het Clevers lab: **Carola, Charelle, Mandy, Gijs, Stieneke, Karien, Johan, Laura, Lisanne, Harry, Jeroen, Veerle, Annemieke, Masha, Marc, Maaike, Wim, Sigrid, Eveliene, Priyanka, Milou en Anjali. Carola**, hoewel wij altijd het verst van elkaar zaten in de kweek was het altijd een gezellige boel. Met een heerlijke vrijdagmiddag muziekje op hebben wij veel tijd in dezelfde ruimte doorgebracht. Nu zal je toch vaker zelf je telefoon moeten verbinden met de stereo voor dezelfde gezelligheid. Ook je gezelligheid bij de other other side office en mijn office zal ik niet snel vergeten. **Stieneke**, jouw input in het Clevers lab is zwaar ondergewaardeerd. Door jou draait het lab op rolletjes en alle papers uit het lab komen eigenlijk gewoon door jou. Je bent erbij vanaf het begin en daarom is het Clevers lab toch ook een beetje het Stieneke lab. **Gijs**, ik wil je bedanken voor alle hulp omtrent het sequencen en de analyse die volgde. **Harry** en **Jeroen**, hoewel jullie vaak als één persoon worden genoemd wil ik jullie afzonderlijk bedanken voor alle hulp. 99% van de studies uit het Clevers lab zijn bestempeld met jullie vrachtwagen aan ervaring met organoid embedding en histologie. Helaas zal jij, Jeroen, nu iemand anders moeten vinden die je muizen uit de sluis ophaalt. Jullie essentiële functies voor het snelle en goede onderzoek uit het lab zal ik nooit vergeten. **Johan**, jouw administratie en management achter de schermen is door veel mensen onderschat. Als financieel bewaker van de groep zorg jij ervoor dat er überhaupt nog onderzoek gedaan kan worden. Daarnaast waardeerde ik altijd erg je mening over de muisproeven en protocollen. **Laura**, onze gezellige gesprekjes bij de bench hebben mij altijd veel plezier tijdens het pipetteren en erbuiten gegeven. Ook je input over kloneringen hebben aan het begin van mijn PhD zeker geholpen om het gewenste eindresultaat te krijgen. Vergeet vooral niet zaken uit handen te geven en te vertrouwen op dat alles wel goed komt! **Annemieke**, de PA van de eeuw! Hoewel een kopje koffie halen soms uitliep tot 2 koppen koffie in de deuropening bij je kantoor, heb ik altijd veel genoten van de gezellige gesprekjes. Je drive om alles snel maar vooral goed geregeld te krijgen, waardeer ik enorm. Het is

1

2

3

4

5

6

7

8

9

&

jammer dat we niet meer direct samenwerken maar ik weet je te vinden mocht ik nog iets nodig hebben.

Lynn en Stijn. Ik heb de eer gehad om jullie te begeleiden als studenten. Jullie scherpe leercurves wijzen op jullie motivatie en drang om te leren. Hoewel jullie allebei een andere route hebben gekozen weet ik zeker dat jullie allebei goed terecht gaan komen!

All my collaborators, in particular **Mart, Bart, Kèvin, Willine, Carmen, Peter, Alex, Kerem, Anneta, Jorieke, Renate, Kelsey, Anne, Onno, Menno** and **Hanneke**. **Mart** en **Bart**, onze samenwerking in de COVID-projecten waren vernieuwend en lieten zien dat virologen en celbiologen prima samen kunnen werken. **Kèvin, Willine, Carmen** and **Peter**, your electron microscopy expertise exceeded my expectations every single time. Your great help in the COVID-projects as well as the organoid projects really underlined the essence of good collaborations. The team from Israel, **Alex** and **Kerem**. Although we have never met in person, the contact was always valuable after Lena left the lab. Together we could bring clinical impact to the PCD organoids. Het huidige en voormalige UPORT-team: **Anneta, Jorieke, Renate, Kelsey, Anne** en **Onno**. Zonder jullie had er nooit een paper gelegen over welke organoid dan ook. Jullie zijn een essentiële schakel in het proces van patiënt naar organoids. Ik waardeerde altijd jullie duidelijke communicatie en gezellige kletspraatjes bij het ophalen van de weefsels. **Menno** en **Hanneke**, mijn endocriene kliniek team. Jullie enthousiasme over het project en de mogelijkheden hebben mijn motivatie alleen maar meer aangewakkerd voor het project. Daarbij heeft jullie klinische input geleid tot een modelsysteem die de juiste vragen kan beantwoorden voor patiënten.

Many thanks to my new lab, the **Madelon Maurice Lab!** I've been welcomed into a passionate research group with open arms. I'm excited to continue working on the disease modelling in organoids in the lab.

De meiden uit Utrecht, after tentamen kletsers, toekomstig van der Vaart-lab, of onder welke noemer wij onze groep al wel hebben genoemd: **Eline, Lisette, Suzanne** en **Saskia**. Wat begon als gezellig na elk tentamen een hapje eten of drinken in de stad, is geëindigd in een jaarlijkse vakantie en heel veel gezellige middagen en avonden. Hoewel we elkaar niet zo heel vaak zien, is onze groepsapp een heerlijke plek om even over (lab gerelateerde) zaken te zeuren. De steun die ik van jullie heb gehad de afgelopen jaren hoop ik even hard terug te geven wanneer nodig.

Een belangrijke plek verdienen jullie, **familie Huygens** en **familie Nugteren** met in het specifiek **Simone, Marcel, Heleen, Charlie** en natuurlijk **Eveline**. Jullie begrip wanneer ik weer door de file naar huis moest komen om vervolgens 5 minuten na thuiskomst naar

training te moeten, heeft mij de kracht gegeven om door te blijven gaan. Jullie warme familiesfeer zorgde altijd voor ontspanning. Lieve **Eveline**, jou wil ik in het bijzonder bedanken voor je geduld, zorgzaamheid en doorzettingsvermogen. Zonder jou had ik dit traject nooit vol kunnen houden. Tijdens mijn keuzestress heb jij mij gestimuleerd en gesteund om te starten bij het Clevers lab, hoewel je wist dat dit veel van onze tijd zou vragen. Maar waar ik ook was, Utrecht, Oxford of verder weg, je was er altijd voor mij.

Zoals studenten zeggen, mijn vvv'tjes, vrienden van vroeger, **Martijn, Dennis, Wessel, Olivier, Tu, Johnny, Koen, Ricardo** en **Tu**. We spraken elkaar nog vaak in Zwijndrecht maar inmiddels is iedereen van ons uitgevlogen naar andere delen van Nederland. Toch vinden we zo nu en dan de tijd om weer bij elkaar te komen. Eenieder van jullie heeft los en als groep bijgedragen aan dit proefschrift door er te zijn wanneer nodig maar ook door juist even een avondje te denken aan die goede oude tijd waarbij je ergste probleem het 8^{ste} uur was. Onze legendarisch examenreis zal zeker nog eens een goed weekend als opvolging krijgen en mijn koffer staat al klaar!

De ouwe lullen, **Joris, Joep, Ravian, Dennis** en **Axel**. Bij elkaar gekomen tijdens de Master hebben we mooie herinneringen mogen maken met zijn allen. Een weekendje Leuven en meerdere borrelavonden later zijn we allemaal verspreid over Nederland en binnenkort zelfs ook Spanje. We houden de borrels erin!

Alle **spelers van ABC Swindregt** en **BC Iduna**. Gedurende de intensieve vier jaar was het altijd lekker om een shuttle te slaan en alle energie kwijt te raken. Met naam wil graag mijn teamgenoten van de afgelopen 4 jaar bedanken voor zelfs twee kampioenschappen: **Henk, Roderick, Evelien, Inge, Sonja, Mark, Rob, Marco, Esther, Linsey, Cynthia, Arnoud, Armando, Renee** en **Joke** van ABC Swindregt en **Brendan, Lisa, Lisa, Floyd** en **Stefanie** van BC Iduna.

Alle **leden, bestuursleden** en **vrijwilligers van Waterscouting de Vikings**. Elke zaterdag was het tijd om het lab te verlaten en af te reizen naar Zwijndrecht. De opkomsten maar ook onze kampen waren een goede afleiding van het werk. Maar ook als ik even niet konden helpen doordat projecten toch echt voor gingen waren jullie begripvol. In het specifiek wil ik mijn directe huidige en oud-medeleiding van de Birka's bedanken: **Vivian, Manon, Myra**, en **Eveline**. In het speciaal nog **Joachim** voor het maken van de prachtige omslag van het proefschrift

Fellow members of the CSND PhD committee 2018-2019, **Samy, Maarten, Imogen, Jet, Joep** and **Jeff**. Organising borrels, seminars and the retreat was lots of fun with you all. Our regular meetings at the Hubrecht were always filled with laughter but eventually

1

2

3

4

5

6

7

8

9

&

great activities were planned. The big success of our retreat with 100+ PhD-students in Stadskanaal topped up an amazing year together. Thank you all so much.

To all people that are not mentioned by name, know that I am grateful for your support and help in the past years!

